Dissertation zur Erlangung des Doktorgrades
der Fakultät für Chemie und Pharmazie
der Ludwig-Maximilians-Universität München

From small molecules to enzymes –
Biomolecular interaction analysis via a DNA-based biosensor

Irene Ponzo

aus

Velletri, Italien

2023

Erklärung

Diese Dissertation wurde im Sinne von § 7 der Promotionsordnung vom 28. November 2011 von Herrn Prof. Dr. Thomas Carell betreut.

Eidesstattliche Versicherung

Diese Dissertation wurde eigenständig und ohne unerlaubte Hilfe erarbeitet.

München, 02.11.2023

Irene Ponzo

.....

Dissertation eingereicht am	08.11.2023
1. Gutachter:	Prof. Dr. Thomas Carell
2. Gutachter:	Prof. Dr. Friedrich Simmel
Mündliche Prüfung am	07.12.2023

Life is kinetics

Acknowledgements

First and foremost, I express my gratitude to every person who assisted me and supported me during the writing of this dissertation.

I express my gratitude to Prof. Thomas Carell and Prof. Friederich Simmel, who supervised my thesis, and to Dr. Markus Müller, who helped in the proofreading of the thesis draft.

I am very grateful to the whole DBS team, who created a great working atmosphere.

I am grateful to Uli and Ralf, for their precious support through the past 5 years, and for giving me the possibility to grow scientifically and personally.

A special thanks to Alice and Daisy, for the constant encouragement on every level. Without them, it would have been difficult to arrive here!

A big thank you also to Marija, Johannes, Anahi, and Mareike. They made every challenge look fun! I would like to thank also Piotr and Turgut for the (not seldom) technical help.

Last but not least, my gratitude goes to my family and friends in Italy, who supported me with their love remotely.

Table of contents

Abstract

Scientists from all over the world seek to unravel the secrets of life, how diseases develop and how to treat them. To answer these unresolved questions, we have to understand the basis of life. Molecular interactions are the core of all the fundamental biological processes in every living cell and organism. For this reason, gaining information on how different molecules interact between each other is crucial to understand the mechanisms of biological pathways and processes, such as gene expression, protein synthesis, cell regulation, etc. One can imagine these biological processes as the result of an extremely complex and dynamic network of interactions where small molecules, DNA and RNA, proteins and cells are involved. When two molecules interact, they can form a complex in a dynamic equilibrium. The strength and stability of this complex depends on the affinity between the two molecules, which is a measure of the equilibrium between how fast/slow the two molecules associate and dissociate. Nowadays, several types of technologies have been developed in order to resolve the binding affinity between two molecules, and the kinetic rates at which the complex forms and disassembles. In this dissertation, three case studies are presented, in order to show different examples of interactions between various classes of molecules studied on a DNA-based biosensor technology. The first case study presented is on *aptamers*, short nucleic acid molecules designed to bind with high affinity to a specific molecular target. The time-resolved folding and unfolding mechanisms induced by different types of ions binding to the Thrombin-Binding Aptamer (TBA) are shown, demonstrating how the different ions can have diverse and even opposing effects on the aptamer structure, that reflects as well on the affinity of the interaction with its target protein. The second case study presented is on *PROTACs* (PROteolysis TArgeting Chimeras), bifunctional synthetic small molecules that are developed to induce the intracellular degradation of a target protein via the ubiquitin-proteasome system. The development of efficient PROTACs requires the understanding of the binding affinity for each molecular partner, *i.e*. the E3 ligase and the protein of interest (POI), with which it can form the ternary complex, necessary for the ubiquitination of the target protein. Herein, a method involving a supramolecular DNA nanostructure to study the simultaneous binding to the E3 ligase and the POI is introduced, that allows to classify the PROTACs able to form binary interactions and/or ternary interactions with the binding partners. The third case study involves DNA *polymerases*, a class of enzymes that is widely studied for their pivotal role in DNA replication, as well as for their employment worldwide for sequencing and PCR (Polymerase Chain Reaction) techniques. In this work, a strategy to follow in real-time the DNA elongation activity of such enzymes as well as the inhibition of their activity is presented. In addition, the same strategy has been successfully applied to investigate the DNA elongation activity of *reverse transcriptases*, that use an RNA template, and the DNA unwinding activity of *helicases*.

Zusammenfassung

Wissenschaftler aus aller Welt bemühen sich, die Geheimnisse des Lebens zu lüften und herauszufinden, wie Krankheiten entstehen und wie man sie behandeln kann. Um diese ungelösten Fragen zu beantworten, müssen wir die Grundlagen des Lebens verstehen. Molekulare Interaktionen sind der Kern aller grundlegenden biologischen Prozesse in jeder lebenden Zelle und jedem Organismus. Aus diesem Grund ist die Kenntnis der Wechselwirkungen zwischen verschiedenen Molekülen von entscheidender Bedeutung für das Verständnis der Mechanismen biologischer Abläufe und Prozesse, wie z. B. Genexpression, Proteinsynthese, Zellregulation usw.. Man kann sich diese biologischen Prozesse als das Ergebnis eines äußerst komplexen und dynamischen Netzes von Wechselwirkungen vorstellen, an denen kleine Moleküle, DNA und RNA, Proteine und Zellen beteiligt sind. Wenn zwei Moleküle interagieren, bilden sie einen Komplex in einem dynamischen Gleichgewicht. Wie stark und stabil dieser Komplex ist, hängt von der Affinität zwischen den beiden Molekülen ab, die ein Maß für das Gleichgewicht zwischen der Geschwindigkeit der Assoziation und der Dissoziation der beiden Stoffe ist. Heutzutage sind verschiedene Technologien entwickelt worden, um die Bindungsaffinität zwischen zwei Molekülen und die kinetischen Raten, mit denen sich der Komplex bildet und auflöst, zu bestimmen. In dieser Dissertation werden drei Fallstudien vorgestellt, um verschiedene Beispiele für Wechselwirkungen zwischen verschiedenen Molekülklassen zu zeigen, die mit einer DNA-basierten Biosensor-Technologie untersucht wurden. Die erste vorgestellte Fallstudie befasst sich mit *Aptameren*, kurzen Nukleinsäuremolekülen, die mit hoher Affinität an ein spezifisches molekulares Ziel binden sollen. Die zeitaufgelösten Mechanismen der Faltung und Entfaltung, die durch die Bindung verschiedener Arten von Ionen an das Thrombin-Binding Aptamer (TBA) induziert werden, zeigen, wie die verschiedenen Ionen unterschiedliche und sogar gegensätzliche Auswirkungen auf die Aptamerstruktur haben können, was sich auch auf die Struktur des Aptamers auswirkt Affinität der Interaktion mit seinem Zielprotein. Die zweite vorgestellte Fallstudie befasst sich mit *PROTACs* (PROteolysis TArgeting Chimeras), bifunktionalen synthetischen kleinen Molekülen, die entwickelt werden, um den intrazellulären Abbau eines Zielproteins über das Ubiquitin-Proteasom-System zu induzieren. Die Entwicklung effizienter PROTACs erfordert das Verständnis der Bindungsaffinität für jeden molekularen Partner, d. h. die E3-Ligase und das Protein Of Interest (POI), mit dem es den ternären Komplex bilden kann, der für die Ubiquitinierung des Zielproteins notwendig ist. Hierin wird eine Methode vorgestellt, die eine supramolekulare DNA-Nanostruktur zur Untersuchung der gleichzeitigen Bindung an die E3-Ligase und den POI verwendet und die es ermöglicht, die PROTACs zu klassifizieren, die in der Lage sind, binäre Wechselwirkungen und/oder ternäre Wechselwirkungen mit den Bindungspartnern einzugehen. Die dritte Fallstudie befasst sich mit DNA-*Polymerasen*, einer Klasse von Enzymen, die umfassend auf ihre zentrale Rolle bei der DNA-Replikation sowie auf ihren weltweiten Einsatz für Sequenzierungs- und PCR-Techniken (Polymerase Chain Reaction) untersucht wird. In dieser Arbeit wird eine Strategie vorgestellt, um die DNA-Verlängerungsaktivität solcher Enzyme sowie die Hemmung ihrer Aktivität in Echtzeit zu verfolgen. Darüber hinaus wurde die gleiche Strategie erfolgreich angewendet, um die DNA-

Verlängerungsaktivität von Reversen *Transkriptasen*, die eine RNA-Vorlage verwenden, und die DNA-Abwicklungsaktivität von *Helikasen* zu untersuchen.

Publications

1. Ponzo, I.; Möller, F.M.; Daub, H.; Matscheko, N. A DNA-Based Biosensor Assay for the Kinetic Characterization of Ion-Dependent Aptamer Folding and Protein Binding. Molecules 2019, 24, 2877. https://doi.org/10.3390/molecules24162877.

2. Kosinski, R.; Perez, J. M.; Schönweiss, E. C.; Ponzo, I.; Bravo-Rodriguez, K.; Erkelenz, M.; Schlücker, S.; Uhlenbrock, G.; Sanchez-Garcia, E.; Saccà, B. The role of DNA nanostructures in the catalytic properties of an allosterically regulated protease. Science Advances, 2022. doi: 10.1126/sciadv.abk0425.

3. Ponzo, I.; Soldà, A.; Crowe, C.; Ciulli, A.; Dahl, G.; Geschwindner, S.; Rant, U. Proximity Biosensor Assay for PROTAC Ternary Complex Analysis. 2023 (*submitted*).

PART I.

PRINCIPLES, DESIGNS AND WORKFLOWS

Chapter 1

Measuring biomolecular interactions

1.1 General introduction

All biological processes inside every cell are governed by a complex network of specific molecular interactions, involving for example nucleic acids, proteins, and small molecules. The ability to study, describe and characterize biomolecular interactions and cellular networks is therefore crucial to explain how these processes are regulated. It is of high interest in biomedical and pharmaceutical research to characterize metabolic pathways and other cellular processes, in order to understand for example the molecular mechanism underlying diseases, and to develop therapeutical drugs [1]. For this reason, several experimental approaches and technologies have been established to analyze biomolecular interactions. There are techniques that were developed to simply detect the binding between two molecules, to know whether different molecules can interact and have a role in regulating certain biological mechanism. Other techniques instead allow not only to detect the binding between molecules, but also to gain more information on the type and mechanism of interaction, such as the binding strength between the two interacting molecules, the stability of the complex they form, and the binding kinetics of their interaction, including how fast they bind and dissociate (association and dissociation rates, referred to as k_{ON} and k_{OFF}, respectively). These technologies can be distinguished in *label-based* and *label-free* methods. Label-based methods require molecules to be modified with a *label* or *tag* in order to be studied (e.g. fluorescent- [2], chemiluminescent- [3], and radioactive-labels [4]). These techniques have the advantage of studying interactions in native environments, such as living cells [5], but they own the main disadvantage of modifying the molecules to be studied by impairing their native conditions and possibly altering their chemical and functional properties. The label-free technologies, on the contrary, allow to study molecular interactions in quasi-native conditions without modifying the intrinsic chemical and functional properties of the investigated molecules. The label-free technologies can be subdivided into two main categories: i) those that measure interactions *in solution* and ii) those that measure interactions *on a surface*. There is a wide range of commercially available technologies utilizing label-free approaches, e.g. Isothermal Titration Calorimetry (ITC), Surface Plasmon Resonance (SPR), switchSENSE®, BioLayer Interferometry (BLI), and Microscale Thermophoresis (MTC), among others. In the following paragraphs, the most known and recognised label-free technologies for the analysis of molecular interactions (ITC and SPR) are presented and compared to switchSENSE®, the technology utilized for the case studies described in the following chapters of this thesis. These technologies are

compared on the principle underlying binding detection, information content, and advantages and disadvantages are discussed.

1.2 Isothermal Titration Calorimetry (ITC)

Isothermal Titration Calorimetry, also commonly known as ITC, is a solution-calorimetry technique that is used to study the affinity between biomolecules and thermodynamics of molecular interactions in biological systems. Pioneering works by Keily and Hume [6] and Tyson and collaborators [7] described how heat and temperature difference could be correlated to reactions in solution. Then, Wiseman and collaborators [8] developed the first prototype of ITC, demonstrating how a calorimeter can infer the binding affinity of two interacting biological species, through analysis of changes in heat released or consumed during their interaction.

1.2.1 Principle of ITC

ITC-based instruments incorporate a sample cell, a reference cell, and an injection syringe. The change in temperature is measured while performing a titration of one binding molecule (named *analyte*, carried by the injection syringe) to the other binding partner (named *ligand*, placed in the sample cell) (Figure 1). From the resulting heat changes, it is possible to extrapolate binding isotherms that provide information of the affinity, stoichiometry, and thermodynamics of the interaction.

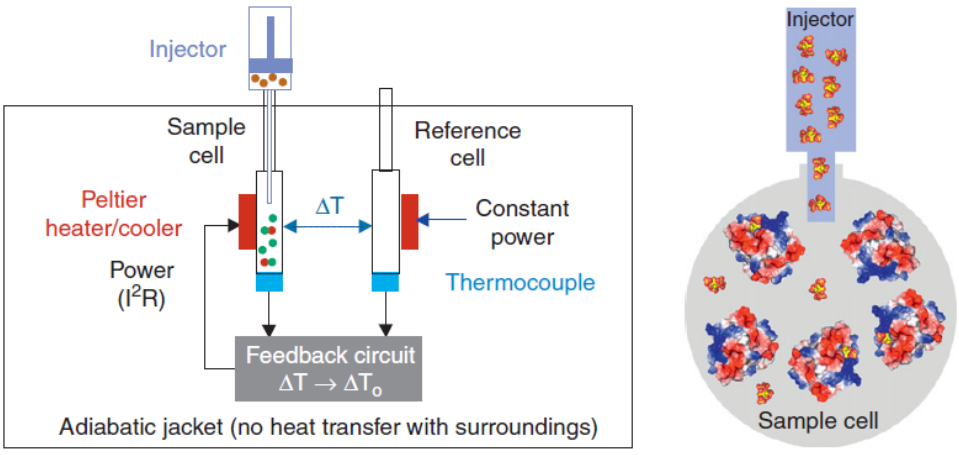

Figure 1. *Schematic representation of an ITC instrument and the reaction cell where the interaction between two molecules is measured. When the syringe injects the analyte in the sample cell, the binding with the other interaction partner induces heat changes. The feedback circuit keeps a constant temperature difference (ΔT) between the sample cell and the reference cell. Adapted from [9].*

In ITC instruments, the sample cell and the reference cell are kept at a constant temperature, and the temperature difference (ΔT) between these two cells is measured. ITC measures the amount of heat that is released or absorbed during a reaction [10], correlating the temperature changes to enthalpy changes (ΔH). If heat is released, the reaction is *exothermic*, while if heat

is absorbed, the reaction is *endothermic*. According to the Gibbs equation, enthalpy changes contribute with entropy changes (ΔH) to the free energy changes (ΔG) of a given reaction:

$$\Delta G = RT \ln K_D = \Delta H - T\Delta S \quad \text{(I)}$$

The enthalpy of a binding reaction reflects the strength of the interactions formed between the two interacting species (e.g. hydrogen bonds, van der Waals interaction, etc.) relative to those existing with the solvent, whereas the entropy changes are mainly related to changes in solvation entropy and changes in conformational entropy that result upon binding.

1.2.2 General workflow

The sample cell is the compartment where the interaction takes place, and contains the ligand molecule. The reference cell, containing only buffer, is used to normalise the ΔH of the sample cell during the measurement. A series of injections with the analyte are performed in the sample cell with the ligand in order to let the two molecules interact. When the analyte interacts with the ligand, a change in heat is observed and recorded as heat pulse (Figure 2, top), and the amount of heat released or absorbed is proportional to the amount of molecules binding. Hence, when the temperature changes due to interactions occurring in the sample cell, the ITC instrument applies the necessary power to maintain constant temperature between the sample cell and the reference cell, so that ΔT is equal to zero. The heat and the corresponding enthalpy changes resulting after each injection are calculated with the area under each injection peak. The quantity measured and displayed on the y-axis is the time dependence of the electric power (µcal/sec) necessary to maintain constant the temperature difference between the reaction and reference cells after each injection of analyte. From the elaboration of these signals it is possible to infer the binding strength or affinity (K_D) of the two molecules of interest [11]: heat pulses are converted into a titration curve that relates the energy (kcal/mol of analyte) to the molar ratio of titrated analyte over ligand amount in the sample cell (Figure 2, bottom).

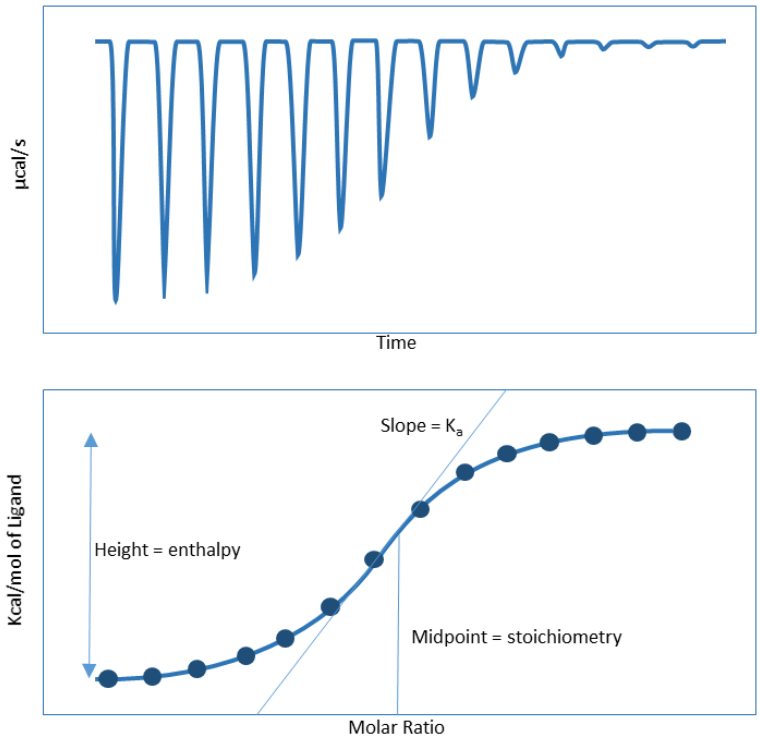

Figure 2. *ITC thermogram. A series of analyte injections are performed in the sample cell, and the resulting heat changes given by the interaction with the ligand are counterbalanced by ITC instrument to keep a constant ΔT with the reference cell. The total heat associated with each injection is proportional to the integrated power required to maintain a constant ΔT between the sample and reference cells. Fitting the resulting isotherm yields the thermodynamic parameters, e.g. ΔH and K_D (= 1/K_A). Top: heat pulses recorded after each analyte injection, related to the energy required to keep constant the temperature difference. Bottom: heat pulses are converted into a titration curve that relates the heat (kcal/mol of analyte) to the molar ratio of titrated analyte over ligand amount in the sample cell. Adapted from [12]. ITC Thermogram by Simon Caulton is licensed under CC BY 4.0.*

At the beginning of the titration, the *ΔH* of each injection is usually large because it derives from a large excess of available binding sites. The more the number of injections increases, the more the available binding sites in the sample cell decreases because of sites occupancy from the analyte, resulting in fewer new interactions and hence also the absolute changes in *ΔH* decreases. Numerous applications have been reported, including protein-protein [13], protein-DNA [14], and protein-small molecule [15] interaction studies.

1.2.3 Advantages and disadvantages

ITC is an *in solution* binding technique, which has several advantages, such as:

i) molecular interactions can be measured in native-like conditions;
ii) the binding molecules are not required to be labelled, avoiding possible interference with their target binding site;
iii) the affinity (K_D) of two interacting molecules can be easily measured;
iv) full thermodynamic information of the reaction (*ΔH*, *ΔS*, *ΔG*) can be provided;

v) it is considered a user-friendly technology.

On the other side, there are some limitations on the applicability of ITC:

i) it allows to study only binding interactions characterized by significant changes in enthalpy, with K_D values in the nM to µM range, while weaker binding reactions are more difficult to be analyzed [9];
ii) the affinity (K_D) is measured from the steady-state equilibrium. This implies that a wide range of concentrations have to be used for accurate affinity calculation, requiring higher sample consumption compared to other binding technologies.

1.3 Surface Plasmon Resonance (SPR)

Surface Plasmon Resonance (SPR) is a label-free and *on surface* detection method, which has emerged during the last two decades as a suitable and reliable strategy in clinical analysis for measuring real time molecular interactions. SPR is a technique that detect changes in refractive index in response to molecular interactions [16]. SPR technology is used to measure thermodynamic binding parameters and determine affinity constants, detect association and dissociation binding rates of interactions between various biomolecules, including antibodies or other proteins, lipids, and nucleic acids. It can also be used for drug candidate screening.

1.3.1 Principle of SPR

SPR-based biosensors measure changes in refractive index that are induced by biomolecular interactions occurring close to the biosensor surface. The response related to an interaction is measured in real time as *resonance units* or *response units* (RU), and it is directly proportional to the mass density of biomolecules bound to the surface (Figure 3). SPR relies on the conversion of energy from the incident light on a thin metal (e.g. gold) layer that is located between two media having different refractive indices [17,18]. Usually, the two media consist of a glass prism coated with the thin gold layer, and an aqueous flow cell. SPR occurs when the incident light is directed through the glass prism at a certain angle and hits the gold layer, and part of the light energy couples with the electrons of the metal layer, leading to electron movements due to excitation [19]. These electron movements are called *plasmons*, and propagate through the metal surface. The angle that generates the surface plasmon is detected by optical detectors by measuring a localized drop in the reflected light intensity. Molecular binding events close to the gold surface can induce variations to the characteristics of the light incident on the surface itself. This in turn causes changes in local refractive index and in the angle of light energy that is coupled to the surface plasmon. Therefore, based on the amount of molecular mass present near the gold surface, the angle of lowest reflected light intensity (the *SPR angle*) may change. In other words, the angle of minimum reflectivity is determined with modulations of the incidence angle, and detecting the changes in the reflected light intensity that occur when biomolecules interact close to the surface allows to

quantify their amount on the surface, their affinity, and the association and dissociation kinetics of their interaction [20].

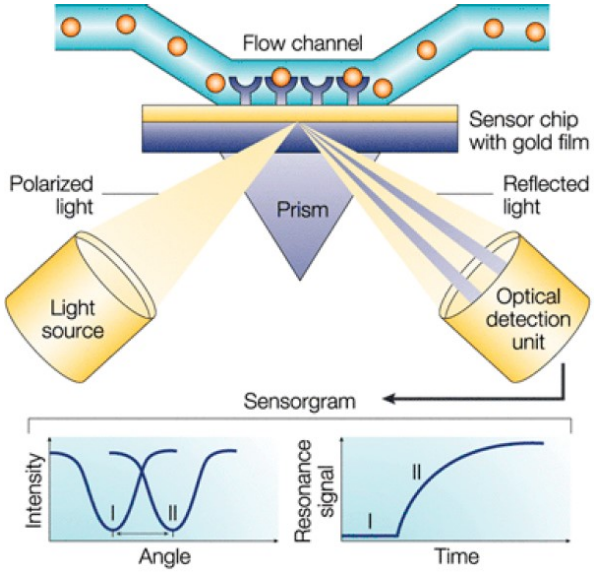

Figure 3. *SPR-based biosensors detect changes in the refractive index on the surface of a sensor chip. SPR is observed as a variation in the reflected light from the surface at an angle that is dependent on the mass of material bound on the surface. The SPR angle shifts when biomolecules bind to the surface and change the mass on the surface. This change in resonant angle can be monitored in real time as resonance signal versus time. Adapted from [20].*

1.3.2 SPR biochip

A typical SPR biochip consists of a glass support coated with a thin gold layer, and a carboxylated dextran layer is covalently attached to the gold surface. The carboxylated surface provides reactive groups for covalent coupling of ligand molecules (Figure 4). There are also alternative types of commercially available SPR biochips [21,22]:

- Sensor chips pre-functionalized with capturing molecules (e.g. Streptavidin, NTA, protein A, etc.) to capture tagged ligands;
- Sensor chips with hydrophobic surfaces for attachment of lipid bilayers;
- Sensor chips with unmodified surface that can be customized.

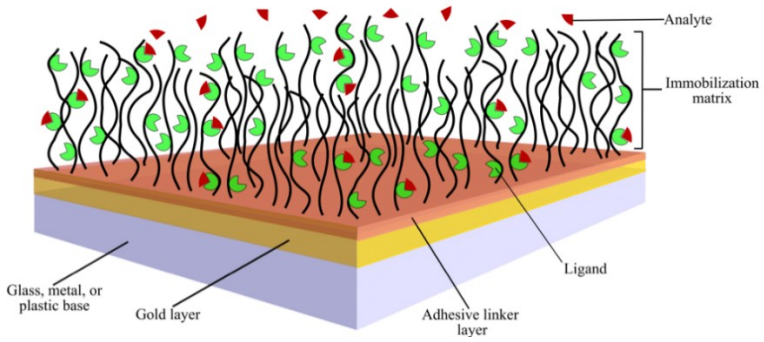

Figure 4. *SPR biochip schematic representation. The biochip typically consists of a glass surface, that is covered by a thin gold layer. A dextran linker layer is attached on top of the gold layer, that provides the reactive groups for covalent immobilization of the ligand molecule. The ligand molecule is therefore distant from the gold surface and can bind the analyte molecule injected across the surface. Adapted from [23].*

The ligand molecule can be immobilized on the surface either via covalent coupling or via capture strategies (e.g. streptavidin-biotin, His-tag, etc.). In the first case, the covalent coupling is achieved via reaction between the carboxylated groups of the dextran matrix and reactive groups of the protein itself, such as amines and thiols, and it is therefore an irreversible process; however, the biochip already functionalized can be used multiple times, if stored correctly. While, in the second case, the ligand is immobilized via a capture group that does not involve any irreversible reaction, which means that the same biochip can be used several times with different ligand molecules, prior regeneration. In addition, it does not require any chemical modification of the ligand molecule and it allows to immobilize the ligand in a defined orientation. However, it is not the most stable strategy, since it requires a capture system with high-affinity interaction (e.g. streptavidin-biotin) or at least higher than the studied one, in order to avoid that the ligand might detach from the surface during the dissociation phase of the kinetic experiment.

1.3.3 General workflow

In SPR biosensor biochips, one molecular species (*ligand*) is immobilized on the metal sensor surface, and a binding partner species (*analyte*) flows across the surface. A general workflow to study molecular interactions with SPR biosensors consists of four main steps (Figure 5):

1. Immobilization of the ligand of interest (e.g. a protein) on the biosensor surface;
2. Association: injection of the analyte (e.g. a second protein), that interacts with the ligand on the surface;
3. Dissociation: injection of a buffer volume, leading the analyte to dissociate from the ligand;
4. Regeneration of the chip, that allows to remove completely the analyte from the chip surface.

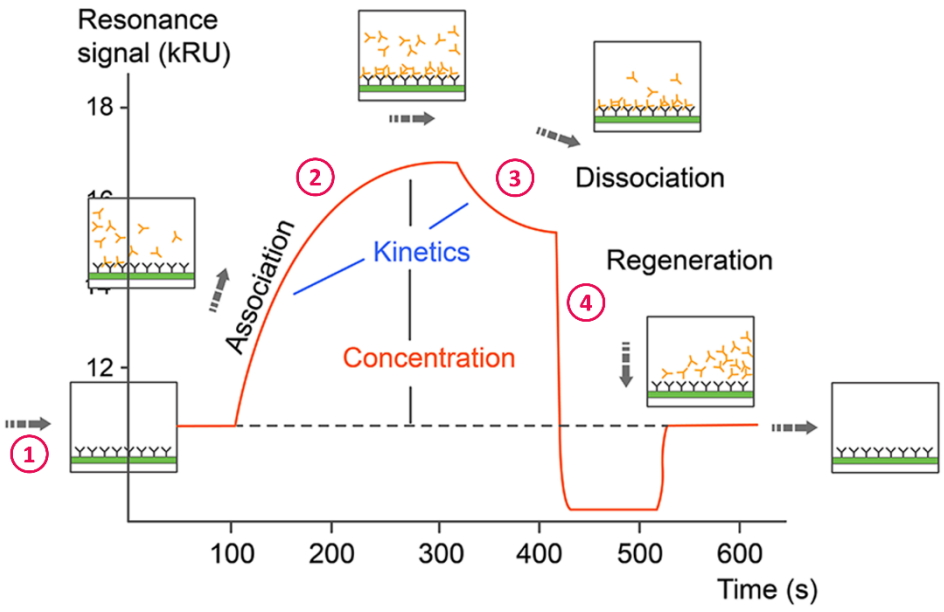

Figure 5. *Schematic representation of a typical SPR workflow, that is commonly composed of four different steps: 1) immobilization of the ligand on the surface; 2) association of the analyte; 3) dissociation of the analyte via buffer injection; 4) final regeneration of the chip. Adapted from [24].*

Normally, increasing concentrations of the analyte are injected at each workflow cycle. A typical SPR sensorgram resulting from a binding kinetic measurement of multiple analyte concentrations is shown in Figure 6. During the association step, the increase in the refractive index is recorded, which results in a change in the angle at which light is absorbed. The changes in the refractive index upon the binding of biomolecules are proportional to the concentration of the analyte injected, but they depend also on the properties of the molecules. The rate at which this change occurs provides a measure of the association rate (k_{ON}) of the molecules. Once the buffer is injected at a specified flow rate (up to 100 µL/min) to let the analyte dissociate from the ligand on the surface, the absorbed angle returns to its original pre-injection level. The time required to the molecules to dissociate is equivalent to the time required to the refractive angle to return to the baseline, and correlates to the dissociation rate (k_{OFF}) of the interaction. The dissociation rate constant (K_D), that is a measure of the affinity of the two molecules, can be determined by the correlation of the association and dissociation rates (see Chapter 2, section 2.2). SPR biosensors have been used to characterize interaction between different class of molecules, including protein-nucleic acid [25,26], protein-protein [27], enzyme-substrate [28], and protein-small molecules [29] and many others.

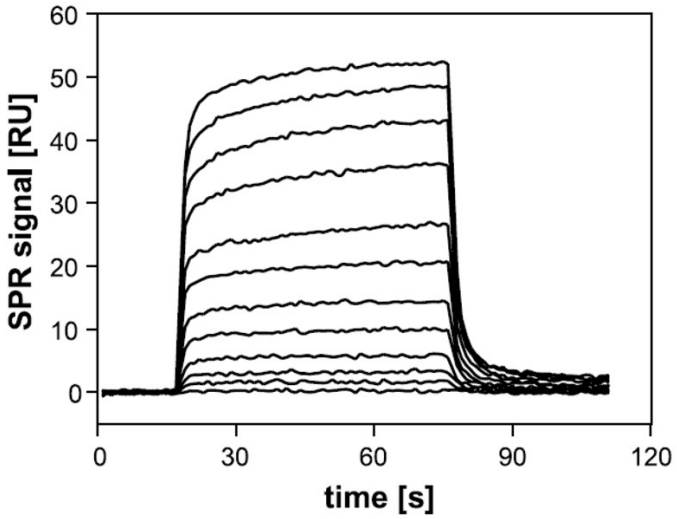

Figure 6. *Example of a SPR sensorgram. Increasing concentrations of analyte result in an increase in response units (RU). Analysis of association and dissociation rates yield information about the binding affinity (K_D) of the analyte-ligand complex. Adapted from [30].*

1.3.4 Advantages and disadvantages

SPR is a label-free *surface*-based method that has the following advantages:

i) the biggest advantage is that it provides real time kinetic information – association (k_{ON}), dissociation (k_{OFF}) rates and affinity constant (K_D) – of molecular binding interactions;
ii) it is a well-established and recognized method with a broad portfolio of applications in the pharmaceutical and medical fields;
iii) since it is widely known and used, in the last years its sensitivity, throughput and automatic analysis have been improved in order to accelerate the validation processes in drug discovery.

However, there are some limitations to take in consideration:

i) one of the most important disadvantages is that one of the two interacting molecules needs to be immobilized on the surface, which is not always straightforward;
ii) high concentrations of immobilized ligand are required to obtain a good signal-to-noise ratio level, since biomolecular interactions induce typically low changes in refractive index [31];
iii) noteworthy, only one ligand species can be immobilized on the SPR biochip, therefore limiting the characterization of more complex interactions such as multivalent binding (e.g. bivalent antibodies, PROTACs, etc.), that require the ability to discriminate between affinity and avidity (term used to refer to the dynamic interplay of all involved interactions that rule ternary complexes formation and decay) (see Appendix, section A2.2);

iv) a long time is required for scouting different regeneration solutions to refresh the dextran matrix of the biochip itself after each kinetic measurement;
v) SPR-based biosensors currently in the market have a maximal flow rate of 100 µL/min, namely the velocity at which the analyte solution and buffer is flowed over the chip surface, which is sometimes not sufficient to resolve tight binders kinetics, leading to some artefacts such as mass transport and rebinding effects (see Appendix, section A2.2);
vi) SPR biochips are also very sensitive to temperature variations: the physical thickness of the biopolymer layer increases with increasing temperature due to thermal expansion [32], affecting the refractive index.

1.4 switchSENSE®

switchSENSE® is a DNA-based biophysical technology for the analysis of molecular interactions in real-time. It is a label-free, *on-surface* technology that relies on surface-anchored DNA nanolevers. The DNA nanolevers are responsive to applied voltage changes [33–35] and are modified with a fluorophore on the distal end, allowing to study molecular interactions via fluorescence changes. switchSENSE® is used to measure binding kinetics and affinity, it allows to evaluate enzymatic activity and to gain information on protein conformational changes.

1.4.1 Principle of switchSENSE® technology

This technology relies on customizable DNA strands immobilized on the surface of a gold electrode (Figure 7). The presence of a fluorophore at the distal end of the DNA strands allows to study interactions in real time through changes in fluorescence intensity, detected by single-photon counters that record fluorescence in green and in red (Figure 7).

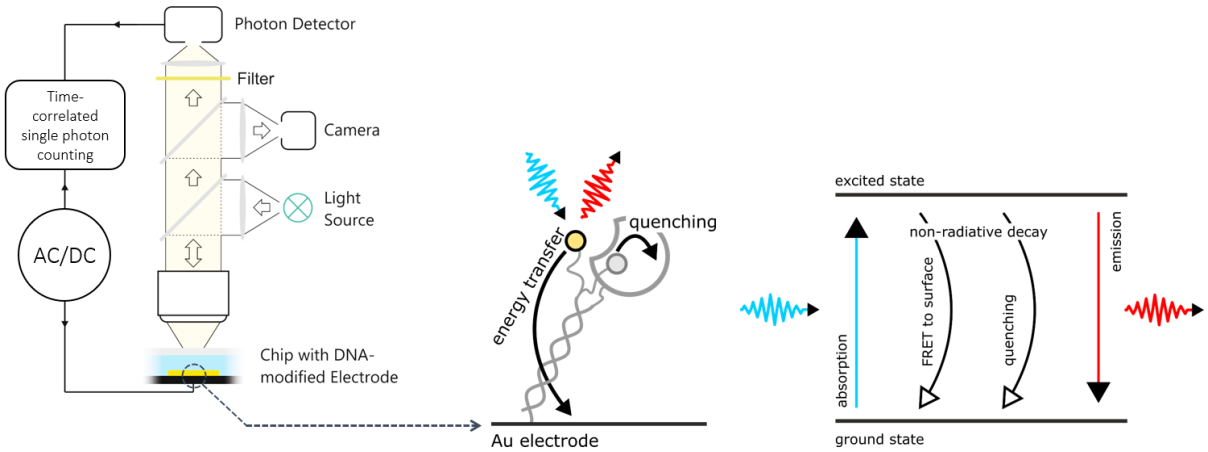

Figure 7. *Simplified scheme of the optical detection system of the switchSENSE® biosensor and its mechanism of detection. Fluorescently-labelled DNA strands are immobilized on a gold surface. The single-photon detectors*

record in a sensitive way the changes in fluorescence intensity resulting from interactions in proximity of the dye or from the proximity of the dye itself to the surface. Copyright: Dynamic Biosensors.

The fluorescence intensity depends on the local environment of the dye and on its position in relation to the biochip surface [36]. For instance, fluorescence changes are observed when i) two molecules interact in proximity of the dye (Figure 8) and ii) the DNA strands are brought closer to the gold surface, due to the energy transfer mechanism from the fluorophore on the DNA to the gold surface, resulting in a quenching of fluorescence (Figure 9) [36].

Owing to their negatively-charged structure, DNA strands anchored on a gold surface can be controlled by applying electric potentials to the chip surface. With a negative potential the negatively-charged DNA strands get repulsed from the surface itself, resulting in a upward, "standing" conformation. On the contrary, with a positive potential the negatively-charged DNA strands get attracted to the surface, resulting in a "laying" conformation [33–35,37,38]. Consequently, whenever the DNA strands are repulsed from the surface, a fluorescent signal is recorded, *vice versa*, whenever the DNA strands are attracted to the surface, a lower fluorescent signal can be observed. Thanks to this principle, two different measurement modes can be used, named the *static mode* and the *dynamic mode*.

- In static mode, a fixed negative potential is applied. The DNA nanolever is constantly repulsed from the gold surface, and it stands in an upward orientation. In this way, the dye, being far away from the biosensor surface, is not quenched by the gold electrode and the interaction between the analyte molecule and the ligand molecule is detected through fluorescence changes, based on the influence exerted on the local environment of the dye. For this reason, this mode of detection is also called *Fluorescence Proximity Sensing* (FPS) mode (Figure 8). This measurement mode is the standard method to study binding kinetics between two molecules with high sensitivity (from 2-digit fM up to mM K_D) and high signal-to-noise ratio.

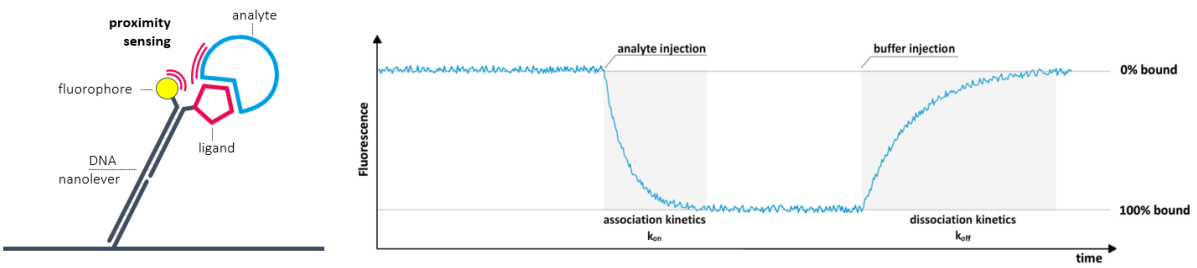

Figure 8. *switchSENSE® measurement modes: static mode. A fixed negative potential is applied and, as consequence, the nanolever does not move and it stands in a upward position. The dye, not quenched by the gold surface, detects the binding of molecules in real-time through changes in the local environment (fluorescence proximity sensing). Copyright: Dynamic Biosensors [39].*

- In dynamic mode, an alternated potential is applied, and the DNA nanolevers are subjected to a continuous switching between an upward position and a downward position (Figure 9). The nanolever movement happens on the microsecond scale. This motion is recorded in real-time by monitoring the fluorescence intensity of the dyes on the nanolevers. The fluorescence intensity depends on the distance between the fluorophore and the gold surface, and hereby on the orientation of the nanolevers in relation to the gold surface. The fluorescence intensity is based on a distance-dependent, non-radiative energy transfer from the fluorophores on the distal end of the nanolevers to the gold surface. The fluorescence intensity is recorded as a function of time, resulting in fluorescence response curves. The slope and form of the sigmoidal transition within the response curve is affected by the hydrodynamic drag of the nanolevers. As such, a nanolever carrying a protein ligand at its distal end experiences a notably larger hydrodynamic drag, corresponding to the *hydrodynamic radius* of the sampled protein. The switching dynamics of DNA-protein complexes gradually slow down with increasing protein size. By comparing the measured upward switching fluorescence response of a sample under investigation (DNA-protein conjugate) to bare DNA and DNA protein conjugate standards, the *hydrodynamic friction* and, as a consequence, the protein size can be related to some selected standard proteins and finally estimated.

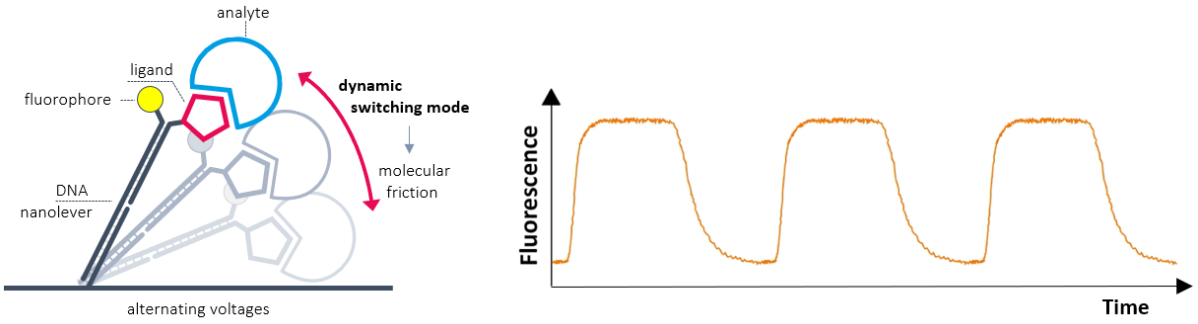

Figure 9. *switchSENSE® measurement modes: dynamic mode. An alternating potential is applied and, as consequence, the DNA nanolevers are electrically actuated to oscillate at high frequencies, providing information about its molecular friction. The measured instantaneous velocity of the nanolever depends on the hydrodynamic friction of the attached molecules. When the nanolevers are repulsed from the surface, a fluorescent signal is recorded, and when the nanolevers are attracted to the surface, a lower fluorescent signal can be observed. Copyright: Dynamic Biosensors [40].*

- Besides the two abovementioned measurement modes, the possibility to use different red and green dyes can be considered an additional way of detection. In fact, it is a unique way for studying multispecific interactions, e.g. a bispecific antibody binding to two different targets [41], or formation of ternary complexes among three different molecules (see chapter 3). Hence, the *dual color* detection (Figure 10) allows to examine two distinct signals from two interactions at the same time, that is extremely valuable for studying avidity component *vs* affinity (see Appendix, section A2.2), and

also to detect binding via fluorescence resonance energy transfer (FRET) from the green dye to the red dye (details in chapter 3), occurring specifically when the analyte brings two ligands at a FRET-sensitive distance (within 15 nm).

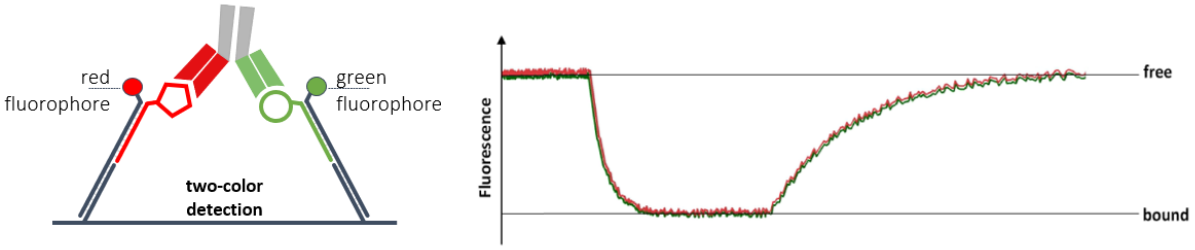

Figure 80. *switchSENSE® measurement modes: two-colour detection. The unique use of two different fluorophores makes it possible to monitor two independent signals from two interactions at the same time and on the same sensor spot. In this example it is possible to observe a biphasic dissociation of an antibody binding to two distinct antigen ligands at the same time. Copyright: Dynamic Biosensors [42].*

1.4.2 switchSENSE® biochips

The biochip surface includes gold microelectrodes, where two different 48mer DNA oligonucleotides, also called *anchor strands*, are grafted via a gold-sulphur bond. The anchor DNA is hybridized with the complementary DNA sequence, leading to double strands, named *nanolevers*. Two different series of biochips have been developed and shortly described in Figure 11:

A. The *multi-purpose (MP)* chip, for the DRX instrument series. This biochip has four flow channels with six gold electrodes, or *spots*, each. The anchor sequence on the electrodes surface is functionalized at the distal end with a red or a green dye. The anchor DNA gets directly hybridized with the *ligand strand*, that is the sequence functionalized with the ligand of interest (e.g. a DNA overhang, a protein, etc.);
B. The *adapter (ADP)* chip, for the heliX® instrument series. This biochip has a single channel with two spots (two equal gold electrodes). The 48mer anchor DNA does not carry any dye. The anchor strand gets hybridized with the *adapter strand*, harbouring a red or a green dye at the distal end. The adapter strand is partially complementary to the anchor strand, and partially to the ligand strand.

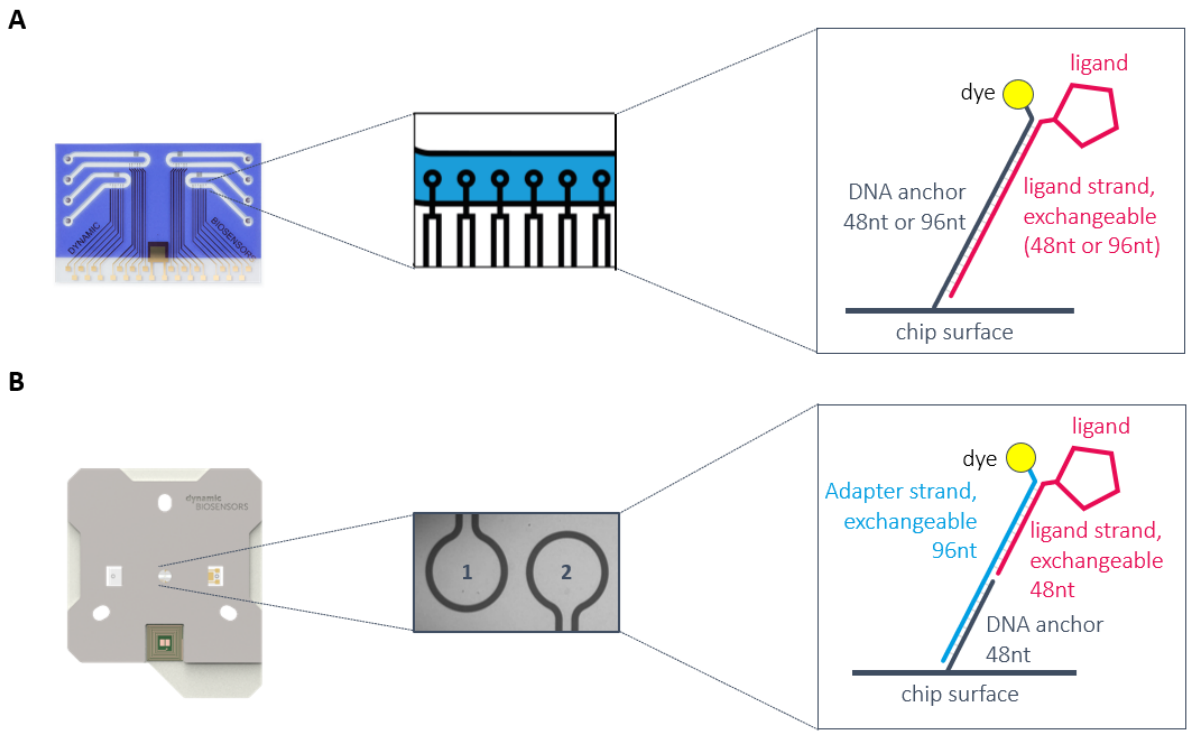

Figure 11. *switchSENSE® biochips. A) MP biochip for DRX instrument. Four channels with six electrodes each are present. The surface of the electrodes is functionalized with an anchor strand carrying a fluorescent dye. The ligand strand directly hybridizes to the anchor strand. B) ADP biochip for heliX® instrument. There are two electrodes in a single channel. The surface is embedded with a DNA anchor without dye. The adapter strand, carrying the dye, hybridizes to the ligand strand and to the anchor strand. Copyright: Dynamic Biosensors.*

The switchSENSE® biochips are designed to have more spots, that are used as measurement spots and as real-time reference spots or multianalyte. The reference spots are characterized by a different sequence respect to the measurement spot allowing to hybridize with a specific sequence the anchors strands in each electrode. The MP biochips are characterized by four channels with six spots each, where four spots are used as measurement spots and the other two are used as reference spots. The ADP biochips present two spots in a single channel, where the first spot is generally used as measurement spot and the second spot as a real time reference. Reference spots are crucial to investigate unspecific binding of the analyte of interest to an off-target ligand. However, both electrodes can be also used as measurements spots, and in combination with the two-colour mode, more interactions at the same time can be studied, known as *multiplexing analysis*. There are several advantages of the ADP biochip over the previous MP biochip, such as: i) the possibility to have fresh ligand and dye as many time as needed; ii) its robustness (the chip skeleton is in metal instead of glass); iii) the possibility to immobilize up to four ligands at the same time;

The ligand of interest can be placed on the ligand strand either by direct covalent coupling or by tag-capturing methods (Figure 12). In the first case, different coupling strategies can be used (described in Appendix, section A1) to conjugate the ligand (e.g. a protein) to the ligand strand,

by taking advantage of naturally present reactive groups, such as amines or thiols or his-tag mediated [43,44] on the ligand. The covalent coupling is very stable, but requires a subsequent purification process. In the second case, different capturing methods can be used, depending on the tag present on the ligand molecule (e.g. streptavidin-tag, biotin-tag, his-tag, protein A, etc.). The capture of the ligand on the surface does not require any purification step and occurs via a specific tag present on the protein; however, normally the capture is less stable than the covalent coupling methods. Alternatively, in case the molecule of interest is another DNA or RNA strand, it is possible either to elongate the ligand strand with the sequence of interest (see chapter 2) or to customize the sequence of the ligand strand itself (see chapter 4).

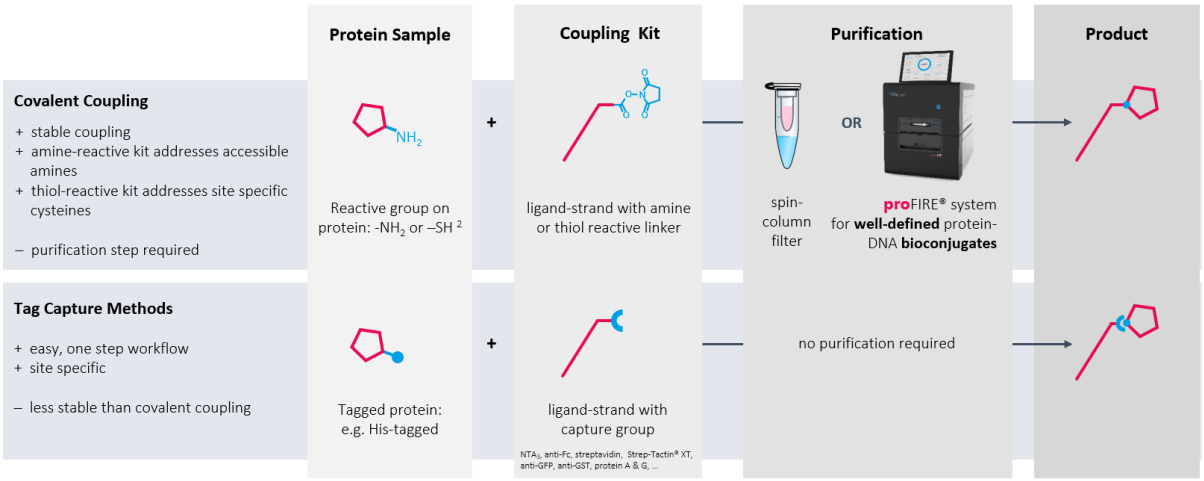

Figure 12. *Comparison of ligand preparation strategies: covalent coupling versus capture via tag. Covalent coupling is accomplished via conjugation to reactive groups on the protein, resulting in a stable conjugate DNA-ligand that requires to be purified before use. Capture via tags on the protein is more site-specific, does not require purification before use, but it is less stable than a covalent coupling. Copyright: Dynamic Biosensors.*

Thanks to this biochip design, it is also possible to modulate the density of the ligand on the surface, allowing to adjust the distance between the ligand strands. The ligand density control on the surface is achieved with both biochip types. In MP biochip, adjusting the ligand density on the surface is carried out by mixing the ligand strand with an adjustable ratio of strand with a quencher, in order to turn off the fluorescence of the dye already present on the surface and to reduce the ligand density on the surface. In ADP biochip, the ligand density is varied by mixing an adjustable ratio of the ligand strand with the adapters with a dye, with *cAnchor* strand, the complementary sequence of the anchor strands (Figure 13A). This strategy is useful also to study tight binders kinetics, since the low density surfaces avoid possible rebinding effects, which might cause artefacts on the kinetic values, and to study affinity vs avidity of multivalent analytes that can bind to more than a target ligand (e.g. bi- and multi-specific antibodies, proteins or small molecules). In this specific case, the ligand strands carrying two different target ligands are hybridized with adapters with different dyes (red and green), and they are mixed in variable ratios according to the desired density on the biochip surface (Figure 13B) to mimic for example a cellular surface.

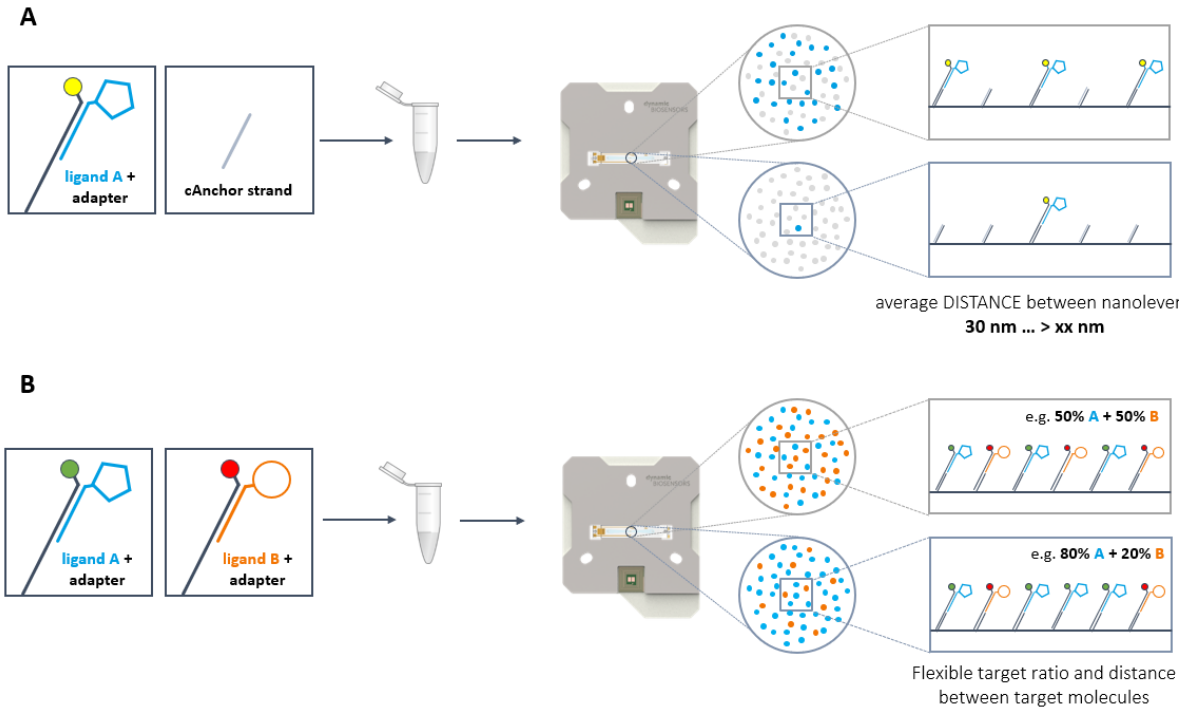

Figure 13. Density control in ADP biochip. A) density control of a ligand on the biochip surface is achieved by mixing the ligand strand with adapters with a dye together with a variable ratio of cAnchors without dye. In this way the distance of the ligand on the surface can be increased. B) density control of two different ligands on the surface is realized by mixing one ligand with the adapter with a red dye and the second ligand with the adapter with a green dye. It is possible to achieve different ligand densities of the two ligands by mixing them with the adapters in different ratios (e.g. 50:50, 80:20, etc.). Copyright: Dynamic Biosensors.

1.4.3 General workflow

Despite their slightly different designs, MP and ADP biochips allow to perform binding measurements in a similar way (Figure 14). A typical switchSENSE® kinetic binding assay workflow consists of three subsequent steps:

1) *Functionalization* of the biochip surface, which consists in the hybridization of the complementary strands of the anchor DNA strands, bringing the ligand of interest (e.g. protein, small molecules, DNA/RNA sequence, etc.) on the surface, with (ADP chip) or without (MP chip) a fresh dye. It is possible to follow the chip functionalization in real time as an increase in fluorescence thanks to the presence of the dye on the anchor strand (for MP chips). The functionalization on the ADP chip requires a pre-hybridization (ca. 20 min) of the adapter strand with the ligand strand, since the adapter strand is the one carrying the fluorescent dye, needed for the analysis.
2) *Kinetics* analysis, which take place through the analyte injection and ejection. The binding kinetics consist of analyte association and dissociation phases. The analyte interaction with the ligand can be detected via fluorescence signal changes, as explained beforehand. The time needed for the analyte to interact with the ligand is correlated with the association rate (k_{ON}), and depends on the concentration of the

analyte. Afterwards, the buffer is injected at a specified flow rate (up to 500 µL/min) and as consequence the analyte dissociates from the ligand. The time needed for the full dissociation of the analyte correlates to the dissociation rate (k_{OFF}), and the stronger the binding between the two molecules, the longer the buffer is required to flow on the surface.

3) *Regeneration*, in which the biochip surface is washed with a high pH solution, that disrupts the weak bonds of the duplex nanolever. This step is extremely fast (few seconds contact time) and fundamental to restore the original condition of the biochip surface with anchor strands ready to be re-functionalized with the new ligand strand. This switchSENSE® step is different from all the other technologies (e.g. SPR), because in this case the regeneration solution removes everything (ligand included) from the surface, and not only the analyte. The regeneration step is especially important when the analyte is tightly bound to the ligand, and a buffer injection is not sufficient to let it dissociate completely. Furthermore, the chip regeneration allows to use several times the same biochip for different applications (up to 50-60 times).

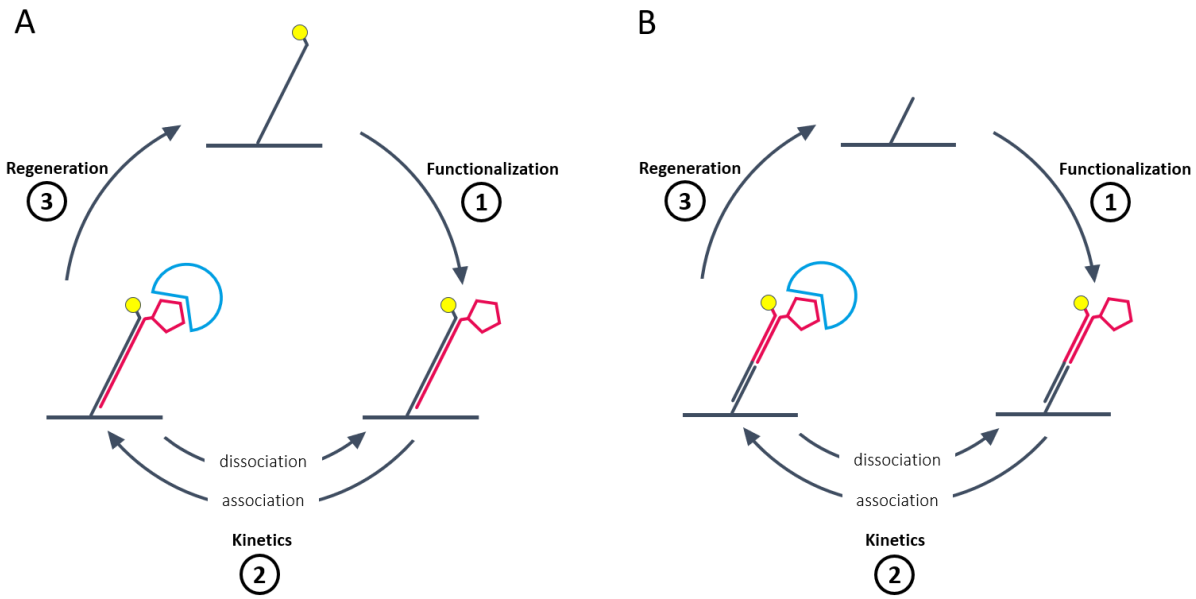

Figure 9. *General workflow of a switchSENSE® experiment by using a MP chip (A) or ADP chip (B). 1) Functionalization of the surface biosensor is the step where the ligand of interest is immobilized on the surface. 2) Kinetics analysis, where the analyte is injected and ejected. The analyte interacts with the ligand during the association phase, and then dissociate from the ligand and gets ejected when the running buffer is injected in the channel. 3) Regeneration step after each kinetics can be performed to restore the initial condition of the surface by washing away analyte and ligand with the injection of a high pH solution. Copyright: Dynamic Biosensors.*

switchSENSE® allows to measure binding kinetics and affinity, and to discriminate between affinity and avidity [41,45], it allows to evaluate enzymatic activity [46,47], to gain structural information on size and conformation [48–50], and to assess protein stability (melting temperature) [51]. There are many reported case studies, ranging from DNA- and RNA-binding proteins and enzymes [46,52], protein and small molecules [53] and multivalent peptides [54],

bivalent molecules, such as bivalent antibodies [45,55] like Hemlibra® [41], bispecific small proteins (e.g. DARPIns), and bispecific or multispecific small molecules like PROTACs (described in chapter 3) and molecular glues.

1.4.4 Advantages and disadvantages

switchSENSE® technology is a DNA-based label-free *on surface*-based method that has the following advantages:

i) real time kinetic information of molecular binding interactions are provided, including association rate (k_{ON}), dissociation rate (k_{OFF}) and affinity constant (K_D);
ii) analysis of avidity, multispecific binders, and enzymatic activity (k_{cat} and K_M) and conformational change can also be studied;
iii) simple biochip functionalization, either via covalent coupling or different capture methods, allowing control of ligand density and dual targets ratio;
iv) fast and clean regeneration step.

However, it presents also some disadvantages, such as:

i) it requires the immobilization of the ligand on the surface, like in SPR, that it is not always straightforward, especially for big proteins, and it might affect the functional properties;
ii) since switchSENSE® is a method based on electrical stimulation and optical detection with a DNA-based technology chip, possible limitations might occur when measuring autofluorescent or heavily charged molecules, or unwanted DNA binders, which might interfere with the results. However, there are some experimental tricks that can be applied to overcome these aspects.

1.5 Objectives

The aim of this PhD project is to study the interaction between different classes of molecules, ranging from small molecules, aptamers, to proteins and enzymes. Indeed, obtaining detailed information on how these molecules interact is fundamental to deeply understand the biological processes that are of high interest in biomedical and pharmaceutical research, in the biotechnology field and in the drug discovery process. Herein, three different case studies have been selected and fully characterized using switchSENSE® technology:

1. The Thrombin-Binding-Aptamer (TBA) was deeply characterized on the DNA-based biosensor surface. This project was focused on the study of aptamer folding and unfolding induced by ions, and on the salt-dependency of the thrombin affinity and binding kinetics. The results show that these mechanisms are strongly dependent on the type and concentration of ions present in solution, affecting significantly both the folding orientation and the binding affinity for the target molecule. It was demonstrated how the assay orientation (whether the aptamer or the target protein is the ligand immobilized on the surface) plays also a major role in the recorded values, emphasizing how careful must be the evaluation of the characteristics of specific aptamers for relative targets. The described strategy is applicable in a straightforward manner to any other DNA or RNA aptamer, showing its value in diagnostic applications.

2. A supramolecular DNA construct, named Y-structure, was developed to describe the formation of ternary complexes induced by PROteolysis TArgeting Chimeras (PROTACs), a class of synthetic bifunctional small molecules able to induce protein-protein interactions for targeted protein degradation. In more detail, this project focuses on the development of a new strategy for studying PROTACs binding into a monovalent way to a single ligand (binary interaction) or in a bivalent way to two target ligands at the same time (ternary interaction), therefore allowing to distinguish between affinity and avidity in a single experiment. PROTACs are becoming more and more popular in the drug discovery field for their ability to induce intracellular degradation of specific target proteins. The described results showcase a novel strategy for high throughput screening and full kinetic characterization of ternary complex formation upon PROTACs binding in the pre-clinical phase.

3. A method to investigate DNA-modifying enzymes was established (e.g. polymerases, reverse transcriptases, helicases, etc.) for studying their DNA binding properties, substrate-induced elongation activity, and activity inhibition. Polymerases are of great value in biotechnological field, for their use in the PCR (Polymerase Chain Reaction) and sequencing techniques, as well as in the biomedical field for their role in DNA replication. In this project, based on a previous method developed by Langer [46], the versatility of the DNA-based biosensor was expanded by describing a simple experimental workflow for kinetics, activity and inhibition assay that can be easily adapted to any DNA- or RNA-modifying enzyme.

References

1. Renaud, J.-P.; Chung, C.; Danielson, U.H.; Egner, U.; Hennig, M.; Hubbard, R.E.; Nar, H. Biophysics in Drug Discovery: Impact, Challenges and Opportunities. *Nature Reviews Drug Discovery* 2016, *15*, 679–698, doi:10.1038/nrd.2016.123.
2. Toseland, C.P.; Webb, M.R. Fluorescence Tools to Measure Helicase Activity in Real Time. *Methods* 2010, *51*, 259–268, doi:10.1016/j.ymeth.2010.02.012.
3. Yan, Y.; Shi, P.; Song, W.; Bi, S. Chemiluminescence and Bioluminescence Imaging for Biosensing and Therapy: In Vitro and In Vivo Perspectives. *Theranostics* 2019, *9*, 4047–4065, doi:10.7150/thno.33228.
4. Neri, D.; Petrul, H.; Winter, G.; Light, Y.; Marais, R.; Britton, K.E.; Creighton, A.M. Radioactive Labeling of Recombinant Antibody Fragments by Phosphorylation Using Human Casein Kinase II and [γ-32P]-ATP. *Nature Biotechnology* 1996, *14*, 485–490, doi:10.1038/nbt0496-485.
5. DINANT, C.; VAN ROYEN, M.E.; VERMEULEN, W.; HOUTSMULLER, A.B. Fluorescence Resonance Energy Transfer of GFP and YFP by Spectral Imaging and Quantitative Acceptor Photobleaching. *Journal of Microscopy* 2008, *231*, 97–104, doi:10.1111/j.1365-2818.2008.02020.x.
6. Keily, H.J.; Hume, D.N. Thermometric Titration Curves. *Anal. Chem.* 1956, *28*, 1294–1297, doi:10.1021/ac60116a018.
7. Tyson, B.C.; McCurdy, W.H.; Bricker, C.E. Differential Thermometric Titrations and Determination of Heats of Reaction. *Anal Chem* 1961, *33*, 1640–1645, doi:10.1021/ac60180a009.
8. Wiseman, T.; Williston, S.; Brandts, J.F.; Lin, L.-N. Rapid Measurement of Binding Constants and Heats of Binding Using a New Titration Calorimeter. *Analytical Biochemistry* 1989, *179*, 131–137, doi:10.1016/0003-2697(89)90213-3.
9. Lambright, D.G. 5.11 Membrane Recruitment of Signaling Domains. In *Comprehensive Biophysics*; Elsevier, 2012; pp. 223–244 ISBN 978-0-08-095718-0.
10. Atkins, P.W.; De Paula, J. *Physical Chemistry: Thermodynamics, Structure, and Change*; Tenth edition.; W.H. Freeman: New York, 2014; ISBN 978-1-4292-9019-7.
11. Archer, W.R.; Schulz, M.D. Isothermal Titration Calorimetry: Practical Approaches and Current Applications in Soft Matter. *Soft Matter* 2020, *16*, 8760–8774, doi:10.1039/D0SM01345E.
12. Caulton, S. Isothermal Titration Calorimetry. *Wikipedia* 2023.
13. Knapp, S.; Zamai, M.; Volpi, D.; Nardese, V.; Avanzi, N.; Breton, J.; Plyte, S.; Flocco, M.; Marconi, M.; Isacchi, A.; et al. Thermodynamics of the High-Affinity Interaction of TCF4 with β-Catenin. *Journal of Molecular Biology* 2001, *306*, 1179–1189, doi:10.1006/jmbi.2001.4463.
14. Privalov, P.L.; Jelesarov, I.; Read, C.M.; Dragan, A.I.; Crane-Robinson, C. The Energetics of HMG Box Interactions with DNA: Thermodynamics of the DNA Binding of the HMG Box from Mouse Sox-5. *JMB* 1999, *294*, 997–1013, doi:10.1006/jmbi.1999.3285.
15. Velazquez-Campoy, A.; Vega, S.; Freire, E. Amplification of the Effects of Drug Resistance Mutations by Background Polymorphisms in HIV-1 Protease from African Subtypes. *Biochemistry* 2002, *41*, 8613–8619, doi:10.1021/bi020160i.
16. Liedberg, B.; Nylander, C.; Lunström, I. Surface Plasmon Resonance for Gas Detection and Biosensing. *Sensors and Actuators* 1983, *4*, 299–304, doi:10.1016/0250-6874(83)85036-7.
17. Homola, J.; Piliarik, M. Surface Plasmon Resonance (SPR) Sensors. In *Surface Plasmon Resonance Based Sensors*; Homola, J., Ed.; Springer Series on Chemical Sensors and Biosensors; Springer: Berlin, Heidelberg, 2006; pp. 45–67 ISBN 978-3-540-33919-9.
18. Fee, C.J. Label-Free, Real-Time Interaction and Adsorption Analysis 1: Surface Plasmon Resonance. In *Protein Nanotechnology: Protocols, Instrumentation, and Applications, Second Edition*; Gerrard, J.A., Ed.; Methods in Molecular Biology; Humana Press: Totowa, NJ, 2013; pp. 287–312 ISBN 978-1-62703-354-1.
19. *Surface Plasmon Resonance Based Sensors*; Homola, J., Ed.; Springer Series on Chemical Sensors and Biosensors; Springer Berlin Heidelberg: Berlin, Heidelberg, 2006; Vol. 4; ISBN 978-3-540-33918-2.

20. Cooper, M.A. Optical Biosensors in Drug Discovery. *Nat Rev Drug Discov* 2002, *1*, 515–528, doi:10.1038/nrd838.
21. Cytiva Sensor Chips Available online: https://www.cytivalifesciences.com/en/us/solutions/protein-research/knowledge-center/surface-plasmon-resonance/sensor-chips.
22. Cytiva Biacore SPR – Surface Plasmon Resonance Available online: https://www.cytivalifesciences.com/en/us/solutions/protein-research/interaction-analysis-with-biacore-surface-plasmon-resonance-spr.
23. Reichert Technologies Explained: Sensor Chips for Surface Plasmon Resonance and Other Applications Available online: https://bitesizebio.com/34644/biosensor-chips-surface-plasmon-resonance/.
24. Creative Biomart Principle and Protocol of Surface Plasmon Resonance (SPR) - Creative BioMart Available online: https://www.creativebiomart.net/resource/principle-protocol-principle-and-protocol-of-surface-plasmon-resonance-spr-361.htm.
25. Katsamba, P.S.; Park, S.; Laird-Offringa, I.A. Kinetic Studies of RNA–Protein Interactions Using Surface Plasmon Resonance. *Methods* 2002, *26*, 95–104, doi:10.1016/S1046-2023(02)00012-9.
26. Teh, H.F.; Peh, W.Y.X.; Su, X.; Thomsen, J.S. Characterization of Protein−DNA Interactions Using Surface Plasmon Resonance Spectroscopy with Various Assay Schemes. *Biochemistry* 2007, *46*, 2127–2135, doi:10.1021/bi061903t.
27. Madeira, A.; Vikeved, E.; Nilsson, A.; Sjögren, B.; Andrén, P.E.; Svenningsson, P. Identification of Protein-Protein Interactions by Surface Plasmon Resonance Followed by Mass Spectrometry. *Current Protocols in Protein Science* 2011, *65*, 19.21.1-19.21.9, doi:https://doi.org/10.1002/0471140864.ps1921s65.
28. Fong, C.-C.; Lai, W.-P.; Leung, Y.-C.; Lo, S.C.-L.; Wong, M.-S.; Yang, M. Study of Substrate–Enzyme Interaction between Immobilized Pyridoxamine and Recombinant Porcine Pyridoxal Kinase Using Surface Plasmon Resonance Biosensor. *Biochimica et Biophysica Acta (BBA) - Protein Structure and Molecular Enzymology* 2002, *1596*, 95–107, doi:10.1016/S0167-4838(02)00208-X.
29. Navratilova, I.; Dioszegi, M.; Myszka, D.G. Analyzing Ligand and Small Molecule Binding Activity of Solubilized GPCRs Using Biosensor Technology. *Analytical Biochemistry* 2006, *355*, 132–139, doi:10.1016/j.ab.2006.04.021.
30. Schmidt, J.; Müsken, M.; Becker, T.; Magnowska, Z.; Bertinetti, D.; Möller, S.; Zimmermann, B.; Herberg, F.W.; Jänsch, L.; Häussler, S. The Pseudomonas Aeruginosa Chemotaxis Methyltransferase CheR1 Impacts on Bacterial Surface Sampling. *PLoS ONE* 2011, *6*, e18184, doi:10.1371/journal.pone.0018184.
31. Schuck, P.; Zhao, H. The Role of Mass Transport Limitation and Surface Heterogeneity in the Biophysical Characterization of Macromolecular Binding Processes by SPR Biosensing. In *Surface Plasmon Resonance*; Mol, N.J., Fischer, M.J.E., Eds.; Methods in Molecular Biology; Humana Press: Totowa, NJ, 2010; Vol. 627, pp. 15–54 ISBN 978-1-60761-669-6.
32. Proll, G.; Markovic, G.; Fechner, P.; Proell, F.; Gauglitz, G. Reflectometric Interference Spectroscopy. In *Biosensors and Biodetection*; Rasooly, A., Prickril, B., Eds.; Methods in Molecular Biology; Springer New York: New York, NY, 2017; Vol. 1571, pp. 207–220 ISBN 978-1-4939-6846-6.
33. Takeishi, S.; Rant, U.; Fujiwara, T.; Buchholz, K.; Usuki, T.; Arinaga, K.; Takemoto, K.; Yamaguchi, Y.; Tornow, M.; Fujita, S.; et al. Observation of Electrostatically Released DNA from Gold Electrodes with Controlled Threshold Voltages. *The Journal of chemical physics* 2004, *120*, 5501–5504, doi:10.1063/1.1643729.
34. Kaiser, W.; Rant, U. Conformations of End-Tethered DNA Molecules on Gold Surfaces: Influences of Applied Electric Potential, Electrolyte Screening, and Temperature. *J. Am. Chem. Soc.* 2010, *132*, 7935–7945, doi:10.1021/ja908727d.

35. Knezevic, J.; Langer, A.; Hampel, P.A.; Kaiser, W.; Strasser, R.; Rant, U. Quantitation of Affinity, Avidity, and Binding Kinetics of Protein Analytes with a Dynamically Switchable Biosurface. *J Am Chem Soc* 2012, *134*, 15225–15228, doi:10.1021/ja3061276.
36. Chance, R.R.; Miller, A.H.; Prock, A.; Silbey, R. Fluorescence and Energy Transfer near Interfaces: The Complete and Quantitative Description of the Eu+3/Mirror Systems. *J. Chem. Phys.* 1975, *63*, 1589–1595, doi:10.1063/1.431483.
37. Kelley, S.O.; Barton, J.K.; Jackson, N.M.; McPherson, L.D.; Potter, A.B.; Spain, E.M.; Allen, M.J.; Hill, M.G. Orienting DNA Helices on Gold Using Applied Electric Fields. *Langmuir* 1998, *14*, 6781–6784, doi:10.1021/la980874n.
38. Rant, U.; Pringsheim, E.; Kaiser, W.; Arinaga, K.; Knezevic, J.; Tornow, M.; Fujita, S.; Yokoyama, N.; Abstreiter, G. Detection and Size Analysis of Proteins with Switchable DNA Layers. *Nano Lett.* 2009, *9*, 1290–1295, doi:10.1021/nl8026789.
39. Dynamic Biosensors *SwitchSENSE Fluorescence Proximity Sensing - in Static Mode. Https://Www.Youtube.Com/Watch?V=SqhY5SYdYCw*; 2018;
40. Dynamic Biosensors *SwitchSENSE Protein Size. Different Size = Different Switching Speed. Https://Www.Youtube.Com/Watch?V=uiQ5ldynzWY*; 2018;
41. Mak, S.; Marszal, A.; Matscheko, N.; Rant, U. Kinetic Analysis of Ternary and Binary Binding Modes of the Bispecific Antibody Emicizumab. *mAbs* 2023, *15*, 2149053, doi:10.1080/19420862.2022.2149053.
42. Dynamic Biosensors *SwitchSENSE Bispecific Antibodies. Https://Www.Youtube.Com/Watch?V=_FwYM3OmcIo*; 2018;
43. Rosen, C.B.; Kodal, A.L.B.; Nielsen, J.S.; Schaffert, D.H.; Scavenius, C.; Okholm, A.H.; Voigt, N.V.; Enghild, J.J.; Kjems, J.; Tørring, T.; et al. Template-Directed Covalent Conjugation of DNA to Native Antibodies, Transferrin and Other Metal-Binding Proteins. *Nat Chem* 2014, *6*, 804–809, doi:10.1038/nchem.2003.
44. Gothelf, K.V. Site Selective Conjugation of an Oligonucleotide Conjugate or a Small Molecule to a Metal Binding Protein 2016.
45. Hampel, P.A.; Strasser, R.; Fischer, F.; Rant, U. Assembly and Characterization of a Slingshot DNA Nanostructure for the Analysis of Bivalent and Bispecific Analytes with Biosensors. *Langmuir* 2018, *34*, 14796–14801, doi:10.1021/acs.langmuir.8b02124.
46. Langer, A.; Schräml, M.; Strasser, R.; Daub, H.; Myers, T.; Heindl, D.; Rant, U. Polymerase/DNA Interactions and Enzymatic Activity: Multi-Parameter Analysis with Electro-Switchable Biosurfaces. *Scientific Reports* 2015, *5*, 12066, doi:10.1038/srep12066.
47. Bec, G.; Ennifar, E. SwitchSENSE Technology for Analysis of DNA Polymerase Kinetics. In *Multiprotein Complexes: Methods and Protocols*; Poterszman, A., Ed.; Methods in Molecular Biology; Springer US: New York, NY, 2021; pp. 145–153 ISBN 978-1-07-161126-5.
48. Staffler, R.; Pasternack, R.; Hils, M.; Kaiser, W.; Möller, F.M. Nucleotide Binding Kinetics and Conformational Change Analysis of Tissue Transglutaminase with SwitchSENSE. *Analytical Biochemistry* 2020, *605*, 113719, doi:10.1016/j.ab.2020.113719.
49. Daub, H.; Traxler, L.; Ismajli, F.; Groitl, B.; Itzen, A.; Rant, U. The Trimer to Monomer Transition of Tumor Necrosis Factor-Alpha Is a Dynamic Process That Is Significantly Altered by Therapeutic Antibodies. *Sci Rep* 2020, *10*, 9265, doi:10.1038/s41598-020-66123-5.
50. Sun, L.; Wei, N.; Kuhle, B.; Blocquel, D.; Novick, S.; Matuszek, Z.; Zhou, H.; He, W.; Zhang, J.; Weber, T.; et al. CMT2N-Causing Aminoacylation Domain Mutants Enable Nrp1 Interaction with AlaRS. *Proceedings of the National Academy of Sciences* 2021, *118*, e2012898118, doi:10.1073/pnas.2012898118.
51. Welte, T.; Rant, U. *Inhibitor Induced Shifts in the Thermal Stability of Carbonic Anhydrase (Application Note)*; Dynamic Biosensors GmbH, 2014;
52. Cléry, A.; Sohier, T.J.M.; Welte, T.; Langer, A.; Allain, F.H.T. SwitchSENSE: A New Technology to Study Protein-RNA Interactions. *Methods* 2017, *118–119*, 137–145, doi:10.1016/j.ymeth.2017.03.004.

53. Ramotowska, S.; Spisz, P.; Brzeski, J.; Ciesielska, A.; Makowski, M. Application of the SwitchSense Technique for the Study of Small Molecules' (Ethidium Bromide and Selected Sulfonamide Derivatives) Affinity to DNA in Real Time. *J. Phys. Chem. B* 2022, *126*, 7238–7251, doi:10.1021/acs.jpcb.2c03138.
54. Schulte, C.; Soldà, A.; Spänig, S.; Adams, N.; Bekić, I.; Streicher, W.; Heider, D.; Strasser, R.; Maric, H.M. Multivalent Binding Kinetics Resolved by Fluorescence Proximity Sensing. *Commun Biol* 2022, *5*, 1070, doi:10.1038/s42003-022-03997-3.
55. Kast, F.; Schwill, M.; Stüber, J.C.; Pfundstein, S.; Nagy-Davidescu, G.; Rodríguez, J.M.M.; Seehusen, F.; Richter, C.P.; Honegger, A.; Hartmann, K.P.; et al. Engineering an Anti-HER2 Biparatopic Antibody with a Multimodal Mechanism of Action. *Nat Commun* 2021, *12*, 3790, doi:10.1038/s41467-021-23948-6.

PART II.

CASE STUDIES

Chapter 2

The results presented in this chapter have been published in:

Ponzo, I.; Möller, F.M.; Daub, H.; Matscheko, N. A DNA-Based Biosensor Assay for the Kinetic Characterization of Ion-Dependent Aptamer Folding and Protein Binding. Molecules 2019, 24, 2877. https://doi.org/10.3390/molecules24162877

My personal contribution to this manuscript was the collection and curation of all the experimental data presented in this chapter, their analysis and visualization, and the preparation and writing of the original draft.

2. Kinetic characterization of ion-dependent aptamer folding and protein binding

Abstract

Therapeutic and diagnostic nucleic acid aptamers are designed to bind tightly and specifically to their target. The combination of structural and kinetic analyses of aptamer interactions has gained increasing importance. Here, we present a fluorescence-based switchSENSE® aptasensor for the detailed kinetic characterization of aptamer–analyte interaction and aptamer folding, employing the thrombin-binding aptamer (TBA) as a model system. Thrombin-binding aptamer folding into a G-quadruplex and its binding to thrombin strongly depend on the type and concentration of ions present in solution. We observed conformational changes induced by cations in real-time and determined the folding and unfolding kinetics of the aptamer. The aptamer's affinity for K^+ was found to be more than one order of magnitude higher than for other cations ($K^+ > NH_4^+ >> Na^+ > Li^+$). The aptamer's affinity to its protein target thrombin in the presence of different cations followed the same trend but differed by more than three orders of magnitude (K_D = 0.15 nM to 250 nM). While the stability (k_{OFF}) of the thrombin–TBA complex was similar in all conditions, the cation type strongly influenced the association rate (k_{ON}). These results demonstrated that protein–aptamer binding is intrinsically related to the correct aptamer fold and, hence, to the presence of stabilizing ions. Because fast binding kinetics with on-rates exceeding 10^8 $M^{-1}s^{-1}$ can be quantified, and folding-related phenomena can be directly resolved, switchSENSE® is a useful analytical tool for in-depth characterization of aptamer–ion and aptamer–protein interactions.

2.1. Introduction

Aptamers are single-stranded oligonucleotides with ideally high-binding affinity and specificity for their targets [1,2]. Currently, numerous aptamers have been selected for a wide range of targets, including proteins, small molecules, and even whole cells [3–5]. Due to the presence of some similarities and its many advantages, aptamers are often compared to antibodies, with similar hopes for diagnostic and therapeutic applications [6]. Both can be designed to bind their targets with very high affinities. The observable trend in the field of antibodies to develop bispecific or trispecific antibodies with two or more binding sites combined, applies to aptamers as well [7]. Multi-specific antibodies or aptamers mediate increased specificity, even slower off-rates from the target, or recruitment of specific effectors to a targeted site. However, multiple binding sites challenge the analysis of binding and unbinding rates, important factors in pharmacokinetics. Advantages of aptamers over antibodies start at the development stage. Raising a specific aptamer via an *in vitro* systematic evolution of ligands by exponential enrichment (SELEX) process takes less time in comparison to raising a new antibody, and does not have any animal requirements, which results in overall lower costs. During the very reproducible production it is easy to include site-specific chemical

modifications or labels in aptamers. Nucleic acid aptamers exhibit a high thermal stability and good tissue penetration due to their small size [6]. Disadvantages of aptamers include their susceptibility to nucleases in the blood stream, which can be overcome by site-specific chemical modifications. For example, modifications of the 2′-OH of the nucleobase ribose, together with a 3′ inverted deoxythymidine (idT) cap, has led to an increased half-life in the blood stream of the first aptamer approved for clinical applications, the polyethylene glycol (PEG)-conjugated, anti-vascular epithelial growth factor (VEGF) aptamer NX1838 [8]. However, any modification introduced into an aptamer might change its affinity and specificity for its target as well, which needs to be carefully controlled. A long-known and well-described example of a G-quadruplex aptamer is the 15mer thrombin-binding aptamer (TBA), recognizing the fibrinogen-recognition exosite I of thrombin via predominantly ionic interactions [9]. Thrombin is a serine protease and has a central role in the coagulation cascade. In normal conditions, thrombin is not present in human blood, but during coagulation its concentration varies from pM to µM levels [10,11]. Therefore, analytical assays with high sensitivity, but broad active range, for thrombin detection are of crucial importance in clinical practice. Numerous assays for thrombin detection have been developed up to date, with more than a hundred based on detection by aptamers alone [12]. All these assays come with strong differences in detection limits and have revealed a very broad range of dissociation constants (K_D) for this aptamer–protein interaction, ranging from 200 pM [13] to 3 digit nM affinities [14]. The sensitivity of the interaction towards changes in the buffer system, assay orientation, detection method, and more, results in weak reproducibility of the K_D. Nevertheless, the often-reported detection limit of lower pM thrombin concentrations could not be achieved with a nM K_D, indicating that in, ideal conditions, thrombin is binding to TBA with a pM K_D. Moreover, historically, the TBA has been used as model system to demonstrate the proof-of-principle of aptamer-based assays in general [12]. Notably, single-molecule nanopore conductance studies have been performed to obtain data on label-free TBA folding and unfolding in the presence of different types of cations [15]. Considering the importance of the correct fold of the aptamer for its binding ability, it is of crucial importance to develop an easy assay that allows investigation of the role of solution components and target interaction on the aptamer fold. Since the binding site of aptamers is not the primary nucleic acid sequence, but the secondary structure, folding has a tremendous influence on the binding efficiency. Many aptamers that recognize biologically relevant protein targets reach activity by folding into G-quadruplex structures [16]. The DNA or RNA G-quadruplex structures have four guanines positioned in a square plane (G-tetrad) and have two or more G-tetrads stacked on top of each other [17]. The guanines coordinate a cation in the middle or in between G-tetrads, which is essential for correct folding. Interestingly, the type of cation is of great importance to the folding conformation. While both Na^+ and K^+ have been found to bind to the TBA, steady-state nuclear magnetic resonance (NMR) provided good indications that they do not form the same interactions with TBA and might induce alternative folds. NH_4^+, however, binds less stably than K^+, but induces the same anti-parallel G-quadruplex fold [18]. The correct coordination of the cation among the two G-tetrads seems to depend on the ionic radius, since cations with ionic radii in the range of 1.3-1.5 Å fit well (K^+: 1.33 Å, NH_4^+: 1.45 Å). In contrast, smaller or larger cations are not able to coordinate properly with the guanines. The Li^+ and Na^+ ionic radii are

0.6 Å and 0.95 Å, respectively, and therefore too small to fill the position of the central ion [15,19,20].

In addition to the induction of the folding of the G-quadruplex by ion coordination only, the role of target interaction is discussed as well. Structures of aptamers free of (apo) or bound by their target in a steady state have been solved by circular dichroism (CD) [14], crystal structures [21], and NMR [18]. These studies provide insight into the capability of different molecules to induce folding of aptamers which are not fully folded in their apo state (induced fit) [22]. Observation of the folding and unfolding processes in real-time, however, is limited by a scarcity of suitable methods. Commonly, fluorescence spectroscopy methods (e.g., fluorescence resonance energy transfer (FRET)) have been employed for the measurement of folding kinetics upon initiation by ions or target molecules. Even more challenging is the measurement of the unfolding rate, which requires fast wash-out of the analyte. This is not amenable in spectroscopy methods and to date mainly relies on modeling approaches. The application of standard methods for rate elucidation, notably surface plasmon resonance (SPR), to aptamer folding is limited. Both the detection of conformational changes, as well as binding of very small molecules such as ions to aptamers immobilized by large complexes, typically streptavidin, have proven difficult in SPR [23]. A better understanding of factors influencing folding and binding rates is necessary to gain control and build confidence in the sensitivity and specificity of aptamers. Here, we introduce a convenient technology for the study of aptamers and their target interaction. switchSENSE® [24–26] is an emerging technology for biophysical quantification of binding and activity rates, in addition to a friction read-out. Adaptation of the DNA-based switchSENSE® biosensors for aptamer measurements allowed us to profit from the inherent advantages of the technology for nucleic acid ligands, including quasi modification-free aptamer immobilization on the biosensor by hybridization. We characterized the well-described TBA model system by ranking K^+, Na^+, NH_4^+, and Li^+ in their anti-parallel G-quadruplex folding capacity. We quantified the ion association (k_{ON}) and dissociation (k_{OFF}) rate and observed the folding and unfolding rates (k_F, k_U) in real time. Furthermore, we reported extraordinarily fast on-rates and dissociation constants (K_D) down to the pM range for thrombin binding to TBA, depending on the buffer conditions. The broad dynamic range of detection of the aptasensor renders it a superior choice for quantification of thrombin from serum samples in diagnostics. Resolution of residence times and complex binding stoichiometries, on the other hand, are believed to aid in the development of therapeutics. Lastly, the resolved folding and binding processes allowed the conclusion of thrombin actively inducing the G-quadruplex fold.

In summary, targeting aptamers for diagnostics and therapy requires a detailed understanding of folding and interaction kinetics. We developed a powerful aptasensor for rapid and in-depth characterization of aptamers based on the switchSENSE® technology, which can be easily adapted to various DNA/RNA aptamers.

2.2 Results

2.2.1 Development of the aptasensor

Quantification of kinetic rates can be achieved on various commercial technologies. Since the switchSENSE® biosensor comes with pre-immobilized DNA, it is designated for nucleic acid ligands. The general switchSENSE® assay workflow is depicted in Figure 1A. We created an aptasensor by functionalizing the single-stranded (ss) DNA covalently immobilized on the switchSENSE® biosensor (termed nanolever) via hybridization of a complementary strand (cNL-B) elongated with the aptamer sequence (Figure 1A, ①). The aptasensor setup can be seen in more detail in Figure 1B (right electrode). We extended the 5′ end of cNL-B with a short linker that is followed by the TBA sequence (see Material and Methods section for exact sequences). A quencher can be placed on the distal end of the aptamer sequence to enhance the folding read-out. Upon anti-parallel G-quadruplex formation, the quencher comes into proximity of the immobilized dye. Alternative conformations can be detected by placing the quencher at different positions on the aptamer, the resulting quenching efficiency will provide insight into the relative distance of the respectively targeted nucleotide to the dye. Here, the quencher can help to confirm aptamer immobilization on the surface. The hybridization of the complementary strand of the nanolever without TBA leads to the formation of a double-stranded (ds) DNA on the surface (Figure 1B, left electrode). Thereby, the fluorophore is pushed further away from the gold surface of the biosensor, since dsDNA is more rigid than ssDNA. This results in an increase of fluorescence due to the reduction in the quenching by the gold surface (Figure 1C, red trace). The hybridization of the TBA- and quencher-functionalized cNL-B leads to an increase in fluorescence as well, since the formation of the dsDNA base increases the distance of the dye from the gold surface. However, at the same time the quencher reduces the total fluorescence during the real-time functionalization of the sensor. Consequently, the fluorescence increase is smaller (Figure 1C, blue trace). The difference in fluorescence increase at full surface saturation (indicated by arrows on the right side of Figure 1C) allows to differentiate the biosensor functionalized with dsDNA from the aptasensor.

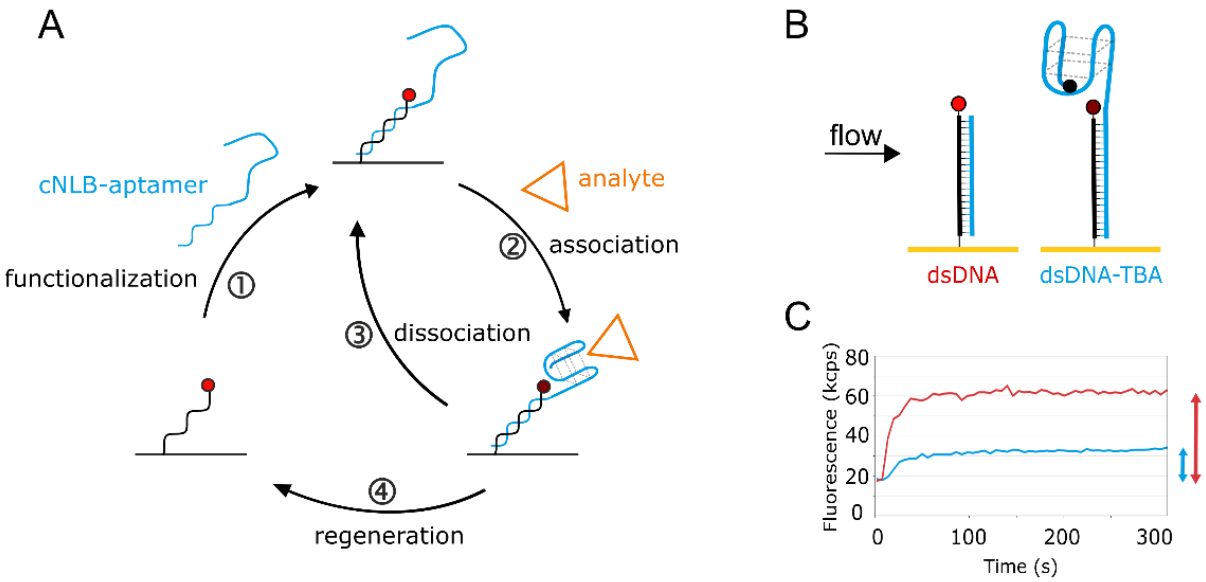

Figure 1. *Aptasensor setup. (A) The aptasensor workflow consisting of ① sensor functionalization, ② + ③ analyte kinetics, and ④ sensor regeneration. The cycle can be automated to continue to bring various targets of interest onto the surface. (B) Scheme of the aptasensor surface. On the left, the immobilized single-stranded nanolever (NL) is functionalized with a complementary sequence (cNL), forming dsDNA. On the right, cNL is extended with the thrombin-binding aptamer (TBA) sequence, carrying a quencher on the distal end. (C) Real-time surface functionalization with dsDNA (red) and dsDNA-TBA with quencher (blue). Fluorescence amplitudes reached are marked with respective arrows.*

Once the functionalization of the surface with TBA has been confirmed, the ion or protein analyte is injected. Folding and binding kinetics can be measured in real-time upon association and washing out of analyte, respectively. The analyte influences the local fluorophore environment leading to a fluorescence change upon binding (Figure 1A, ②) and restoring the original fluorescence level upon removal (Figure 1A, ③). Washing the biosensor surface with regeneration solution allows to remove any hybridized ligand and prepares the immobilized ssNL for the injection of the next sample (Figure 1A, ④). This automated workflow enables sampling of various targets of interest with low sample consumption.

2.2.2 Real-time kinetics of aptamer folding

As discussed in the introduction, cations influence the formation and stability of the G-quadruplex structure. However, rates of ion-induced folding and unfolding have only been reported in sporadic studies [15]. Therefore, we first subjected the immobilized aptamers to K^+, NH_4^+, Na^+, and Li^+ ions and compared their influence on the G-quadruplex folding. Employing the setup shown in Figure 1A, the association of ions to TBA was observed by a concentration-dependent fluorescence decrease. The aptamer sequences were functionalized with a quencher (BBQ-650®) at the 5′ end for enhanced signal amplitude for these experiments. Importantly, the microfluidic setup was able to wash out the ions tested on an millisecond (ms) timescale, allowing the aptamers to release bound cations and come back to

an unfolded state. Correspondingly, dissociation of ions resulted in a fluorescence increase back to starting levels, representing the unfolding. Addition of salt as analyte changes the ionic strength of the solution and might have an influence on the fluorophore itself. To correct for the influence of the ionic strength on the fluorescence signal, data shown in Figure 2 are referenced with the signals obtained by injection of the same analyte solutions to a non-folding control, the "scrambled TBA" (TBAsc). It contains the same nucleotides as TBA, but in a changed order that prevents G-quadruplex formation (Figure 2A). Figure 2B–E shows the real-time concentration-dependent folding in the presence of K^+, NH_4^+, Na^+, and Li^+.

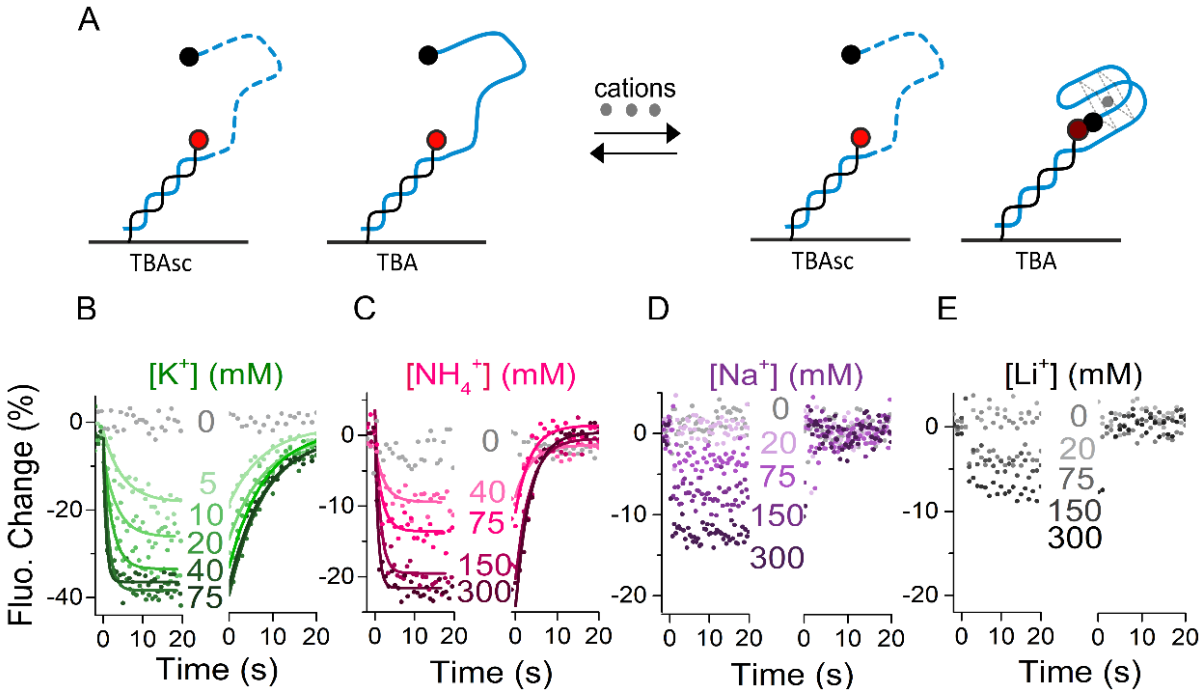

Figure 2. *Kinetics of cation-dependent aptamer folding. (A) Schematic representation of the effect of cations on thrombin-binding aptamer (TBA) and scrambled TBA sequence (TBAsc) folding. Upon G-quadruplex formation the 5′ quencher is brought into proximity of the fluorophore, thus the fluorescence decreases. (B–E) Real-time fluorescence signal (dots) and fits (solid lines) of a representative experiment measuring the association and dissociation phases of: (B) K^+; (C) NH_4^+; (D) Na^+; (E) Li^+ to immobilized TBA carried out in 50 mM Tris. Binding signal to TBA is referenced with binding signal to TBAsc.*

We observed a strong signal decrease upon injection of K^+, related to an efficient ion binding and, thus, aptamer folding (Figure 2B). Fitting the K^+ kinetics yielded a K_D of 8 mM (k_{ON} and k_{OFF} rates are reported in Table 1). We observed a similar behaviour for NH_4^+ ions (Figure 2C), though with slower on and faster off rates and a K_D of 104 mM. The dependence of the conformational change on ion concentration indicated that the rate-limiting step was ion binding and not folding. At highest ion concentration, the ion binding was not rate-limiting anymore, therefore we interpreted the observed rate as the maximum possible folding rate (see the Discussion section). We observed TBA folding at a rate of 1.26 s^{-1} in the presence of 75 mM KCl, and only slightly slower at 1.18 s^{-1} in the presence of 300 mM NH_4^+. Interestingly, in both KCl and NH_4Cl we got close to the maximum saturation levels (amplitudes levelling off

at minimum), the total fluorescence change was much larger in KCl (~40%) than in NH_4Cl (~25%). Since the extent of quenching was directly related to the distance of the quencher from the dye, a lower amplitude represents an average larger distance. It should be noted that the differences in amplitude can be caused by less ion binding/folding and/or an alternative folding state. Association and dissociation of Na^+ and Li^+ ions resulted in concentration-dependent step function signal decreases and increases, respectively, which could not be fit with a mono-exponential fit function (Figure 2D–E). This indicates very low affinity of these ions to the aptamer or low antiparallel G-quadruplex folding capacity. Our findings correspond with Li^+ generally being regarded as a monovalent cation having no effect on G-quadruplex folding [15,27]. The slight decrease in fluorescence signal upon Li^+ injection was likely caused by non-G-quadruplex like conformational changes that alter the distance of the quencher to the dye. Similarly, Na^+ has been reported to induce folding of an alternative conformation, which is more dynamic and does not end with the 5′ quencher in close proximity of the dye [18].

Table 1. *Summary of ion-TBA kinetic parameters in 50 mM Tris buffer, observed by the conformational change they induce. Rates of ion binding were obtained by global mono-exponential fits. The ion dissociation rate k_{off} represents the minimum rate to allow the observed unfolding rate k_U. The folding rate k_F was the observed rate at highest salt concentration tested. Values shown represent the mean (± standard deviation, SD) of three independent experiments.*

Ion	k_{ON} ($M^{-1}s^{-1}$)	$k_{OFF} = k_U$ (10^{-1} s^{-1})	K_D (mM)	k_F (s^{-1})	K_F (no unit)
NH_4^+	2.96 ± 0.8	3.07 ± 0.3	104 ± 40	1.18 ± 0.23	3.84 ± 0.8
K^+	15.2 ± 1.7	1.20 ± 0.01	7.89 ± 1.3	1.26 ± 0.14	10.4 ± 1.1
Na^+	-	-	-	-	-
Li^+	-	-	-	-	-

k_{ON} = rate constant of ion binding to TBA ($M^{-1}s^{-1}$); k_{OFF} = minimum rate constant of ion dissociation from TBA (s^{-1}); K_D = equilibrium dissociation constant of ion (M) calculated by $K_D = k_{OFF}/k_{ON}$; k_F = observed rate of TBA folding (s^{-1}); k_U = rate constant of TBA unfolding (s^{-1}); K_F = ratio of TBA folding versus unfolding calculated by $K_F = k_F/k_U$.

Overall, our results show G-quadruplex folding induced by K^+ and, with lower affinity for TBA, by NH_4^+. Na^+ was shown to have a very low affinity and likely induces alternative conformations, while hardly any binding of Li^+ was observed.

2.2.3 Influence of salt species on Thrombin binding Kinetics

Analysis of the folding and unfolding rates and extent of TBA folding showed a clear dependence on the nature of the ion present in solution. The effect of pre-folded G-quadruplex on thrombin binding was not clear. Therefore, we next determined the influence of the different ions on the kinetic rates of thrombin binding to TBA (Figure 3A). All ions were used at a fixed concentration of 140 mM. In contrast to the folding experiments, we did not functionalize the aptamer with a quencher for these binding experiments, because fluorescence signal changes due to the changes in the local environment of the immobilized

dye were observed upon thrombin binding even without quencher. Both the protein itself, as well as the 5′ terminal guanine of TBA, are able to affect the fluorescence. Figure 3B–E shows the real-time concentration-dependent association and dissociation curves of thrombin interaction in the presence of K^+, NH_4^+, Na^+, and Li^+. In this case, the association of thrombin to TBA was detected by a concentration-dependent fluorescence decrease, and its dissociation resulted in a fluorescence increase back to initial levels. Single-exponential binding behavior was observed as expected for a one-to-one-interaction. Global fitting of the curves yielded on-rates strongly dependent on the nature of the ions in solution. Surprisingly, K^+ enabled an extraordinarily fast on-rate of $k_{ON} = 3.8 \times 10^8\ M^{-1}s^{-1}$. We would like to highlight that these extremely fast on-rates can only be resolved with sufficiently high flow rates. Figure S1, in the Supplementary Materials, shows in fact the effect on k_{ON} and k_{OFF} in the presence of K^+ at 100, 500, and the applied 2000 µL/min flow rates. Slower analyte transport yielded lower on-rates due to the mass transport limitations, as well as reduced off-rates due to the rebinding.

Comparing the two physiologically relevant ions K^+ and Na^+, we found that k_{ON} of thrombin in the presence of Na^+ was 10 times lower than in the presence of K^+ ($k_{ON} = 3.3 \times 10^7\ M^{-1}s^{-1}$, Figure 3C). This is in good agreement with the folding data and literature: K^+ ions stabilize the folding of TBA into a G-quadruplex and thus facilitate thrombin binding [28,29]. In contrast, alternative conformations in the presence of Na^+ [18] first need to be transformed to the thrombin-binding anti-parallel G-quadruplex fold. Furthermore, we analyzed the kinetics in the presence of ammonium ions, which have been reported to pre-fold the same G-quadruplex as K^+, though with lower affinity [18]. The previously determined K_D of NH_4^+ results in more than 50% of TBA being pre-folded in the applied condition of 140 mM salt. Interestingly, we found that the affinity of thrombin was in the same range as in the presence of K^+, with the k_{ON} rate reduced by a factor of 2 ($1.7 \times 10^8\ M^{-1}s^{-1}$, Figure 3D).

The effect of the presence of Li^+ ions is controversial, but it is considered to be the least efficient in folding the active G-quadruplex [19]. Nevertheless, we observed concentration-dependent association of thrombin to TBA in LiCl buffer. Here, the on-rate of thrombin was significantly lower at $2.6 \times 10^5\ M^{-1}s^{-1}$, which is 1000 times slower than in the presence of K^+. Accordingly, the interaction was observed only in the presence of comparably high thrombin concentrations above 7 nM (Figure 3E). Intriguingly, the ion-dependent shift in affinity was solely caused by changes in the on-rate, while the off-rate was well comparable in all conditions tested. This results in K_Ds in the picomolar to nanomolar range, as listed in Table 2 and visualized in the rate plot in Figure 3F.

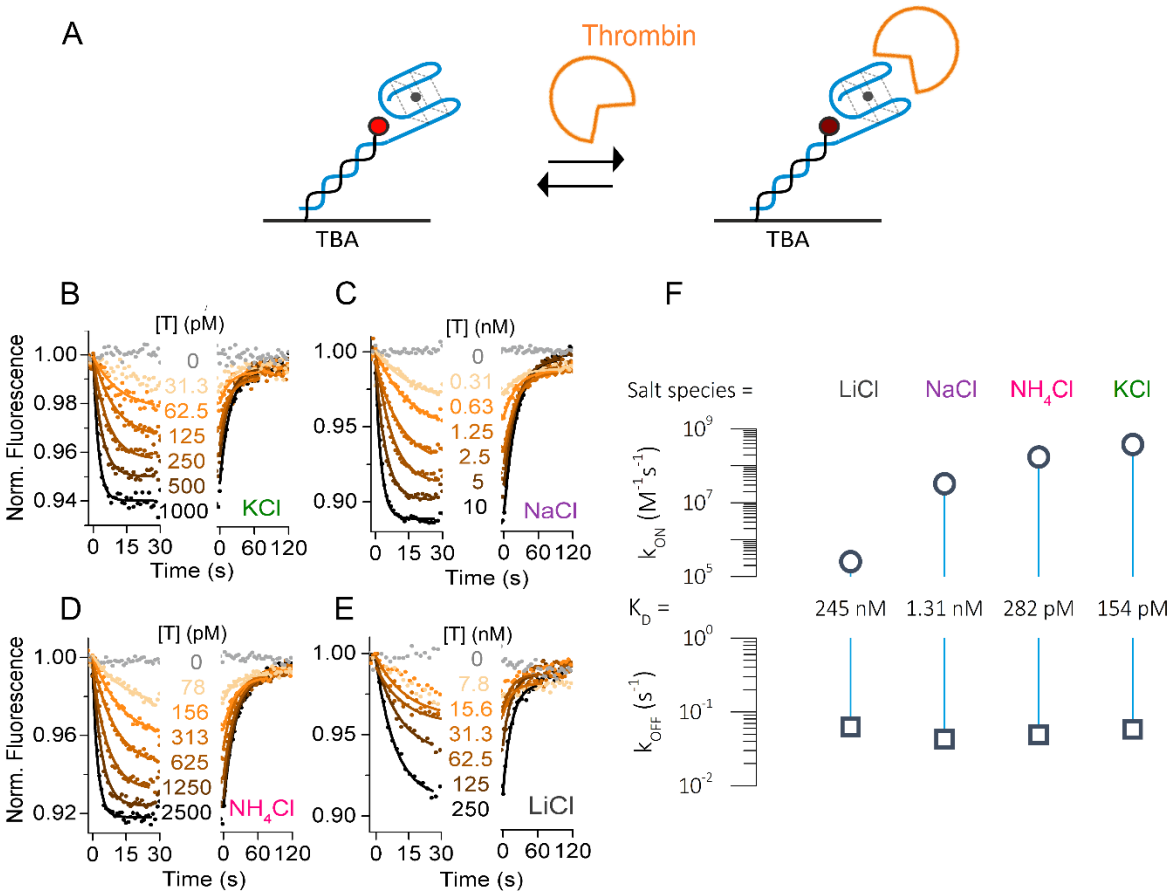

Figure 3. *Influence of cation on thrombin–TBA kinetic rates. (A) Schematic representation of thrombin–TBA interaction. (B–E) Real-time fluorescence signal (dots) and fits (solid lines) of a representative experiment measuring the association and dissociation phases of thrombin (T) to immobilized TBA carried out in: (B) TE140-KCl; (C) TE140-NaCl; (D) TE140-NH4Cl; (E) TE140-LiCl. (F) Rate plot. The error bars (SD of three consecutively measured datasets) are smaller than the symbol size.*

Table 2. *Summary of thrombin–TBA kinetic parameters in indicated buffers. Data represent the mean (± standard deviation, SD) of three independent experiments.*

Buffer	**k_{ON} (10^7 $M^{-1}s^{-1}$)**	**k_{OFF} (10^{-2} s^{-1})**	**K_D (nM)**
TE140-KCl	38 ± 1.3	5.8 ± 0.1	0.15 ± 0.01
TE140-NH_4Cl	17 ± 1.0	4.8 ± 0.1	0.28 ± 0.02
TE140-NaCl	3.3 ± 0.2	4.3 ± 0.1	1.31 ± 0.12
TE140-LiCl	0.03 ± 0.01	6.3 ± 0.4	245 ± 94

In conclusion, we demonstrated the dependence of thrombin association on the type of cation in solution and resolved on-rates of thrombin to TBA up to the 10^8 $M^{-1}s^{-1}$ range in best conditions, which contain cations that facilitate thrombin binding by pre-folding of the G-quadruplex.

2.2.4 Specificity of TBA for Thrombin interaction allows broad dynamic range

Herein, we firstly demonstrated the influence of the cation species on the TBA–thrombin kinetics, applying thrombin concentrations from 31 pM to 250 nM to reach significant fractions bound in all buffers. Many methods are limited in their dynamic range, by lacking sensitivity for low concentrations and increasing the background at high concentrations. The challenging detection of low pM concentrations can be achieved by the switchSENSE® aptasensor within 30s contact time (Figure 3B). Next, we designed specificity controls to exclude background contributing to our binding signals at higher protein concentrations. To study the sequence and structure specificity of the thrombin–aptamer interaction, we used two control sequences: *i)* TBAsc which does not fold into a G-quadruplex structure¸ *ii)* Human Telomeric repeat Aptamer (HTA), which is another G-quadruplex forming aptamer. Both aptamers were tested in the best binding conditions (TE140-KCl) with a thrombin concentration of up to 10 nM, covering the range of concentrations applied in K^+, NH_4^+, and Na^+ buffers. As shown in Figure 4A, we could not observe any association of thrombin to TBAsc, indicating that our obtained binding signal in Figure 3 was specific for the folded TBA structure. Furthermore, we neither observed thrombin binding to HTA (Figure 4B), which is known to form a G-quadruplex structure in the presence of K^+ [30]. These findings underline not only the structure-, but also sequence-specificity of the thrombin binding aptamer. Lastly, we increased the protein concentration to 250 nM in TE140-LiCl and checked for non-specific interactions of this high protein concentration with TBAsc. The lack of signal in Figure 4C confirms that even at high concentrations, thrombin binding is specific at the salt concentration applied for the binding experiments. In conclusion, we showed a broad dynamic range of the aptasensor from low pM to high nM target concentrations.

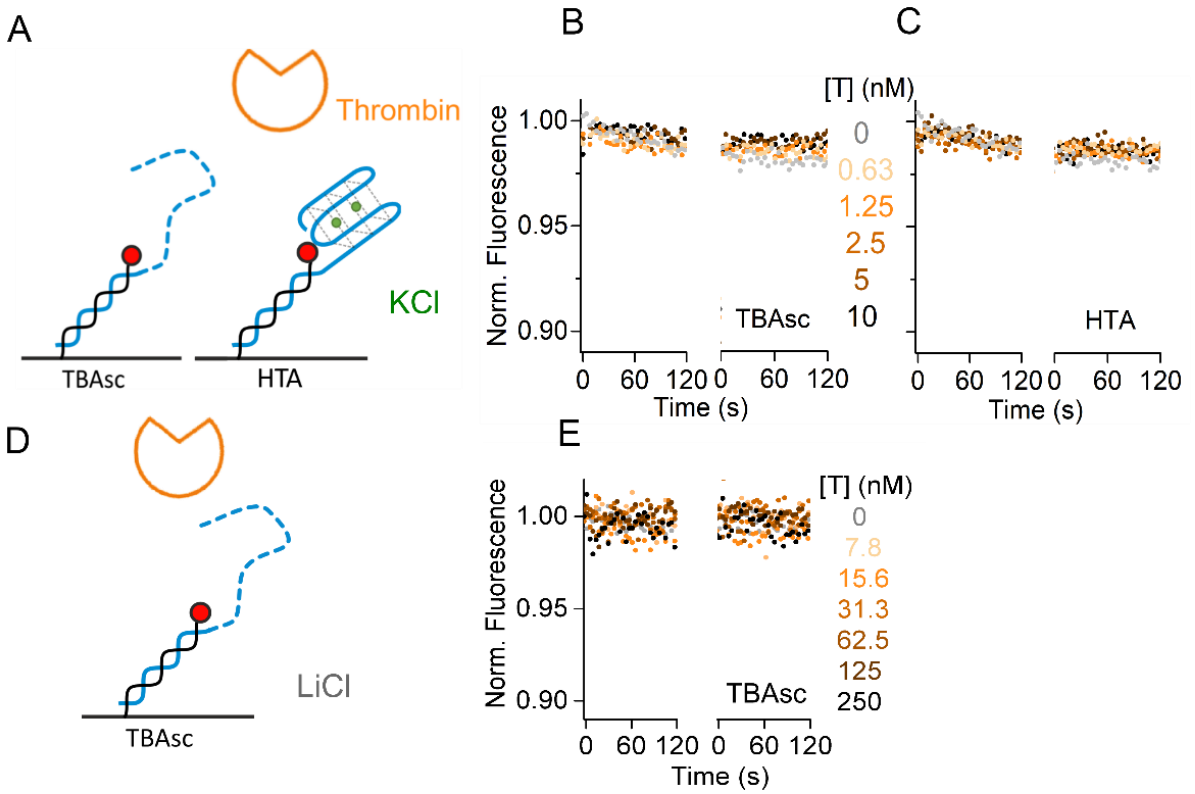

Figure 4. *Specificity controls of thrombin–TBA interaction. (A,D) Schematic representation of the controls used. Real-time fluorescence signal (dots) during thrombin (T) kinetics with: (B) immobilized TBAsc; (C) immobilized human telomeric repeat aptamer (HTA) in TE140-KCl; (E) immobilized TBAsc in TE140-LiCl with indicated protein concentrations. In these conditions, no folding and/or binding were observed.*

Importantly, we maintained an ionic strength of 150 mM in all tested conditions and only altered the type of cation added to the buffer. This was a prerequisite for specific thrombin interaction, since in a background of 50 mM Tris without any additional salt, we observed non-specific interaction of thrombin with dsDNA at high protein concentrations (>100 nM) (Figure S2C). The presence of TBA or TBAsc in this no-salt condition reduced the minimum thrombin concentration leading to a non-specific signal to 62.5 nM thrombin, with an overall higher signal amplitude (Figure S2A,B). These controls indicate that low ionic strength can lead to non-specific interaction of thrombin with ds and ssDNA.

2.2.5 Immobilized target for aptamer screening

All data shown so far were obtained with the aptamers immobilized on the sensor surface. However, the process of aptamer selection SELEX [1,2] yields a variety of different aptamers, which need to be screened against one target. Next, we show a reversed assay format that facilitates such screenings of the obtained aptamers. In this setup, thrombin is immobilized on the sensor surface as covalent conjugate to the cNL-B sequence. The same measurement workflow as described in Figure 1 was applied for the immobilization of thrombin on the sensor. In the first step, the DNA conjugated to thrombin was hybridized to the surface-

immobilized ssDNA nanolever. Subsequently, the thereby thrombin-functionalized surface was exposed to different aptamers (TBA, TBAsc, HTA) in TE140-KCl buffer, as indicated in Figure 5A. Association of TBA to thrombin was detected by a concentration-dependent fluorescence increase, and its dissociation resulted in a fluorescence decrease back to initial levels. Figure 5B–D show the real-time concentration-dependent association and dissociation data of TBA, TBAsc, and HTA with thrombin. We confirmed specific binding of TBA to immobilized thrombin (Figure 5B). The resulting association and dissociation rates were $k_{ON} = 4.6 \pm 1.9 \times 10^{7}\ M^{-1}s^{-1}$ and $k_{OFF} = 2.8 \pm 0.6 \times 10^{-1}\ s^{-1}$, respectively, yielding a $K_D = 6.2 \pm 4$ nM. It is noteworthy that the dissociation constant was higher than determined in the previous assay orientation. Nonetheless, the screening correctly identified TBA as the binding partner. In contrast, neither TBAsc nor HTA showed any interaction (Figure 5C,D). These controls confirm that the immobilized thrombin was only recognized by specifically raised aptamers.

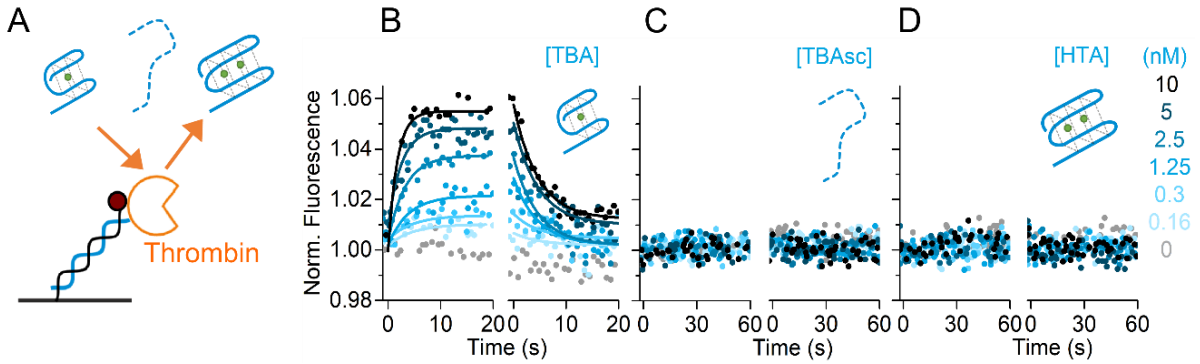

Figure 5. Reversed assay orientation. (A) Schematic representation. (B–D) Real-time fluorescence signal (dots) and fits (solid lines) during association and dissociation phases of aptamers to immobilized thrombin carried out in TE140-KCl. Thrombin binding kinetics of (B) TBA; (C) TBAsc; (D) HTA. In (C) and (D) no binding was observed.

2.3 Discussion

The purpose of this study was to facilitate high-quality, in-depth analysis of aptamers. We demonstrated how the switchSENSE® technology can resolve aptamer folding and unfolding upon interaction with small molecules, such as ions, and provide rates of target kinetics. We chose thrombin and its well-described 15mer TBA [9] as a model system to develop an aptasensor and investigate advantages and limitations of the switchSENSE® technology for aptamer measurements.

2.3.1 Real-time folding and unfolding rates coupled to ion binding

The conformational change in TBA was directly dependent on the cation binding to the aptamer. The association of positively charged cations to the negatively charged DNA was strongly driven by ionic interaction and affected the DNA self-interaction. Furthermore,

fluorophores were sensitive to ionic strength. This resulted in control DNA TBAsc showing the same concentration-dependent, but cation type-independent, signal change in response to all cations (see raw data in Figure S4). In contrast, TBA reacted in a cation-dependent way beyond the signal of ion binding alone. To extract the TBA-specific rates, we therefore referenced the TBA with TBAsc signal. This leaves us with a rate that had in fact two components: 1) the kinetics of the ion with TBA; 2) the rate of the conformational switch in response to the ion. Though, we observed some degree of folding in response to all cations tested, only in the presence of K^+ and NH_4^+ we could apply a global mono-exponential fit and observe concentration-dependent signal saturation. The dependence of the folding rate on the ion concentration indicated that the ion-binding was the rate-limiting step at lower concentrations. The observed rate constant, therefore, represents k_{ON} of the cation. We report k_{ON} of K^+ = 15.2 $M^{-1}s^{-1}$ and k_{ON} of NH_4^+ = 2.96 $M^{-1}s^{-1}$. Since unfolding dynamics cannot be synonymized with ion residence time [19], the ion must dissociate from the complex to allow unfolding. By the example of NH_4^+, this is allowed by an exchange rate from TBA-bound to bulk of 1.0 s^{-1} at 15°C [18]. This rate is very close to the unfolding rate in our setup $k_U(NH_4^+)$ = 0.31 s^{-1}, measured at 25°C. In contrast to binding, it is not possible to limit the unfolding rate by changing the ion concentration. We, therefore, used TBA unfolding rates synonymously to the minimal ion dissociation rates. In line with literature, K^+ not only showed faster on-rates, but also slower off-rates ($k_U(K^+)$ = 0.12 s^{-1}) than NH_4^+. Both Na^+ and Li^+ exhibited residence lifetimes below our ms resolution, which indicates that they were inducing rapidly, switching alternative conformations. We have concluded that sub-maximum ion concentrations limit the folding rate. Conversely, applying ion concentrations above their binding saturation level should result in maximum folding rates. We therefore report a K^+-dependent observed folding rate of 1.26 s^{-1} in a background of 75 mM KCl. NH_4^+ induced slower folding at 1.18 s^{-1} at 300 mM. It should be noted that this rate was still limited by ion concentration, since the K_D = 104 mM indicates NH_4Cl should be used at ~1 M to reach saturation. Measured by an entirely different method, Shim *et al*. [15] obtained very comparable folding kinetics of TBA, particularly the unfolding rate ($k_U(K^+)$ = 0.07 s^{-1}; $k_U(NH_4^+)$ = 0.25 s^{-1}). The employed method of single-molecule nanopore conductance studies directly measures the unfolding rate k_U. However, the observed folding rate k_F was calculated from $K_F = k_F/k_U$. In contrast, here we observed both folding and unfolding rate directly. The K_D of potassium (K_D = 8 mM) was more than one magnitude higher than for NH_4^+, while folding by Na^+ and Li^+ could not be quantified. The difference in folding capacity has been related to the ionic radius: Na^+ is too small to properly coordinate with the guanines of the G-tetrad (see Introduction). Therefore, TBA mainly folds into a parallel-type G-quadruplex structure in the presence of Na^+ ions [18], which did not result in efficient quenching in our setup. Correspondingly, we could not quantify folding rates in the presence of Na^+ and Li^+. Nevertheless, the amplitudes reached at a fixed ion concentration, representing the fraction folded, confirmed the order of the folding capacity to be $K^+ > NH_4^+ > Na^+ > Li^+$ (Figure S3A), as suggested by the literature [31,32]. Due to the surface immobilization by a complementary sequence, the total DNA oligo studied here differs from the label-free TBA sequence used in solution assays. The TBA sequence was originally identified as consensus sequence from several longer DNA oligos interacting with thrombin [9]. This indicates that TBA is able to form the thrombin binding site even in the presence of additional ssDNA. The good agreement of folding rates determined by our method and by the label-free conductance study

indicates that the immobilization of aptamers via extended DNA does not alter folding rates significantly. This is not surprising, since the additional DNA is rendered dsDNA by hybridization to the surface and is therefore removed from the folding reaction. Consequently, we consider TBA in our setup to be quasi label free.

2.3.2 Resolution of high affinity TBA-protein interaction

As in the folding experiment, the kinetic rates of thrombin binding showed a strong dependence on the applied flow rate (Figure S1). This indicates that artefacts such as mass-transport limitation during the association and rebinding during the dissociation are easily distorting measured TBA–thrombin kinetic rates. To minimize these technical limitations, all folding and binding experiments were performed at a high flow rate of 2000 µL/min and a low surface density. One electrode can be functionalized with approximately 200 TBA molecules/µm^2, which results in roughly 2 × 10^6 molecules per electrode. Profiting from the high-performance microfluidic system, we were able to resolve thrombin binding to TBA at unprecedented rates. Impressive is the on-rate of 3.8 × 10^8 M^{-1}s^{-1} in the background of KCl, considering how close this is to the theoretical diffusion-limited on-rate in the range of ~10^9 M^{-1}s^{-1}. In line with literature, K$^+$-based buffers are the most efficient in promoting thrombin binding [15,33,34]. The corresponding dissociation constant K_D = 154 pM compares well with the lowest values reported in the literature of 200 pM [13]. Replacement of K$^+$ by other cations, while keeping the ionic strength constant, reduced the on-rate down to 2.6 × 10^5 M^{-1}s^{-1}, resulting in a K_D = 245 nM (LiCl buffer). Situated in between is the low nM K_D in NaCl-based buffer, which compares well with K_D = 7.1 nM determined in similar conditions by SPR [35]. Interestingly, the off-rate was rather independent of the cation present and remained at ~ 5 × 10^{-2} in all tested buffers. The developed aptasensor is a high-sensitivity assay with a detection limit of < 30 pM in TE140-KCl (Figure 3B). Even lower concentrations of thrombin have been reported in the literature, e.g., 10 pM were measured by cationic polythiophene derivatives, which produce a fluorometric read-out [36]. These detection limits fit with a K_D in the pM range, since a nM K_D would not result in any significant surface saturation at low pM concentrations. Importantly, the low pM detection limit does not prevent the application of high nM concentrations of thrombin to the aptasensor.

In conclusion, for the first time, we can report TBA–thrombin rates resulting in a K_D of 150 pM, explaining the high sensitivity of many existing assays.

2.3.3 Differentiation of pre-folded aptamer from induced fit

Although Li$^+$ and Na$^+$ ions do not promote TBA to fold into a G-quadruplex, specific thrombin binding was observed at high concentrations anyways. This finding is in line with the literature reporting thrombin binding even in the absence of salts [22,37,38]. Although our controls (Figure S2) caution that binding of thrombin at low salt might be strongly non-specific, well-

referenced studies can conclude binding due to the induced fit. Here, thrombin-binding experiments were performed at a fixed cation concentration of 140 mM in the buffer. In the case of K^+, which was shown to have a K_D of 8 mM in Figure 2, this led to the majority of TBA on the chip being folded. In contrast, NH_4^+, Na^+, and Li^+ at the same concentration showed significantly less signal quenching, i.e., G-quadruplex formation (Figure S3A). Due to the lower thrombin affinity, higher concentrations of thrombin had to be applied in these buffers to reach comparable surface saturation in the background of NH_4^+ and Na^+. In the presence of Li^+, even with 250 nM of thrombin, only about 50% saturation was reached (Figure S3B). The surface saturation at specific protein concentrations can be calculated as fraction bound (%) from the measured kinetic rates (Figure S3D–G). Interestingly, despite the thrombin binding rate was the highest in presence of K^+, this condition shows the smallest signal amplitude (6%) (Figure 2 and S3C). Though saturating a comparable fraction of TBA, both NH_4^+ and more so Na^+, induced larger signal changes (8% and 11%, Figure 2 and Figure S3C). Even in the presence of Li^+, when only half of the TBAs were saturated with thrombin, the quenching effect was larger than in K^+ and NH_4^+ (9%). The comparison of the signal amplitudes from folding and binding suggests that the higher the fraction of aptamers already correctly folded by the ion alone, the smaller the signal change upon thrombin binding. Therefore, the thrombin binding assay was not only detecting the protein itself, but the induction of G-quadruplex folding. This is feasible even without quencher, since the guanine on the 5′ end has quenching properties itself [39]. These results corroborate previous findings that thrombin binding induces G-quadruplex conformation in those conditions that have not induced the correct fold before target association [33]. Another hint at folding induction by thrombin binding can be found in the protein off-rate. Considering that the off-rate of thrombin is the same in all buffers, it is likely that the induced fit creates a similar binding site in all conditions tested. This corresponds to crystal structures of the TBA–thrombin complexes in the presence of K^+ and Na^+, both of which have a very similar TBA structure [21]. This is in contrast to TBA without thrombin, which exhibits alternative conformations in the presence of the abovementioned cations [18].

Taken together, our folding studies provide clear evidence for folding of the G-quadruplex depending on the type and concentration of the cation present. Combined with the thrombin interaction studies, we can conclude that thrombin further forces unfolded TBA into the correct G-quadruplex structure. Therefore, our data confirm the induced fit model of TBA–thrombin binding.

2.3.4 Contribution of results to therapeutic and diagnostic applications

One important application of aptamers is in diagnostic applications. These require detection limits low enough to cover all naturally relevant concentrations. Moreover, minimal sample processing prior to measurements is an advantage. By the example of thrombin, the range of free thrombin varies between low pM and µM concentrations in the blood and indicate the level of thrombosis risk [10,11]. Many aptamer-dependent assays have been developed with pM sensitivity, while others only detect thrombin at a nM concentration with the same probe and target. The detection limit is directly correlated with the interaction affinity. We show a

clear dependency of the TBA–thrombin affinity on the type of cation present. Due to the ionic nature of the interaction it is not surprising that an increase in salt concentration results in a decrease of the binding affinity [14]. Here, we kept the ionic strength of the buffer constant and only changed the type of cation present. This simple buffer adaptation decreased the K_D from 1.3 nM in the presence of NaCl to 154 pM in the presence of KCl. Since many assays have been developed with NaCl-based buffers, they might be further improved by comparable alterations to the buffer composition. Another advantage of the switchSENSE® technology, not shown here with the applied *in vitro* samples, is the possibility to directly inject up to 80% serum samples onto the sensor (according to compatibility sheet [40]). This paves the way for a highly sensitive diagnostic application of the aptasensor. Another highly anticipated application of aptamers is in therapeutic applications. Research mainly investigates the replacement of antibodies by aptamers [6]. Concerning the affinity, we showed here that TBA can easily keep up with high-affinity antibodies such as the human epidermal growth factor receptor 2 (HER2)-binding cancer drug Trastuzumab (K_D = 660 pM) [41]. However, although both exhibit similar affinities in the 3-digit pM range, the antibody has a much longer residence time, indicated by $k_{OFF} = 1.3 \times 10^{-4}\ s^{-1}$. TBA, on the other hand, has an off-rate in the range of $5 \times 10^{-2}\ s^{-1}$. Residence time is a crucial factor during drug development, and this comparison highlights the importance of rate determination to understand the dynamics of a potential drug in vivo. To increase residence times and specificity, antibodies are increasingly designed in bi- or even trispecific formats. If the antibody is bound by two binding sites, its off-rate decreases due to the avidity effects. This development has already been picked up for aptamer design as well [7]. Measuring off-rates of individual binding sites and the joint avidity can be challenging. First, it is difficult to mimic the mixed-target distribution in vitro, and second, the avidity can lead to affinities below the resolution limit of many methods. The switchSENSE® sensor allows to immobilize different targets in a spatial- and ratio-controlled manner, enabled by a dual-color detection system. In the future, this will be applied to the combination of several thrombin-binding aptamers. Although the aptasensor can be easily functionalized with different aptamers, the signal read-out depends on the individual sample. In the TBA example, ion binding can be resolved due to the induction of folding. Thrombin binding creates a significant signal due to the induction of folding and/or the presence of a large protein in the local surrounding of the sensing dye. Nevertheless, the detection of small molecules binding to a binding site distal to the fluorophore can require some assay optimization. If no conformational change is induced upon binding, the aptamer can be destabilized by buffer optimization or increased temperature on the sensor. Competition assays with fluorescent competitor compounds can create strong signal changes. Albeit requiring some knowledge of the binding site, additional fluorophores can be included site-specific at positions close to the binding site or where conformational changes are to be expected. Lastly, it can be advantageous to reverse the assay orientation and immobilize the target on the surface. Capturing the aptamer from solution by a small molecule is expected to create a significant signal.

2.3.5 Effect of reversing the assay orientation

We have shown data of the aptasensor being functionalized with both the aptamer on the surface (Figures 2–4) as well as the target thrombin on the surface (Figure 5). Besides creating different signal intensities by reversing the assay orientation, the setup with the target immobilized can have further applications. While a surface-immobilized aptamer can be easily subjected to all kinds of interaction tests, it is sometimes the aptamer itself that should be altered and screened, e.g., directly after the SELEX process. This can be facilitated by having the aptamer as analyte in solution. It should be noted that the rates measured with the target being immobilized could differ from the rates measured with the aptamer being immobilized. Although we used the exact same buffers and measurement scripts, for the TBA–thrombin interaction the K_D increased from 150 pM to 6 nM just by changing the assay orientation. Considering the broad range of pM to nM affinities reported in literature and measured with different methods [12], the assay setup is likely to have a significant influence on the values measured. However, we can neither exclude that the chemical process of thrombin conjugation to DNA alters the protein and affects the binding affinity. The optimal assay setup should be chosen based on experimental aim and include signal enhancement modifications, e.g., quenchers, if required.

2.4 Materials and Methods

2.4.1 Materials

Human α-thrombin was purchased from Haematologic Technologies Inc. (Essex Junction, VT, USA) and suspended in TE140 buffer (10 mM Tris-HCl pH 7.4, 140 mM NaCl, 0.05% Tween20, 50 µM EDTA, 50 µM EGTA) and stored at −80 °C. The HPLC-purified DNA oligonucleotides were purchased from Ella Biotech GmbH (Martinsried, DE) and used without further purification. All oligonucleotides were suspended to a final concentration of 100 µM in TE40 (10 mM Tris-HCl pH 7.4, 40 mM NaCl, 0.05% Tween 20, 50 µM EDTA, 50 µM EGTA) buffer and stored at −20 °C.

The DNA sequences used are listed below; bold bases represent the aptamer sequence and bases in italics represent the cNL-B sequence (complementary to nanolever NL-B48 immobilized on the chip surface). Underlined bases in TBAsc represent the shuffled portion that prevents folding into a G-quadruplex. For the folding experiment (Section 2.1), TBA and TBAsc sequences were modified with a BlackBerry® Quencher (BBQ-650®) on their 5′ end.

1. TBA: 5′(BBQ)-**GGT TGG TGT GGT TGG** TTT *ATC AGC GTT CGA TGC TTC CGA CTA ATC AGC CAT ATC AGC TTA CGA CTA*-3′;
2. TBAsc: 5′(BBQ)-**GTG TGG TGT GTG TGG** TTT *ATC AGC GTT CGA TGC TTC CGA CTA ATC AGC CAT ATC AGC TTA CGA CTA*-3′;
3. HTA: 5′-**TTT GGG TTA GGG TTA GGG TTA GGG** TTT *ATC AGC GTT CGA TGC TTC CGA CTA ATC AGC CAT ATC AGC TTA CGA CTA*-3′.

2.4.2 Covalent coupling of thrombin to cNL-B

For assays requiring thrombin to be immobilized as ligand on the biochip surface, it was covalently conjugated to the 5′ end of the cNL-B48 oligonucleotide via amine chemistry in MES buffer (50 mM 2-(N-Morpholino)ethanesulfonic acid, 150 mM NaCl, pH 6.5) (amine coupling kit CK-NH2-7-B48, Dynamic Biosensors GmbH, DE). The DNA–protein conjugate was separated from non-conjugated oligonucleotide and protein by a proFIRE chromatography system (Dynamic Biosensors GmbH, DE) and aliquots of the pure conjugate were stored in MES buffer at −80 °C.

2.4.3 switchSENSE® experiments

All experiments were performed on a DRX^2 instrument (Dynamic Biosensors GmbH, DE) on standard multipurpose switchSENSE® chips (MPC2-48-2-G1R1-S) using static measurement mode (Fluorescence Proximity Sensing, FPS). In FPS mode, the DNA strands are repelled from the surface (constant voltage, $V_{attractive} = V_{repulsive} = -0.1$ V). The fluorophore attached to the distal end of the DNA therefore remains at maximum distance from the gold electrode. For signal detection of biomolecular interactions, the fluorescence intensity of the dye is read out. It changes its fluorescence emission upon altered static or collisional quenching by complex formation of ligand and analyte. The fluorescence signal change is proportional to the surface bound analytes. The immobilized dye was excited in the range of 600–630 nm and emission in the range of 650–685 nm was recorded. The experimental workflow was set-up using the proprietary switchBUILD software. The aptamers were diluted to a concentration of 1 µM in the relevant running buffer, heated at 82 °C for 1 min, and then cooled to 22 °C prior to use. Surface functionalization was achieved by hybridizing 500 nM of cNL-B oligonucleotide (extended by or covalently linked to the respective ligand) to the single-stranded pre-immobilized NL-B48 oligo on the chip surface in auxiliary buffer TE40. Association of analyte of interest (ions, thrombin, aptamers) and dissociation in running buffer were performed with a flow rate of 2000 µL/min at 25 °C, except where noted otherwise. Surface regenerations were only performed at the beginning of a measurement set, no regenerations were carried out in between different concentrations of one set. The folding measurements were carried out in a background of Tris50 buffer (50 mM Tris-HCl pH 7.4, 0.005% Tween 20), and the kinetic measurements in TE140-XCl buffer (10 mM Tris-HCl pH 7.4, 140 mM XCl, 0.05% Tween 20, 50 µM EDTA, 50 µM EGTA, with XCl representing different salt species: KCl, NaCl, NH_4Cl, LiCl).

2.4.4 Data analysis

Fluorescence recorded was referenced with the control TBAsc in Figure 2 (raw data are shown in Figure S4 – S6); all other figures show raw data normalized to the baseline before analyte

injection. The fluorescence traces were analyzed with the switchANALYSIS software (Dynamic Biosensors GmbH, DE) by fitting all association and dissociation curves of one dataset simultaneously (global fit) with a single-exponential fit model. Measurements for Figure 2 and Figure 3 were performed in triplicates, and values reported represent the mean k_{ON} and k_{OFF} of three datasets, leading to an average K_D by:

$$K_D = \frac{k_{OFF,avg}}{k_{ON,avg}}$$

± standard deviation with error propagation:

$$SD = K_D \cdot \left(\left(\frac{\delta k_{OFF}}{k_{OFF}} \right)^2 + \left(\frac{\delta k_{ON}}{k_{ON}} \right)^2 \right)^{\frac{1}{2}}$$

Measurements for Figure 5B were performed in triplicates and recorded data were averaged before applying the global single-exponential fit to derive k_{ON} and k_{OFF}. The folding rate at highest salt concentration applied was deduced from the time constant τ of mono-exponential fits by:

$$K_F = \frac{1}{\tau_{on}}$$

Surface saturation levels were calculated based on the measured rates in the Kinetics tool of the switchBUILD software (Dynamic Biosensors GmbH, DE).

Rate plot in Figure 2 and Supplementary Materials Figure S1 were plotted via www.affinity-avidity.com and the labeling was adjusted to the color code.

2.5 Conclusions

In this work, we presented a rapid, sensitive, and selective aptamer-ion/protein assay based on an aptasensor. The significance of this work lies in the easy transfer of the assay from TBA–thrombin interaction to any aptamer-–target pair. The DNA-based switchSENSE® technology allows quasi modification-free immobilization of low amounts of aptamer on the biosensor via hybridization. High-information content data of folding, unfolding, association, and dissociation rates enabled conclusions about ion-induced aptamer folding and a protein-induced fit mechanism. The type-of-cation-dependent k_{ON} rates are direct evidence as to why detection limits and affinities achieved for TBA–thrombin strongly vary in literature. A broad dynamic range from low pM to high nM suggests a future diagnostic application of the developed aptasensor. Furthermore, the resolution of highly dynamic target association and dissociation rates helps to understand residence times in therapeutic applications. In conclusion, the described aptasensor can contribute significantly to the areas of aptamer development and characterization, aptamer-based diagnostics, as well as apta-therapeutics.

2.6 Supplementary material

Figure S1. Thrombin kinetics in TE140-KCl at different flow rates.

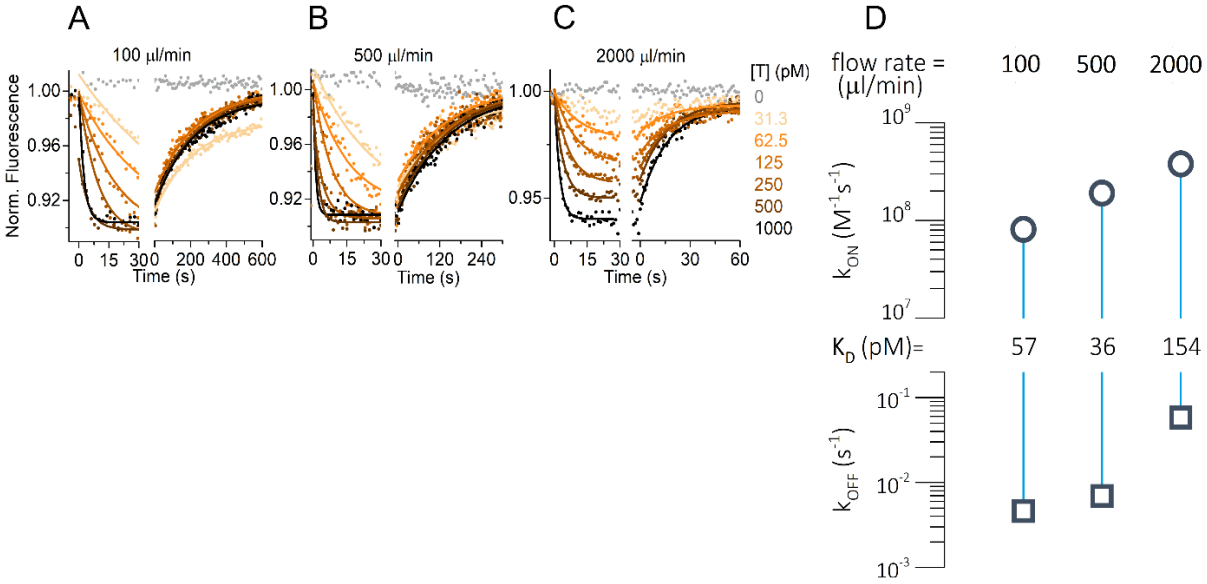

Figure S1. *Thrombin kinetics in TE140-KCl at different flow rates. Interaction of thrombin at specified concentrations with surface-immobilized TBA carried out at A) 100 µl/min, B) 500 µl/min, C) 2000 µl/min. D) Rate plot of values obtained by global mono-exponential fits from A)-C). Lower flow rates result in reduced on-rate and reduced off-rate. Increase of the flow rate reduces measurement artifacts such as mass transport limitation or rebinding.*

Figure S2. Thrombin association at low ionic strength (50 mM Tris with no salts added).

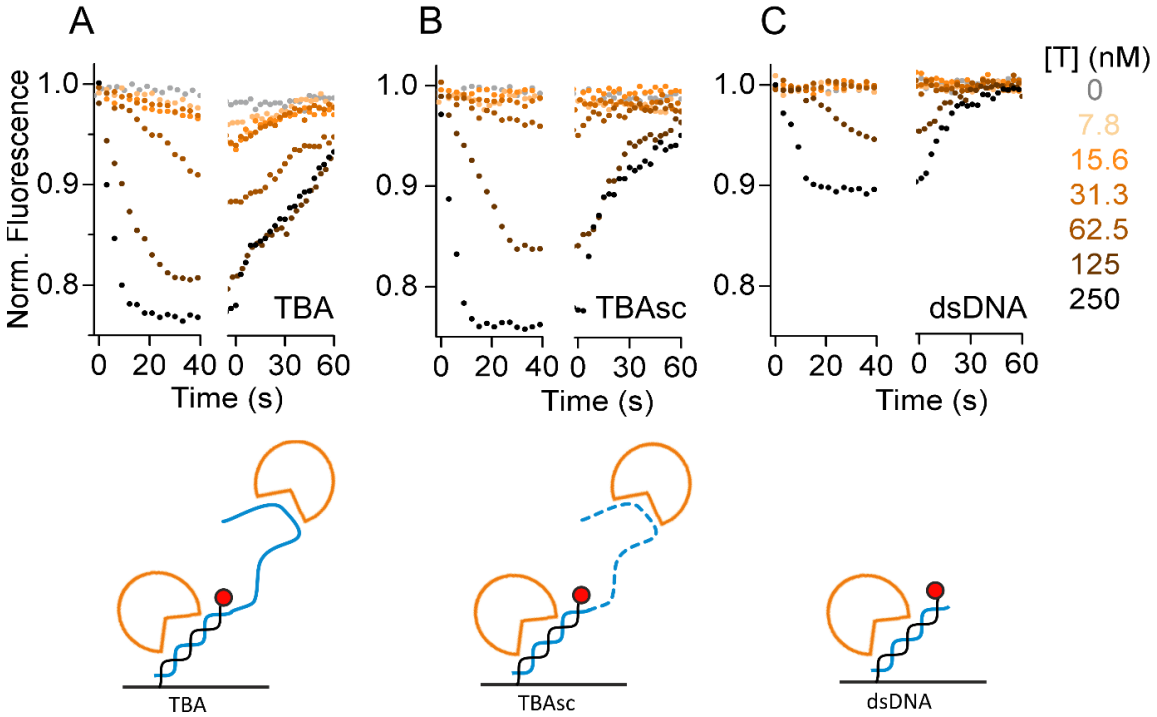

Figure S2. Thrombin association at low ionic strength (50 mM Tris with no salts added). A) Thrombin binding to both TBA and B) TBAsc is observed at ≥ 62.5 nM thrombin. C) Non-specific thrombin binding to dsDNA is observed at ≥ 125 nM thrombin.

Figure S3. Comparison of quenching amplitudes with surface saturation.

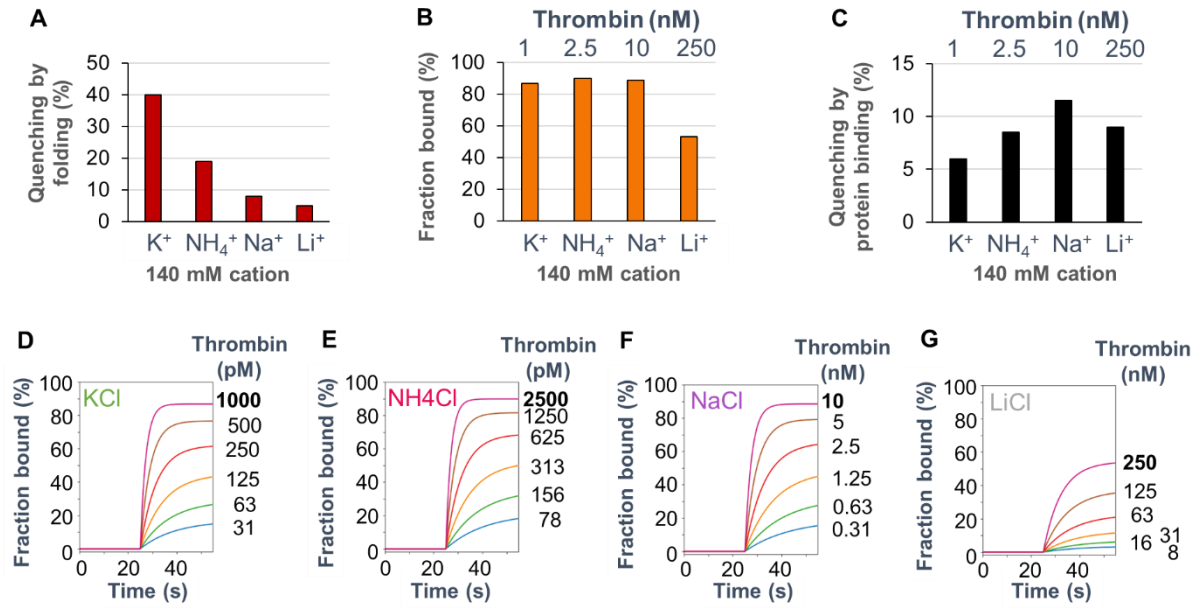

Figure S3. Comparison of quenching amplitudes with surface saturation. A) Fluorescence quenching (%) induced by 140 mM cation derived from Figure 2. K^+ reached signal saturation at 75 mM, therefore the same quenching was assumed for 140 mM. B) Plot of the calculated fraction of TBA bound by thrombin (%) at the highest protein concentration tested in the respective buffers. Fractions bound were derived from the plots in D-G). C) Fluorescence quenching (%) induced by thrombin binding. Values were extracted from Figure 3. Total quenching is lower than in A) since quenching was achieved by guanine instead of BBQ. D-G) The cation-dependent fractions bound (%) of

TBA at different thrombin concentrations, plotted by the switchBUILD software based on the kinetic rates determined in Figure 3.

Figure S4. Raw data of TBA (triplicates) and TBAsc folding experiments with: K^+ (green traces), NH_4^+ (pink traces), Na^+ (purple traces), Li^+ (grey traces).

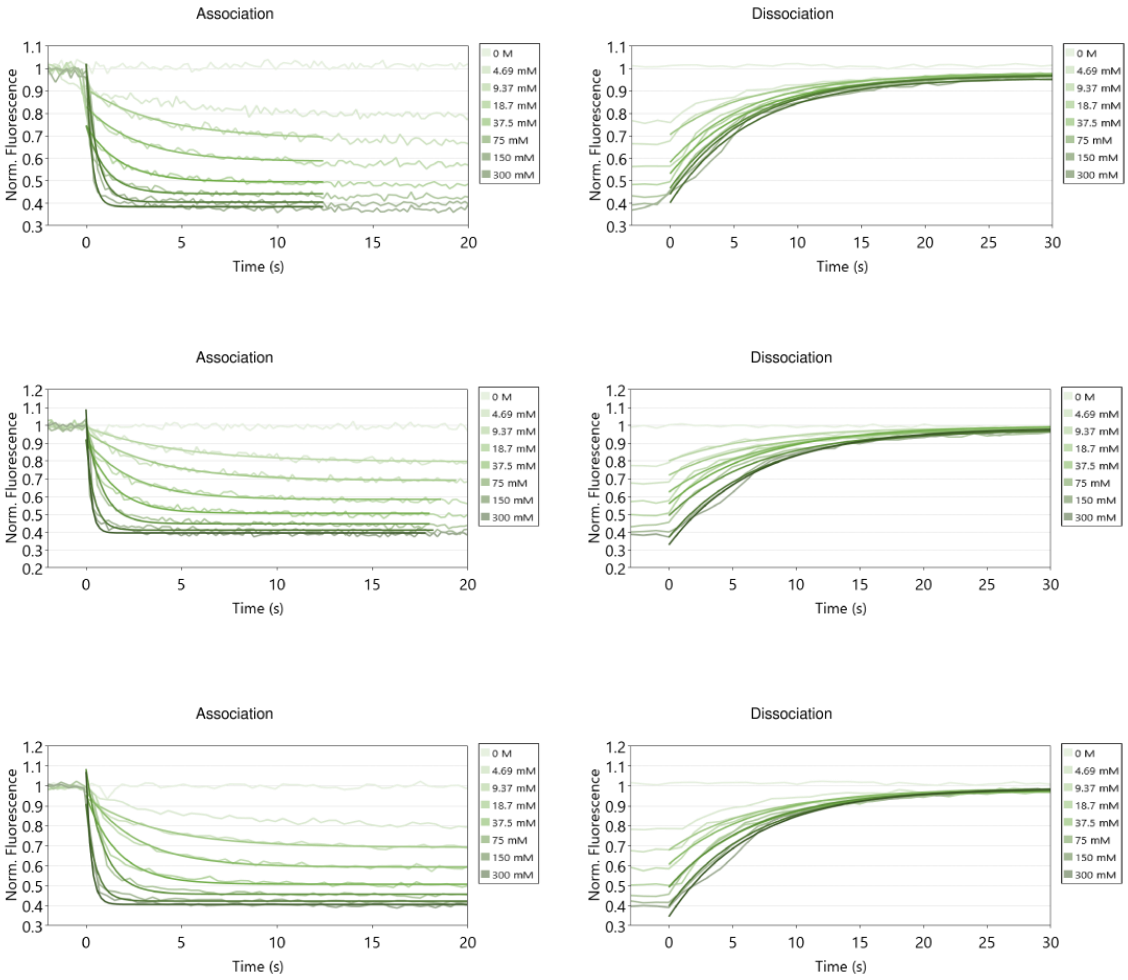

Table S1. Kinetic binding rates of TBA folding experiments in K^+.

k_{ON} ($M^{-1}s^{-1}$)	k_{OFF} (s^{-1})	K_D (M)
11.0 ± 0.3	1.59 ± 0.03 E-1	14.3 ± 0.5 E-3
14.6 ± 0.4	1.43 ± 0.02 E-1	9.83 ± 0.29 E-3
12.2 ± 0.3	1.50 ± 0.02 E-1	12.3 ± 0.3 E-3

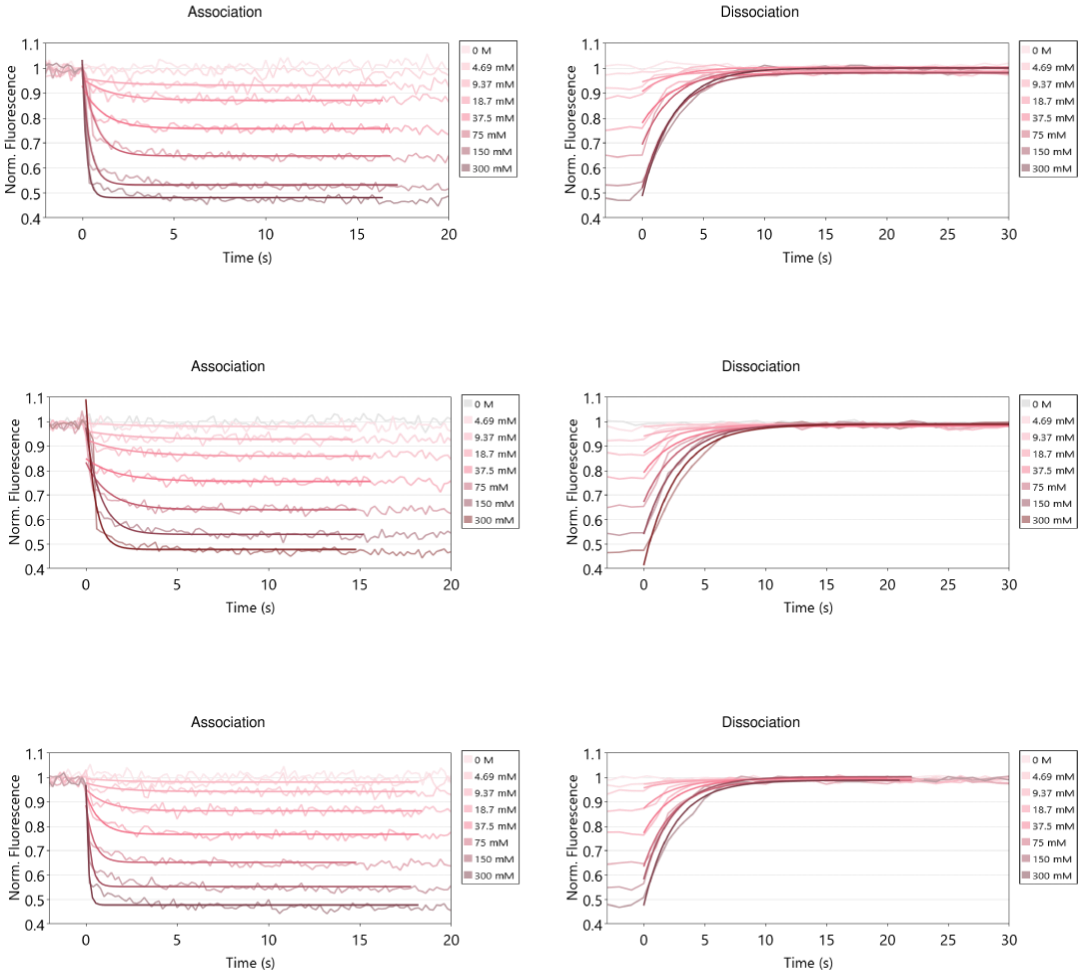

Table S2. Kinetic binding rates of TBA folding experiments in NH_4^+

k_{ON} ($M^{-1}s^{-1}$)	k_{OFF} (s^{-1})	K_D (M)
13.2 ± 0.6	3.94 ± 0.08 E-1	29.9 ± 1.5 E-3
5.93 ± 0.3	3.66 ± 0.08 E-1	61.8 ± 3.5 E-3
24.0 ± 1.4	4.10 ± 0.11 E-1	17.1 ± 1.1 E-3

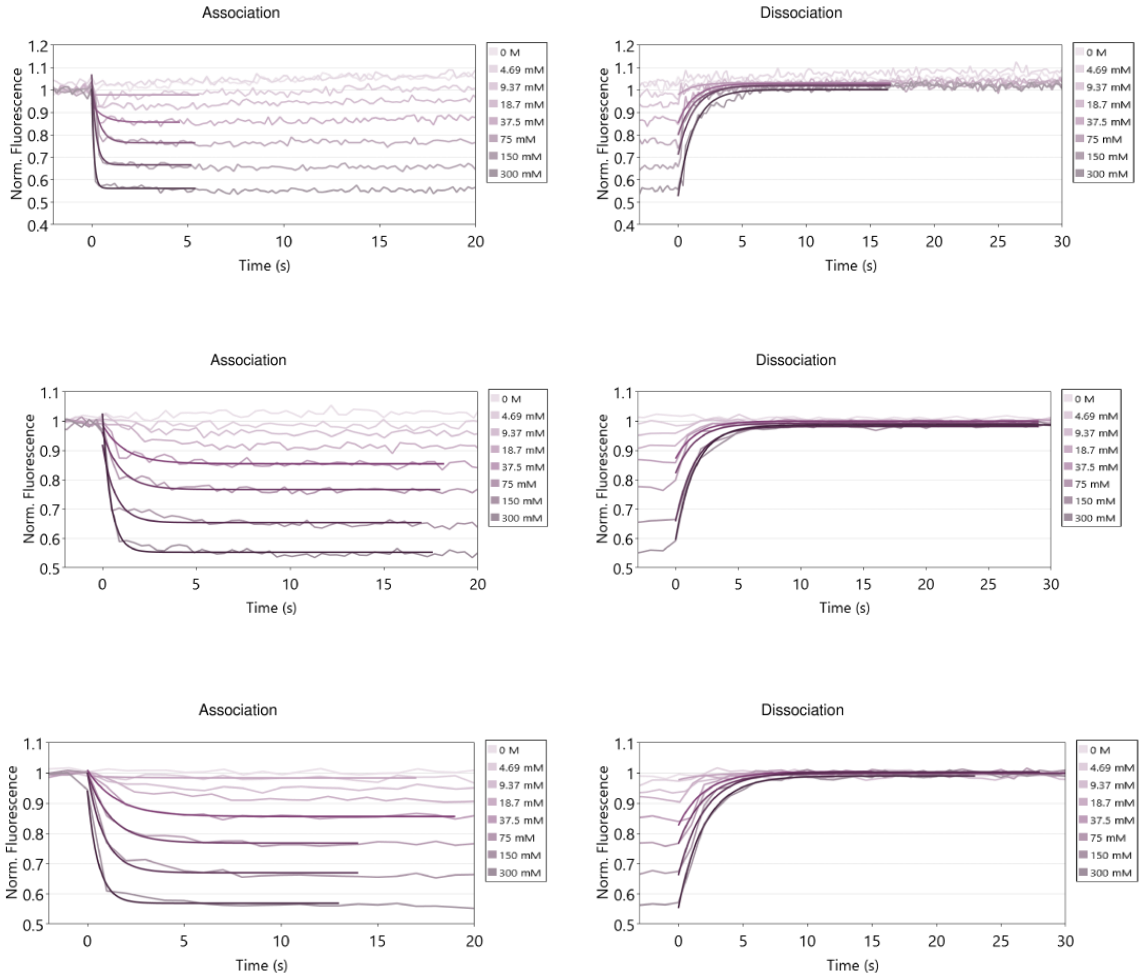

Table S3. Kinetic binding rates of TBA folding experiments in Na^+

k_{ON} ($M^{-1}s^{-1}$)	k_{OFF} (s^{-1})	K_D (M)
24.4 ± 2.25	8.15 ± 0.24 E-1	33.5 ± 3.2 E-3
5.44 ± 0.43	6.33 ± 0.19 E-1	116 ± 10 E-3
4.33 ± 0.37	4.93 ± 0.16 E-1	114 ± 10 E-3

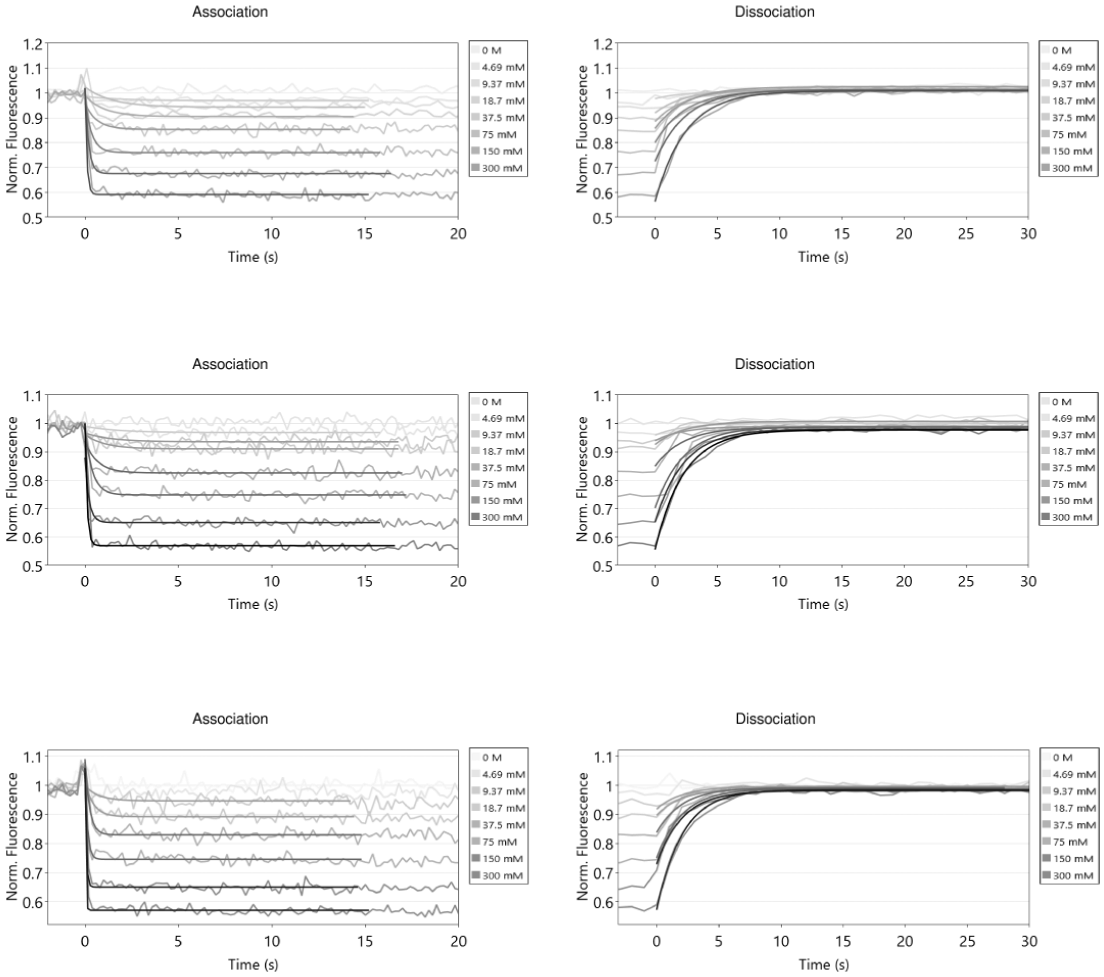

Table S4. Kinetic binding rates of TBA folding experiments in Li^+

k_{ON} ($M^{-1}s^{-1}$)	k_{OFF} (s^{-1})	K_D (M)
31.9 ± 2.59	4.07 ± 0.11 E-1	12.8 ± 1.1 E-3
27.9 ± 2.19	4.38 ± 0.11 E-1	15.6 ± 1.3 E-3
94.2 ± 7.36	4.86 ± 0.14 E-1	5.16 ± 0.43 E-3

TBAsc folding

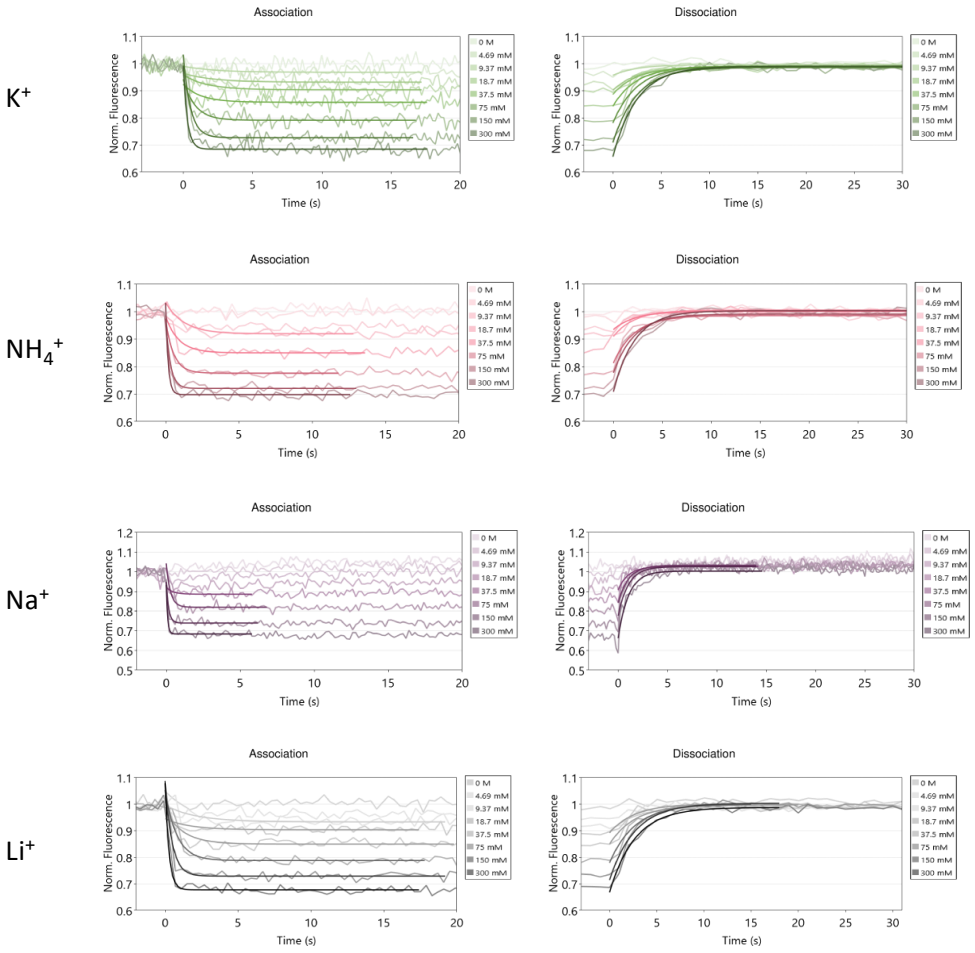

Table S5. Kinetic binding rates of TBAsc folding experiments.

Salt	k_{ON} ($M^{-1}s^{-1}$)	k_{OFF} (s^{-1})	K_D (M)
K^+	10.15 ± 0.81	4.04 ± 0.12 E-1	39.8 ± 3.4 E-3
NH_4^+	17.89 ± 1.64	4.64 ± 0.19 E-1	25.9 ± 2.6 E-3
Na^+	33.52 ± 4.8	9.53 ± 0.52 E-1	28.4 ± 4.3 E-3
Li^+	11.68 ± 0.94	3.74 ± 0.17 E-1	32.0 ± 3.0 E-3

Figure S5. Triplicates of thrombin kinetics experiments in K^+ (green traces), Na^+ (purple traces), NH_4^+ (pink traces), and Li^+ (grey traces).

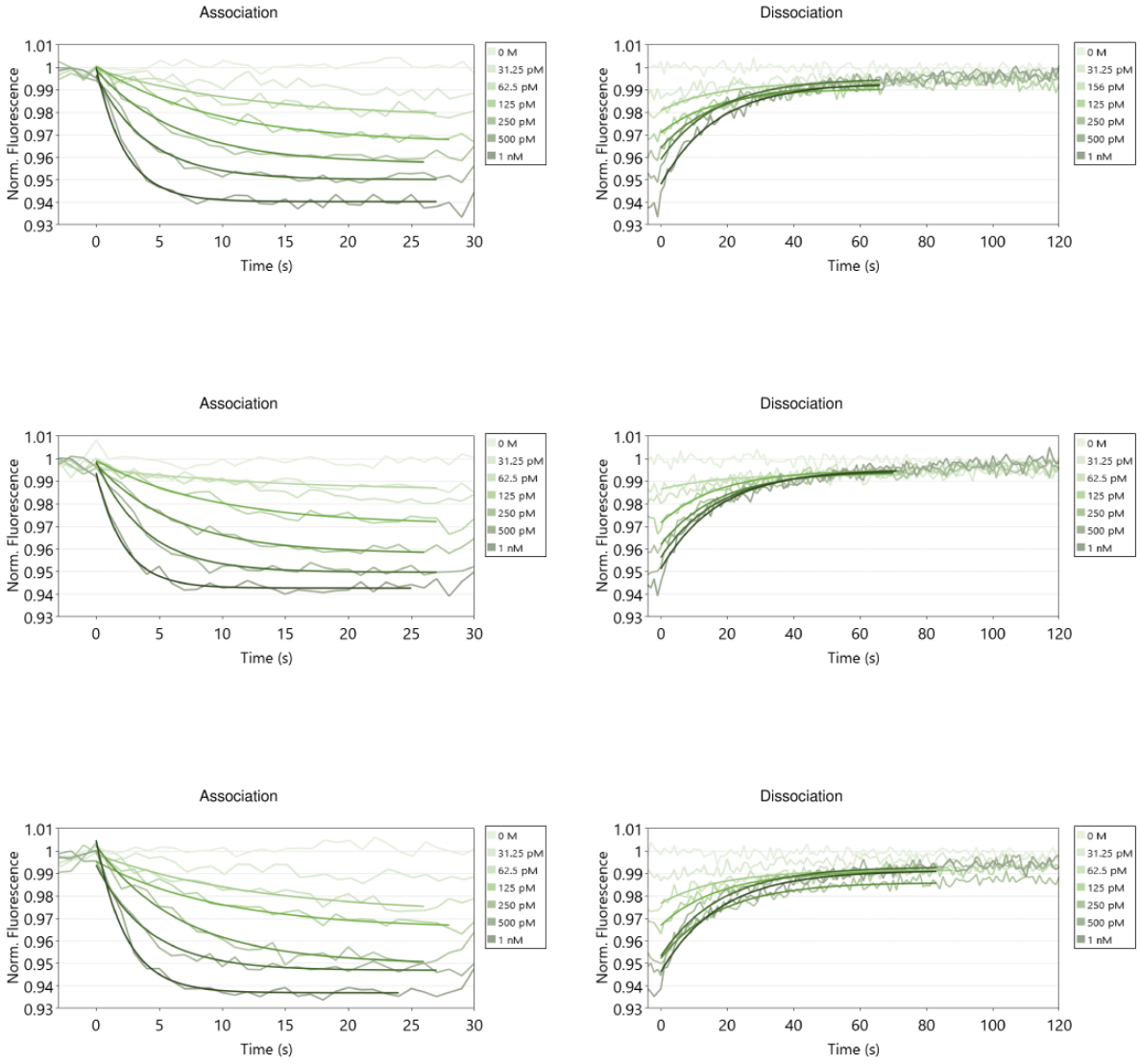

Table S6. Kinetic binding rates of TBA-thrombin binding experiments in TE140-KCl.

k_{ON} ($M^{-1}s^{-1}$)	k_{OFF} (s^{-1})	K_D (M)
3.72 ± 0.20 E+8	5.99 ± 0.19 E-2	161 ± 10 E-12
3.97 ± 0.20 E+8	5.82 ± 0.18 E-2	147 ± 9 E-12
3.66 ± 0.18 E+8	5.66 ± 0.17 E-2	155 ± 9 E-12

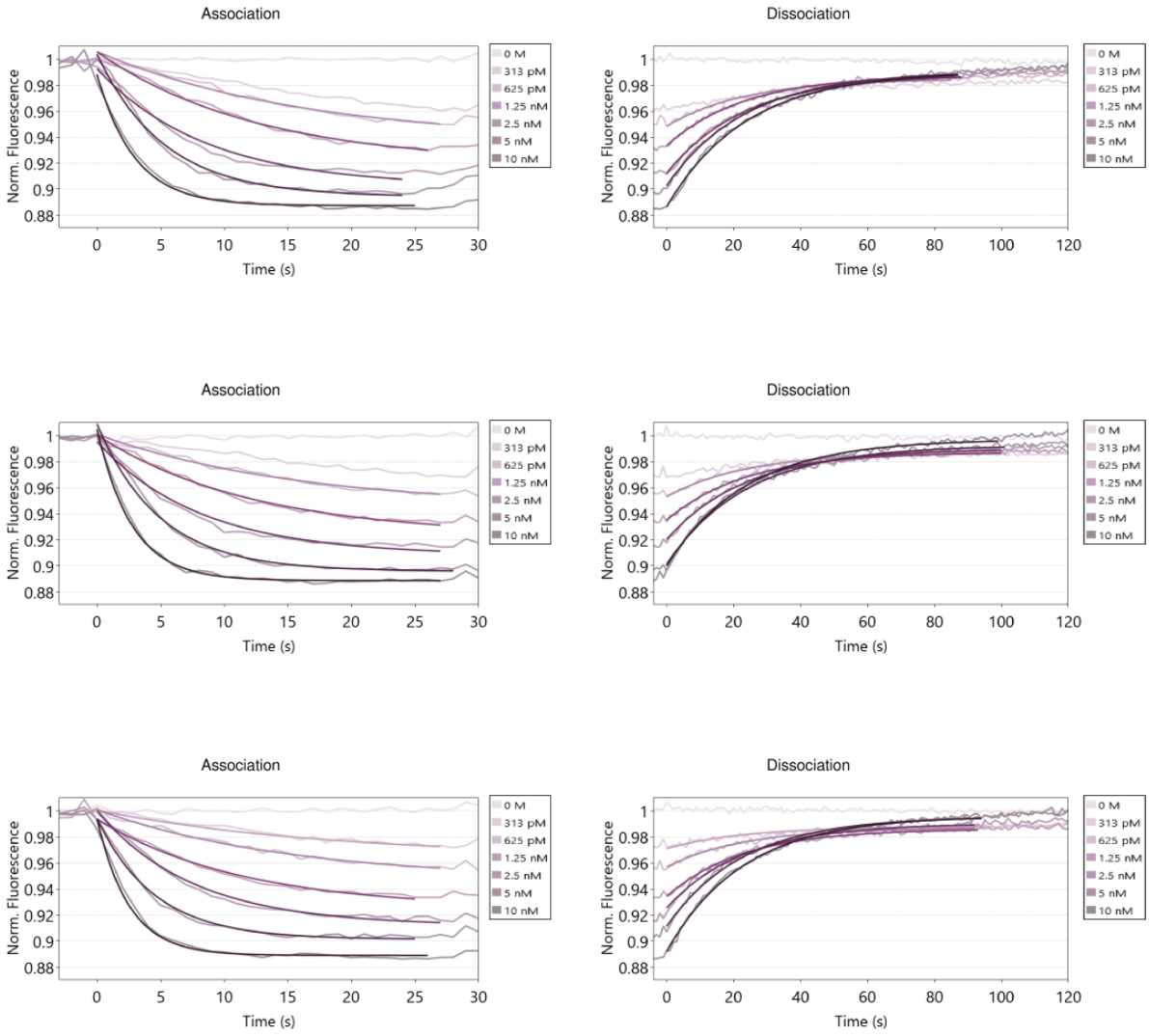

Table S7. Kinetic binding rates of TBA-thrombin binding experiments in TE140-NaCl

k_{ON} ($M^{-1}s^{-1}$)	k_{OFF} (s^{-1})	K_D (M)
2.95 ± 0.11 E+7	4.25 ± 0.04 E-2	1.44 ± 0.05 E-9
3.24 ± 0.09 E+7	4.21 ± 0.04 E-2	1.30 ± 0.01 E-9
3.55 ± 0.10 E+7	4.39 ± 0.04 E-2	1.24 ± 0.03 E-9

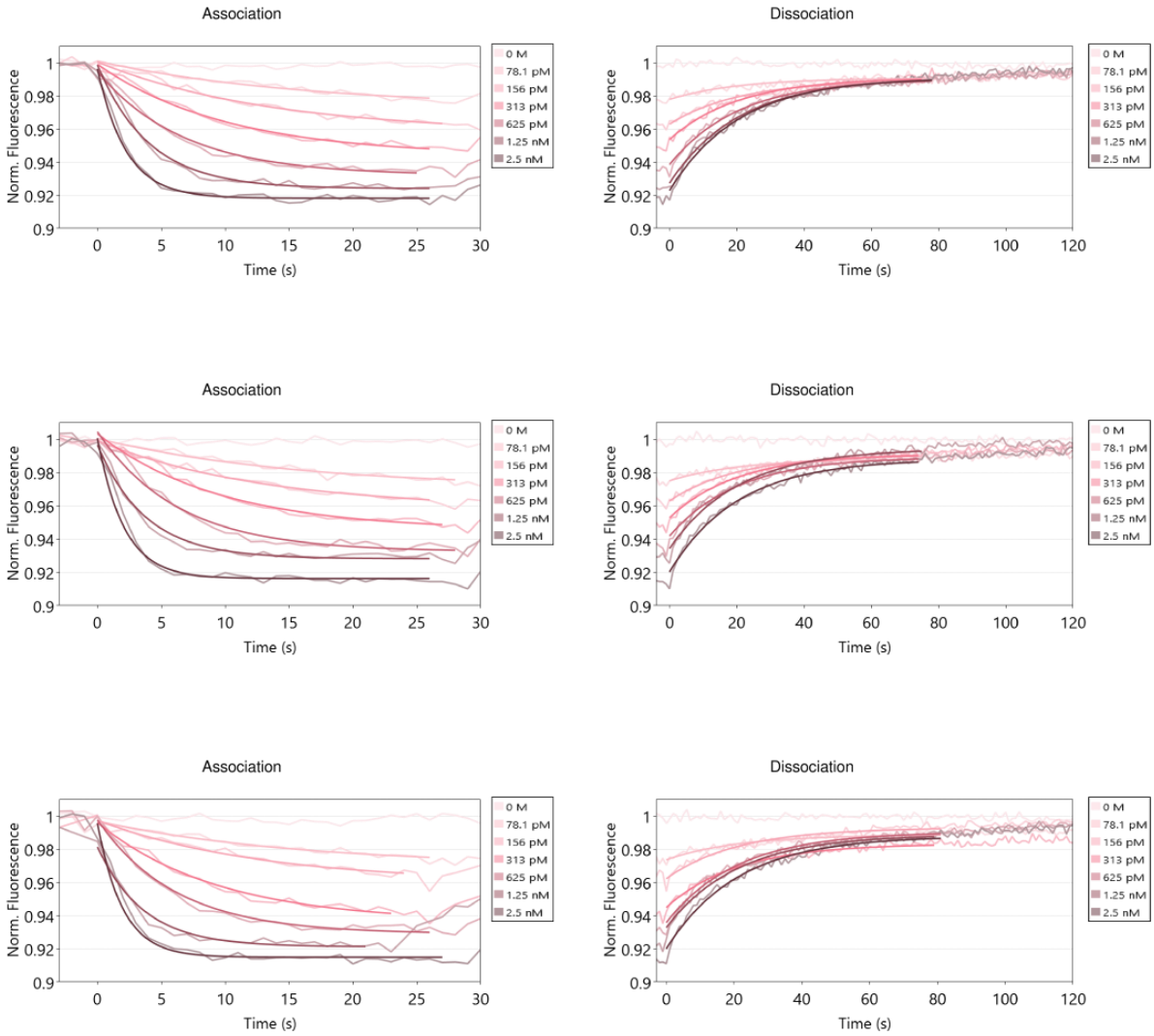

Table S8. Kinetic binding rates of TBA-thrombin binding experiments in TE140-NH_4Cl

k_{ON} ($M^{-1}s^{-1}$)	k_{OFF} (s^{-1})	K_D (M)
1.60 ± 0.06 E+8	4.88 ± 0.09 E-2	306 ± 12 E-12
1.74 ± 0.07 E+8	4.94 ± 0.10 E-2	284 ± 13 E-12
1.84 ± 0.08 E+8	4.79 ± 0.09 E-2	260 ± 12 E-12

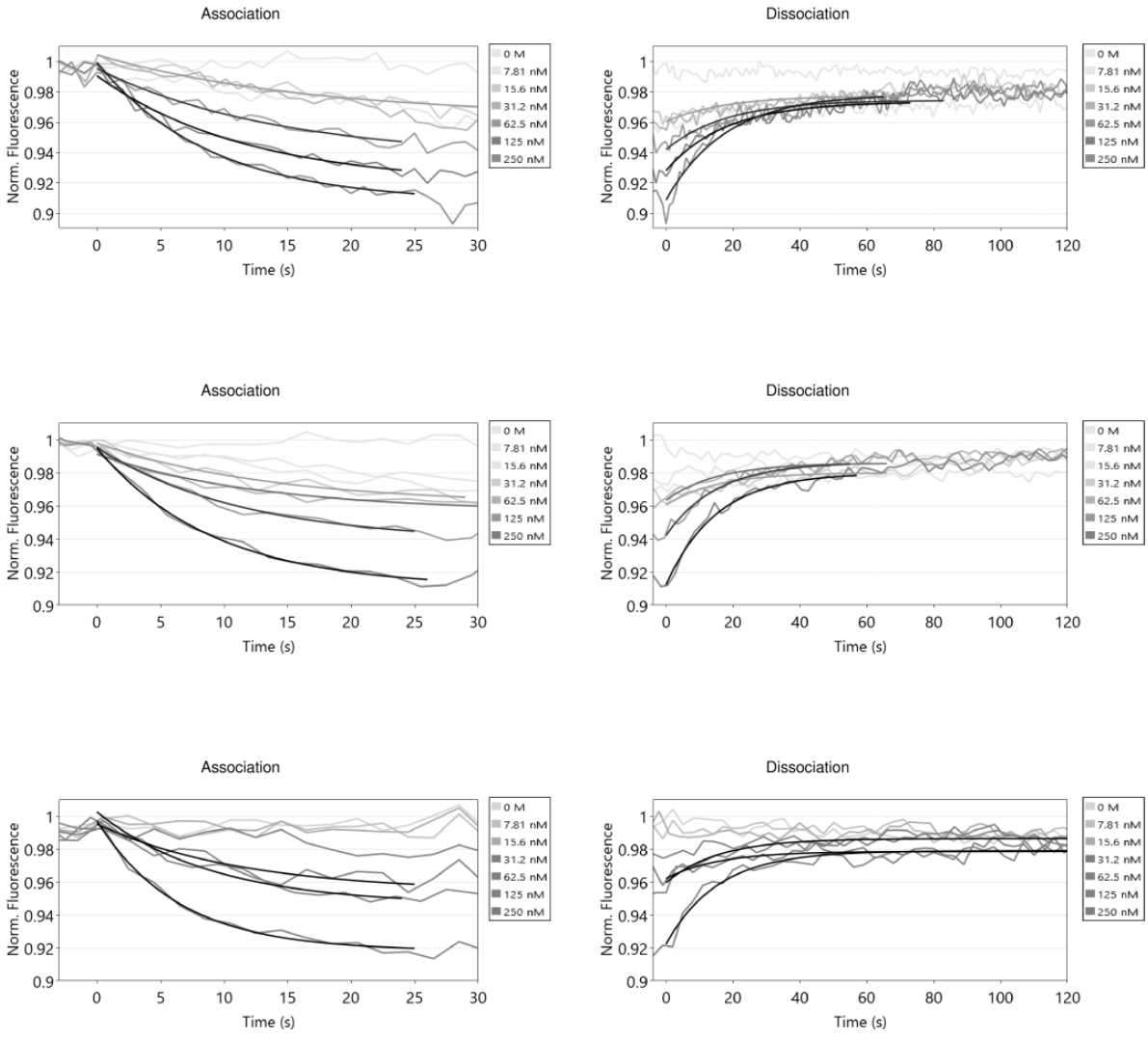

Table S9. Kinetic binding rates of TBA-thrombin binding experiments in TE140-LiCl

k_{ON} ($M^{-1}s^{-1}$)	k_{OFF} (s^{-1})	K_D (M)
2.28 ± 0.34 E+5	5.64 ± 0.30 E-2	248 ± 39 E-9
1.74 ± 0.36 E+5	6.66 ± 0.37 E-2	381 ± 83 E-9
3.64 ± 0.74 E+5	6.49 ± 0.41 E-2	179 ± 38 E-9

Figure S6. Triplicates of reversed assay orientation kinetics experiment in K^+.

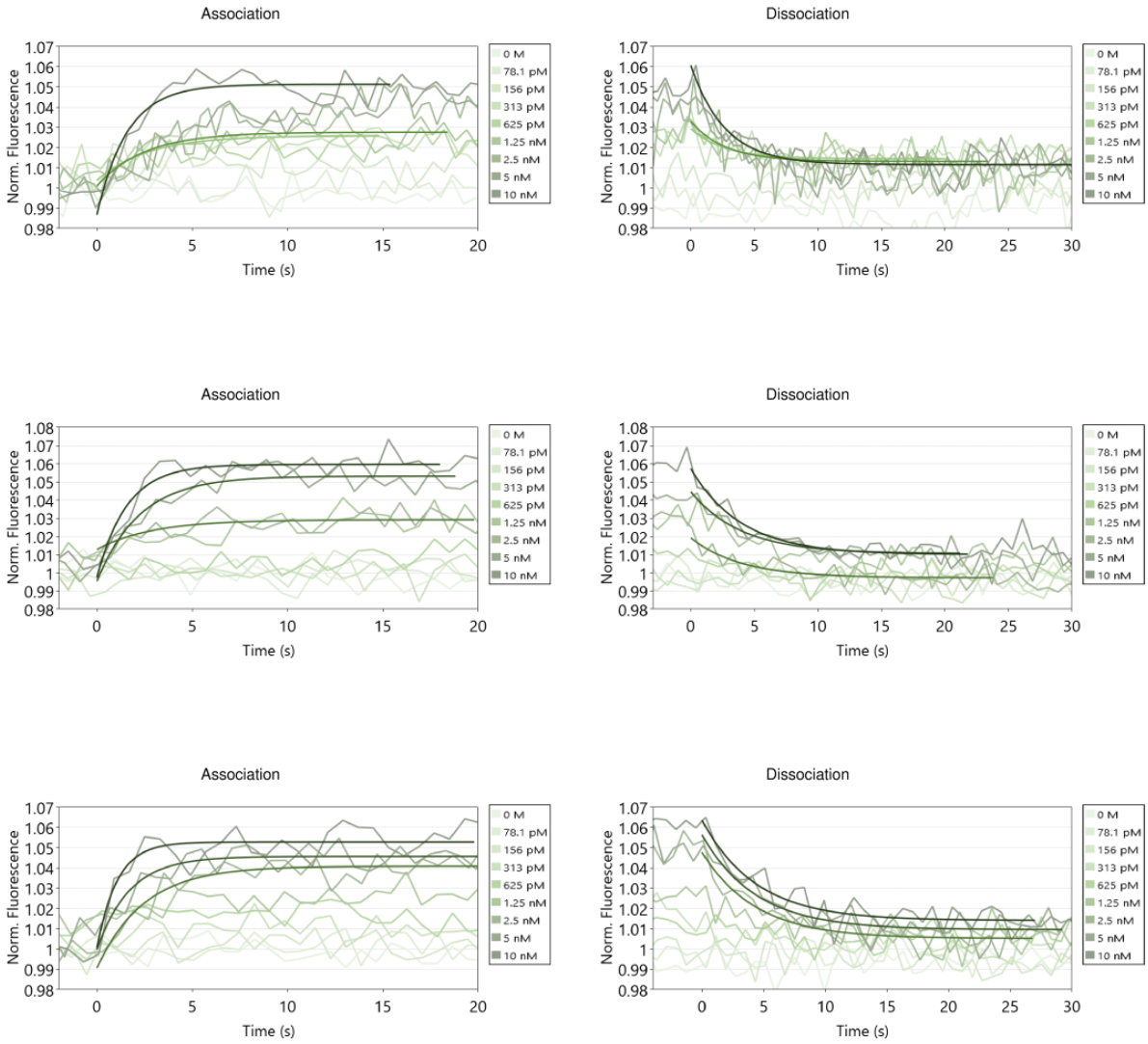

Table S10. Kinetic binding rates of thrombin-TBA binding experiments in TE140-KCl

k_{ON} ($M^{-1}s^{-1}$)	k_{OFF} (s^{-1})	K_D (M)
2.61 ± 1.00 E+7	3.71 ± 0.55 E-1	14.2 ± 5.8 E-9
3.91 ± 0.86 E+7	2.51 ± 0.34 E-1	6.42 ± 1.65 E-9
7.18 ± 1.54 E+7	2.30 ± 0.23 E-1	3.2 ± 0.8 E-9

References

1. Tuerk, C.; Gold, L. Systematic Evolution of Ligands by Exponential Enrichment: RNA Ligands to Bacteriophage T4 DNA Polymerase. *Science* 1990, *249*, 505–510, doi:10.1126/science.2200121.
2. Ellington, A.D.; Szostak, J.W. In Vitro Selection of RNA Molecules That Bind Specific Ligands. *Nature* 1990, *346*, 818–822, doi:10.1038/346818a0.
3. Banerjee, J.; Nilsen-Hamilton, M. Aptamers: Multifunctional Molecules for Biomedical Research. *J Mol Med* 2013, *91*, 1333–1342, doi:10.1007/s00109-013-1085-2.
4. Jayasena, S.D. Aptamers: An Emerging Class of Molecules That Rival Antibodies in Diagnostics. *Clinical Chemistry* 1999, *45*, 1628–1650, doi:10.1093/clinchem/45.9.1628.
5. Keefe, A.D.; Pai, S.; Ellington, A. Aptamers as Therapeutics. *Nature Reviews Drug Discovery* 2010, *9*, 537–550, doi:10.1038/nrd3141.
6. Zhou, J.; Rossi, J. Aptamers as Targeted Therapeutics: Current Potential and Challenges. *Nature Reviews Drug Discovery* 2017, *16*, 181–202, doi:10.1038/nrd.2016.199.
7. Vorobyeva, M.; Vorobjev, P.; Venyaminova, A. Multivalent Aptamers: Versatile Tools for Diagnostic and Therapeutic Applications. *Molecules* 2016, *21*, 1613, doi:10.3390/molecules21121613.
8. Drolet, D.W.; Green, L.S.; Gold, L.; Janjic, N. Fit for the Eye: Aptamers in Ocular Disorders. *Nucleic Acid Ther* 2016, *26*, 127–146, doi:10.1089/nat.2015.0573.
9. Bock, L.C.; Griffin, L.C.; Latham, J.A.; Vermaas, E.H.; Toole, J.J. Selection of Single-Stranded DNA Molecules That Bind and Inhibit Human Thrombin. *Nature* 1992, *355*, 564–566, doi:10.1038/355564a0.
10. Shuman, M.A.; Majerus, P.W. The Measurement of Thrombin in Clotting Blood by Radioimmunoassay. *J Clin Invest* 1976, *58*, 1249–1258, doi:10.1172/JCI108579.
11. Brummel-Ziedins, K.E.; Vossen, C.Y.; Butenas, S.; Mann, K.G.; Rosendaal, F.R. Thrombin Generation Profiles in Deep Venous Thrombosis. *J Thromb Haemost* 2005, *3*, 2497–2505, doi:10.1111/j.1538-7836.2005.01584.x.
12. Deng, B.; Lin, Y.; Wang, C.; Li, F.; Wang, Z.; Zhang, H.; Li, X.-F.; Le, X.C. Aptamer Binding Assays for Proteins: The Thrombin Example--a Review. *Anal Chim Acta* 2014, *837*, 1–15, doi:10.1016/j.aca.2014.04.055.
13. Miyachi, Y.; Shimizu, N.; Ogino, C.; Kondo, A. Selection of DNA Aptamers Using Atomic Force Microscopy. *Nucleic Acids Res* 2010, *38*, e21, doi:10.1093/nar/gkp1101.
14. Lin, P.-H.; Chen, R.-H.; Lee, C.-H.; Chang, Y.; Chen, C.-S.; Chen, W.-Y. Studies of the Binding Mechanism between Aptamers and Thrombin by Circular Dichroism, Surface Plasmon Resonance and Isothermal Titration Calorimetry. *Colloids Surf B Biointerfaces* 2011, *88*, 552–558, doi:10.1016/j.colsurfb.2011.07.032.
15. Shim, J.W.; Tan, Q.; Gu, L.-Q. Single-Molecule Detection of Folding and Unfolding of the G-Quadruplex Aptamer in a Nanopore Nanocavity. *Nucleic Acids Res* 2009, *37*, 972–982, doi:10.1093/nar/gkn968.
16. Platella, C.; Riccardi, C.; Montesarchio, D.; Roviello, G.N.; Musumeci, D. G-Quadruplex-Based Aptamers against Protein Targets in Therapy and Diagnostics. *Biochim Biophys Acta Gen Subj* 2017, *1861*, 1429–1447, doi:10.1016/j.bbagen.2016.11.027.
17. Henderson, E.; Hardin, C.C.; Walk, S.K.; Tinoco, I.; Blackburn, E.H. Telomeric DNA Oligonucleotides Form Novel Intramolecular Structures Containing Guanine-Guanine Base Pairs. *Cell* 1987, *51*, 899–908, doi:10.1016/0092-8674(87)90577-0.
18. Trajkovski, M.; Šket, P.; Plavec, J. Cation Localization and Movement within DNA Thrombin Binding Aptamer in Solution. *Org. Biomol. Chem.* 2009, *7*, 4677–4684, doi:10.1039/B914783G.
19. Bhattacharyya, D.; Mirihana Arachchilage, G.; Basu, S. Metal Cations in G-Quadruplex Folding and Stability. *Front Chem* 2016, *4*, 38, doi:10.3389/fchem.2016.00038.

20. Avino, A.; Fabrega, C.; Tintore, M.; Eritja, R. Thrombin Binding Aptamer, More than a Simple Aptamer: Chemically Modified Derivatives and Biomedical Applications. *Curr Pharm Des* 2012, *18*, 2036–2047, doi:10.2174/138161212799958387.
21. Russo Krauss, I.; Merlino, A.; Randazzo, A.; Novellino, E.; Mazzarella, L.; Sica, F. High-Resolution Structures of Two Complexes between Thrombin and Thrombin-Binding Aptamer Shed Light on the Role of Cations in the Aptamer Inhibitory Activity. *Nucleic Acids Res* 2012, *40*, 8119–8128, doi:10.1093/nar/gks512.
22. Baldrich, E.; O'Sullivan, C.K. Ability of Thrombin to Act as Molecular Chaperone, Inducing Formation of Quadruplex Structure of Thrombin-Binding Aptamer. *Anal Biochem* 2005, *341*, 194–197, doi:10.1016/j.ab.2005.02.031.
23. Chang, A.L.; McKeague, M.; Liang, J.C.; Smolke, C.D. Kinetic and Equilibrium Binding Characterization of Aptamers to Small Molecules Using a Label-Free, Sensitive, and Scalable Platform. *Anal Chem* 2014, *86*, 3273–3278, doi:10.1021/ac5001527.
24. Rant, U.; Arinaga, K.; Fujita, S.; Yokoyama, N.; Abstreiter, G.; Tornow, M. Dynamic Electrical Switching of DNA Layers on a Metal Surface. *Nano Lett.* 2004, *4*, 2441–2445, doi:10.1021/nl0484494.
25. Knezevic, J.; Langer, A.; Hampel, P.A.; Kaiser, W.; Strasser, R.; Rant, U. Quantitation of Affinity, Avidity, and Binding Kinetics of Protein Analytes with a Dynamically Switchable Biosurface. *J Am Chem Soc* 2012, *134*, 15225–15228, doi:10.1021/ja3061276.
26. Cléry, A.; Sohier, T.J.M.; Welte, T.; Langer, A.; Allain, F.H.T. SwitchSENSE: A New Technology to Study Protein-RNA Interactions. *Methods* 2017, *118–119*, 137–145, doi:10.1016/j.ymeth.2017.03.004.
27. Kankia, B.I.; Marky, L.A. Folding of the Thrombin Aptamer into a G-Quadruplex with Sr(2+): Stability, Heat, and Hydration. *J Am Chem Soc* 2001, *123*, 10799–10804, doi:10.1021/ja010008o.
28. Kumar, N.; Maiti, S. Quadruplex to Watson–Crick Duplex Transition of the Thrombin Binding Aptamer: A Fluorescence Resonance Energy Transfer Study. *Biochemical and Biophysical Research Communications* 2004, *319*, 759–767, doi:10.1016/j.bbrc.2004.05.052.
29. Joachimi, A.; Benz, A.; Hartig, J.S. A Comparison of DNA and RNA Quadruplex Structures and Stabilities. *Bioorg Med Chem* 2009, *17*, 6811–6815, doi:10.1016/j.bmc.2009.08.043.
30. Parkinson, G.N.; Lee, M.P.H.; Neidle, S. Crystal Structure of Parallel Quadruplexes from Human Telomeric DNA. *Nature* 2002, *417*, 876–880, doi:10.1038/nature755.
31. Hardin, C.C.; Watson, T.; Corregan, M.; Bailey, C. Cation-Dependent Transition between the Quadruplex and Watson-Crick Hairpin Forms of d(CGCG3GCG). *Biochemistry* 1992, *31*, 833–841, doi:10.1021/bi00118a028.
32. Mergny, J.-L.; Phan, A.-T.; Lacroix, L. Following G-Quartet Formation by UV-Spectroscopy. *FEBS Letters* 1998, *435*, 74–78, doi:10.1016/S0014-5793(98)01043-6.
33. Cho, M.; Kim, Y.; Han, S.-Y.; Min, K.; Rahman, M.A.; Shim, Y.-B.; Ban, C. Detection for Folding of the Thrombin Binding Aptamer Using Label-Free Electrochemical Methods. *BMB Rep* 2008, *41*, 126–131, doi:10.5483/bmbrep.2008.41.2.126.
34. Hong, E.S.; Yoon, H.-J.; Kim, B.; Yim, Y.-H.; So, H.-Y.; Shin, S.K. Mass Spectrometric Studies of Alkali Metal Ion Binding on Thrombin-Binding Aptamer DNA. *J Am Soc Mass Spectrom* 2010, *21*, 1245–1255, doi:10.1016/j.jasms.2010.03.035.
35. Müller, J.; Freitag, D.; Mayer, G.; Pötzsch, B. Anticoagulant Characteristics of HD1-22, a Bivalent Aptamer That Specifically Inhibits Thrombin and Prothrombinase. *J Thromb Haemost* 2008, *6*, 2105–2112, doi:10.1111/j.1538-7836.2008.03162.x.
36. Ho, H.-A.; Leclerc, M. Optical Sensors Based on Hybrid Aptamer/Conjugated Polymer Complexes. *J. Am. Chem. Soc.* 2004, *126*, 1384–1387, doi:10.1021/ja037289f.
37. Nagatoishi, S.; Tanaka, Y.; Tsumoto, K. Circular Dichroism Spectra Demonstrate Formation of the Thrombin-Binding DNA Aptamer G-Quadruplex under Stabilizing-Cation-Deficient Conditions. *Biochem Biophys Res Commun* 2007, *352*, 812–817, doi:10.1016/j.bbrc.2006.11.088.

38. Hamaguchi, N.; Ellington, A.; Stanton, M. Aptamer Beacons for the Direct Detection of Proteins. *Anal Biochem* 2001, *294*, 126–131, doi:10.1006/abio.2001.5169.
39. Torimura, M.; Kurata, S.; Yamada, K.; Yokomaku, T.; Kamagata, Y.; Kanagawa, T.; Kurane, R. Fluorescence-Quenching Phenomenon by Photoinduced Electron Transfer between a Fluorescent Dye and a Nucleotide Base. *Anal Sci* 2001, *17*, 155–160, doi:10.2116/analsci.17.155.
40. Dynamic Biosensors GmbH SwitchSENSE Compatibility Sheet Available online: https://www.dynamic-biosensors.com/wpcms/wp-content/uploads/2016/05/switchSENSE-compatiblity-sheet-v171129.pdf.
41. Su, C.T.-T.; Ling, W.-L.; Lua, W.-H.; Poh, J.-J.; Gan, S.K.-E. The Role of Antibody Vκ Framework 3 Region towards Antigen Binding: Effects on Recombinant Production and Protein L Binding. *Sci Rep* 2017, *7*, doi:10.1038/s41598-017-02756-3.

Chapter 3

The results presented in this chapter are included in the paper (submitted):

Ponzo I., Soldà A., Crowe C., Ciulli A., Dahl G., Geschwindner S., and Rant U. Proximity Biosensor Assay for PROTAC Ternary Complex Analysis. 2023.

My personal contribution to this manuscript was, together with Soldà A., the collection and curation of all the experimental data presented in this chapter, their analysis and visualization, and the preparation and writing of the original draft.

3. Analysis of PROTAC Ternary Complex Formation by Induced Proximity with a DNA Y-structure

Abstract

Thermodynamically stable and kinetically long-lived degrader-mediated ternary complexes can drive faster and more complete degradation [1,2] however additional methods for screening ternary complex formation are required. We developed a novel heliX® biosensor assay in which E3 ligases and target proteins are immobilized onto a DNA Y-structure with built-in fluorescent dyes. The Y-structure closes upon small molecule binding, and the subsequent ternary complex formation brings together the green donor and the red acceptor dye into a closer, FRET-sensitive, distance. Binding affinity of binary and ternary complexes, along with avidity were measured using a single FRET assay, allowing us to perform a high-throughput screen with a library of PROTACs against VHL, CRBN and BET proteins. Our findings establish novel biosensor assays to quantify the kinetic parameters required for effective target ubiquitination and degradation in a high-throughput manner using only nano- or picomolar amounts of protein and PROTAC.

3.1 Introduction

Initially described in 2001 [3], PROTACs (PROteolysis TArgeting Chimeras) has emerged as a powerful therapeutic strategy to selectively degrade proteins via the ubiquitin-proteasome system (UPS). PROTACs are heterobifunctional small molecules consisting of two protein-binding moieties joined by a linker: one moiety has binding affinity for a target protein of interest (POI), while the other recruits an E3 ubiquitin ligase. The simultaneous engagement of both the E3 ligase and the POI form a ternary complex which is the key species necessary for ubiquitination and subsequent degradation of the POI. PROTACs are promising new therapeutic agents, for their advantages in engaging intracellular targets, and potential for oral bioavailability due to their lower molecular weight compared to other therapeutic tools, e.g., monoclonal antibodies.

The first generation of PROTACs was designed by employing bulky peptide-based E3 ligands, limiting their clinical application [4]. Significant advancements were made in the last decade, leading to the development of PROTACs with improved physical-chemical properties: a great interest in the field was raised after the development of small molecules PROTACs that could recruit the E3 ligases von Hippel-Lindau (VHL) [5] and cereblon (CRBN) [6]. In particular, CRBN was identified as the molecular target of the immunomodulatory imide (IMiDs) drugs, thalidomide and derivatives, that are indicated for multiple myeloma [7]. For this reason, PROTACs able to recruit CRBN have a great pharmaceutical interest. One of the most studied PROTAC targets is Brd4, belonging to the BET family of proteins. Brd4 contains two bromodomains, BD1 and BD2, known to be involved in the transcriptional regulation of gene expression [8].

While biophysical methods are used extensively in hit finding (fragment-based screening), hit validation, and in-depth characterization of “classical” small molecule drugs, there is an unmet need for advanced analytical methods to identify and characterize novel, more complex drug candidates such as bifunctional molecules, which are engineered to induce or suppress protein-protein interactions. In particular, the characterization and optimization of PROTACs requires novel biophysical assays that probe the ternary nature.

Studies in vitro and in vivo demonstrated that an efficient ternary complex formation is a key step in the PROTAC mechanism of action [1,2,9,10], affecting the success of target protein degradation [5]. Different and complementary in vitro orthogonal assay are therefore needed for a deeper understanding of the mechanism of action of PROTAC-induced degradation. Several technologies provide suitable strategies for the characterization of the binary and ternary complex formation [11,12]: SPR, BLI and ITC are biophysical technologies that have found applications in PROTAC binding studies [1,13–17]. Both BLI and SPR can detect binding events on biosensor surfaces in real time through a spectroscopic method, while ITC allows to determine the thermodynamic parameters of the interaction in solution. However, both SPR and BLI require the immobilization of a ligand, and only one ligand species can be immobilized on the biosensor surface, necessitating a pre-incubation of PROTAC with one of the two proteins to form the ternary complex. ITC does not require ligand immobilization, but it demands high sample consumption.

The heliX® biosensor, based on switchSENSE® technology, can offer a powerful alternative to the aforementioned technologies. The DNA Y-structure involves simultaneous immobilization of two ligands, with the sole analyte species being the PROTAC. Both monovalent and bivalent PROTAC binding can be detected, providing information about binary target engagement and ternary complex formation. This allows for extrapolation of kinetic parameters such as affinity and avidity.

All switchSENSE® experiments are performed on a standard adapter biochip (Figure 1A), in which single-stranded DNA (anchor strands) are covalently attached to the chip surface. The proteins are attached via flexible linkers to the DNA and, therefore, can rotate and bend quickly, thereby exposing a large portion of their surfaces to the dye and reducing the effect of the immobilization on the measurement. Each chip is equipped with 2 gold electrodes (hereby referred to as “spots”) harboring different DNA anchor strands, placed in proximity in a single flow channel. It can therefore be considered that the binding reactions on spots 1 and 2 occur simultaneously.

We introduce here the DNA Y-structure, a supramolecular construct formed by four single stranded DNA oligonucleotides. Two complementary DNA strands form a duplex stem with protruding single stranded arms, carrying a red and a green dye at their distal ends. Two complementary DNA strands, named ligand strands, can hybridize to the two arms, building together the dsDNA Y-structure (Figure 1B and S1). The target proteins can be functionalized on the end of the two FRET pair color-coded Y-arms of the structure, in an induced proximity system. The Y-structure closes upon small molecule binding, and the subsequent ternary complex formation brings together the green donor and the red acceptor dye into a closer,

FRET-sensitive, distance. The DNA Y-structure approach gives us the ability to simultaneously detect PROTAC binary target engagement and PROTAC-induced ternary complex formation.

Herein, we showcase the capabilities of the switchSENSE® technology for a rapid high-throughput PROTAC screening and kinetic characterization with low sample consumption, overcoming the limitations of other surface-based technologies. The advantageous features of heliX® biosensor were used to screen a PROTAC library against VHL, CRBN and BET proteins. For the first time, we were able to measure the association and dissociation rates of PROTACs with CRBN on a surface.

3.2 Results

3.2.1 Y-structure – zippers

To investigate the suitability of the novel supramolecular DNA Y-structure for studying protein-protein interactions (PPi), we first characterized the range of action of the Y-structure itself by elongating the two FRET pair color-coded Y-arms with DNA sequences at different lengths (from 4 bp to 15 bp). The Y-structure closes upon DNA-DNA binding, forming a zipper system (SI, Figure S1) bringing together the green donor and the red acceptor dye into a closer, FRET-sensitive, distance. In this setup we can record and monitor the stability of the red FRET signal generated by the induced proximity of the 2 dyes. From the study we observed that the 5bp- and 6bp-zipper cannot close the Y-structure, the DNA-DNA interaction is too weak. From 7bp- to 11bp-zipper, the structure is partly open and partially closed, which defines the dynamic range of the DNA Y-structure for studying protein-protein interactions, because we aimed for a system that is flexible enough to measure both the ternary complex formation and inhibition. The 12bp- and 15bp-zippers do not allow the opening of the structure anymore, and the two arms remain fully closed all the time. Finally, we can correlate the percentage of FRET signal generated with the equilibrium dissociation signal (K_D) of the respective DNA-DNA zipper binding pair (Figure 1C), providing useful information about the dynamic range of the DNA Y-structure for studying kinetics of PPi. In detail, this specific DNA Y-structure can resolve PPis with expected K_D from 1 nM to 10 µM. However, we recently developed a new Y-structure design that forces the two (homo- or hetero-) target proteins functionalized on the end of the two FRET pair color-coded Y-arms to a greater distance. This new structure can perfectly resolve PPis with expected K_D between 50 pM to 100 nM (SI, Figure S1).

3.2.2 VHL system as proof of concept

Afterward, to investigate the utility of the heliX® biosensor in monitoring PROTAC ternary complex kinetics, we adopted a well-characterized model system composed of the E3 ligase VHL, the POI BET bromodomain protein $Brd4^{BD2}$ and the PROTACs MZ1 and AT1 [1,18] as a starting case study. As previously explained, the presented Y-structure holds the proteins in an

induced proximity setup which allows to study interactions with affinity between 1nM to 10µM (Figure S1). AT1, with its reported K_D of 20 nM [1] is the perfect example to demonstrate the ability of our system to quantify the binary binding toward the BET protein and the ligase, as well as the ternary complex formation (1:2 interaction), without any preincubation step or particular experimental conditions needed (e.g. buffer, temperature). While we used a different Y-structure design, which allows to study interactions with tight binding affinity with a $K_D \leq 1$nM (Figure S1), to resolve the binary vs ternary binding of MZ1; those results are reported in the SI, Figure S2A.

3.2.3 Binary target engagement

To study the affinity of AT1 toward either VHL or $Brd4^{BD2}$, only one arm of the Y-structure was functionalized with a protein (either VHL-EloB-EloC on the arm with the red fluorescent dye, or $Brd4^{BD2}$ on the arm with the green fluorescent dye), while the other arm was left as duplex ligand-free strand (Figure 1D-F). For the binary affinity study the FRET system was not needed, but we used the classic fluorescent proximity sensing mode (or static mode), where we monitor the direct quenching of the fluorophore which is in proximity of the protein of interest (either VHL in red or $Brd4^{BD2}$ in green) upon binding of the analyte (AT1). As shown in Figure 1D, the binding of increasing concentrations of AT1 (from 4 to 500 nM) to $Brd4^{BD2}$ leads to a decrease in the green fluorescence signal, which can be nicely described by a 1:1 binding model providing one on-rate (k_{ON} = 13.1 ± 2.5 E+6 $M^{-1}s^{-1}$) and one off-rate (k_{OFF} = 181 ± 35.4 E-3 s^{-1}), yielding a K_D equal to 12.4 ± 1.3 nM, which is perfectly in line with what has been previously reported in SPR (K_D = 9 nM)[1]. Nevertheless, a 6 times faster on-rate has been recorded in our setup, as well as a 10 times off-rate, which can be correlated to the difference in the experimental setup (e.g. temperature: RT in our case vs 12°C, different chip density and flow rate)[1], plus a difference in the proteins used. On the other side (Figure 1F), the binding of the same increasing concentrations of AT1 to VHL leads to a decrease in the red fluorescence signal, which can be globally fitted providing the on-rate (k_{ON} = 0.69 ± 0.12 E+6 $M^{-1}s^{-1}$), and off-rate (k_{OFF}= 87.5 ± 26.7 E-3 s^{-1}), yielding a K_D equal to 123 ± 20 nM, which is again perfectly in line with what has been previously reported in SPR (K_D = 110 nM)[1]. The main difference observed between the affinity of AT1 to VHL and $Brd4^{BD2}$ lies in the association rate; AT1 indeed associates 20 times faster to the BET protein than to the E3 ligase.

3.2.4 Ternary complex formation

To measure AT1-mediated ternary complex formation, both arms of the Y-structure were functionalized. The arm bearing the green fluorescent dye was functionalized with $Brd4^{BD2}$, while the VHL-EloB-EloC was immobilized onto the arm carrying the red fluorescent dye (Figure 1E). The Y-structure closes upon AT1 binding, and the subsequent ternary complex formation brings together the green donor and the red acceptor dye into a closer, FRET-sensitive, distance. The change in red FRET fluorescence signal intensity directly correlates with ternary

complex formation kinetics (Figure 1E), while the green signal is correlated with both the direct quenching of the dye upon analyte binding and affected by the formation of the ternary complex. This is the reason why we can conclude that the red FRET signal describes exclusively the ternary complex formation with high sensitivity, while the green signal contains information about both the binary and the ternary binding.

Figure 1E shows the simultaneous binding of increasing concentrations of AT1 (from 160 pM to 20 nM) to both VHL and $Brd4^{BD2}$. The red FRET signal can be globally fitted providing a k_{ON} equal to 15.9 ± 1.88 E+6 $M^{-1}s^{-1}$ and k_{OFF} equal to 8.97 ± 1.39 E-3 s^{-1}, yielding a K_D equal to 0.58 ± 0.16 nM. This value differs from the values reported in literature [1]; however, if we compare closely the values, we observe that the off-rates are very similar, but the on-rates obtained using the Y-structure are 10 time faster than the one reported by using SPR in the same work, which leads to the difference in the final K_D. This difference can be explained by the fact that: i) we use an induced proximity setup, where the two proteins are in close proximity, but still free to move in the semi-solution environment and to react independently to the single PROTAC, which allows us to follow the avidity component of the interaction, but can also lead to rebinding (see introduction); ii) in our setup the PROTAC is injected alone, without any prior incubation with either of the target proteins, as is normally the case in SPR, which means that its steric hindrance is much smaller than the whole protein-PROTAC complex and the association rate can be affected; iii) the flow rate used in our experiment is 500 µL/min, which is on average 5 to 10 times faster than in SPR, therefore we avoid any possible effect of mass transport limitation during the association phase. In addition, it is very interesting to observe that the on-rate of the ternary complex formation is identical to the on-rate of AT1 binding to $Brd4^{BD2}$ (Figure 1G), which suggests that $Brd4^{BD2}$ is the stronger binding partner and triggers the binding of AT1 to the E3 ligase. The off rate is governed by the avidity effect, which slows down the overall dissociation phase, because the presence of the two proteins holds the PROTAC bound for longer time. As side note, higher concentrations of AT1 were omitted in the analysis of the ternary complex formation (Figure 1E), because we observed a decrease of the red FRET signal (SI, Figure S2B) caused by the saturation of the Y-structure, which leads to the opening of the arms. This happens because at high PROTAC concentration, we most probably have two molecules of PROTAC per Y-structure and therefore no FRET is recorded; this situation is also known in the field as *hook effect*.

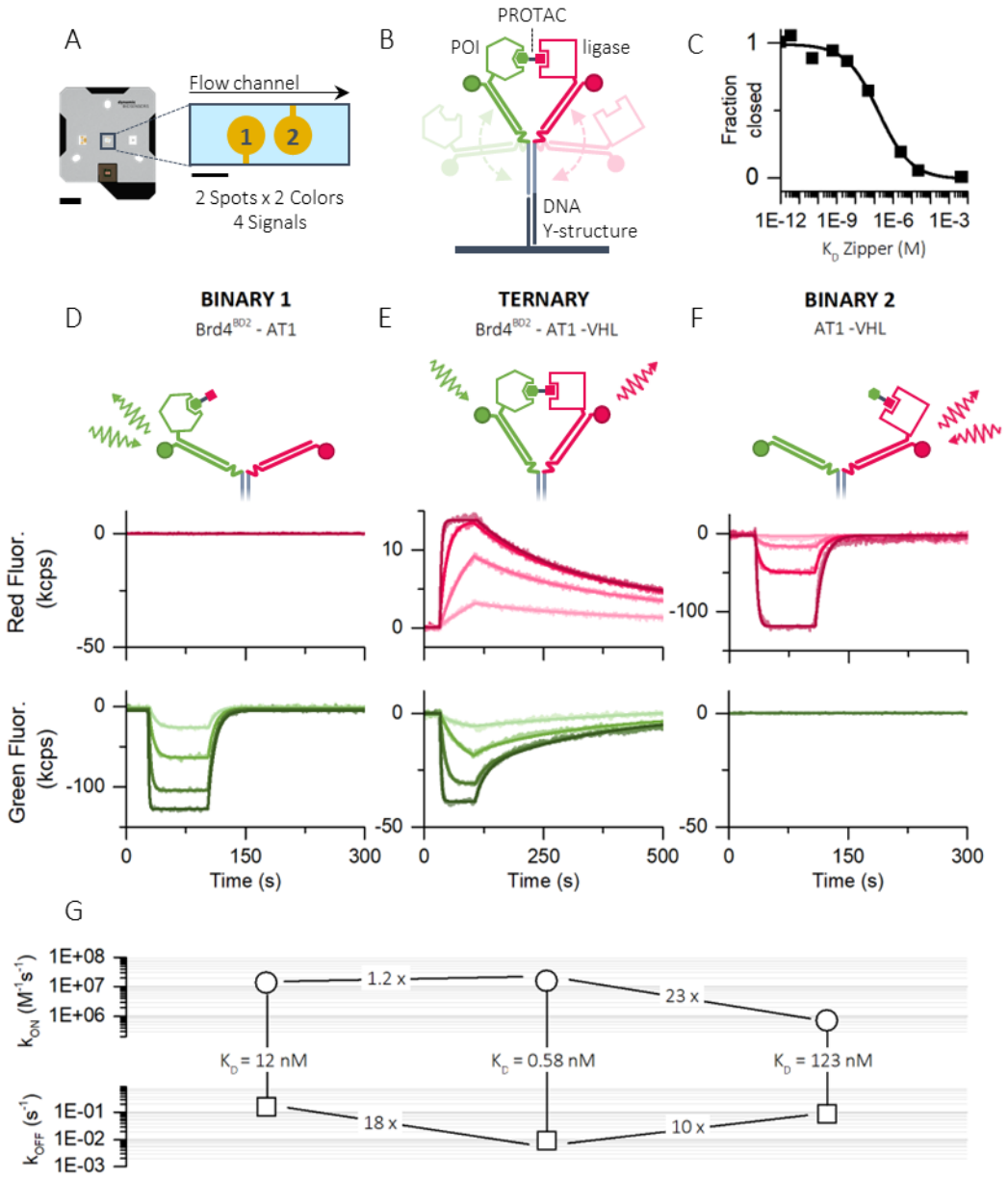

Figure 1. *The DNA Y-structure for studying binary binding and ternary complex formation of bifunctional small molecules, such as PROTACs. Case study: VHL - AT1 - Brd4^{BD2}. A) The heliX® adapter biochip (left, scale bar = 1 cm) is designed with a single flow channel where two gold electrodes (right, scale bar = 100 µm) are spotted in proximity. Each spot harbours a unique DNA anchor strand, allowing to functionalize each spot specifically and independently. B) The Y-structure cartoon which exemplifies the setup used in this study to characterize PROTAC interactions. Four single-stranded DNA oligos are designed to build a Y-shaped structure consisting of a duplex stem with two arms, carrying the ligase and the target protein plus a red and a green dye at the distal ends. Simultaneous binding of the PROTAC to the E3 ligase and target protein causes the formation of a ternary complex and thereby induces red fluorescence due to FRET. C) Study of the dynamic range of the Y-structure, demonstrating a correlation between the proportion (%) of the Y-structure in a closed conformation and the dissociation constant (K_D) of the respective DNA-DNA zipper binding pair. This specific Y-structure can resolve PPi with K_D between 1 nM and 10 µM. D) Binary binding of AT1 to Brd4^{BD2} resulting in a direct quenching of green fluorescence. AT1 was injected at increasing concentrations from 4 nM to 500 nM. E) Ternary binding of AT1 to VHL and Brd4^{BD2}, which results in a quenching of the green signal and a simultaneous increase of the red FRET fluorescence. AT1 was injected at increasing concentrations from 160 pM to 20 nM. F) Binary binding of AT1 to VHL results in a direct quenching of red fluorescence. AT1 was injected at increasing concentrations from 4 nM to 500 nM. G) Rate scale*

plot depicting association and dissociation rates (k_{ON} and k_{OFF}), as well as the resulting dissociation constant (K_D) of the binary and ternary AT1 interactions with Brd4^{BD2} and VHL, above on section D, E and F.

Table 1. *Binding affinities of AT1 to Brd4^{BD2} and VHL and interaction rates of the ternary complex.*

PROTAC	*Interaction*	*Target*	*k_{ON} ($M^{-1}s^{-1}$)*	*k_{OFF} (s^{-1})*	*K_D (nM)*	*half-life $t_{1/2}$ (s)*
AT1	Binary	Brd4^{BD2}	13.1 ± 2.5 E+6	181 ± 35.4 E-3	12.4 ± 1.3	3.8
	Binary	VHL	0.69 ± 0.12 E+6	87.5 ± 26.7 E-3	123 ± 20	7.9
	Ternary	VHL | Brd4^{BD2}	15.9 ± 1.88 E+6	8.97 ± 1.39 E-3	0.58 ± 0.16	77.3

k_{ON} = association rate; k_{OFF} = dissociation rate; K_D = dissociation constant, calculated as k_{OFF}/k_{ON}. Values shown represent the mean ± SD of at least three independent experiments.

3.2.5 PROTAC Screening with CRBN in complex to Brd4^{BD2}

After demonstrating that the Y-structure is a very suitable and unique tool to study ternary complex formation upon PROTAC binding to VHL and Brd4^{BD2}, we herein showcase its ability to perform a screening of different PROTACs and moieties binding to Brd4^{BD2} in complex with CRBN, known to be slightly unstable in solution but extremely important in the clinical field.

For the screening we used the full capacity of heliX® biosensor in combination with our adapter biochip, where in spot 1 we functionalized the ternary system, with CRBN on the red arm (instead of VHL) and Brd4^{BD2} in green, while in spot 2 we functionalized the binary system with only Brd4^{BD2} on the green arm, and the red arm was kept as a ligand-free strand (no CRBN). This configuration allows to simultaneously study both the kinetics of the ternary complex formation to CRBN - Brd4^{BD2} as well as the binary affinity to Brd4^{BD2} within the same experiment. Twenty different small molecules (including full PROTACs, PROTAC moieties and negative controls) were selected, and listed in Table 2. To test the reproducibility of the screening, each small molecule was tested 4 times within the same assay plate. A total of 96 kinetic readouts (blanks included) were obtained (Figure 2). However, considering that we record simultaneously 4 traces, such that spot 1 RED: ternary, spot 1 GREEN: ternary + binary, spot 2 RED: unspecific binding, spot 2 GREEN: only binary to Brd4^{BD2}, we overall record 384 traces in less than 22 hours. For the screening we selected a single and fixed concentration of 20 nM for each PROTAC or moiety, and we included a blank run at the beginning and at the end of each row of a 96 well plate. The biosensor chip was regenerated and freshly functionalized at the end of each row, for a total of 8 regenerations and a total protein consumption of 15 pmol of CRBN and 30 pmol of Brd4^{BD2}, which is extremely low compared to some routine biophysical technologies (e.g., ITC or SPR).

PROTACs that induce the formation of a ternary complex between CRBN and Brd4^{BD2} can be easily identified by the presence of the red FRET signal in conjunction with the quenching of the green signal: for example ARV-825 (Figure 2, well A2). Some PROTACs, such as MZ1, MZ2 and MZ4, instead interact only with Brd4^{BD2}, which can be identified by observing the

fluorescence change only in green (Figure 2, well 7C). Meanwhile the negative controls do not show any signal in either green or red (Figure 2, well B11).The presence of a second spot where the Y-structure is carrying only the $Brd4^{BD2}$ on the green arm provides a real-time reference and a validation of the binary interaction of each PROTAC with the target protein (SI, Figure S3).

The screening of the selected PROTAC library yielded six positive hits: ARV-825, dBET1 and dBET6, dBET6(2), ARV-825(2), and dBET260. Remarkably, the red signal changes are highly reproducible from the first to the last row, suggesting good stability of the functionalized Y-structure over long time (> 24h). Additionally, we observe binary binding to $Brd4^{BD2}$ for nine small molecules, such as: MZ1, MZ2, MZ4, AT1 and cisMZ1, which are known PROTACs for the VHL system, owing to their (+)-JQ1 moiety binding to the BET protein. Indeed, JQ1 alone shows a clear signal in green, emphasizing the high sensitivity of our technology to analyze protein-small molecule binding. In addition, clear binary signal to $Brd4^{BD2}$ is also observed for OTX015, ARV-771, and ZXH-3-26. While do not observe any binding of pomalidomide (Pom) or VH032: these results are expected since they are moieties binding 1:1 to CRBN and VHL, respectively, and in the screening, we are monitoring only the signals coming from the binding to $Brd4^{BD2}$. However, we successfully studied separately the kinetics of pomalidomide binding to CRBN using the classic fluorescence proximity sensing mode in red (SI, Figure S5C) obtaining a K_D around 500 nM. Using spot 2 we can confirm all the binary binding hits and we can resolve the binary binding to $Brd4^{BD2}$ of the ternary positive hits. All the single kinetic traces are shown in the SI, Figure S4A-O.

In Figure 2I, the ternary versus binary hit map is presented, where the recorded ternary signal, expressed as a percentage increase in red fluorescence on spot 1, is plotted as a function of its binary signal, expressed as a percentage decrease in green fluorescence on spot 2. This graph identifies immediately the ternary positive hits (ARV-825 and dBET family) compared to the POI-only binary binders and the negative controls used in the screening. The fluorescent signals of the 96 samples are plotted independently and the high reproducibility of the data during the entire screening can be appreciated.

In addition, a statistical analysis of the entire screening has been performed. Figure 2J shows the p-values of the red ternary signals calculated as a function of the p-values of green binary signals. For the analysis, a two-sample t-test has been carried out, where the mean values and standard deviations of the data coming from the blank traces (n = 16) have been compared with the mean values and standard deviations of traces recorded for a single PROTAC (n = 4), both in red and in green, evaluated individually. The t-test provides indeed p-values for each sample and each color, which were plotted in the graph (Figure 2J), indicating a high statistical significance and high confidence of the screening outcome. The hit confidence can be used to discriminate the samples which have a strong ternary complex formation compared to the ones that have only binary affinity for the POI.

Despite the screening being performed at a single PROTAC concentration of 20 nM, all the fluorescent traces can be fitted (see SI, Figure S4A-O) providing quantitative information about the kinetic data for each PROTAC and moiety. Table 2 summarizes all the preliminary kinetic values expressed as a mean value obtained from the four kinetic traces, either measured in

red (for ternary binders) or green (for binary binders). The corresponding kinetic rate map (for both ternary and binary) is displayed in Figure 2K, where the mean values of the on-rates (k_{ON}) are plotted as a function of the off-rates (k_{OFF}), illustrating the preliminary dissociation constant as ratio of the two. The PROTACs that form ternary complexes show the highest avidity effect, with much slower off-rates than the binary system, with a K_D very comparable among each other in the low nM range. This demonstrates once again the importance of measuring the relative rates and not only the simple K_D. Among the ternary binders, dBET260 appears to have the slowest off-rate, but also the slowest on-rate, while the two samples of ARV-825 coming from different providers are perfectly superimposable as well as the two dBET6 and dBET1. From the hit screening we can also get important preliminary information about the individual binding rates, affinities and avidities of the tested PROTACs. Table 2 shows the kinetic parameters of the PROTACs binding to CRBN and/or $Brd4^{BD2}$ obtained from the single screen shown in Figure 2.

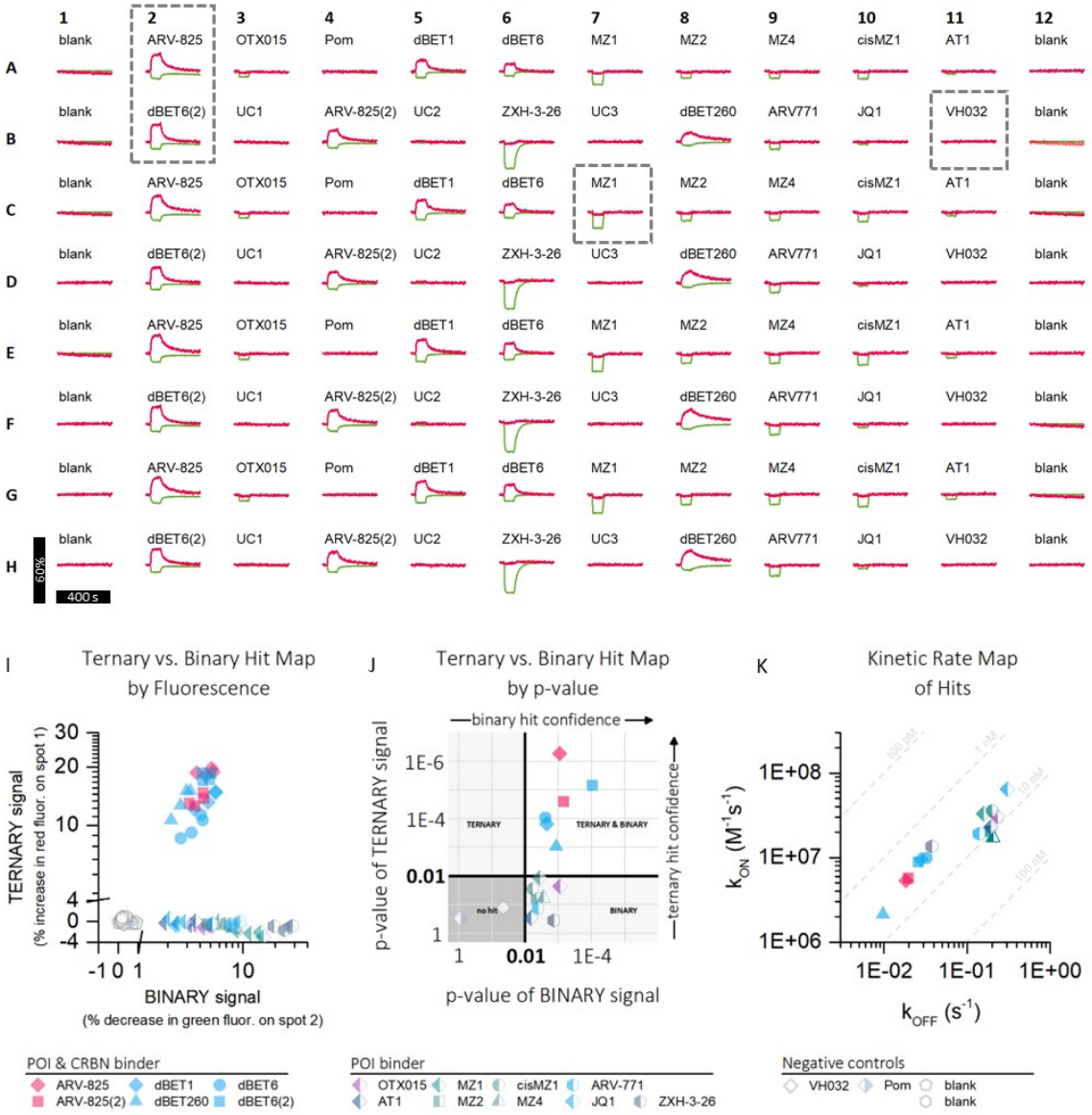

Figure 2. *PROTAC screening. A-H) Fluorescence signals resulting from the PROTAC interaction with CRBN (red signal) and Brd4^{BD2} (green signal): ARV-825, ARV-825$_{(2)}$, dBET1, dBET6, dBET6$_{(2)}$, and dBET260 lead to the formation of the ternary complex between CRBN, PROTAC and Brd4^{BD2}, which can be easily recognized by the presence of the red FRET signal in conjunction with the quenching of the green signa. I) Ternary vs Binary Hit Map by Fluorescence: recorded ternary signal, expressed as percentage increase in red fluorescence on spot 1, are plotted in function of its binary signal, expressed as percentage decrease in green fluorescence on spot 2. All the 96 samples are displayed. J) Ternary vs Binary Hit Map by p-value: confidence of the red ternary signals calculated in function of the green binary signals. A two-sample t-test have been carried out, where all the data coming from the blank traces (n=16) have been compared with the traces recorded for a single PROTAC (n=4), both in red and in green and evaluated individually. The t-test (Welch's correction included) provides the p-value for each sample and each color. K) Kinetic rate map: mean values of the on-rates (k_{ON}) are plotted in function of the off-rates (k_{OFF}), illustrating the preliminary dissociation constant (K_D) as ratio of the two (n=4). PROTACs which lead to ternary complex formation are depicted as fully colored symbols, while binary binders are depicted as half empty and negative controls are fully empty.*

Table 2. *Kinetic parameters of PROTACs binding to CRBN and/or Brd4^{BD2} obtained from the single screen shown in Figure 2. Each value is an average ± SD of 4 diagrams obtained at 20 nM PROTAC concentration.*

PROTAC		*Target*	*k_{ON} ($M^{-1}s^{-1}$)*	*k_{OFF} (s^{-1})*	*K_D (nM)*	*half-life $t_{1/2}$ (s)*
ARV-825	Ternary	CRBN| Brd4^{BD2}	5.30 ± 1.1 E+6	18.6 ± 0.6 E-3	3.6 ± 1.0	37.3
dBET1	Ternary	CRBN| Brd4^{BD2}	8.90 ± 0.7 E+6	26.0 ± 0.6 E-3	3.0 ± 0.3	26.7
dBET6	Ternary	CRBN| Brd4^{BD2}	9.90 ± 0.5 E+6	32.6 ± 1.3 E-3	3.3 ± 0.2	21.3
dBET6$_{(2)}$	Ternary	CRBN| Brd4^{BD2}	9.50 ± 0.7 E+6	28.2 ± 1.6 E-3	3.0 ± 0.1	24.6
ARV-825$_{(2)}$	Ternary	CRBN| Brd4^{BD2}	5.70 ± 0.4 E+6	20.0 ± 1.0 E-3	3.5 ± 0.3	34.7
dBET260	Ternary	CRBN| Brd4^{BD2}	2.10 ± 0.1E+6	9.8 ± 0.2 E-3	4.6 ± 0.1	70.7
OTX015	Binary	Brd4^{BD2}	30.5 ± 2.6 E+6	234 ± 71 E-3	7.6 ± 2	2.97
MZ1	Binary	Brd4^{BD2}	32.9 ± 3.7 E+6	159 ± 12 E-3	4.9 ± 0.4	4.36
MZ2	Binary	Brd4^{BD2}	20.4 ± 2.6 E+6	194 ± 17 E-3	9.7 ± 1.5	3.57
MZ4	Binary	Brd4^{BD2}	17.1 ± 2.7 E+6	207 ± 44 E-3	13 ± 5.2	3.35
cisMZ1	Binary	Brd4^{BD2}	35.9 ± 3.7 E+6	200 ± 16 E-3	5.6 ± 0.9	3.46
AT1	Binary	Brd4^{BD2}	22.8 ± 3.2 E+6	193 ± 14 E-3	8.7 ± 1.5	3.59
ZXH-3-26	Binary	Brd4^{BD2}	13.6 ± 1.9 E+6	37.6 ± 2.0 E-3	2.8 ± 0.4	18.4
ARV771	Binary	Brd4^{BD2}	19.1 ± 1.9 E+6	141 ± 5.0 E-3	7.5 ± 0.7	4.92
JQ1	Binary	Brd4^{BD2}	64.0 ± 22 E+6	308 ± 4.8 E-3	5.2 ± 1.3	2.25
VH032	N.D.	Brd4^{BD2}	-	-	-	-
Pom	N.D. Binary*	Brd4^{BD2} CRBN$_{Red}$*	- 0.50 ± 0.02 E+6	- 252 ± 9.5 E-3	- 499 ± 0.01	- 2.8

k_{ON} = association rate; k_{OFF} = dissociation rate; K_D = dissociation constant, calculated as k_{OFF}/k_{ON}.

3.2.6 Kinetic characterization of the positive hits

After the identification of the positive hits from the high throughput screening, namely ARV-825, dBET1, dBET6 and dBET260, we further characterized three of them by performing full concentration-dependent kinetics. Binary affinities to CRBN and Brd4^{BD2} as well as ternary complex formation of ARV-825, dBET1, dBET6 have been investigated by using the same experimental conditions described previously for VHL and the same setup used during the screening.

As shown in Figure 3A, the binding of increasing concentrations of ARV-825 (from 4 nM to 100 nM) to Brd4^{BD2} leads to a decrease in the green fluorescence signal, which can be nicely described by a 1:1 global mono-exponential fit providing on-rate (k_{ON} = 7.10 ± 2.2 E+6 $M^{-1}s^{-1}$) and off-rate (k_{OFF} = 83.0 ± 21 E-3 s^{-1}), yielding a K_D equal to 12.7 ± 3.7 nM, in good agreement with a K_D of 28 nM reported by Lu *et al*. [6] by using BROMOscanTM. The same quenching effect has been observed upon dBET1 and dBET6 binding to Brd4^{BD2} (see SI, Figure S5A-B) and for both the resulting K_D is around 5-10 nM, which is expected since they possess the same (+)-

JQ1 moiety as AT1 and the binary binding toward Brd4^{BD2} should be similar. However, dBET1 has a faster off-rate compared to dBET6. In Figure 3C, we characterize for the first time the binding affinity of ARV-825 (from 4 nM to 100 nM) to CRBN, which leads to a decrease in the red fluorescent signal, that can be globally fitted providing the on-rate (k_{ON}= 0.59 ± 0.17 E+6 $M^{-1}s^{-1}$), and off-rate (k_{OFF}= 79.0 ± 19 E-3 s^{-1}), yielding a K_D equal to 138 ± 36 nM. Compared to ARV-825, dBET6 has a very similar affinity towards CRBN, while for dBET1 the recorded on-rate is slightly faster, yielding a K_D of 40 nM.

In Figure 3B, we report for the first time the kinetic parameters of ternary complex formation between CRBN, ARV-825 and Brd4^{BD2}. In detail, upon binding of increasing concentrations (from 800 pM to 20 nM) of the three tested PROTACs (ARV-825, dBET1 and dBET6), we observe a quenching of the green fluorescent signal and a consequent increase in the red FRET signal, which can be globally fitted providing the kinetic rates of the ternary binding. Interestingly, like for the VHL-AT1-Brd4^{BD2} system, the on-rate of the ternary complex is triggered by the BET protein (the two k_{ON} are extremely similar, 7.20 E+6 vs 7.10 E+6 $M^{-1}s^{-1}$), which is the stronger binding partner compared to the E3 ligase (Figure 3D). The dissociation rate is affected by the avidity effect, which causes a 5-times slower off rate compared to the binary binding (k_{OFF}= 17.8 ± 2.7 E-3 s^{-1}). Therefore, we can conclude that the simultaneous binding of the PROTAC to CRBN and Brd4^{BD2} leads to an increase in the PROTAC affinity.

Surprisingly, the obtained ternary complex K_D of the three PROTACs are very similar: 2.7 nM for ARV-825 and dBET6, and 2.9 nM for dBET1. Nevertheless, if we compare the on- and off-rates (Table 3), we observe clear differences: ARV-825 has a slower on-rate compared to dBET1 and dBET6, however its off-rate is almost doubly slower, contributing to a longer half-life (40 s versus 22 s), which can be correlated to a more efficient target degradation process in cells [19]. Kaji *et al.* observed the same, that ARV-825 keeps the ternary complex formation in cells longer than dBET1 and, in addition, they also suggest a strong correlation between the level of time-dependent formation of ternary complex and the level of targeted protein degradation, supporting the idea that a stable ternary complex leads to efficient targeted protein degradation [19]. This underlines in general the importance of measuring kinetic rates (on- and off-) and not only the dissociation constant, which can be approximatively interpreted.

Table 3. *Kinetic rates and dissociation constants of PROTACs binding to CRBN and Brd4^{BD2}.*

PROTAC		*Target*	*k_{ON} ($M^{-1}s^{-1}$)*	*k_{OFF} (s^{-1})*	*K_D (nM)*	*half-life $t_{1/2}$ (s)*
ARV-825	Binary	Brd4^{BD2}	7.10 ± 2.2 E+6	83.0 ± 21 E-3	12.7 ± 3.7	8.3
	Binary	CRBN	0.59 ± 0.17 E+6	79.0 ± 19 E-3	138 ± 36	8.8
	Ternary	CRBN| Brd4^{BD2}	7.20 ± 2.0 E+6	17.8 ± 2.7 E-3	2.77 ± 1.1	38.9
dBET1	Binary	Brd4^{BD2}	38.6 ± 6.7 E+6	229 ± 57 E-3	5.95 ± 0.4	3.0
	Binary	CRBN	2.22 ± 0.56 E+6	89.6 ± 8.3 E-3	40 ± 10.9	7.7
	Ternary	CRBN| Brd4^{BD2}	11.4 ± 3.8 E+6	31.6 ± 9.1 E-3	2.91 ± 0.65	21.9
dBET6	Binary	Brd4^{BD2}	7.25 ± 3.04 E+6	91.2 ± 33 E-3	12.6 ± 4.9	7.6

Binary	CRBN	0.47 ± 0.35 E+6	48.7 ± 9.7 E-3	104 ± 126	14.2
Ternary	CRBN| $Brd4^{BD2}$	11.3 ± 0.39 E+6	31.3 ± 1.2 E-3	2.77 ± 1.42	22.1

k_{ON} = association rate; k_{OFF} = dissociation rate; K_D = dissociation constant, calculated as k_{OFF}/k_{ON}. Values shown represent the mean ± SD of at least three independent experiments.

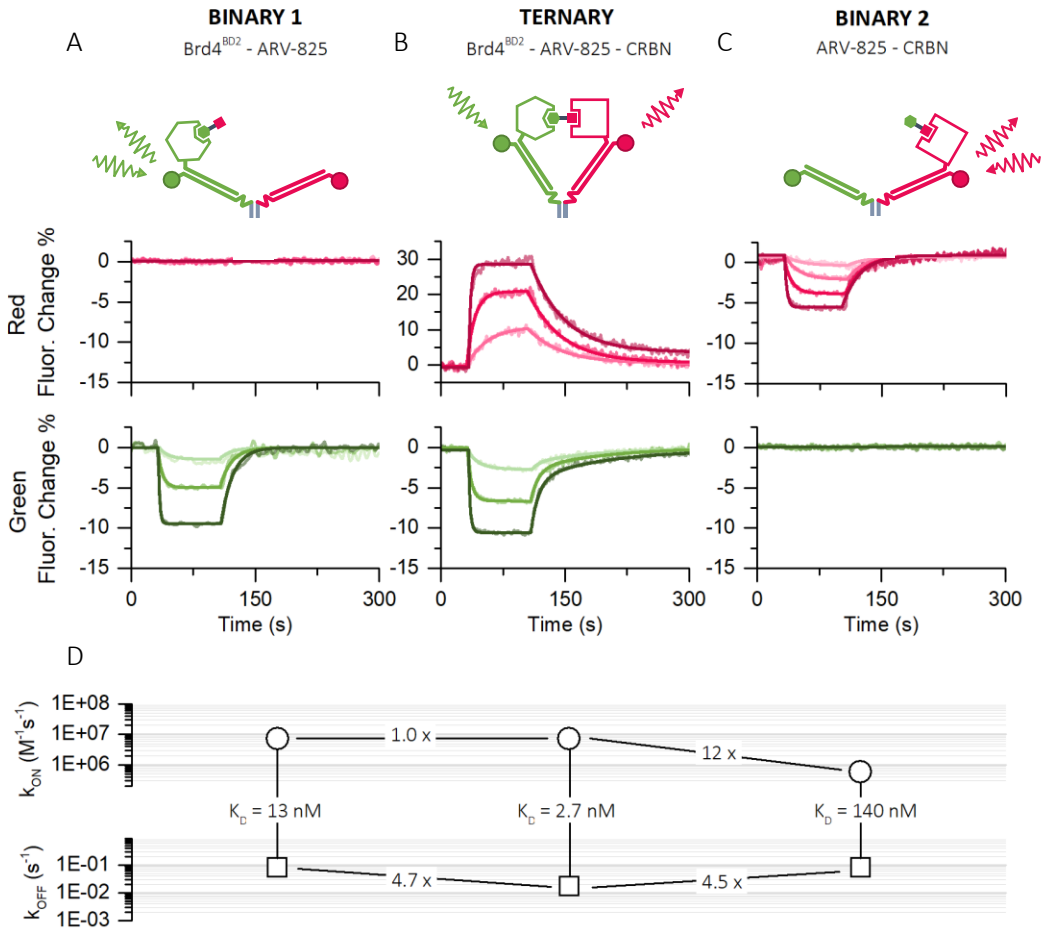

Figure 3. *Kinetic characterization of binary vs ternary binding of ARV-825 to CRBN and $Brd4^{BD2}$. A) Binary binding of ARV-825 to $Brd4^{BD2}$ resulting in a direct quenching of the green fluorescence. ARV-825 was injected at increasing concentrations from 4 nM to 100 nM (dilution 5x). B) Ternary binding of ARV-825 to CRBN and $Brd4^{BD2}$, which results in a quenching of the green signal and a simultaneous increase of the red FRET fluorescence. ARV-825 was injected at increasing concentrations from 800 pM to 20 nM (dilution 5x). C) Binary binding of ARV-825 to CRBN resulting in a direct quenching of the red fluorescence. ARV-825 was injected at increasing concentrations from 4 nM to 100 nM (dilution 5x). D) Rate scale plot depicting association and dissociation rates (k_{ON} and k_{OFF}), as well as the resulting dissociation constant (K_D) of the binary and ternary binding of ARV-825 to $Brd4^{BD2}$ and CRBN.*

3.2.7 Screening of different BET proteins

After proving the ability of our technology to successfully study the ternary complex formation upon binding of several PROTACs to two different E3 ligases (VHL and CRBN) using $Brd4^{BD2}$ as a representative BET bromodomain, we sought to study the ternary complex formation with

other BET bromodomains (Table 3 and Figure 4). The aim was to showcase the high versatility of the Y-structure as well as to study the potential specificity of CRBN PROTACs on binding and degrading particular BET proteins, like it has been studied for VHL [1]. For this evaluation, we used the identical setup that has been previously presented for VHL. In spot 1, we subsequently immobilized the ternary system with the individual bromodomains (BD1 or BD2) of each BET protein (Brd2, Brd3, Brd4 and BrdT) in green and CRBN in red. Meanwhile in spot 2, the Y-structure was functionalized with only the individual bromodomains (BD1 or BD2) of each BET protein in green and the red arm was kept as ligand-free strand, allowing to study simultaneously ternary and binary binding of ARV-825.

ARV-825 was repeatedly injected over the surface at increasing concentrations from 800 pM to 100 nM and, as previously described, the red FRET fluorescence signal is detected only when ARV-825 can form the ternary complex with CRBN and the BET protein.

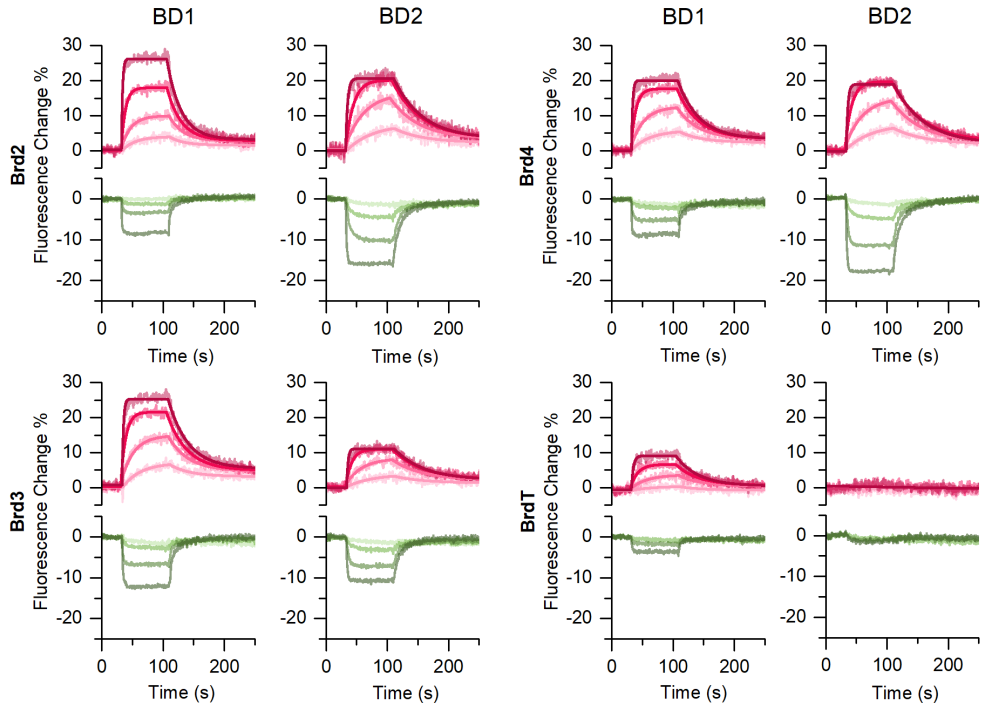

Figure 4. *Sensograms of ternary complex formation upon ARV-825 binding to CRBN and individual bromodomains (BDs) of different BET proteins (Brd2, Brd3, Brd4 and BrdT). Each POI was immobilized on the green arm of the Y-structure to be screened with ARV-825 in the presence of CRBN on the red arm. Red signals coming from the ternary interaction with BrdX-BD1 (left column) and with BrdX-BD2 (right column) are shown. ARV-825 was injected at increasing concentrations from 800 pM to 100 nM (dilution 5x).*

From Figure 4, we observe that ARV-825 can efficiently form the ternary complex with most of the BRD bromodomains, only $BrdT^{BD2}$ does not show any ternary binding at all. If we look closely to the green signals (both ternary and binary) of each diagram (SI, Figure S6A), we observe higher fluorescent signals for ARV-825 binding to $Brd2^{BD2}$ and $Brd4^{BD2}$ respect to the $Brd2^{BD1}$ and $Brd4^{BD1}$, respectively, while no difference is observed for Brd3 and almost no binding is detected for BrdT (both units). All the binding rate constants of the binary binding

are reported in Table S4 of the SI. However, when we discuss the ternary complex formation, we need to focus on the red signal (Figure 4). The difference in fluorescence quenching depends exclusively on the FRET efficiency between the two pairs, which in turn depends on their spatial distance of the two dyes upon ternary complex formation, which is ruled by the target proteins' structural dimension and their conformation after binding: systems bigger than 16 nm long, will not show any FRET signal. However, the fitting of the FRET signal and the calculated association and dissociation rates give information about the real kinetics of the ternary complex formation, and as shown in Table 4, the on-/off-rates and equilibrium dissociation constant are relatively close, while the half-life ($t_{1/2}$) of BD2 is in general slightly longer than the relative BD1 of the same BET protein. Another interesting point is that for all the BD2s we reach the saturation of the red FRET signal at 100 nM of ARV-825, while for BD1 this behavior differs among the BET proteins. This effect leads to a constant difference on the on-rates between BD1 (slightly faster k_{ON}) and BD2 (slightly slower k_{ON}) for each BET protein tested (see Table 4). For $Brd4^{BD2}$ we almost observe the so-called *hook effect*, where the red FRET signal is decreasing upon increasing concentrations of PROTAC. In conclusion, CRBN is not highly selective in the degradation of the BET proteins, as previously observed also in MV4; 11 leukemia cells [20], and as opposed to what has been observed for VHL [1]. However, also in this case, consistent with the known degradation-driving complexes, BD2s are slightly more-stable and longer-lived complexes.

Table 4. *Screening of BET proteins. Ternary binding of ARV-825 to VHL and BD1 or BD2 subunit of Brd2, Brd3, Brd4 and BrdT have been tested. Only the red FRET signals are herein reported.*

PROTAC	*Targets ternary*		*k_{ON} ($M^{-1}s^{-1}$)*	*k_{OFF} (s^{-1})*	*K_D (nM)*	*half-life $t_{1/2}$ (s)*
ARV-825	CRBN	**$Brd2^{BD1}$**	8.11 ± 2.50 E+6	3.32 ± 0.02 E-2	4.52 ± 1.41	20.9
	CRBN	**$Brd2^{BD2}$**	4.45 ± 1.01 E+6	2.59 ± 0.21 E-2	5.82 ± 0.89	26.7
	CRBN	**$Brd3^{BD1}$**	6.80 ± 1.62 E+6	2.78 ± 0.18 E-2	4.08 ± 0.75	24.9
	CRBN	**$Brd3^{BD2}$**	5.58 ± 0.92 E+6	2.49 ± 0.43 E-2	4.46 ± 1.55	27.8
	CRBN	**$Brd4^{BD1}$**	8.09 ± 0.12 E+6	2.83 ± 0.19 E-2	3.50 ± 0.29	24.5
	CRBN	**$Brd4^{BD2}$**	5.99 ± 0.26 E+6	2.52 ± 0.29 E-2	4.20 ± 0.67	27.5
	CRBN	**$BrdT^{BD1}$**	4.91 ± 1.03 E+6	2.87 ± 0.31 E-2	5.84 ± 1.38	24.1
	CRBN	**$BrdT^{BD2}$**	N/D	N/D	N/D	

k_{ON} = association rate; k_{OFF} = dissociation rate; K_D = dissociation constant, calculated as k_{OFF}/k_{ON}. Values shown represent the mean ± SD of at least three independent experiments.

3.3 Conclusion

In conclusion, we showed here a novel assay with which we can characterize ternary complex formation of bifunctional small molecules, like PROTACs and molecular glues with the heliX® biosensor. The E3 ligase (e.g. VHL, CRBN) and target POI are immobilized on the end of the two

FRET pair color-coded arms of the Y-structure, allowing to study ternary complex formation in an induced proximity system. When the Y-structure closes upon PROTAC binding to both proteins, the subsequent ternary complex formation brings together the green donor and the red acceptor dye into a closer, FRET-sensitive, distance. Herein, we demonstrated how we can characterize kinetic rates and compound ranking in a high-throughput manner, gaining kinetic information on binary interaction and ternary complex formation of PROTACs binding simultaneously E3 ligases (VHL and CRBN) and BET proteins. At the best of our knowledge, this is the first time that the kinetics of ternary complex formation between CRBN and a POI were resolved on a biosensor surface.

3.4 Materials and Methods

3.4.1 Materials

PROTACs MZ1, ARV825 and PROTACs used in the screening (dBET6, ARV825, ZXH-3-26, dBET260, ARV771) were provided by S. Geschwindner and G. Dahl (AstraZeneca); PROTACs MZ1, MZ2, MZ4 were provided by C. Crowe and A. Ciulli (University of Dundee). Other PROTACs were commercially available: dBET1 (Tocris), cisMZ1, AT1, dBET6 and moieties (+)-JQ1, VH032, OTX015 and pomalidomide (MedChemExpress). E3 ligases VHL and CRBN, and target protein $Brd4^{BD2}$ were provided by AstraZeneca. Target proteins $Brd2^{BD1}$, $Brd2^{BD2}$, $Brd3^{BD1}$, $Brd3^{BD2}$, $Brd4^{BD1}$, $Brd4^{BD2}$, $BrdT^{BD1}$ and $BrdT^{BD2}$ used for BET bromodomain screening were provided by C. Crowe (University of Dundee). Y-structure DNA strands were designed by DBS (HK-YS-1, HK-YS-2, Dynamic Biosensors). PROTAC molecules and moieties were dissolved in DMSO at 10 mM final concentration and stored at -20°C or at -80°C, according to the provider instructions.

3.4.2 Protein expression and purification

All BET bromodomains ($Brd2^{BD1}$, $Brd2^{BD2}$, $Brd3^{BD1}$, $Brd3^{BD2}$, $Brd4^{BD1}$, $Brd4^{BD2}$, $BrdT^{BD1}$ and $BrdT^{BD2}$) were expressed in *E. coli* BL21 and purified according to established protocols. In short, single colonies of cDNA transformed into *E. coli* BL21(DE3) cells were grown overnight in lysogeny broth (LB) supplemented with antibiotics (50 μg mL^{-1} kanamycin) at 37°C with shaking. The overnight culture was diluted 1:100 in LB supplemented with antibiotics and grown to an optical density (OD600) of ~0.6. Protein expression was induced overnight at 18°C with 0.3 mM isopropyl β-d-1-thiogalactopyranoside (IPTG). The cells were harvested by centrifugation and frozen at -80°C as pellets until further purification. The bacterial pellets were resuspended in buffer and lysed by cell disruption. Cellular debris was removed by centrifugation. 6His-tagged proteins were purified on a HisTrapTM FF Ni NTA affinity column (Cytiva) and eluted with an imidazole concentration gradient. The protein was dialyzed into a low concentration imidazole buffer, incubated with TEV protease, and flowed through a HisTrap FF Ni NTA affinity column. The proteins were finally purified by size exclusion

chromatography on a HiLoadTM 16/600 SuperdexTM 75 pg column (Cytiva) in 20 mM HEPES, pH 7.5, 150 mM sodium chloride and 0.5 mM TCEP, concentrated, flash frozen with liquid nitrogen and stored at -80°C.

For expression of VHL in complex with Elongin B and Elongin C (VCB), N-terminally His6-TEV-tagged VHL (54–213), ElonginC (17–112) and ElonginB (1–104) were all co-expressed in *E. coli* BL21 star (DE3) using auto-induction. Cells were first grown 8 h at 37°C and then another 24 h at 18°C before being harvested at 6000 rpm for 10 min and stored at -80°C. Pellet was resuspended in Lysis buffer (50 mM HEPES pH 7.9, 300 mM NaCl, 5 mM Tris(2-carboxyethyl) phosphine hydrochloride (TCEP), 20 mM Imidazole, 10% Glycerol, 1x Complete EDTA-free protease inhibitors (Roche) and benzonase nuclease (5 U/ml, Sigma). Lysate was clarified using centrifugation at 15000 rpm for 2 h. The clarified supernatant was incubated with 30 mL of Talon Supeflow resin (Clontech) overnight whilst rotating. The resin was then collected in an econocolumn (BioRad) and washed with 300 mL of Equilibration Buffer (50 mM HEPES pH 7.9, 300 mM NaCl, 20 mM imidazole,1 mM TCEP) and then eluted with 8 x 20 mL of Elution Buffer (50 mM HEPES pH 7.9, 300 mM NaCl, 300 mM imidazole, 1 mM TCEP). Eluted protein was pooled and, 2 mM TEV protease was added, and the sample was dialyzed overnight in Dialysis buffer (50 mM HEPES pH 7.4, 100 mM NaCl,1 mM TCEP). The dialyzed sample treated with TEV protease was passed through 4 ml of Talon resin and the flow through was collected. The resin was washed with 5 mL dialysis buffer. Eluted TEV-cleaved protein was loaded onto a 120 mL S75 column that had been equilibrated in Dialysis Buffer and peak fractions were collected, pooled, and concentrated 10k MWCO membrane before being snap frozen in liquid nitrogen and stored at -80°C.

Sequence for single-chain (sc) CRBN-DDB1 is (Cereblon(40-442)-GGGSGGGSGGSGGG-DDB1-([(1-395_GNGNSG_706-1140)Δ396-705])). The BPB domain of DDB1 (396-705) is replaced by the GNGNSG-linker, resulting in a construct similar to the one used in Nowak *et al.* [21]. This gene was cloned into a pFastBac1 and bacmid DNA was produced in *E. coli* DH10 Bac cells. Recombinant baculoviruses were generated in Sf21 cells (Thermofisher) and protein expression was conducted at 27°C for 48 h. Cells were harvested by centrifugation using 6500 rpm, 15 min at 4°C. The pellet was resuspended in lysis buffer (40 mM HEPES pH 8.0, 500 mM NaCl, 1 mM TCEP, 5% glycerol, 20 mM imidazole EDTA-free protease inhibitors (Roche) and benzonase nuclease (5 U/mL, Sigma)), frozen in -80°C overnight and then thawed before being centrifuged at 24000 rpm for 1 h at 10°C. Lysate was incubated overnight with 15 mL equilibrated Ni-NTA beads (QIAGEN) at 4°C. Beads were washed twice with 50 mL Wash buffer (40 mM HEPES pH 8.0, 500 mM NaCl, 1 mM TCEP, 5% glycerol, 20 mM imidazole) before elution using 6 x 7.5ml Elution buffer (40 mM HEPES pH8.0, 500 mM NaCl, 1 mM TCEP, 5% glycerol, 500 mM imidazole). TEV protease was added to the eluted protein and the sample was dialyzed overnight into Dialysis buffer (40 mM HEPES pH7.5, 500 mM NaCl, 1 mM TCEP, 5% glycerol, 20 mM imidazole). Dialyzed sample was passed through 12 mL washed Ni-NTA beads which were then washed twice with 14 mL Dialysis buffer and eluted using 2 x 7mL Elution buffer. Flow-through and the first wash fraction were collected. Buffer was exchanged to a Low salt buffer (40 mM HEPES pH 7.4, 150 mM NaCl, 5% glycerol, 1 mM TCEP) using HiPrep 26/10 Desalting

column before being loaded on a MonoQ HP ion exchange column preequilibrated with Buffer A (40 mM HEPES pH7.4, 150mM NaCl, 5% glycerol, 1 mM TCEP). Wash and elution were conducting by stepwise gradient from Buffer A to Buffer B ((40 mM HEPES pH7.4, 1 M NaCl, 5% glycerol, 1 mM TCEP). The eluate from the ion exchange step was loaded on a HiLoad 26/600 Superdex 200 column preequilibrated with SEC buffer (40 mM HEPES pH7.4, 200 mM NaCl, 0.5 mM TCEP), collecting 1.2mL fractions. Sample was concentrated using 100k MWCO centricon, spinning at 4000 rpm, 4°C, mixing the sample regularly, before being snap frozen in liquid nitrogen and stored at -80°C.

3.4.3 Conjugation of proteins to DNA

VHL and CRBN ligases were covalently coupled via their primary amines to the 5' end of ssDNA (cNL-A48) (coupling kit HK-NHS-1, Dynamic Biosensors), and Brd proteins to the 3' end of ssDNA (cNL-B48) (coupling kit HK-NHS-4, Dynamic Biosensors). The protein-DNA conjugate was purified from the free protein and free DNA using the proFIRE® system (Dynamic Biosensors) [22,23]. The embedded Data Viewer software provides protein-DNA conjugate purity and concentration based on the chromatogram. After liquid nitrogen freezing, the conjugates were stored at a concentration of 10 µM in HE40 buffer (10 mM HEPES, 40 mM NaCl, 0.05 % Tween20, 50 µM EDTA, 50 µM EGTA) at −80°C and were freshly thawed before each experiment.

3.4.4 Chip surface functionalization

All switchSENSE® experiments were performed on a dual-color heliX^{+} instrument using a standard heliX Adapter Biochip (ADP-48-2-0, Dynamic Biosensors), in which single-stranded DNA (anchor strands) are covalently attached to the chip surface. Each chip is equipped with 2 gold electrodes (or spots), with different DNA anchor strands. Herein, we used spot 1 as a measurement spot, with the Y-structure harboring the E3 ligase (VHL or CRBN) and the Brd target protein, and spot 2 as real time referencing spot, with the Y-structure carrying only Brd target protein, in order to gain at the same time information about binary and ternary complex formation (See Figure 1B). For spot 1, the Y-structure-red and -green DNA strands were premixed with the conjugated Brd protein and E3 ligase, whereas for spot 2 they were premixed with conjugated Brd protein and the complementary DNA strand of the red arm. The Y-structure constructs were then let at 25°C for 3 h on a shaker at 600 rpm. Secondly, the Y-structure constructs were immobilized on the biochip via hybridization of complementary anchor strand. The chip was regenerated and freshly functionalized only before the first concentration of a measurement series. For chip regeneration, a high-pH regeneration solution (HK-REG-1, Dynamic Biosensors) was used to denature the double stranded DNA nanolevers, disrupting the hydrogen bonds between base pairs: the Y-structure constructs are washed away while the covalently attached single-stranded nanolevers remain on the surface and can be reused for a new functionalization step.

3.4.5 Fluorescence Proximity Sensing (FPS) mode - FRET Kinetics

Interaction analysis was performed in fluorescence proximity sensing (FPS) mode with a constant voltage of -0.2 V applied, which forces the surface-tethered DNA Y-structure into a fixed angle. In the FPS measurements, the series of PROTACs were injected at specified concentrations over the two electrodes of the biochip. When the PROTACs reach the Y-structure on spot 1 (carrying the target protein Brd and CRBN or VHL E3 ligase), a decrease in green fluorescence signal can be measured, and a simultaneous increase in the red fluorescence signal due to FRET from the donor green dye to the acceptor red dye in proximity is indication of ternary complex formation. When the PROTACs reach the Y-structure on spot 2 (carrying only the target protein Brd), a quenching of the green signal can be observed. The fluorescence signal changes occur on the timescale of seconds, and the time dependence of the fluorescence signal directly reflects the PROTAC-protein kinetics. Upon the injection of running buffer, PROTACs dissociate and a restoration of the original fluorescence signals can be observed. The sample tray containing the Y-structure constructs and PROTACs samples was set to 15°C during measurements, while the experiment temperature on the biochip was set to 25°C. PROTACs analytes were diluted and measured in HE140 buffer (10 mM HEPES pH 7.4, 140 mM NaCl, 0.05 % Tween20, 50 µM EDTA, 50 µM EGTA). No buffer correction for DMSO is required. Flow rate for association and dissociation reactions was set to 500 µL/min. The green LED power was set to 4. Experiment design, workflow and data analysis were performed with the heliOS software (Dynamic Biosensors). The association and dissociation rates (k_{ON} and k_{OFF}), dissociation constants (K_D) and the respective error values were derived from a global single exponential fit model, upon blank referencing correction.

3.5 Supplementary Information

Figure S1. Different Y-structure designs and Zipper experiment.

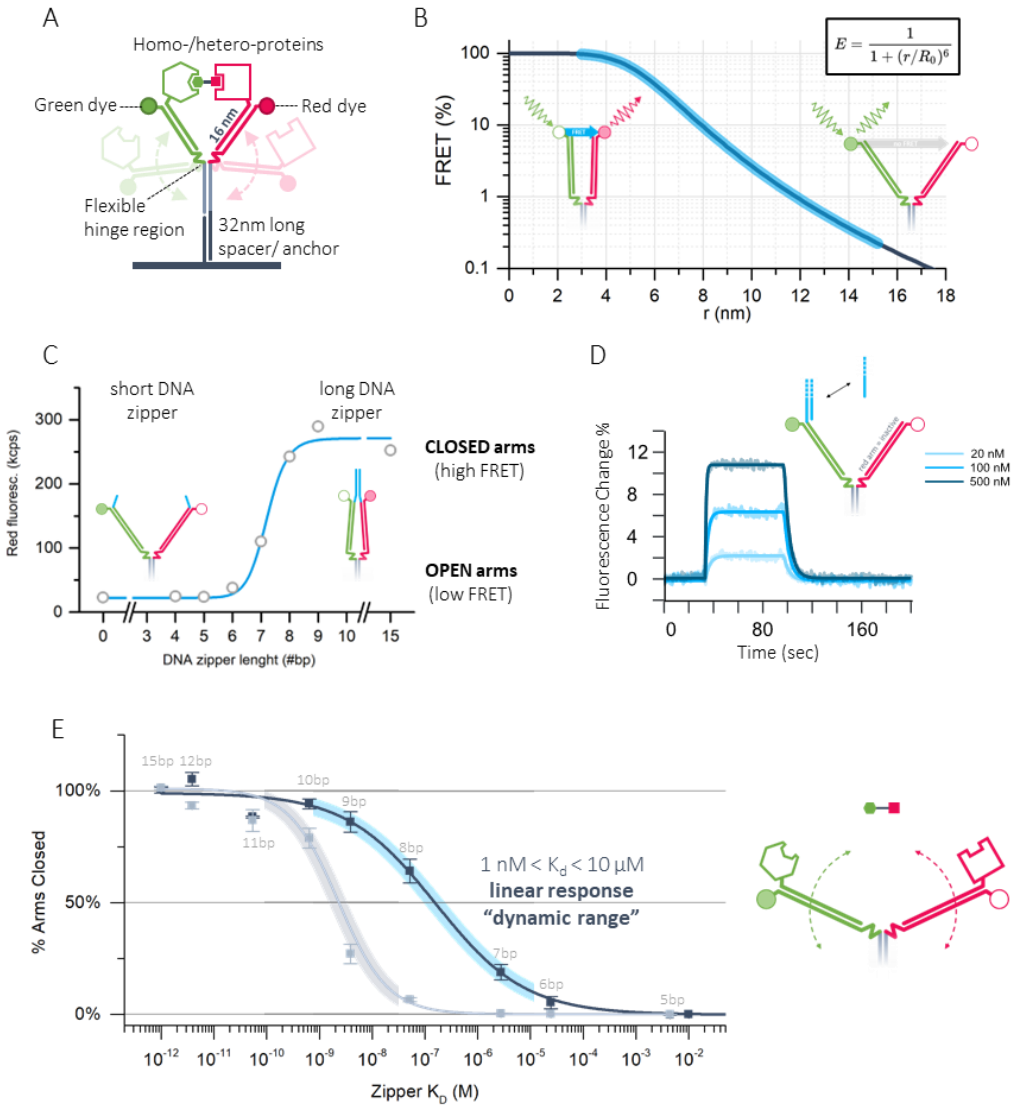

Figure S1. *The DNA Y-structure and its dynamic range characterization. A) DNA Y-structure design. The (homo- or hetero-) target proteins can be functionalized on the end of the two FRET pair color-coded Y-arms of the structure, where a green and a red dye are located, which allow FRET and classic fluorescence proximity sensing measurement modes. In addition the presence of a long spacer (32nm) allows a quasi-native solution environment and the flexible hinge region allows an unrestricted movement of the arms. B) Fluorescence Resonance Energy Transfer (FRET) efficiency curve. From a simple simulation study we can assess that the heliX® biosensor has a FRET sensitivity equal up to 15 nm dye-distance. C) The DNA zipper study. DNA zippers of increasing length were used to characterize the Y-structure: short and weak DNA zippers (4-6 bp) cannot close completely the Y-structure leading to a no or low FRET, medium length zippers (7-10 bp) lead to a partial closure of the Y-structure (dynamic range), whereas longer and strong zippers (12-15 bp) can close completely the Y-structure, leading to high FRET. D) Kinetic characterization of the DNA zipper. For each DNA zipper we characterized the simple 1:1 binding affinity; herein, an example of 8bp-8bp kinetic. E) Linear response "dynamic range" of the Y-structure. FRET efficiency has been plotted against the zipper binding affinities (K_Ds of DNA zippers), in order to characterize the dynamic range of the standard Y-structure (blue line), which shows a dynamic and active range between 1nM and 10µM. This structure has been used for characterizing AT1 ternary complex formation (with an expected K_D of 20 nM) and the*

whole CRBN study-BET protein study. A new alternative Y-structure design (grey line) has been also developed for studying system with an expected K_D in the pM and low nM range, such as MZ1, to limit the rebinding effect of the ternary complex formation (Figure S2A).

Figure S2A-B. MZ1 binary and ternary interactions. AT1 ternary interaction – *hook effect*.

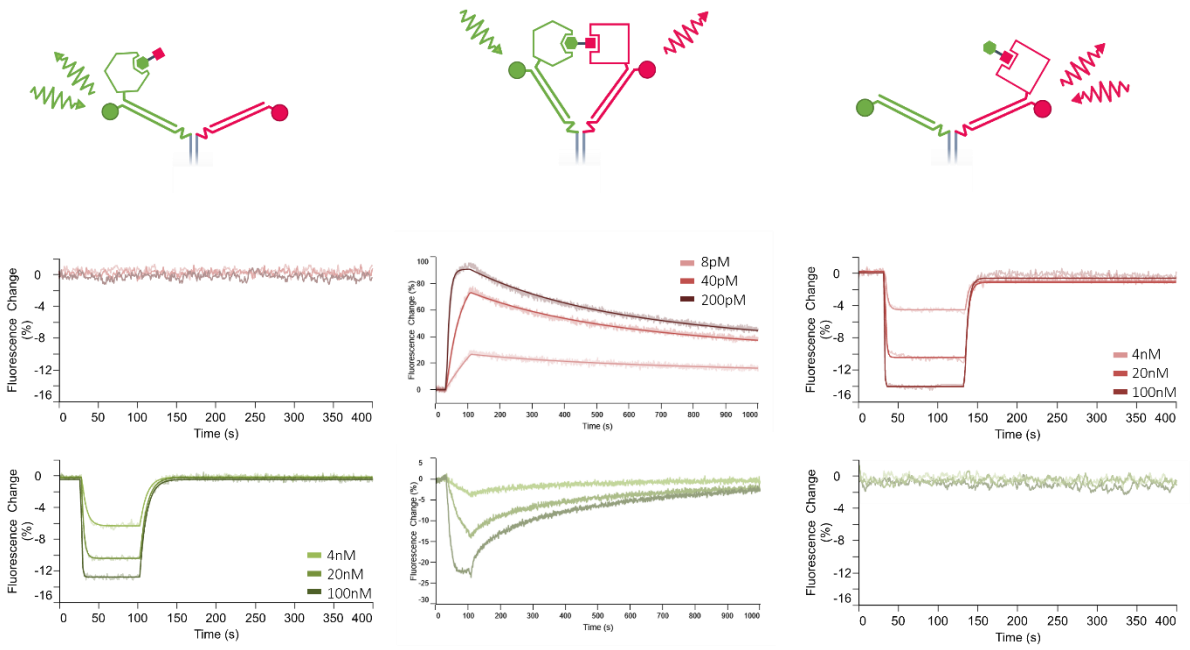

Figure S2A. *MZ1 binary and ternary interactions. The E3 ligase VHL was immobilized on the red arm of the Y-structure, and the target protein of interest Brd4^{BD2} was immobilized on the green arm. To characterize the PROTAC affinity toward the single proteins involved in the ternary complex, a single protein was immobilized on the arms of the Y-structure, allowing therefore to detect the binary interaction (left and right figures). For the binary interaction, the PROTAC concentration range injected was from 4 nM to 100 nM. To study the ternary interaction, both proteins were immobilized at the same time on the two arms. Upon MZ1 injection, the simultaneous binding to VHL and Brd4^{BD2} leads to an induced proximity of the two Y-structure arms carrying the red and green dyes, generating FRET (middle figure). Increasing concentrations of MZ1 (from 8 pM to 200 pM) were injected on the surface with the Y-structure carrying VHL and Brd4^{BD2} on the two arms. The resulting k_{ON}, k_{OFF} and K_D of binary and ternary interactions are listed in Table below.*

Table S5. MZ1 binary and ternary interaction rates

	k_{ON} ($M^{-1}s^{-1}$)	**k_{OFF} (s^{-1})**	***K_D* (M)**
Binary Brd4^{BD2}	11.4 ± 0.7 E+6	112 ± 16.3 E-3	9.78 ± 0.9 E-9
Binary VHL	3.61 ± 0.75 E+6	66.1 ± 17.1 E-3	18.3 ± 0.9 E-9
Ternary (VHL)	24.2 ± 4 E+6	(k_{OFF1}) 1.48 ± 0.9 E-3; (k_{OFF2}) 0.27 ± 0.1 E-3	(K_{D1}) 61.2 ± 1.6 E-12 (K_{D2}) 11.3 ± 1.1 E-12

Values shown represent the mean ± SD of at least three independent experiments.

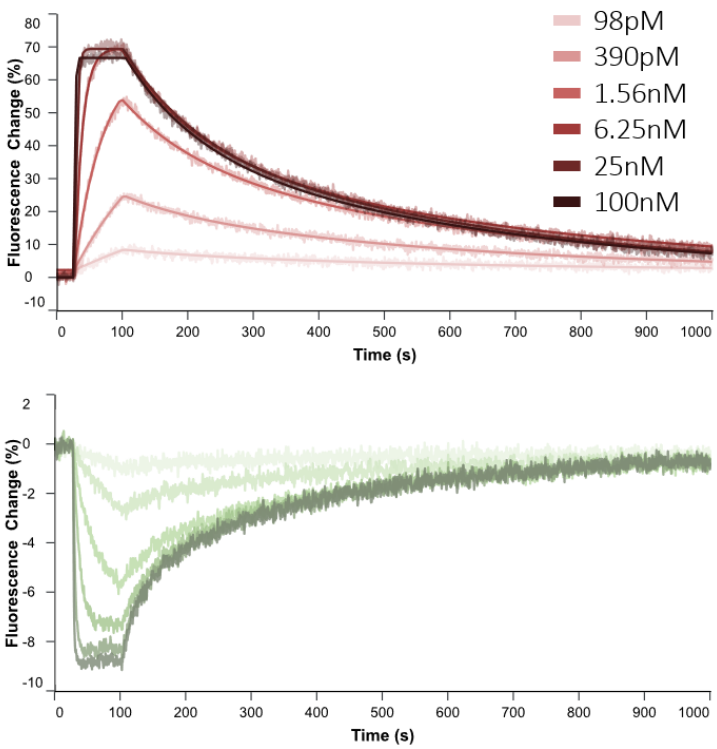

***Figure S2B**. AT1 ternary interaction – Hook effect. High concentrations of AT1 binding simultaneously to VHL and Brd4^{BD2} lead to a lower fluorescence change in red signal, because of an oversaturation of the Y-structure, where the binary binding of AT1 with each partner is favored in spite of the ternary interaction. Therefore, we observe the opening of the arms of the Y-structure, that results in a decrease of red FRET signal.*

Figure S3. PROTACs HTS | E2.

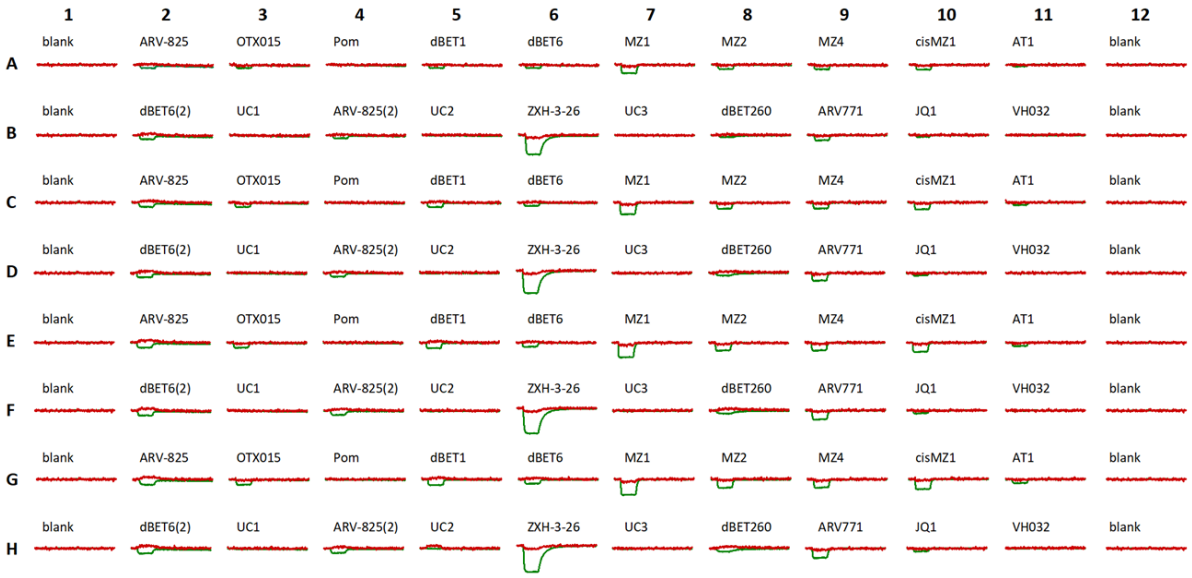

Figure S3. *PROTAC screening (spot 2). In spot 2, where the Y-structure carrying only Brd4^{BD2} is immobilized, no red FRET signals resulting from ternary interactions are observable. The presence of a second spot on the same chip provides a real time referencing and also a validation for each PROTAC-Brd4^{BD2} binary interactions observed in Spot 1. Binary binding to Brd4^{BD2} in Spot 2 is observable for the following PROTACs: ARV-825, OTX015, dBET1, dBET6, MZ1, MZ2, MZ4, cisMZ1, AT1, dBET6(2), ARV-825(2), ZXH-3-26, dBET260, ARV771, and JQ1.*

Figure S4(A-O). PROTACs HTS: single Kinetics.

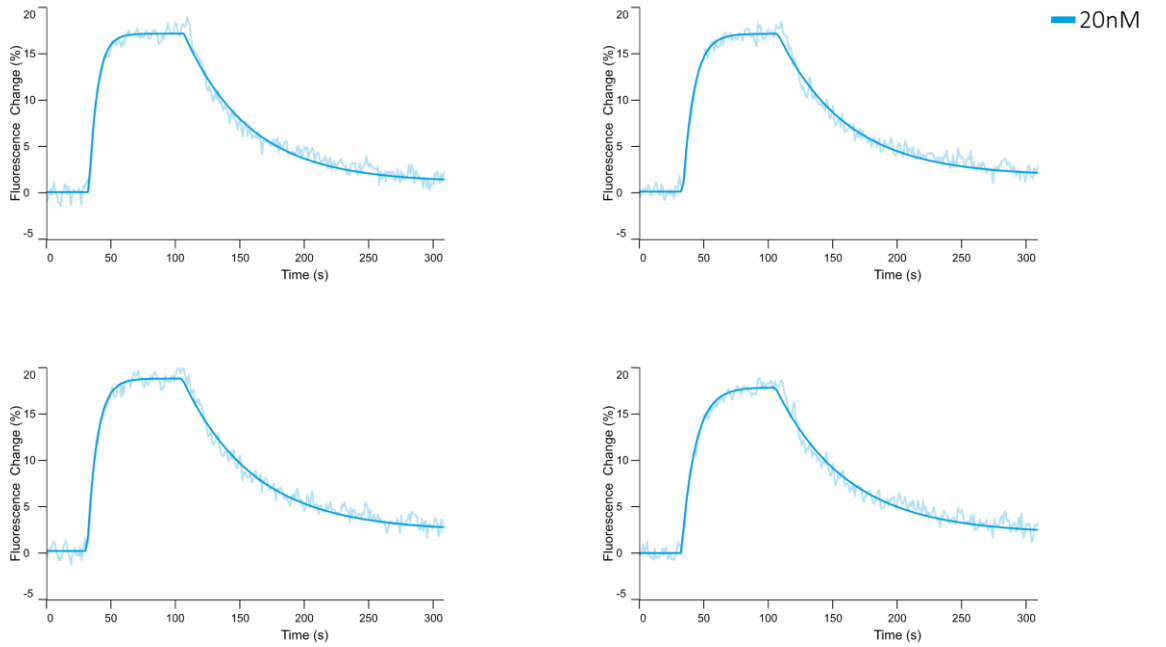

***Figure S4A**. PROTACs high-throughput screening: ARV-825 20 nM kinetics.*

Table S2A. Kinetic binding rates of ARV-825 resulting from the screening.

k_{ON} ($M^{-1}s^{-1}$)	k_{OFF} (s^{-1})	K_D (M)
6.81 ± 0.51 E+6	19.6 ± 0.6 E-3	2.88 ± 0.23 E-9
4.90 ± 0.35 E+6	18.8 ± 0.6 E-3	3.85 ± 0.30 E-9
5.78 ± 0.41 E+6	18.1 ± 0.6 E-3	3.13 ± 0.24 E-9
3.81 ± 0.28 E+6	17.9 ± 0.6 E-3	4.71 ± 0.38 E-9

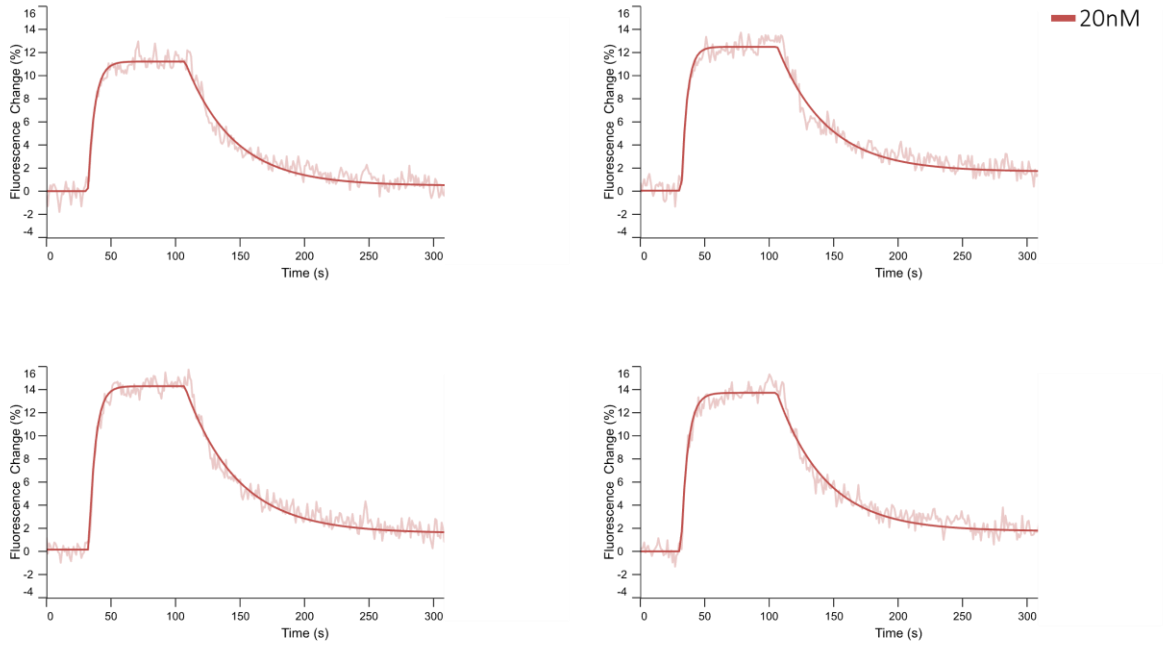

***Figure S4B**. PROTACs high-throughput screening: dBET1 20 nM kinetics.*

Table S2B. Kinetic binding rates of dBET1 resulting from the screening.

k_{ON} ($M^{-1}s^{-1}$)	k_{OFF} (s^{-1})	K_D (M)
8.30 ± 1.12 E+6	26.5 ± 1.2 E-3	3.20 ± 0.45 E-9
8.85 ± 0.88 E+6	24.8 ± 1.0 E-3	2.80 ± 0.30 E-9
10.0 ± 1.14 E+6	26.1 ± 1.2 E-3	2.61 ± 0.32 E-9
8.33 ± 0.91 E+6	26.5 ± 1.1 E-3	3.18 ± 0.37 E-9

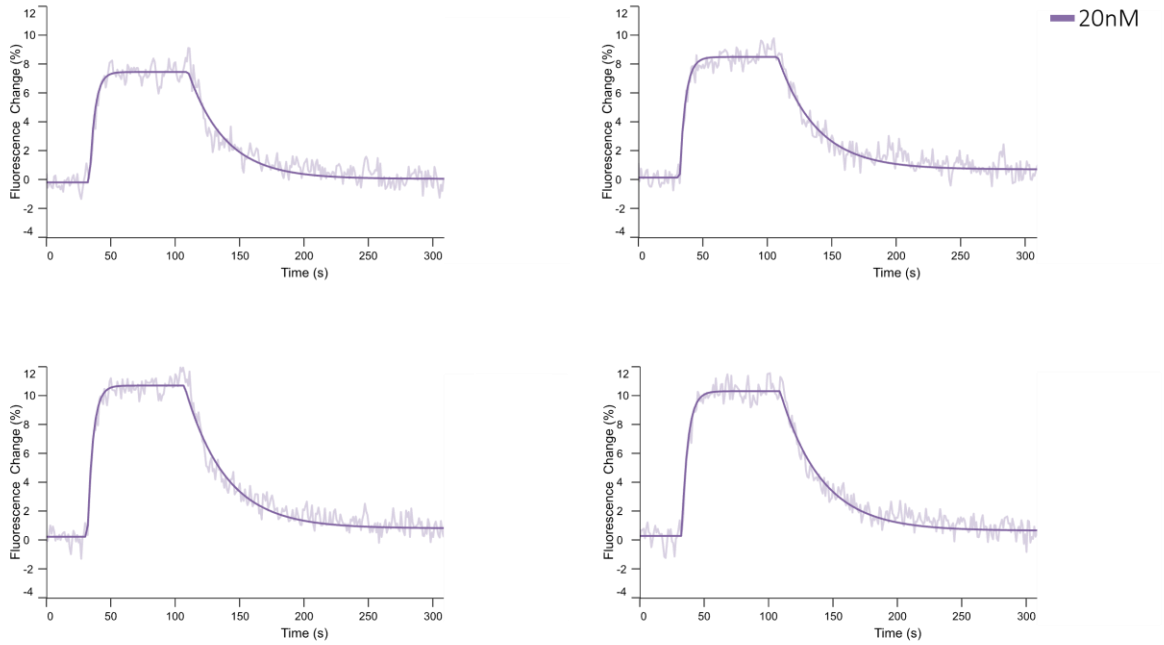

Figure S4C. *PROTACs high-throughput screening: dBET6 20 nM kinetics.*

Table S2C. Kinetic binding rates of dBET6 resulting from the screening.

k_{ON} ($M^{-1}s^{-1}$)	k_{OFF} (s^{-1})	K_D (M)
10.4 ± 2.0 E+6	34.7 ± 2.3 E-3	3.34 ± 0.69 E-9
10.3 ± 1.3 E+6	31.5 ± 1.6 E-3	3.08 ± 0.42 E-9
9.59 ± 1.79 E+6	33.1 ± 2.0 E-3	3.45 ± 0.68 E-9
9.30 ± 1.30 E+6	31.0 ± 1.6 E-3	3.34 ± 0.50 E-9

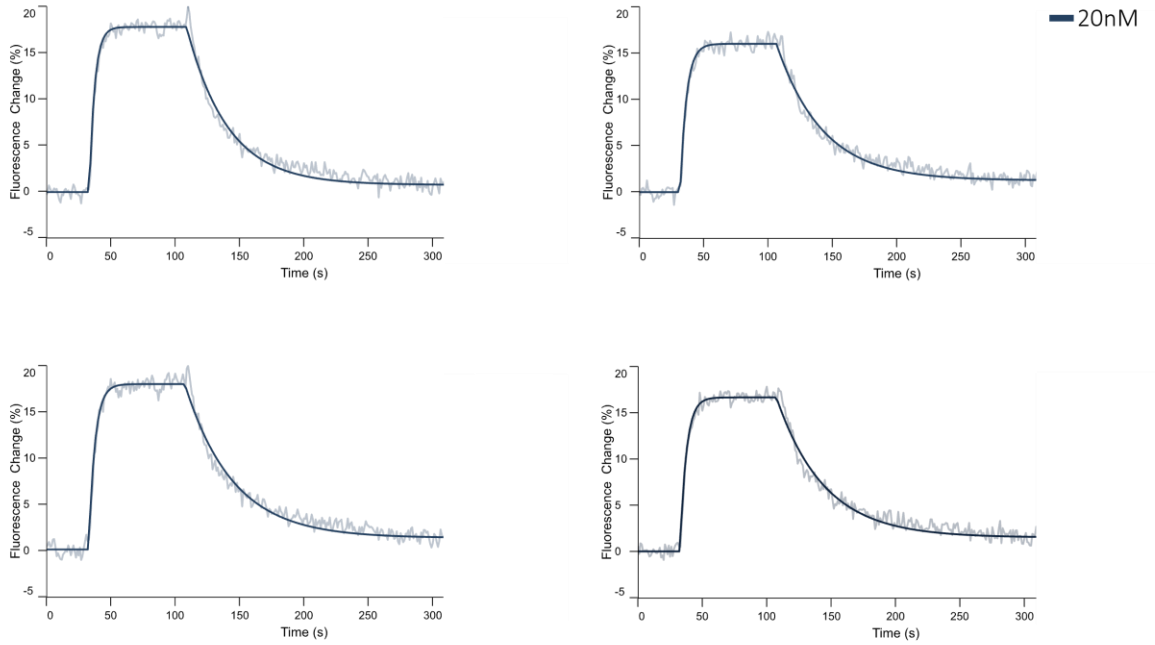

Figure S4D. *PROTACs high-throughput screening: dBET6(2) 20 nM kinetics.*

Table S2D. Kinetic binding rates of dBET6(2) resulting from the screening.

k_{ON} ($M^{-1}s^{-1}$)	k_{OFF} (s^{-1})	K_D (M)
10.7 ± 1.0 E+6	31.3 ± 1.0 E-3	2.92 ± 0.29 E-9
9.22 ± 0.70 E+6	26.7 ± 0.8 E-3	2.89 ± 0.24 E-9
9.01 ± 0.79 E+6	27.8 ± 1.0 E-3	3.09 ± 0.29 E-9
9.12 ± 0.75 E+6	26.9 ± 0.9 E-3	2.95 ± 0.26 E-9

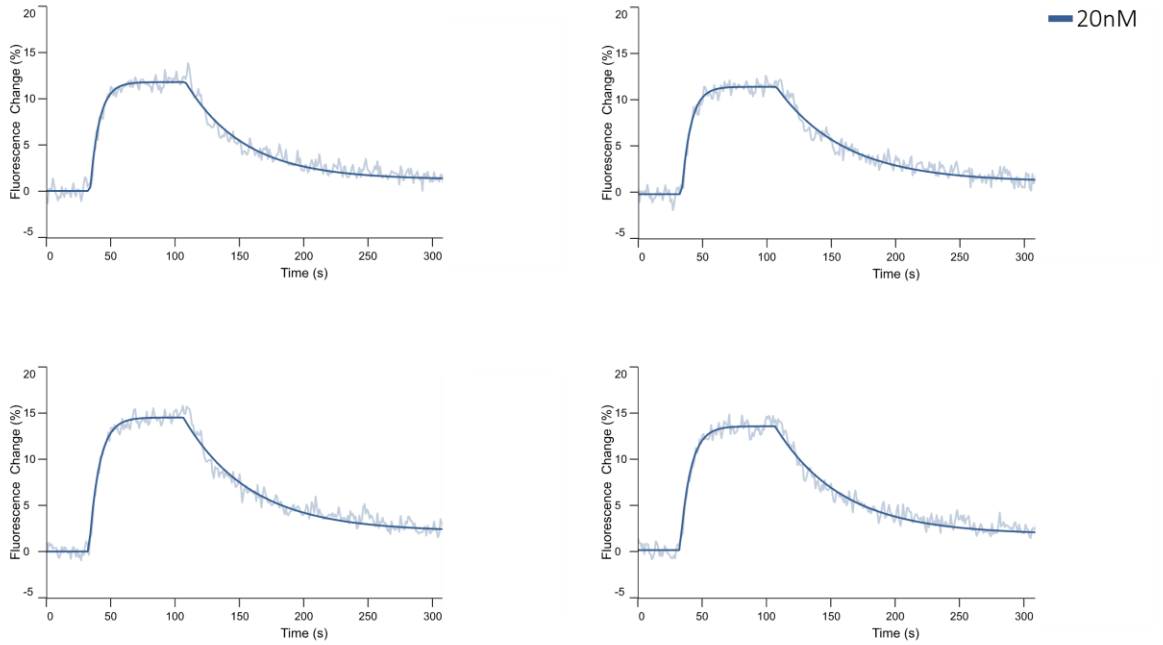

Figure S4E. *PROTACs high-throughput screening: ARV825(2) 20nM kinetics.*

Table S2E. Kinetic binding rates of ARV825(2) resulting from the screening.

k_{ON} ($M^{-1}s^{-1}$)	k_{OFF} (s^{-1})	K_D (M)
5.91 ± 0.57 E+6	21.9 ± 0.9 E-3	3.70 ± 0.39 E-9
5.40 ± 0.47 E+6	19.2 ± 0.7 E-3	3.56 ± 0.34 E-9
6.17 ± 0.62 E+6	19.0 ± 0.8 E-3	3.07 ± 0.34 E-9
5.28 ± 0.49 E+6	19.3 ± 0.8 E-3	3.65 ± 0.37 E-9

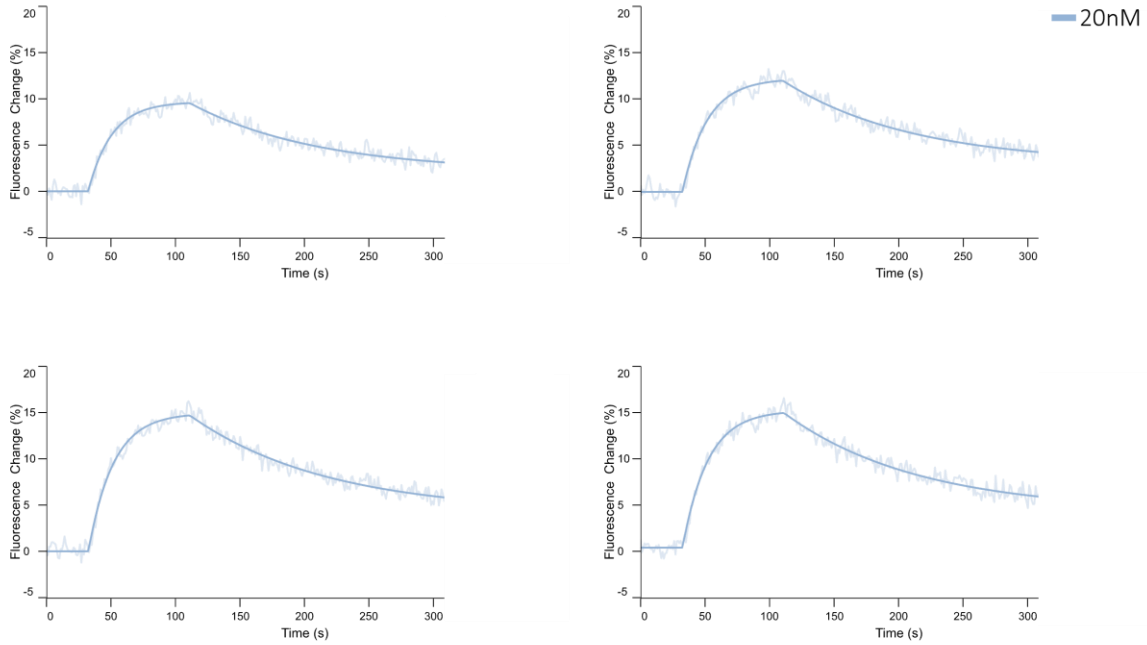

***Figure S4F**. PROTACs high-throughput screening: dBET260 20 nM kinetics.*

Table S2F. Kinetic binding rates of dBET260 resulting from the screening.

k_{ON} ($M^{-1}s^{-1}$)	k_{OFF} (s^{-1})	K_D (M)
2.22 ± 0.28 E+6	10.1 ± 0.8 E-3	4.55 ± 0.66 E-9
2.13 ± 0.17 E+6	9.42 ± 0.54 E-3	4.42 ± 0.43 E-9
2.09 ± 0.22 E+6	10.0 ± 0.7 E-3	4.80 ± 0.60 E-9
2.08 ± 0.18 E+6	9.66 ± 0.56 E-3	4.64 ± 0.47 E-9

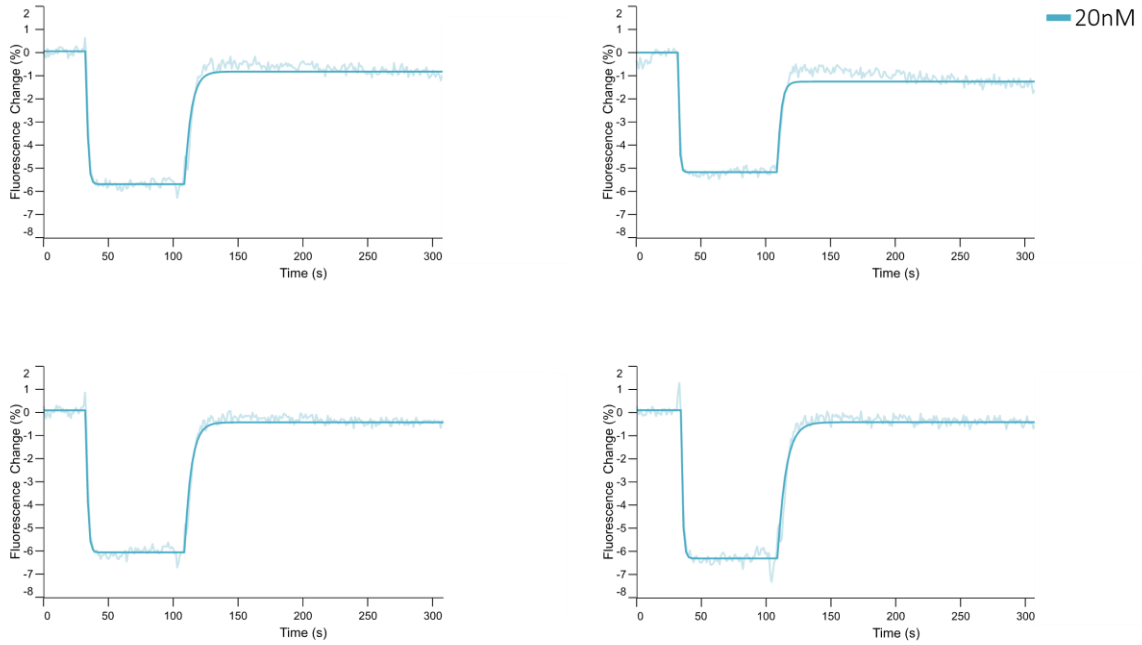

Figure S4G. *PROTACs high-throughput screening: OTX015 20 nM kinetics.*

Table S2G. Kinetic binding rates of OTX015 resulting from the screening.

k_{ON} ($M^{-1}s^{-1}$)	k_{OFF} (s^{-1})	K_D (M)
28.4 ± 4.8 E+6	205 ± 16 E-3	7.22 ± 1.34 E-9
28.0 ± 3.8 E+6	199 ± 12 E-3	7.12 ± 1.05 E-9
34.5 ± 18.2 E+6	369 ± 54 E-3	10.7 ± 5.9 E-9
31.1 ± 7.3 E+6	162 ± 9 E-3	5.19 ± 1.26 E-9

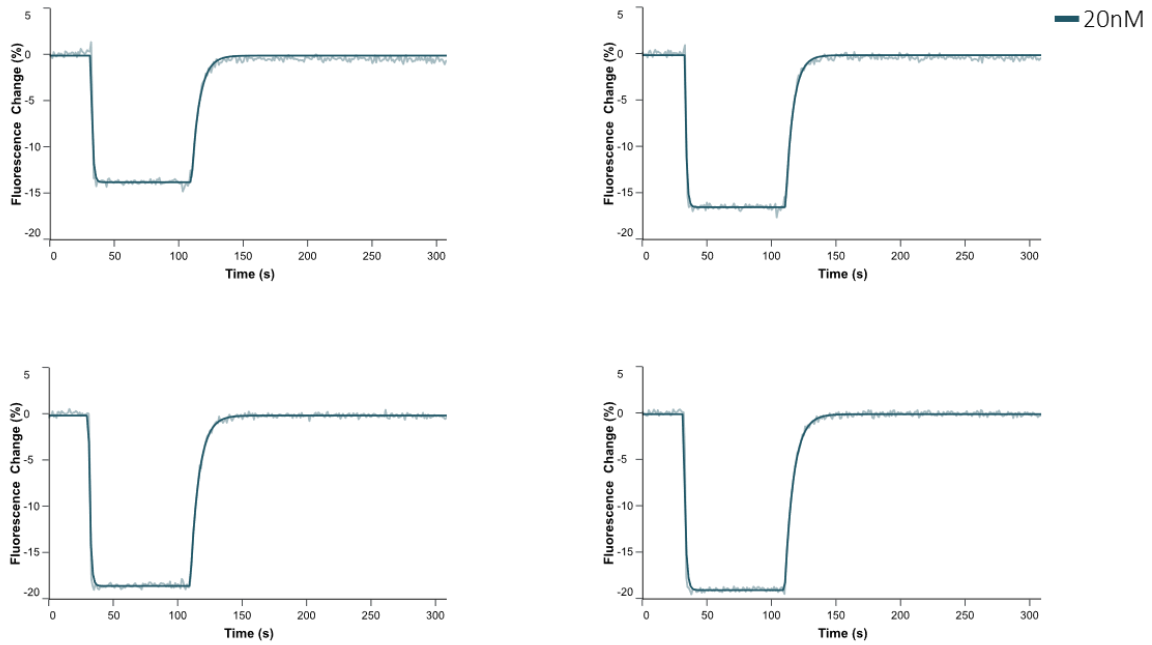

***Figure S4H**. PROTACs high-throughput screening: MZ1 20 nM kinetics.*

Table S2H. Kinetic binding rates of MZ1 resulting from the screening.

k_{ON} ($M^{-1}s^{-1}$)	k_{OFF} (s^{-1})	K_D (M)
34.2 ± 3.0 E+6	162 ± 7 E-3	4.75 ± 0.46 E-9
35.5 ± 2.1 E+6	175 ± 5 E-3	4.94 ± 0.32 E-9
34.6 ± 1.4 E+6	152 ± 3 E-3	4.38 ± 0.20 E-9
27.4 ± 1.3 E+6	148 ± 4 E-3	5.38 ± 0.29 E-9

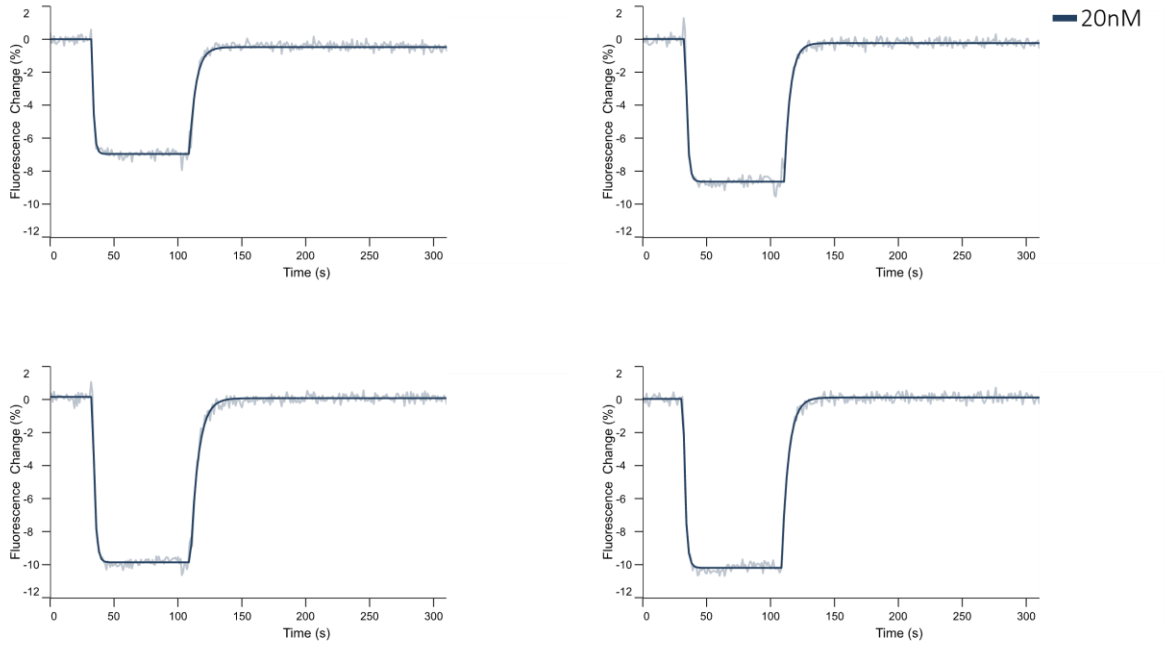

Figure S4I*. PROTACs high-throughput screening: MZ2 20 nM kinetics.*

Table S2I. Kinetic binding rates of MZ2 resulting from the screening.

k_{ON} ($M^{-1}s^{-1}$)	k_{OFF} (s^{-1})	K_D (M)
24.7 ± 3.0 E+6	202 ± 9 E-3	8.17 ± 1.06 E-9
20.1 ± 1.9 E+6	167 ± 5 E-3	8.30 ± 0.81 E-9
18.7 ± 2.1 E+6	218 ± 8 E-3	11.6 ± 1.4 E-9
18.1 ± 1.3 E+6	189 ± 5 E-3	10.5 ± 0.8 E-9

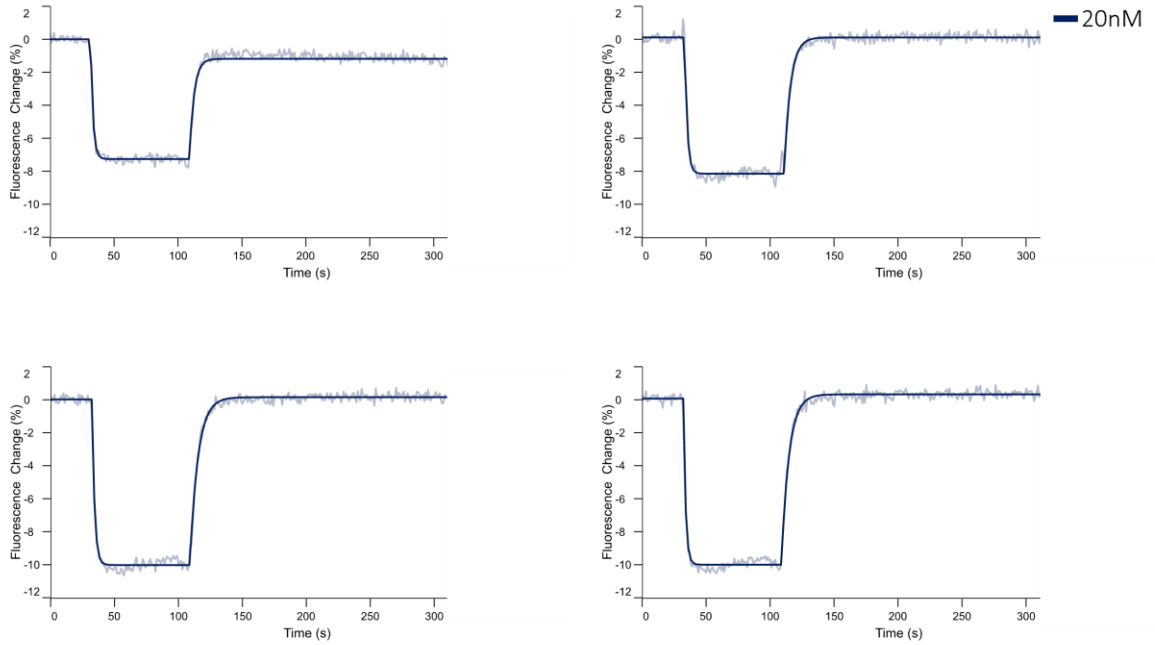

***Figure S4J**. PROTACs high-throughput screening: MZ4 20 nM kinetics.*

Table S2J. Kinetic binding rates of MZ4 resulting from the screening.

k_{ON} ($M^{-1}s^{-1}$)	k_{OFF} (s^{-1})	K_D (M)
13.4 ± 2.5 E+6	287 ± 19 E-3	21.5 ± 4.2 E-9
17.8 ± 1.5 E+6	160 ± 4 E-3	9.04 ± 0.82 E-9
16.3 ± 2.1 E+6	209 ± 8 E-3	12.8 ± 1.7 E-9
21.0 ± 2.1 E+6	172 ± 5 E-3	8.19 ± 0.86 E-9

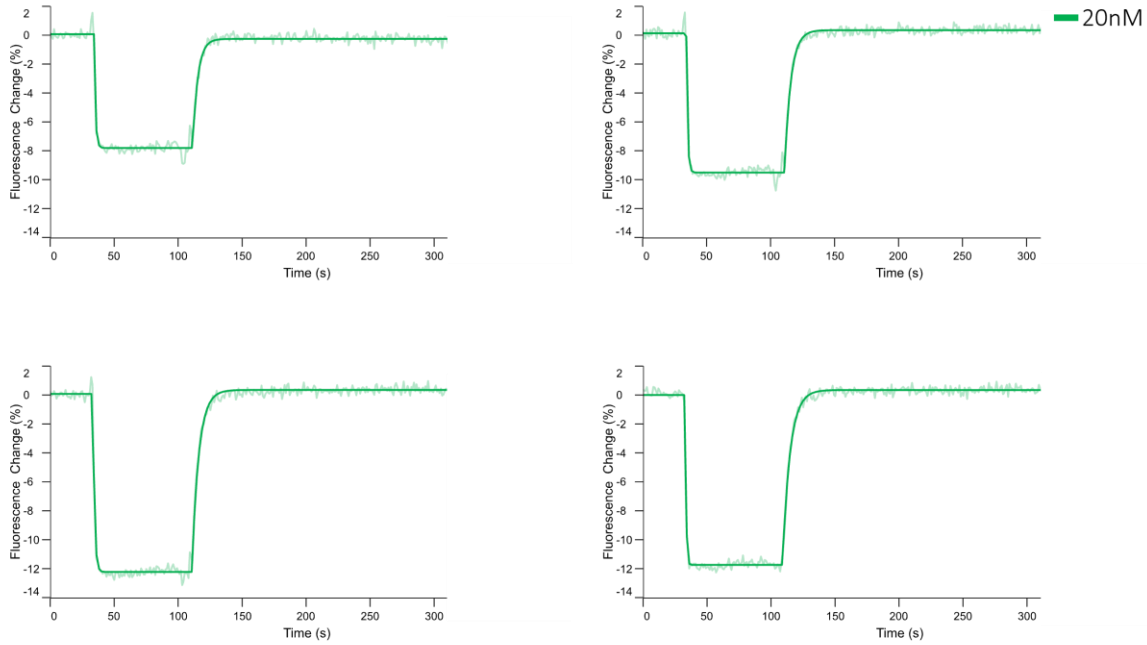

***Figure S4K**. PROTACs high-throughput screening: cisMZ1 20 nM kinetics.*

Table S2K. Kinetic binding rates of cisMZ1 resulting from the screening.

k_{ON} ($M^{-1}s^{-1}$)	k_{OFF} (s^{-1})	K_D (M)
37.1 ± 10.4 E+6	220 ± 12 E-3	5.92 ± 1.70 E-9
41.5 ± 4.7 E+6	174 ± 4 E-3	4.20 ± 0.48 E-9
32.2 ± 2.9 E+6	210 ± 7 E-3	6.53 ± 0.64 E-9
32.8 ± 3.4 E+6	191 ± 5 E-3	5.84 ± 0.63 E-9

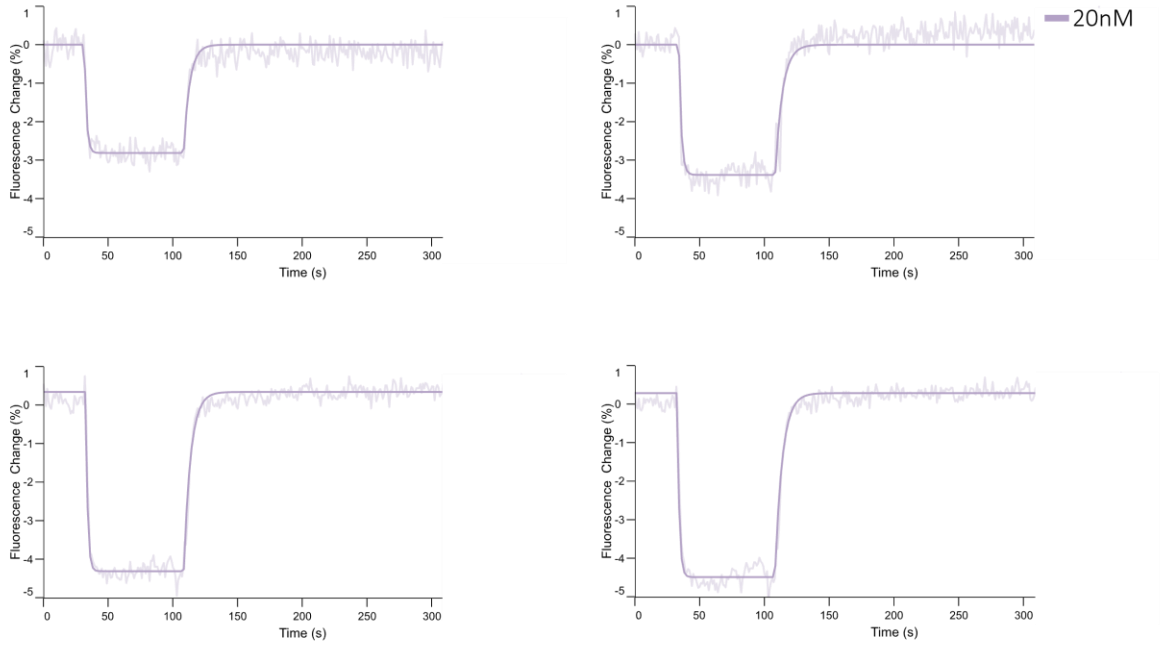

***Figure S4L**. PROTACs high-throughput screening: AT1 20 nM kinetics.*

Table S2L. Kinetic binding rates of AT1 resulting from the screening.

k_{ON} ($M^{-1}s^{-1}$)	k_{OFF} (s^{-1})	K_D (M)
21.1 ± 7.5 E+6	218 ± 32 E-3	10.3 ± 4.0 E-9
26.8 ± 4.9 E+6	192 ± 14 E-3	7.15 ± 1.41 E-9
18.4 ± 5.6 E+6	182 ± 26 E-3	9.88 ± 3.31 E-9
24.7 ± 4.2 E+6	180 ± 13 E-3	7.30 ± 1.36 E-9

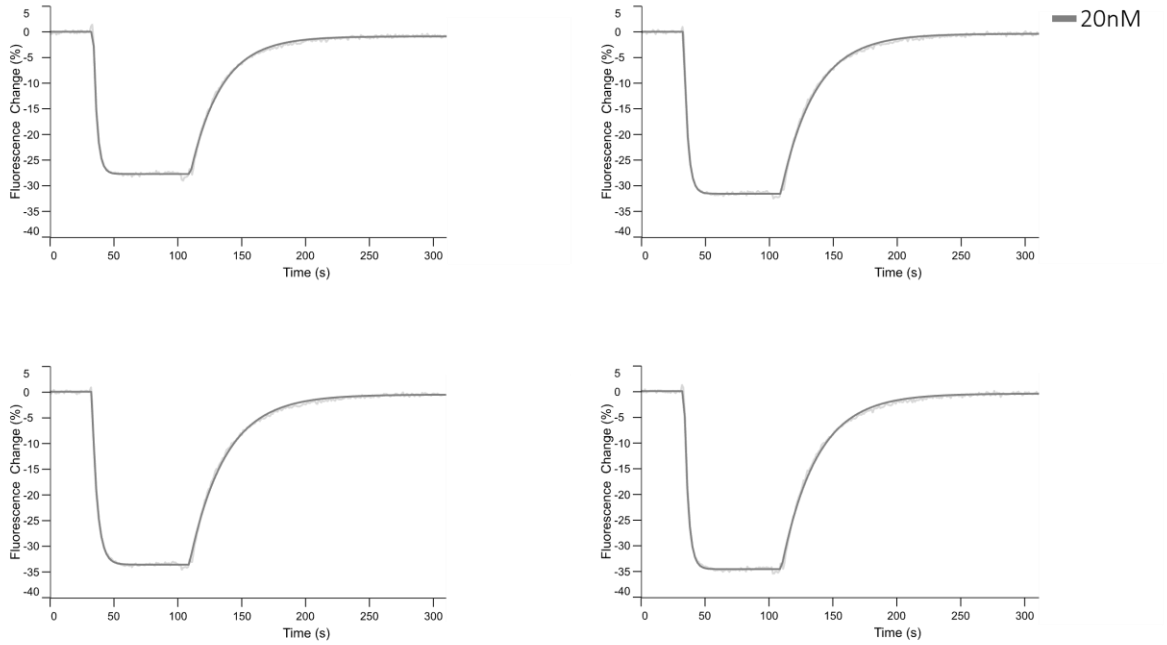

***Figure S4M**. PROTACs high-throughput screening: ZXH-3-26 20 nM kinetics.*

Table S2M. Kinetic binding rates of ZXH-3-26 resulting from the screening.

k_{ON} ($M^{-1}s^{-1}$)	k_{OFF} (s^{-1})	K_D (M)
15.4 ± 0.3 E+6	41.2 ± 0.3 E-3	2.68 ± 0.06 E-9
10.4 ± 0.2 E+6	35.6 ± 0.2 E-3	3.42 ± 0.07 E-9
14.5 ± 0.3 E+6	37.6 ± 0.3 E-3	2.60 ± 0.05 E-9
14.1 ± 0.3 E+6	36.1 ± 0.3 E-3	2.56 ± 0.06 E-9

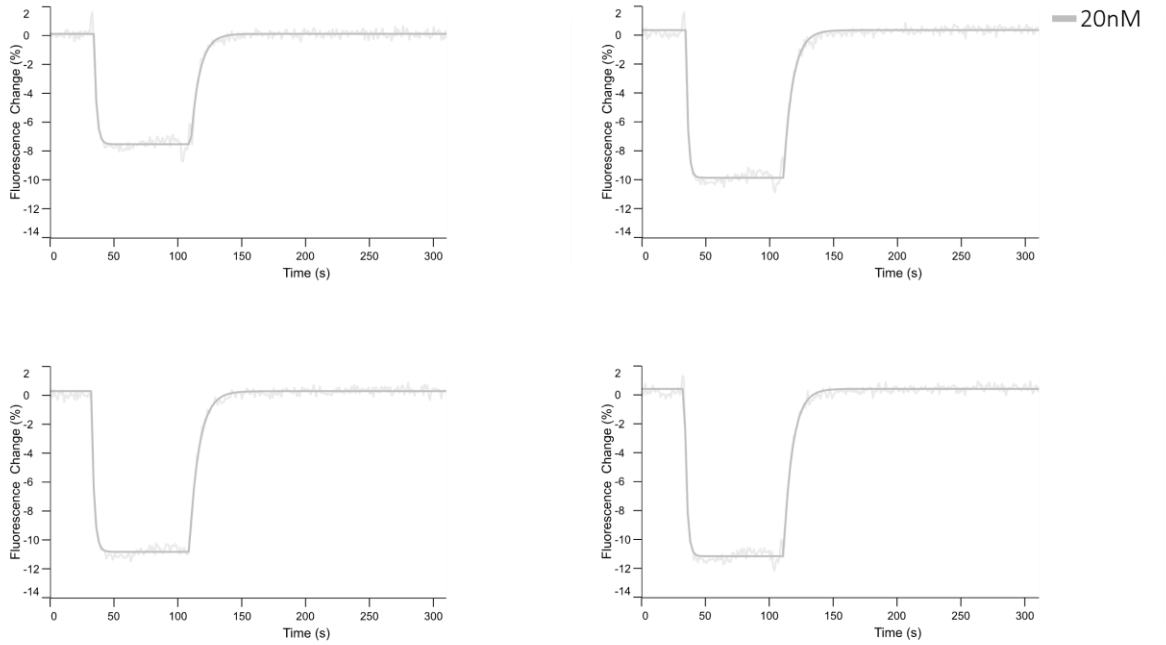

***Figure S4N**. PROTACs high-throughput screening: ARV771 20 nM kinetics.*

Table S2N. Kinetic binding rates of ARV771 resulting from the screening.

k_{ON} ($M^{-1}s^{-1}$)	k_{OFF} (s^{-1})	K_D (M)
17.9 ± 2.4 E+6	147 ± 6 E-3	8.18 ± 1.16 E-9
16.9 ± 1.4 E+6	132 ± 3 E-3	7.82 ± 0.66 E-9
21.9 ± 2.4 E+6	141 ± 4 E-3	6.41 ± 0.74 E-9
19.5 ± 1.4 E+6	144 ± 4 E-3	7.38 ± 0.57 E-9

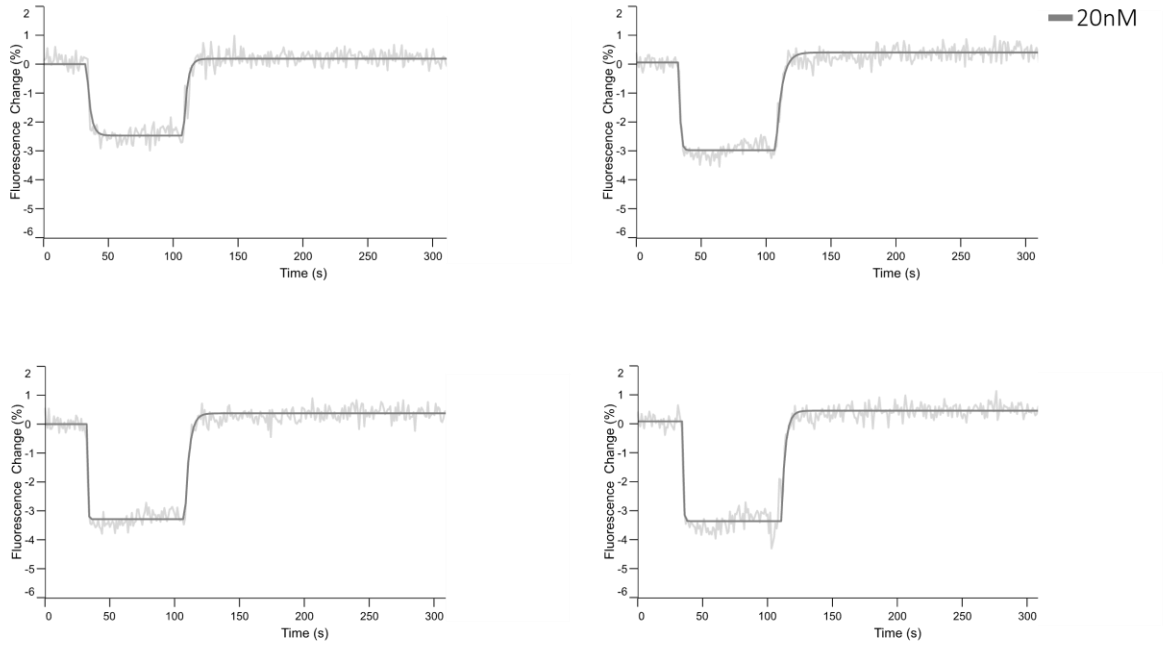

Figure S4O. PROTACs high-throughput screening: JQ1 20 nM kinetics.

Table S2O. Kinetic binding rates of JQ1 resulting from the screening.

k_{ON} ($M^{-1}s^{-1}$)	k_{OFF} (s^{-1})	K_D (M)
60.2 ± 35.1 E+6	367 ± 55 E-3	6.10 ± 2.41 E-9
96.7 ± 92.2 E+6	306 ± 28 E-3	3.16 ± 3.03 E-9
35.1 ± 8.90 E+6	223 ± 22 E-3	6.36 ± 1.74 E-9
64.0 ± 46.6 E+6	337 ± 39 E-3	5.26 ± 3.87 E-9

Figure S5(A-C). CRBN-Brd4^{BD2} binary and ternary PROTACs interactions.

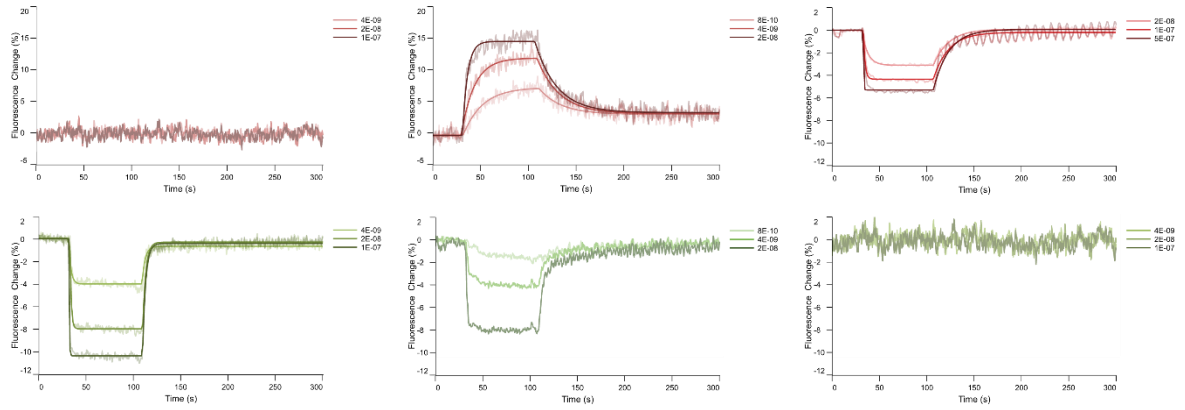

Figure S5A. *dBET1 interaction profiles with CRBN and Brd4^{BD2}. Binary dBET1-Brd4^{BD2} (left), ternary CRBN-dBET1-Brd4^{BD2} (center), binary dBET1-CRBN (right). Kinetic values are listed in Table 3.*

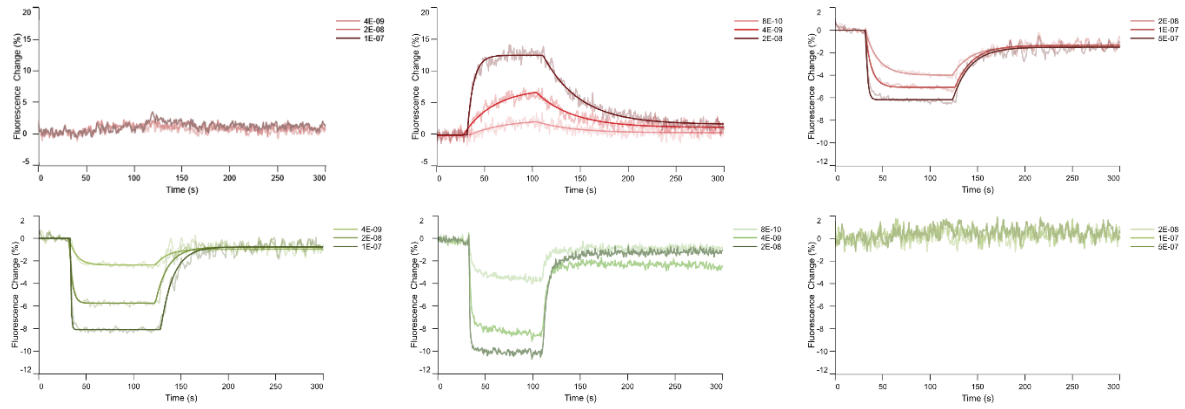

Figure S5B*. dBET6 interaction profiles with CRBN and Brd4^{BD2}. Binary dBET6-Brd4^{BD2} (left), ternary CRBN-dBET6-Brd4^{BD2} (center), binary dBET6-CRBN (right). Kinetic values are listed in Table 3.*

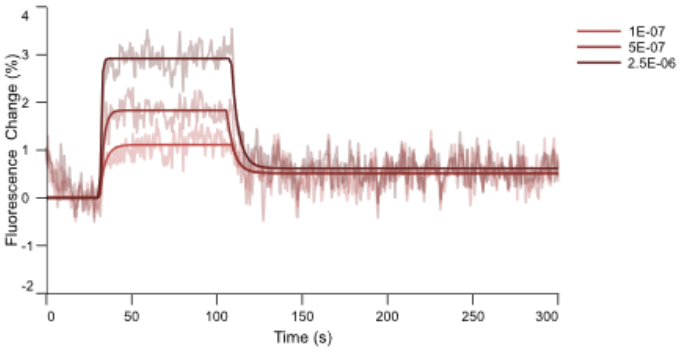

Figure S5C. *CRBN-Brd4^{BD2} binary and ternary PROTACs interaction: Pomalidomide-CRBN binary interaction (k_{ON} = 0.50 ± 0.02 E+6 $M^{-1}s^{-1}$; k_{OFF} = 252 ± 9.5 E-3 s^{-1}; K_D = 499 ± 0.01 nM).*

Figure S6(A-B). Brd Screening – E1 Brd ternary in green and E2 Brd binary.

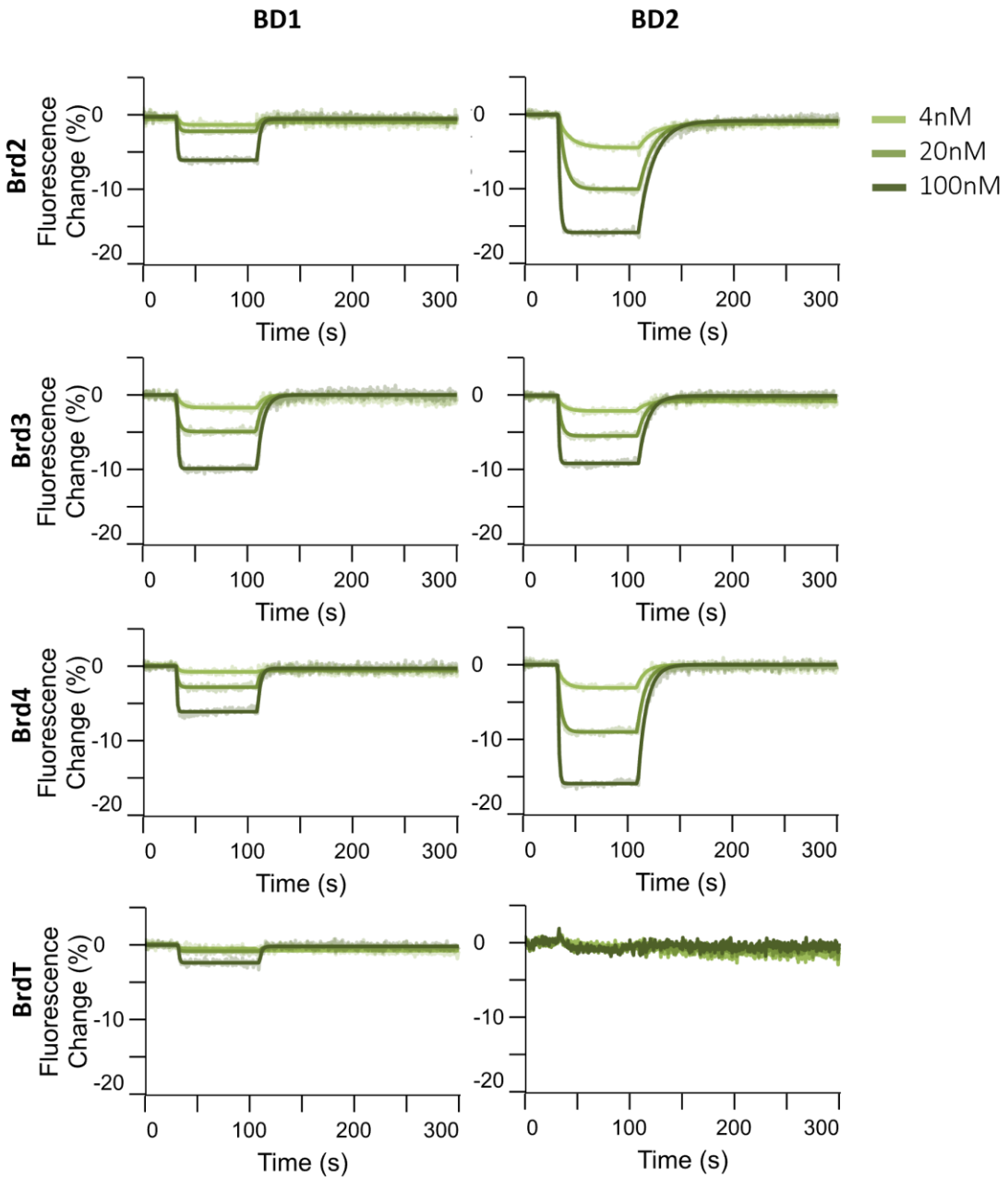

Figure S6A. Brd Screening (Spot 2) - ARV825 binary kinetics. Green signals resulting from the binary complex formation upon ARV-825 binding to the individual bromodomains (BDs) of different BET proteins (Brd2, Brd3, Brd4, and BrdT). Fluorescence signals coming from the interaction with BrdX-BD1 (left column) and with BrdX-BD2 (right column) are shown. Each POI was immobilized on the green arm of the Y-structure to be screened with ARV-825 in the absence of CRBN on the red arm. The measured affinity and kinetic values are reported in Table S4 below.

Table S4. Brd screening – binary ARV825 kinetic values.

		k_{ON} ($M^{-1}s^{-1}$)	k_{OFF} (s^{-1})	K_D (nM)
Brd2	BD1	16.5 ± 6.2 E+6	40.1 ± 3.5 E-2	24.3 ± 9.4
	BD2	5.94 ± 0.21 E+6	9.53 ± 0.1 E-2	16.0 ± 0.6
Brd3	BD1	8.77 ± 0.94 E+6	1.44 ± 0.5 E-2	16.4 ± 1.9
	BD2	10.4 ± 0.9 E+6	12.0 ± 0.3 E-2	11.5 ± 1.0
Brd4	BD1	13.3 ± 3.6 E+6	2.27 ± 1.8 E-2	17.0 ± 4.7
	BD2	11.0 ± 0.4 E+6	11.4 ± 0.1 E-2	10.4 ± 0.4
BrdT	BD1	5.90 ± 3.05 E+6	5.22 ± 99 E-2	88.5 ± 48.7
	BD2	N/D	N/D	N/D

Figure S7(A-C). proFIRE chromatograms.

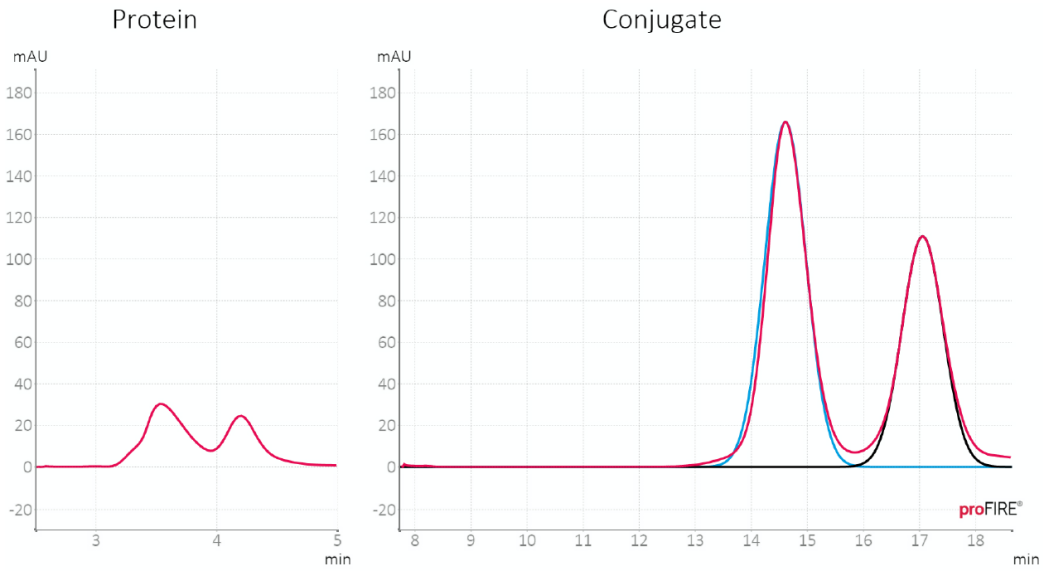

***Figure S7A**. proFIRE chromatogram: Brd4^{BD2}. Purification chromatogram of Brd4^{BD2} conjugated to a 48mer oligonucleotide. Conjugate peak 1 (blue line) shows a single population of a 48mer labelled protein with a 1:1 ratio. The second peak (black line) is the excess of free DNA. Conjugation yielded 17 µM (60 µL) of conjugate-Brd4^{BD2}.*

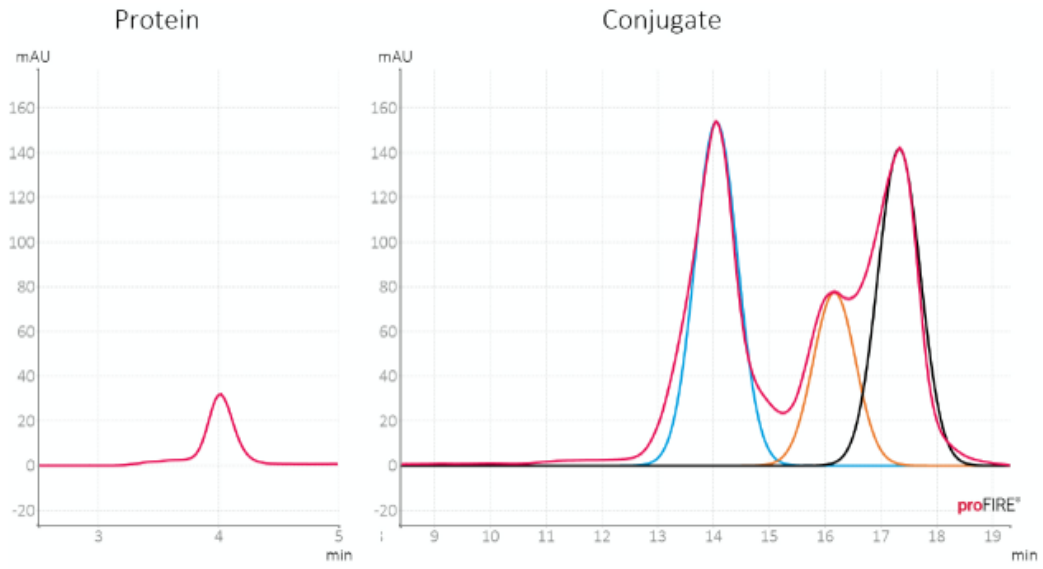

***Figure S7B.** proFIRE chromatogram: VHL. Purification chromatogram of VHL conjugated to a 48mer oligonucleotide. Conjugate peak 1 (blue line yield 15 µM - 60 µL) shows a single population of a 48mer labelled protein with a 1:1 ratio. Conjugate peak 2 (orange line) shows a higher molecular weight, assuming a 2:1 ratio. The third peak (black line) is the excess of free DNA. Only peak 1 was used for the measurements.*

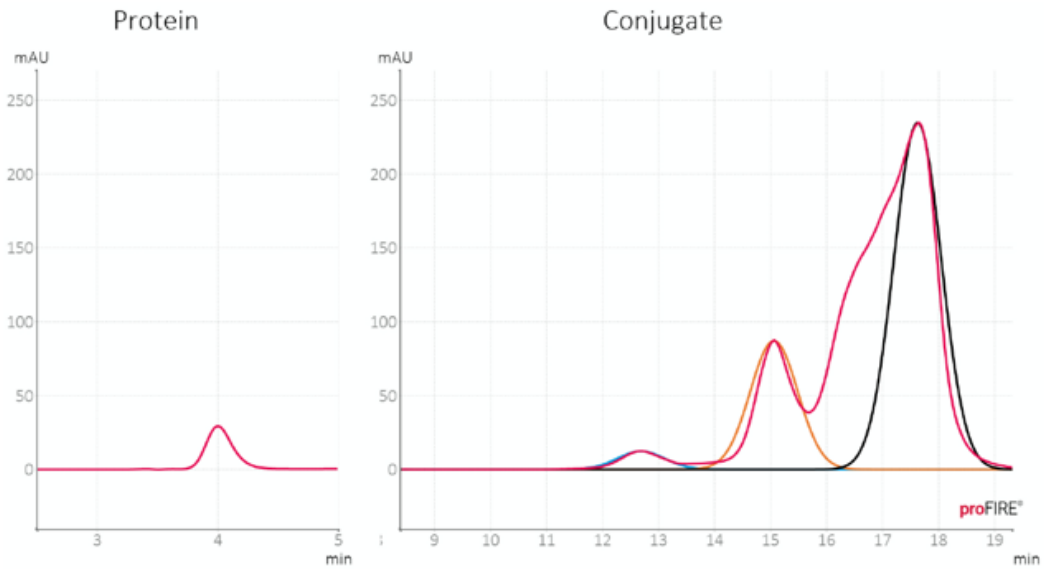

Figure S7C. *proFIRE chromatogram: CRBN. Purification chromatogram of CRBN conjugated to a 48mer oligonucleotide. Conjugate peak 1 (blue line, yield 2 µM - 60 µL) shows a single population of a 48mer labelled protein with a 1:1 ratio. Conjugate peak 2 (orange line yield 10 µM - 60 µL) shows a higher molecular weight, assuming a 2:1 ratio. The third peak (black line) is the excess of free DNA. Both conjugates resulting from the two peaks were used for the measurements.*

References

1. Roy, M.J.; Winkler, S.; Hughes, S.J.; Whitworth, C.; Galant, M.; Farnaby, W.; Rumpel, K.; Ciulli, A. SPR-Measured Dissociation Kinetics of PROTAC Ternary Complexes Influence Target Degradation Rate. *bioRxiv* 2019, 451948, doi:10.1101/451948.
2. Riching, K.M.; Mahan, S.; Corona, C.R.; McDougall, M.; Vasta, J.D.; Robers, M.B.; Urh, M.; Daniels, D.L. Quantitative Live-Cell Kinetic Degradation and Mechanistic Profiling of PROTAC Mode of Action. *ACS Chem. Biol.* 2018, *13*, 2758–2770, doi:10.1021/acschembio.8b00692.
3. Sakamoto, K.M.; Kim, K.B.; Kumagai, A.; Mercurio, F.; Crews, C.M.; Deshaies, R.J. Protacs: Chimeric Molecules That Target Proteins to the Skp1–Cullin–F Box Complex for Ubiquitination and Degradation. *Proceedings of the National Academy of Sciences* 2001, *98*, 8554–8559, doi:10.1073/pnas.141230798.
4. Pettersson, M.; Crews, C. PROteolysis TArgeting Chimeras (PROTACs) - Past, Present and Future. *Drug Discov Today Technol* 2019, *31*, 15–27, doi:10.1016/j.ddtec.2019.01.002.
5. Bondeson, D.P.; Mares, A.; Smith, I.E.D.; Ko, E.; Campos, S.; Miah, A.H.; Mulholland, K.E.; Routly, N.; Buckley, D.L.; Gustafson, J.L.; et al. Catalytic in Vivo Protein Knockdown by Small-Molecule PROTACs. *Nat Chem Biol* 2015, *11*, 611–617, doi:10.1038/nchembio.1858.
6. Lu, J.; Qian, Y.; Altieri, M.; Dong, H.; Wang, J.; Raina, K.; Hines, J.; Winkler, J.D.; Crew, A.P.; Coleman, K.; et al. Hijacking the E3 Ubiquitin Ligase Cereblon to Efficiently Target BRD4. *Chem Biol* 2015, *22*, 755–763, doi:10.1016/j.chembiol.2015.05.009.
7. Ito, T.; Ando, H.; Suzuki, T.; Ogura, T.; Hotta, K.; Imamura, Y.; Yamaguchi, Y.; Handa, H. Identification of a Primary Target of Thalidomide Teratogenicity. *Science* 2010, *327*, 1345–1350, doi:10.1126/science.1177319.
8. Belkina, A.C.; Denis, G.V. BET Domain Co-Regulators in Obesity, Inflammation and Cancer. *Nat Rev Cancer* 2012, *12*, 465–477, doi:10.1038/nrc3256.
9. Dragovich, P.S.; Pillow, T.H.; Blake, R.A.; Sadowsky, J.D.; Adaligil, E.; Adhikari, P.; Chen, J.; Corr, N.; dela Cruz-Chuh, J.; Del Rosario, G.; et al. Antibody-Mediated Delivery of Chimeric BRD4 Degraders. Part 2: Improvement of In Vitro Antiproliferation Activity and In Vivo Antitumor Efficacy. *J. Med. Chem.* 2021, *64*, 2576–2607, doi:10.1021/acs.jmedchem.0c01846.
10. Riching, K.M.; Vasta, J.D.; Hughes, S.J.; Zoppi, V.; Maniaci, C.; Testa, A.; Urh, M.; Ciulli, A.; Daniels, D.L. Translating PROTAC Chemical Series Optimization into Functional Outcomes Underlying BRD7 and BRD9 Protein Degradation. *Current Research in Chemical Biology* 2021, *1*, 100009, doi:10.1016/j.crchbi.2021.100009.
11. Hughes, S.J.; Ciulli, A. Molecular Recognition of Ternary Complexes: A New Dimension in the Structure-Guided Design of Chemical Degraders. *Essays Biochem* 2017, *61*, 505–516, doi:10.1042/EBC20170041.
12. Liu, X.; Zhang, X.; Lv, D.; Yuan, Y.; Zheng, G.; Zhou, D. Assays and Technologies for Developing Proteolysis Targeting Chimera Degraders. *Future Med Chem* 2020, *12*, 1155–1179, doi:10.4155/fmc-2020-0073.
13. Zengerle, M.; Chan, K.-H.; Ciulli, A. Selective Small Molecule Induced Degradation of the BET Bromodomain Protein BRD4. *ACS Chem. Biol.* 2015, *10*, 1770–1777, doi:10.1021/acschembio.5b00216.
14. Zoppi, V.; Hughes, S.J.; Maniaci, C.; Testa, A.; Gmaschitz, T.; Wieshofer, C.; Koegl, M.; Riching, K.M.; Daniels, D.L.; Spallarossa, A.; et al. Iterative Design and Optimization of Initially Inactive Proteolysis Targeting Chimeras (PROTACs) Identify VZ185 as a Potent, Fast, and Selective von Hippel–Lindau (VHL) Based Dual Degrader Probe of BRD9 and BRD7. *J. Med. Chem.* 2019, *62*, 699–726, doi:10.1021/acs.jmedchem.8b01413.
15. Bai, L.; Zhou, H.; Xu, R.; Zhao, Y.; Chinnaswamy, K.; McEachern, D.; Chen, J.; Yang, C.-Y.; Liu, Z.; Wang, M.; et al. A Potent and Selective Small-Molecule Degrader of STAT3 Achieves Complete Tumor Regression In Vivo. *Cancer Cell* 2019, *36*, 498-511.e17, doi:10.1016/j.ccell.2019.10.002.

16. Silva, M.C.; Ferguson, F.M.; Cai, Q.; Donovan, K.A.; Nandi, G.; Patnaik, D.; Zhang, T.; Huang, H.-T.; Lucente, D.E.; Dickerson, B.C.; et al. Targeted Degradation of Aberrant Tau in Frontotemporal Dementia Patient-Derived Neuronal Cell Models. *eLife 8*, e45457, doi:10.7554/eLife.45457.
17. Smith, B.E.; Wang, S.L.; Jaime-Figueroa, S.; Harbin, A.; Wang, J.; Hamman, B.D.; Crews, C.M. Differential PROTAC Substrate Specificity Dictated by Orientation of Recruited E3 Ligase. *Nat Commun* 2019, *10*, 131, doi:10.1038/s41467-018-08027-7.
18. Gadd, M.S.; Testa, A.; Lucas, X.; Chan, K.-H.; Chen, W.; Lamont, D.J.; Zengerle, M.; Ciulli, A. Structural Basis of PROTAC Cooperative Recognition for Selective Protein Degradation. *Nature Chemical Biology* 2017, *13*, 514–521, doi:10.1038/nchembio.2329.
19. Kaji, T.; Koga, H.; Kuroha, M.; Akimoto, T.; Hayata, K. Characterization of Cereblon-Dependent Targeted Protein Degrader by Visualizing the Spatiotemporal Ternary Complex Formation in Cells. *Scientific Reports* 2020, *10*, 3088, doi:10.1038/s41598-020-59966-5.
20. Winter, G.E.; Buckley, D.L.; Paulk, J.; Roberts, J.M.; Souza, A.; Dhe-Paganon, S.; Bradner, J.E. Selective Target Protein Degradation via Phthalimide Conjugation. *Science* 2015, *348*, 1376–1381, doi:10.1126/science.aab1433.
21. Nowak, R.P.; DeAngelo, S.L.; Buckley, D.; He, Z.; Donovan, K.A.; An, J.; Safaee, N.; Jedrychowski, M.P.; Ponthier, C.M.; Ishoey, M.; et al. Plasticity in Binding Confers Selectivity in Ligand-Induced Protein Degradation. *Nat Chem Biol* 2018, *14*, 706–714, doi:10.1038/s41589-018-0055-y.
22. Wiener, J.; Kokotek, D.; Rosowski, S.; Lickert, H.; Meier, M. Preparation of Single- and Double-Oligonucleotide Antibody Conjugates and Their Application for Protein Analytics. *Scientific Reports* 2020, *10*, 1457, doi:10.1038/s41598-020-58238-6.
23. Reinking, H.K.; Stingele, J. Protein-Oligonucleotide Conjugates as Model Substrates for DNA-Protein Crosslink Repair Proteases. *STAR Protoc* 2021, *2*, 100591, doi:10.1016/j.xpro.2021.100591.

Chapter 4

4. Study of the activity of DNA-modifying enzymes

4.1 General introduction

DNA replication is one of the fundamental processes occurring in every living cell. It is an extremely complex process, and it is highly regulated by many interplaying groups of proteins. DNA polymerases are the main enzymes responsible for DNA replication. These enzymes catalyze the incorporation of mononucleotides into a growing strand (*primer*) using another DNA strand (*template*) as a guide for the synthesis of the correct DNA sequence [1]. Therefore, DNA polymerases are of great interest in biomedical research [2], since defects in their activity can lead to cancer initiation and progression [3–5], and also in the biotechnology field [6–8], for their use in DNA sequencing and in Polymerase Chain Reaction (PCR) technologies.

A simplified scheme of the DNA polymerisation reaction performed by DNA polymerases is depicted below (Figure 1), and consists of the following steps:

1) DNA polymerase binds to the junction between the primer strand and the template strand;
2) the polymerase-DNA complex binds a deoxynucleoside triphosphate (dNTP) following the complementarity on the template strand (base-pairing);
3) the polymerase incorporates the dNTP catalyzing a phosphodiester bond formation on the 3' of the primer strand, releasing pyrophosphate (PPi) as waste, before moving to the next template position.

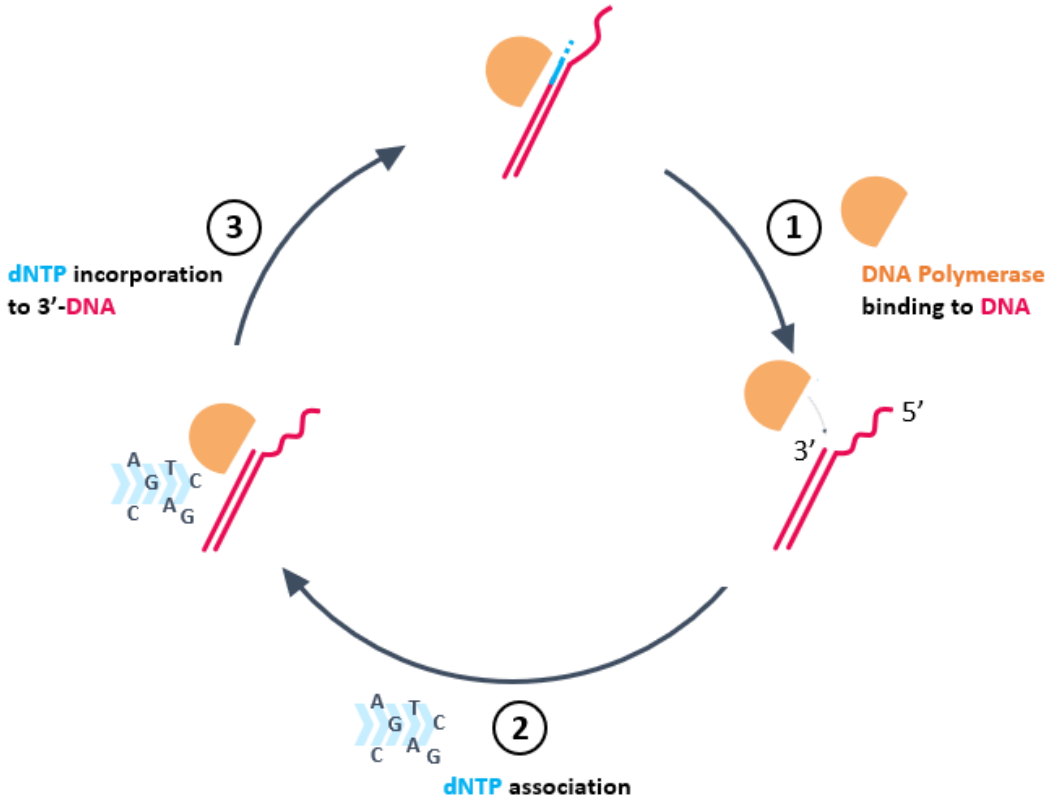

Figure 1. *Simplified scheme of DNA polymerization performed by a DNA polymerase. 1) the DNA polymerase binds to the junction between the primer strand and the template strand. 2) the DNA polymerase binds a dNTP that pairs to the opposing dNTP on the template strand. 3) the DNA polymerase incorporates the dNTP on the 3' end, elongating the primer strand of a base, and then it moves to the next base.*

Therefore, due to the complexity of this process, real-time technologies that can simultaneously provide information on the mechanisms of enzymatic binding (k_{ON}, k_{OFF}, K_D) and activity (k_{cat}, K_M), are extremely valuable. Surface-based methods are well suited to study individual steps of complex pathways, where the interacting molecules can be introduced and removed from the reaction channel, following in real time their association and dissociation phases. In this chapter, the switchSENSE® technology was used for characterising polymerase binding to DNA, as well as its DNA elongation activity and its activity inhibition by a known inhibitor. The workflow described here is applicable to any DNA or RNA polymerase, reverse transcriptase, and it has been successfully tested also with the human *Werner syndrome* (WRN) helicase. The wild type Taq DNA polymerase (Pol) from *Thermus aquaticus*, frequently used in PCR, was chosen as a model system for a proof-of-principle study.

4.2 Results and Discussion

4.2.1 Biochip setup

The binding affinity and the enzymatic activity of Pol were characterized in the same heliX® chip. The two spots of the chip were functionalized with two distinct sequences (Figure 2):

i. Spot 1 is functionalized with *Primer-Template*, a hybrid ssDNA-dsDNA ligand. The *Primer strand* is composed of a sequence of 48 nucleotides that hybridizes to a complementary 80-nucleotide *Template strand*, leaving 32 nucleotides as ssDNA. The Template strand carries a fluorescent dye on the 5' distal end.

ii. Spot 2 is functionalized with a control *dsDNA*, a fully double-stranded ligand analogue of spot 1. In this case, the *Primer strand* is 80-nucleotide long and it fully hybridizes with the 80-nucleotide long *Template strand*. The Template strand carries a fluorescent dye on the 5' distal end.

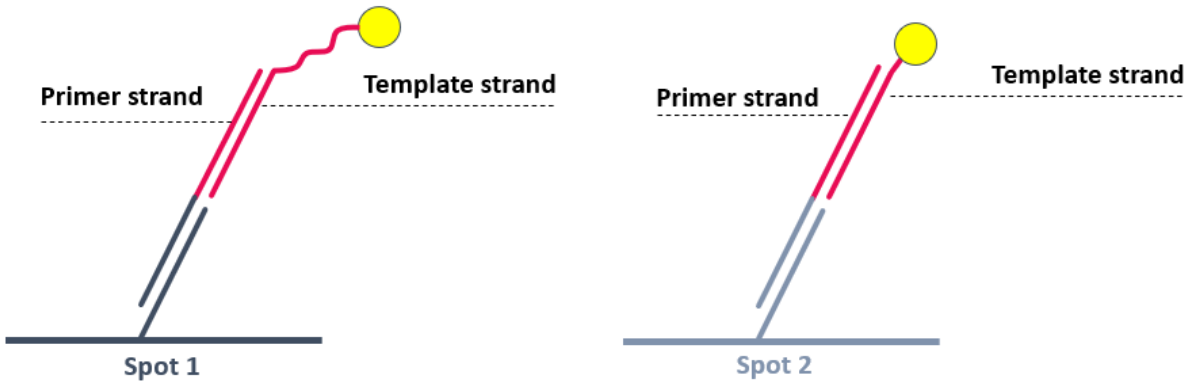

Figure 2. *Biochip setup for the characterization of Taq Polymerase (Pol). The Primer strand in spot 1 is partially complementary to the Template strand, thus leaving a ssDNA sequence of 32 nucleotides. The Primer strand in spot 2 is fully complementary to the Template strand, resulting in a fully dsDNA ligand. The different ligands in the two spots allow to study the affinity of Pol for ssDNA and for dsDNA. In addition, the Primer strand of the ligand in spot 1 can be elongated by the Pol, and the ligand in spot 2 can be used as a control of Pol elongation activity.*

The presence of a fluorescent dye allows to follow in real time the changes in the dye's local environment as a result of the Pol binding to the DNA ligand strand, and therefore to measure the Pol affinity towards the DNA sequences. In addition, with this design, by placing the dye on the 5' distal end, monitoring the DNA elongation activity of Pol in real time is also possible (see Appendix, Figure A17). In fact, Pol can elongate the primer strand from 5' to 3' direction upon dNTPs injection, following the sequence of the template strand. Therefore, in spot 1, the single-stranded primer strand can be elongated by the Pol previously bound, whereas spot 2 can be

used as control since the fully double-stranded ligand cannot be further elongated. The DNA elongation activity of Pol is related to changes in fluorescence intensity, because by elongating the primer strand, the ligand in spot 1 is converted from a flexible ssDNA to a more rigid fully duplex DNA. As a result, the dye is carried away from the gold surface of the chip, which proximity causes a quenching of the dye fluorescence [9]. The binding models used to describe enzyme kinetics and activity are described in more detail in Appendix (section A2.3).

4.2.2 Taq Polymerase characterization: DNA binding kinetics

The first step to characterize a DNA Polymerase, is studying its binding affinity to DNA strands, and its specificity towards a specific sequence. To assess the binding affinity of the model system Taq Polymerase (Pol) to the DNA ligands, a three-step workflow was used (Figure 3), consisting in:

1) Functionalization of the surface with the Primer-Template DNA for spot 1 and control dsDNA for spot 2;
2) Association and dissociation kinetics of Pol at increasing concentrations;
3) Regeneration of the chip surface via the injection of high pH solution to remove the ligand strands and restore the initial chip surface condition.

This workflow has been used for studying the binding kinetics of Taq polymerase wild type to DNA ligands, but it can be also employed for any other DNA- and RNA polymerase and also RNA ligands.

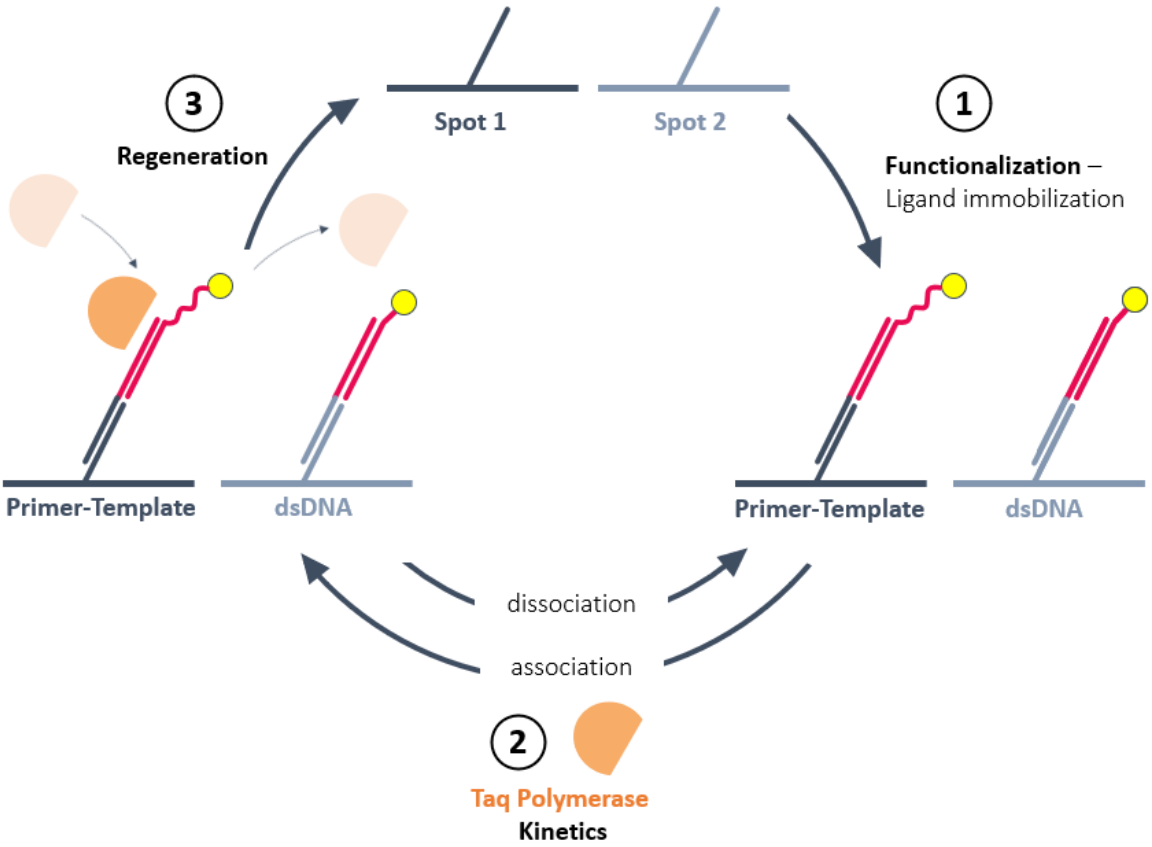

Figure 3. *switchSENSE® workflow used to study the binding kinetics of Taq Polymerase (Pol) to DNA ligands. 1) Functionalization of the biochip surface with two different DNA ligand strands carrying a fluorescent dye: spot 1 with Primer-Template ss/dsDNA, spot 2 with control dsDNA. 2) Kinetics of Pol to the DNA ligands. Pol is injected at increasing concentrations over the surface, followed by injections of running buffer to let it dissociate from the ligands. 3) Regeneration of the chip surface with the injection of a high pH solution.*

The binding kinetics of Pol to both ligands in spot 1 and spot 2 are recorded real time, by following the change in fluorescence intensity (Figure 4): the association of Pol to the DNA strands results in a quenching of fluorescence and its dissociation results in an increase in fluorescence. Pol is injected over the biochip surface for 2 min at 100 µL/min at increasing concentrations, from 2.2 nM to 20 nM, followed by running buffer injections for 8 min to induce the dissociation of the enzyme from the ligand strands. Importantly, the binding kinetics is resolved in absence of dNTPs. As shown in Figure 4, Pol can bind to both DNA ligands present in spot 1 (orange curves, top) and spot 2 (grey curves, bottom). This behavior is expected, since this polymerase naturally binds to all DNA strands without any sequence specificity. However, it can be observed a slightly higher change in fluorescence upon binding in spot 1 compared to spot 2, that can be related to the higher flexibility of the ssDNA ligand in spot 1. The enzyme association and dissociation kinetics are nicely described by a bi-exponential fit, especially at higher concentrations, which can be correlated to the presence of two Pol on each DNA strand exhibiting different binding rates. The resulting association rates ($k_{ON1,2}$) and dissociation rates ($k_{OFF1,2}$), as well as the Pol affinity ($K_{D1,2}$) for the target DNA strands have been obtained and listed below in Table 1. Pol enzymes bind to the DNA strands with affinity in the single-digit nM

range (K_{D1}) and in the three-digit pM range (K_{D2}) to both DNA ligand strands in both spots, with similar association and dissociation rates. In more detail, the slow k_{OFF2} describes the majority of the dissociation phase (90% of the relative amplitude) of Pol from the DNA ligands: therefore, the K_D that better represents the Pol affinity to these DNA ligands is the one in the pM range. Studies performed in SPR, measured the binding affinity of other types of DNA polymerases (Klenow fragment of Escherichia coli DNA polymerase I, eukaryotic polymerase β, and T4 and T7 bacteriophage polymerases) to duplex DNA strands, and reported a K_D in the single-digit nM range [10–12], while other studies reported K_D in the three-digit nM range [13]. Differences in affinity of this class of enzymes between different studies and techniques can be correlated to several reasons, e.g. the intrinsic difference between the types of polymerases, different chip setup, different buffer compositions and/or to different flow rates. Indeed, the abovementioned SPR studies were carried out at a flow rate of 10 µL/min, ten times slower than the flow rate used in the present study.

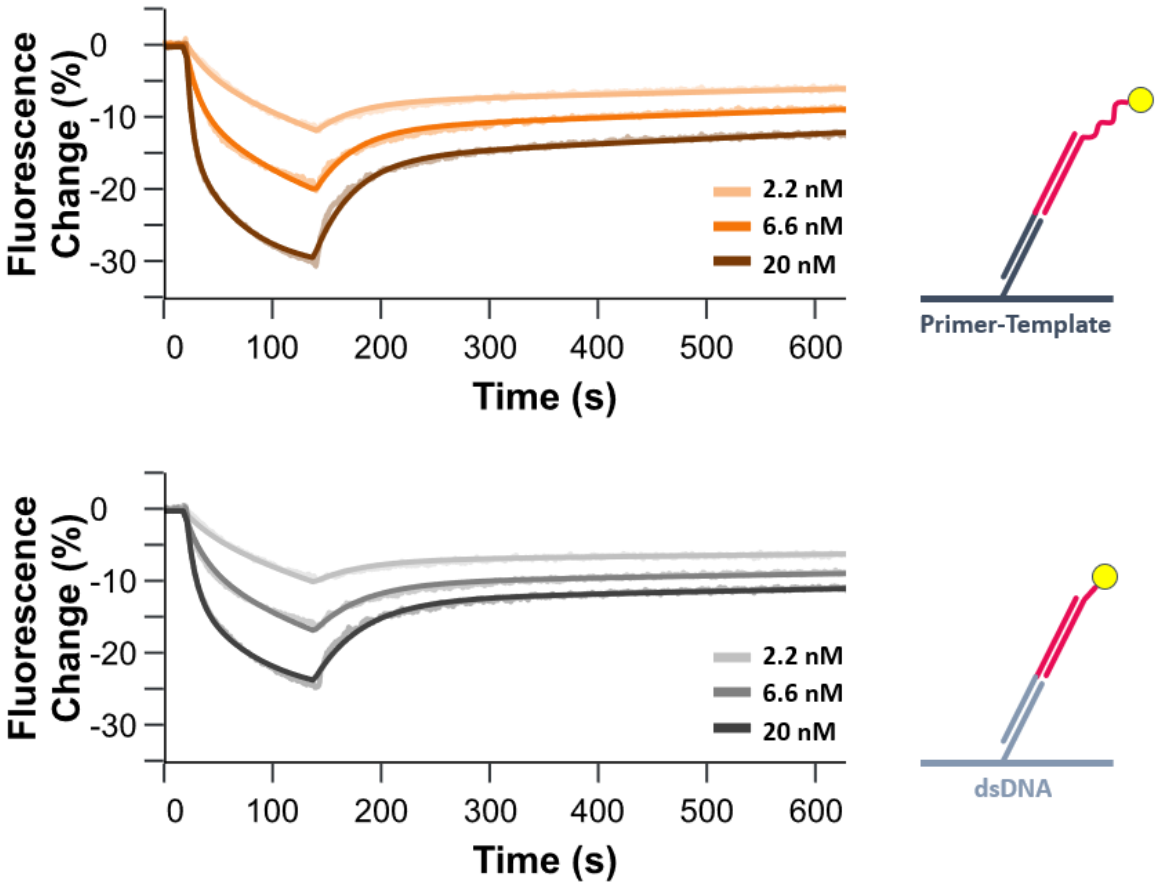

Figure 4. *Binding kinetics of Taq Polymerase (Pol) at increasing concentrations (from 2.2 nM to 20 nM) to DNA ligands in spot 1 (top, orange curves) and in spot 2 (bottom, grey curves). Buffer injections allow Pol to dissociate from the DNA. The enzyme association results in a quenching of fluorescence, and its dissociation can be monitored via the increase in fluorescence upon the buffer injection. The binding kinetics are described by a biphasic fit model in both association and dissociation kinetics.*

Table 1. *Kinetic values of Taq Polymerase binding to the Primer-Template DNA and control dsDNA.*

Ligand	k_{ON1} *(E+6* $M^{-1}s^{-1}$*)*	k_{ON2} *(E+6* $M^{-1}s^{-1}$*)*	k_{OFF1} *(E-3* s^{-1}*)*	k_{OFF2} *(E-3* s^{-1}*)*	K_{D1} *(nM)*	K_{D2} *(pM)*
Primer-Template	7.61 ± 0.30	0.93 ± 0.03	27.9 ± 0.4	0.54 ± 0.01	3.67 ± 0.15	580 ± 20
dsDNA	4.71 ± 0.19	0.74 ± 0.03	22.8 ± 0.3	0.29 ± 0.01	4.83 ± 0.21	390 ± 16

4.2.3 Taq Polymerase characterization: DNA Elongation Activity

The second step for the characterization of Pol is the study of its DNA elongation activity upon the injection of a mix of dNTP. DNA Polymerases elongate DNA in 5' to 3' direction. As explained previously and in Appendix (section A2.3), thanks to the presence of the fluorescent dye on the 5' distal end of the template strand of the ligand, the increase in fluorescence signal is correlated with the primer DNA elongation and hence with the duplex formation.

In this case, for studying the activity of Pol, a four-step workflow was used (Figure 5):

1) Functionalization of the surface with the Primer-Template DNA for spot 1 and control dsDNA for spot 2;
2) Taq Polymerase association at a fixed concentration of 5 nM, to achieve a 1:1 binding of Pol to each DNA ligand strand on the surface;
3) dNTP injection at increasing concentrations to follow in real time the DNA elongation;
4) Regeneration of the chip surface via the injection of a high pH solution to remove the ligand strands and restore the initial chip surface condition.

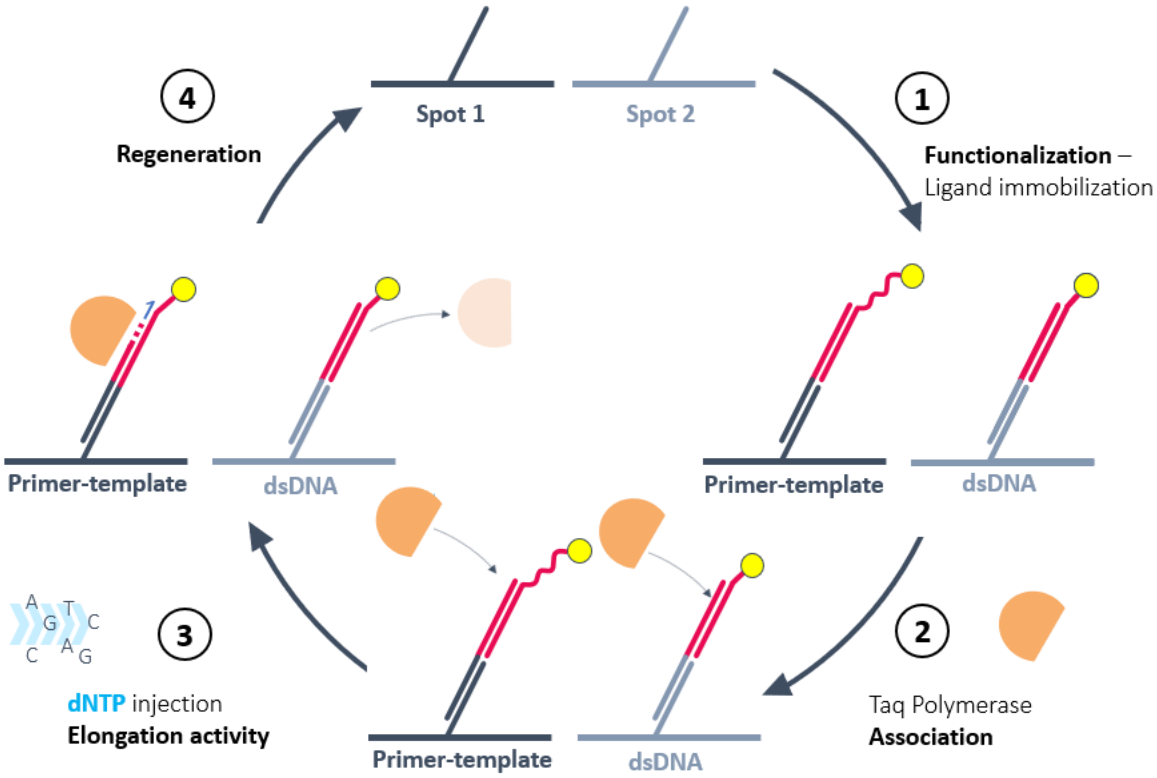

Figure 5. *switchSENSE® workflow used to study the DNA elongation activity of Taq Polymerase (Pol) to DNA ligands. 1) Functionalization of the biochip surface with Primer-Template ss/dsDNA (spot 1), and with control dsDNA (spot 2). 2) Association of Pol to the DNA ligands. Pol is injected at a fixed concentration (5 nM) over the surface. 3) Injection of dNTPs at increasing concentrations (from 0.03 µM to 20 µM) to monitor in real time the DNA elongation. 4) Regeneration of the chip surface achieved by the injection of a high pH solution.*

In the association step (2), Pol was injected at a fixed concentration of 5 nM per each cycle of the workflow. This concentration was chosen because: *i)* it is about 10 times higher than the K_{D2} in the pM range resulting from the binding studies previously described, which ensures that the ligands on the surface are fully saturated with the enzyme, and *ii)* at this concentration it is expected to have one Pol molecule binding per each DNA strand, as opposite to concentrations around 20 nM, thus favoring a 1:1 interaction of enzyme per DNA. As shown in Figure 6, the binding of Pol to the Primer-Template in spot 1 (Figure 6A) and dsDNA in spot 2 (Figure 6C), results in a reproducible quenching of fluorescence. By fitting the association curves with a mono-exponential fit model, the association rates (k_{ON}) of Pol binding to the Primer-Template and to the dsDNA can be obtained, resulting in 6.45 ± 0.05 E+6 and 5.03 ± 0.05 E+6, respectively. The very similar calculated values are precisely matching with the association rates described in the previous binding study (Table 1).

In the activity step (3), following the association of Pol to the DNA ligands, increasing concentrations of dNTPs (from 0.03 µM to 20 µM) were injected over the surface for 3 min with 50 µL/min flow rate. The flow rate used here is slower than the one used in the binding studies described above, because the flow needs to be fast enough to provide dNTPs to the

Pol without being the limiting step of the reaction, but at the same time it does not have to be too fast to avoid the dissociation of the enzyme from the DNA ligands, hindering its activity. As shown in Figure 5B, the injection of substrate results in an increase in fluorescence in spot 1. This is because the dNTPs are incorporated to the Primer strand by Pol that follows the sequence of the Template strand, thereby elongating the Primer strand and forming a duplex DNA. At higher dNTPs concentrations, the elongation of the Primer strand is faster and the maximum fluorescence amplitude is achieved in a shorter time compared to lower dNTP concentrations. In spot 2, on the contrary, increasing concentrations of dNTPs do not induce an increase in fluorescence (Figure 6D), as expected, since the fully dsDNA cannot be elongated further by Pol, which as a consequence dissociates from the ligand.

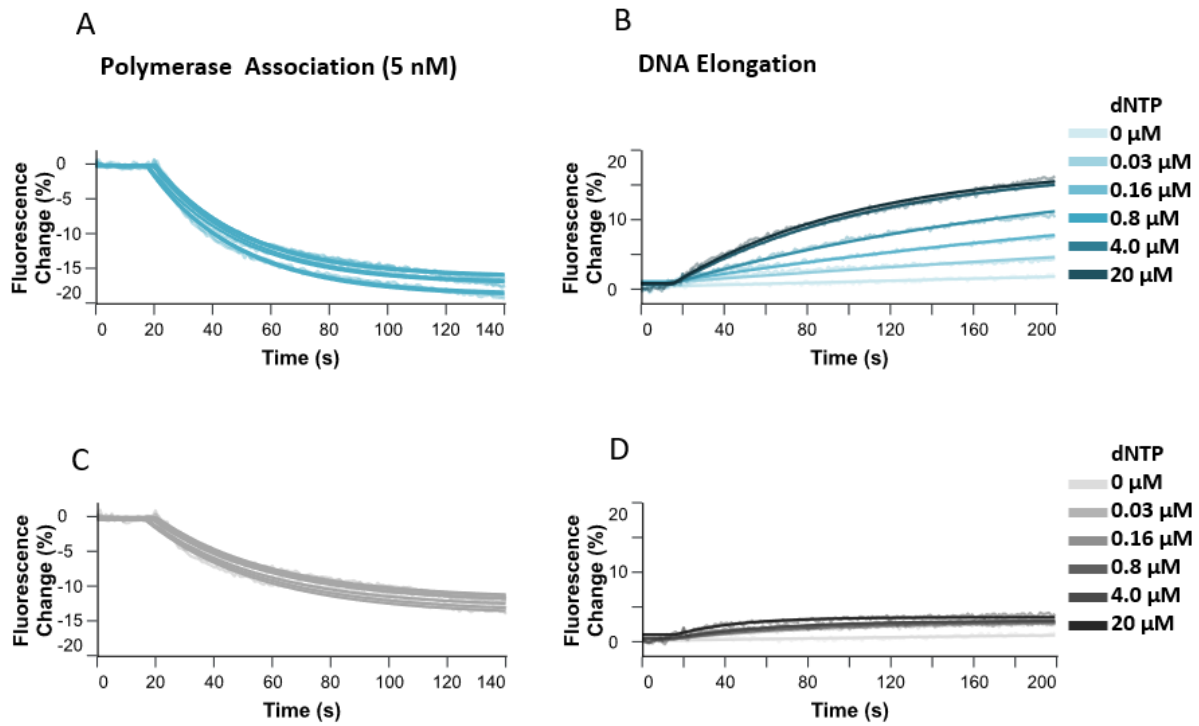

Figure 6. Taq Polymerase activity characterization. A) Pol (5 nM) association to Primer-Template DNA ligand in spot 1. B) Primer strand elongation upon injection of dNTPs at increasing concentrations. The increase in fluorescence changes correspond to the elongation of the Primer strand, performed by Pol following the sequence of the Template strand. C) Pol (5 nM) association to dsDNA ligand in spot 2. D) control measurement with injection of dNTPs at increasing concentrations in spot 2, showing that no elongation is observed if a full dsDNA is on the surface, thus Pol dissociates from dsDNA.

The fluorescence traces increasing during the elongation in spot 1, can be fitted with a mono-exponential model. Hence, the observed rates during the elongation can be plotted for each dNTP concentration (see Appendix, section A2.3), yielding a linear plot (Figure 7) that allows to extrapolate the Pol catalytic rate (k_{cat}) and the affinity (K_D) of Pol for the substrate dNTPs, summarized in Table 2.

Pol elongation activity can be studied by a Michaelis-Menten model described by Walsh and coauthors [14] and summarized in the following equation:

$$Pol \cdot DNA_n + dNTP \rightleftharpoons Pol \cdot DNA_n \cdot dNTP \rightarrow Pol + DNA_{n+1} + PPi$$

where $Pol \cdot DNA_n$ is the Pol in complex with Primer-Template ligand, $Pol \cdot DNA_n \cdot dNTP$ is the complex formed by Pol, Primer-Template ligand and dNTP, and $Pol + DNA_{n+1}$ is the one-base extension product. The complex formation is reversible and described by association rate k_{ON} and dissociation rate k_{OFF}, and the rate of product formation is described by k_{cat}. The observed reaction rate constant is given by:

$$k_{obs} = k_{cat}[dNTP]/(K_D + [dNTP])$$

By plotting the k_{obs} values as a function of nucleotide concentration and analyzing the curves using the equation here above, the dNTPs substrate dissociation or affinity constant (K_D) and enzyme turnover number (k_{cat}) are determined (Figure 9). Given that

$$K_M = \frac{k_{OFF} + k_{cat}}{k_{ON}}$$

it is possible to consider $K_D = K_M$ if rapid equilibrium of nucleotide association and dissociation is assumed ($k_{OFF} >> k_{cat}$) [14].

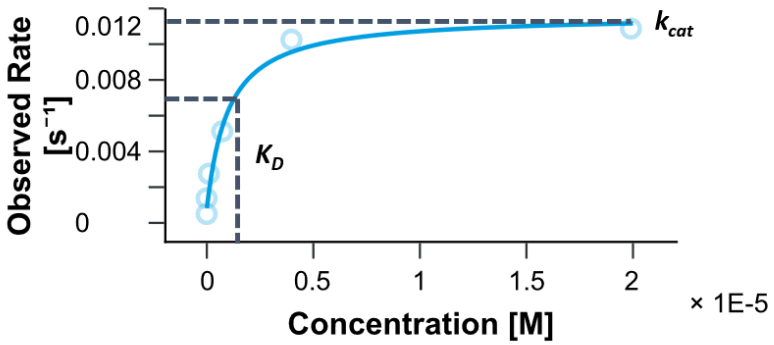

Figure 7. Plot describing Pol DNA elongation activity. The observed rate during DNA elongation are plotted per each dNTP concentration, resulting in a linear plot. The observed rate at saturating substrate concentrations equals the k_{cat}; the dNTP concentration at which is observed the half-maximal elongation rate equals the K_D of Pol for the substrate. When a rapid equilibrium of dNTP association and dissociation is assumed, $K_D = K_M$.

Table 2. *Rate values of Taq Pol binding (k_{ON}) to the Primer-Template DNA and control dsDNA, the DNA elongation activity (k_{cat}) on Primer-template ligand upon dNTP injection, and the affinity (K_D) for the substrate dNTP.*

Ligand	k_{ON} $(M^{-1}s^{-1})$	k_{cat} (s^{-1})	K_D (μM)
Primer-Template	6.45 ± 0.05 E+6	12.0 ± 0.2 E-3	1.86 ± 0.10
dsDNA	5.03 ± 0.05 E+6	N/A	N/A

In this specific case, we do not have all the necessary information to assess whether the K_D equals the K_M, because we do not know the dissociation rate k_{OFF} describing the dNTP dissociation from Pol. Therefore, further studies on the binding kinetics of dNTPs to Pol are needed to clarify the equality. However, gaining information on the affinity of the enzyme for the substrate is important for understanding how fast/slow the dNTPs are in complex with Pol, providing useful information on the activity rate of the enzyme.

Furthermore, by using exactly the same workflow and the same DNA ligands used for Pol, a set of twenty different Pol mutants was tested (Figure 8). The resulting k_{cat}*s* and substrate K_D*s* are listed below in Table 3. Noteworthy, every Pol mutant is able to bind to and elongate the DNA of the Primer-Template ligand, but each Pol mutant has a different elongation activity and speed. For example, Pol mutant #2 can reach a higher fluorescence amplitude during elongation compared to Pol mutant #1 and mutant #5. In addition, by comparing the catalytic values in Table 3, it can be observed that Pol mutant #1 has a slower catalytic rate, while Pol mutant #17 has the fastest activity compared to the other mutants.

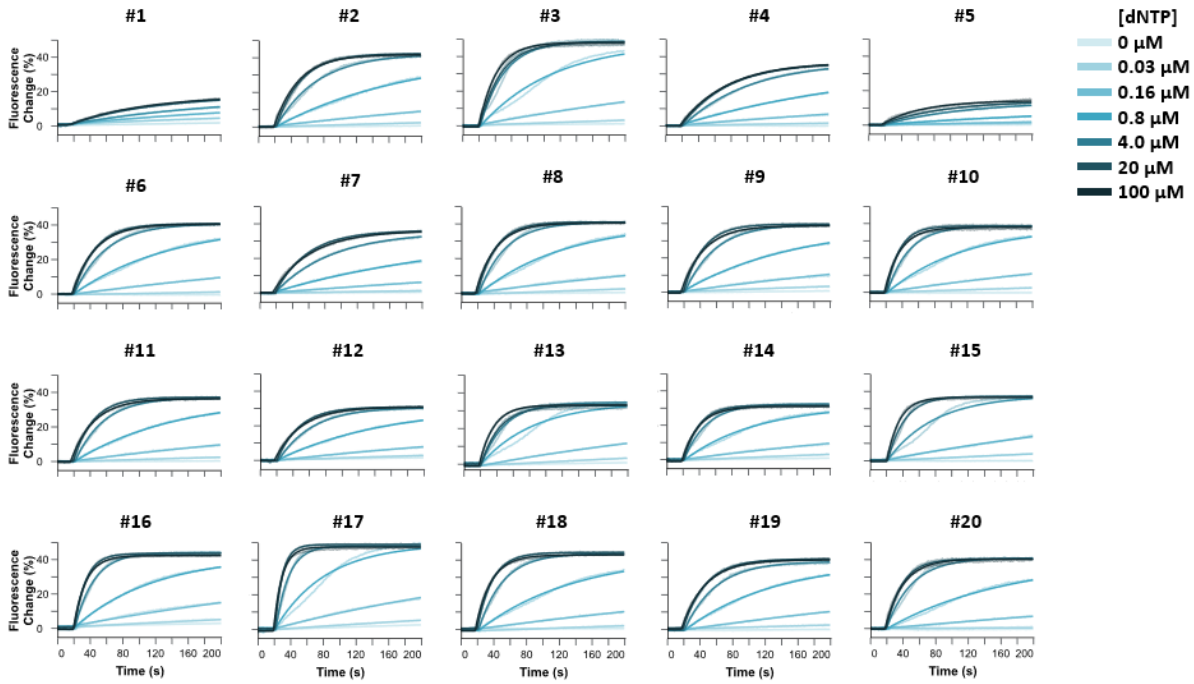

Figure 8. *Screening of Pol mutants. The same workflow and the same Primer-Template ligand that were used to characterize Pol binding and activity (Figure 6), were used to screen a set of 20 different mutant forms of Pol. All the Pol mutants tested showed to be able to elongate the DNA primer strand, although with different speed. Notably, they can lead also to a different maximum fluorescence amplitude.*

Table 3. *Rate values of Pol mutants describing their DNA elongation activity (k_{cat}) on Primer-template ligand upon dNTP injection, and the affinity (K_D) for the substrate dNTP.*

Polymerase mutant (#)	k_{cat} *(E-3 s^{-1})*	K_D *(µM)*	*Polymerase mutant (#)*	k_{cat} *(E-3 s^{-1})*	K_D *(µM)*
1	11.0 ± 0.2	1.00 ± 0.32	**11**	41.6 ± 0.3	2.09 ± 0.43
2	33.2 ± 0.3	2.71 ± 0.37	**12**	35.9 ± 0.3	2.04 ± 0.41
3	48.5 ± 0.7	2.26 ± 0.63	**13**	56.6 ± 1.3	3.06 ± 0.57
4	17.5 ± 0.1	2.17 ± 0.21	**14**	54.5 ± 0.7	2.26 ± 0.46
5	24.8 ± 4.0	3.14 ± 0.46	**15**	67.8 ± 1.9	2.20 ± 0.04
6	40.4 ± 0.3	2.05 ± 0.51	**16**	71.5 ± 0.7	3.20 ± 0.49
7	32.0 ± 0.9	3.01 ± 0.74	**17**	108 ± 3	3.25 ± 0.45
8	45.6 ± 0.4	2.16 ± 0.44	**18**	53.7 ± 0.5	2.78 ± 0.37
9	43.0 ± 0.4	2.34 ± 0.58	**19**	32.9 ± 0.5	2.20 ± 0.24
10	60.1 ± 0.7	2.66 ± 0.65	**20**	54.7 ± 0.6	2.73 ± 0.70

4.2.4 Taq Polymerase characterization: Activity Inhibition

To further characterize Pol binding and activity, an enzyme inhibition assay was performed. The same workflow employed to study Pol activity (Figure 5) was used to test Pol inhibition induced by $CaCl_2$, a known inhibitor of DNA Polymerases [15–17]. However, in this case:

i) In step 2, increasing concentrations of $CaCl_2$ (from 0.16 mM to 10 mM) were added to Pol (5 nM) to test the inhibition of binding to the DNA ligands;

ii) In step 3, a fixed saturating dNTPs concentration (100 µM) was used, while increasing concentrations of $CaCl_2$ (from 0.16 mM to 10 mM) were injected at each cycle to test the activity inhibition.

The result of the presence of $CaCl_2$ can be observed below (Figure 9).

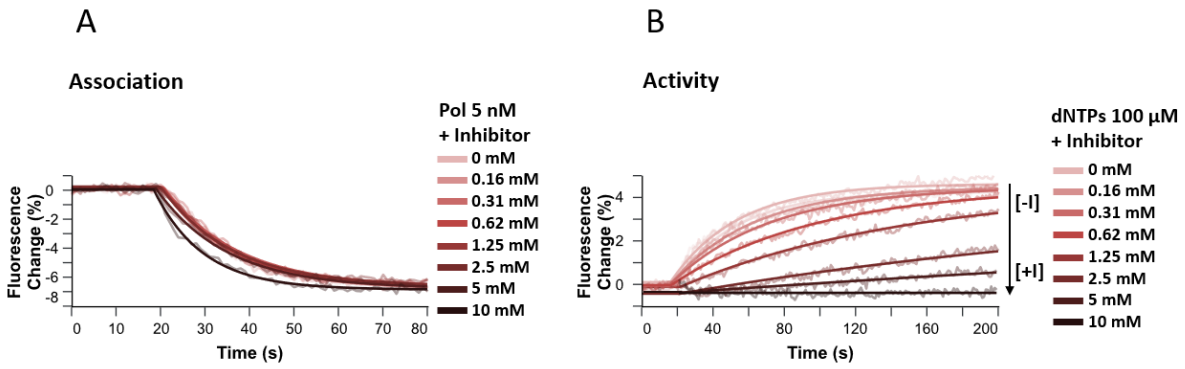

Figure 9. Enzyme inhibition assay. A) Pol binding inhibition. $CaCl_2$ was mixed together with Pol (5 nM) before injection on the surface. Increasing concentrations of $CaCl_2$ do not inhibit Pol binding to DNA. B) Pol activity inhibition. $CaCl_2$ was mixed dNTPs (100 µM) before injection. A decrease in fluorescence levels related to the inhibition of Pol activity can be observed at increasing $CaCl_2$ concentrations.

Pol is injected at a fixed concentration (5 nM) to observe the effect of $CaCl_2$ on the binding to DNA (Figure 8A). However, Pol is able to bind to the DNA ligands despite the presence of the inhibitor, as shown by the quenching of fluorescence signals at each Pol injection. By fitting the association curves with a mono-exponential fit model, the association rate of Pol in presence of $CaCl_2$ can be calculated, resulting in k_{ON} = 3.32 ± 0.05 E+6, very similar to the association rate obtained without $CaCl_2$ (Table 1 and 2), confirming the non-inhibition of its binding ability.

In the next step, $CaCl_2$ is mixed with a fixed concentration of dNTPs (100 µM) to observe the inhibitory effect on the Pol elongation activity (Figure 8B). At low concentrations of $CaCl_2$ (0.16 mM to 0.31 mM), the elongation activity is poorly or not affected, as shown by the increase in fluorescence change that perfectly matches with the run in absence of $CaCl_2$ (blank run with only dNTPs). At intermediate concentrations (0.62 mM to 1.25 mM) the Pol activity is gradually reduced, while higher concentrations (2.5 mM to 5 mM) of $CaCl_2$ drastically decreases the Pol

activity, that is completely inhibited at 10 mM $CaCl_2$. Similarly to the analysis done for the activity, it is possible to plot an inhibition curve by analyzing the activity (%) at each inhibitor concentration (Figure 10), thus providing the half maximal inhibitory concentration (IC_{50}), in this case found to be equal to 0.50 ± 0.03 mM, which is the concentration of inhibitor able to inhibit by 50% the activity of Pol. Other studies on the Pol inhibition reported the IC_{50} of $CaCl_2$ in the single-digit mM range [16], while others observed no inhibition up to 1.5 mM (which is the maximum final concentration used) [18]. However, in these studies the inhibition of the activity is measured as inhibition of the amplification step of PCR, difference that can justify a slightly different value than what observed with the presented system, dynamically studied on a chip surface without incubation step.

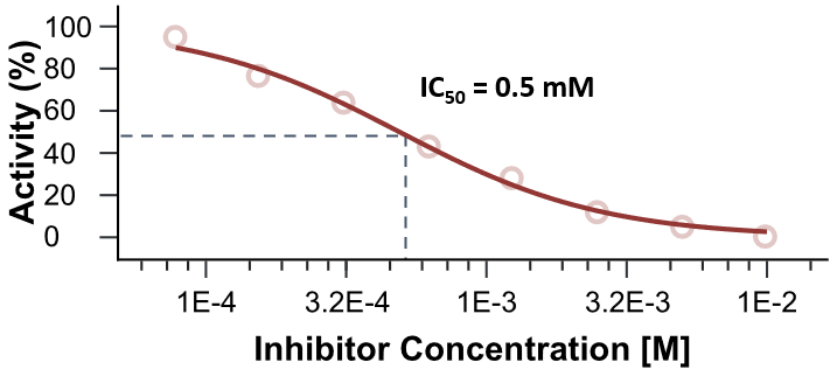

Figure 10. Plot describing Pol inhibition assay. The activity of Pol at saturating concentration of dNTP in presence of increasing concentrations of inhibitor, can be plotted per each concentration of $CaCl_2$. From the resulting curve, it is possible to understand the half maximal inhibitory concentration (IC_{50}).

$CaCl_2$ has been selected as an example of Pol inhibitor for a proof of concept study of the activity inhibition assay. However, this study can be extended to any candidate inhibitor, and also opens the way for a high throughput screening of inhibitors, allowing to identify those that can inhibit the binding to DNA or only their DNA elongation activity, and to compare their IC_{50}.

4.3 Conclusions

The method here reported allows the thorough characterization of DNA polymerases binding to DNA and their polymerization activity, which are topics of great importance in the biomedical and biotechnological field. Binding measurements of polymerase to DNA strands have been performed also with other surface technologies like SPR [19–21], that is also used in a commercially available apparatus developed for sequencing, and commercialized by PacBio [22]. Compared to other technologies [19,23–25], the herein presented switchSENSE®-based method does not require the labeling of the polymerase nor of the dNTPs, which can affect the reliability of the results. In conclusion, with a simple workflow and the same chip,

which can be customized depending on the test system, it is possible to gain information on the mechanism of action of DNA-modifying enzymes, their binding rates (k_{ON}, k_{OFF}), their affinity for DNA and substrates (K_D), and their catalytic properties (k_{cat} and K_M).

4.4 Materials and Methods

4.4.1 Materials

Taq DNA Polymerase (Pol) used in the binding kinetics, in the enzymatic activity assay and in the inhibition assay was purchased from New England Biolabs Inc (product NEB #M0273S). Deoxynucleotide (dNTP) solution mix used in the enzymatic activity assay and in the inhibition assay was purchased from New England Biolabs Inc (product NEB #N0447S). Pol and dNTP mix were stored at -20°C according to the provider instructions, and diluted in the Polymerase running buffer (50 mM HEPES pH 8.3, 75 mM KCl, 2.5 mM $MgCl_2$, 0.05 % Tween20) at the specified concentrations shortly before the measurements. $CaCl_2$ used for the inhibition assay was purchased from Sigma-Aldrich, diluted in the Polymerase running buffer at 50 mM and added to the Pol and dNTP mix solutions at the specified concentrations shortly before the measurement. Biochip surface was functionalized with the DNA ligands of Enzyme Activity kit (HK-EA-1, Dynamic Biosensors).

4.4.2 Chip surface functionalization

All switchSENSE® experiments were performed on a dual-color heliX$^+$ instrument using a standard heliX Adapter Biochip (ADP-48-2-0, Dynamic Biosensors), in which single-stranded DNA (48-mer anchor strands) are covalently attached to the chip surface. Each chip is equipped with 2 gold electrodes (or spots), with different DNA anchor strands. Here, spot 1 was used as a measurement spot, and spot 2 as real-time reference spot. Spot 1 was functionalized with the Primer-Template ligand: the 48-nucleotide ligand strand was elongated with a random sequence of 32 nucleotides carrying a red fluorophore (excitation range 600–630 nm and emission range 650–685 nm) on the 5' distal end, and mixed with the 96-nucleotide dark adapter (not carrying the dye). Spot 2 was functionalized with the dsDNA analogue of spot 1: the 48-nucleotide ligand strand elongated of a random sequence of 32 nucleotides carrying the red fluorophore on the 5' distal end, was mixed with the 96-nucleotide dark adapter (not carrying the dye) elongated of the complementary sequence of 32-nucleotides of the ligand strand (see Figure 2). The ligands were then let hybridize at 25°C for 30 min on a shaker at 600 rpm. Secondly, the ligands were immobilized on the biochip via hybridization of complementary anchor strand. The chip was regenerated and freshly functionalized before each concentration of a measurement series. For chip regeneration, a high-pH regeneration solution (HK-REG-1, Dynamic Biosensors) was used to denature the double stranded DNA nanolevers, disrupting the hydrogen bonds between base pairs: the ligands are washed away

while the covalently attached single-stranded nanolevers remain on the surface and can be reused for a new functionalization step.

4.4.3 Fluorescence Proximity Sensing (FPS) mode

Interaction analysis was performed in fluorescence proximity sensing (FPS) mode with a constant voltage of -0.2 V applied, which forces the surface-tethered DNA ligands into a fixed angle. In the FPS measurements, Pol was injected at the specified concentrations over the two electrodes of the biochip. When Pol binds the DNA ligands on spot 1 (Primer-Template, ss/dsDNA) and on spot 2 (control dsDNA), a decrease in red fluorescence signal can be measured. The fluorescence signal changes occur on the timescale of seconds, and the time dependence of the fluorescence signal directly reflects the Pol-DNA kinetics. Upon the injection of running buffer, Pol dissociates from the DNA ligands and a restoration of the original fluorescence signals can be observed. The sample tray containing the DNA ligands and Pol was set to 15°C during measurements, while the experiment temperature on the biochip was set to 25°C. Pol was diluted and measured in the Polymerase running buffer (50 mM HEPES pH 8.3, 75 mM KCl, 2.5 mM $MgCl_2$, 0.05 % Tween20). Flow rate for association and dissociation reactions was set to 100 µL/min. The red LED power was set to 2. Experiment design, workflow and data analysis were performed with the heliOS software (Dynamic Biosensors). The association and dissociation rates (k_{ON} and k_{OFF}), dissociation constants (K_D) and the respective error values were derived from a global single exponential fit model, upon blank referencing correction.

4.4.4 Enzymatic Activity analysis

Enzymatic activity analysis was performed in FPS mode at 25°C with a constant voltage of -0.2 V applied. Pol was injected at 5 nM concentration over the two electrodes of the biochip for 2 min at 50 µL/min, without any following injection of running buffer. Then, dNTPs were injected at the specified concentrations for 3 min at 50 µL/min, without any following injection of running buffer. When dNTPs reach Pol bound to the Primer-Template ligand in spot 1, an increase in red fluorescence signal can be recorded (see Figure 5). This is thanks to the elongation of the Primer strand by using the Template strand sequence as a guide for DNA elongation. Pol converts the upper part of the DNA from a flexible single-stranded DNA to a more rigid double-stranded DNA, thereby effectively moving away the dye from the fluorescence-quenching surface. The inhibition assay was performed with the same setting specified for the enzymatic activity, and by mixing $CaCl_2$ at the specified concentrations with Pol (5 nM) and dNTPs (100 µM) before the measurements, diluted in running buffer (50 mM HEPES pH 8.3, 75 mM KCl, 2.5 mM $MgCl_2$, 0.05 % Tween20). The red LED power was set to 2. Experiment design, workflow and data analysis were performed with the heliOS software (Dynamic Biosensors). The association rate (k_{ON}), catalytic rate (k_{cat}) and the dissociation

constant (K_D) and the respective error values were derived from a global single exponential fit model (see details in Appendix, section A2.3).

References

1. Keener, J.; Sneyd, J. Biochemical Reactions. In *Mathematical Physiology: I: Cellular Physiology*; Keener, J., Sneyd, J., Eds.; Springer New York: New York, NY, 2009; pp. 1–47 ISBN 978-0-387-75847-3.
2. Berdis, A.J. Mechanisms of DNA Polymerases. *Chem. Rev.* 2009, *109*, 2862–2879, doi:10.1021/cr800530b.
3. Loeb, L.A.; Springgate, C.F.; Battula, N. Errors in DNA Replication as a Basis of Malignant Changes. *Cancer Res* 1974, *34*, 2311–2321.
4. Kunkel, T.A. Considering the Cancer Consequences of Altered DNA Polymerase Function. *Cancer Cell* 2003, *3*, 105–110, doi:10.1016/S1535-6108(03)00027-8.
5. Barbari, S.R.; Shcherbakova, P.V. Replicative DNA Polymerase Defects in Human Cancers: Consequences, Mechanisms, and Implications for Therapy. *DNA Repair (Amst)* 2017, *56*, 16–25, doi:10.1016/j.dnarep.2017.06.003.
6. Aschenbrenner, J.; Marx, A. DNA Polymerases and Biotechnological Applications. *Current Opinion in Biotechnology* 2017, *48*, 187–195, doi:10.1016/j.copbio.2017.04.005.
7. Ishino, S.; Ishino, Y. DNA Polymerases as Useful Reagents for Biotechnology – the History of Developmental Research in the Field. *Frontiers in Microbiology* 2014, *5*.
8. Goodwin, S.; McPherson, J.D.; McCombie, W.R. Coming of Age: Ten Years of next-Generation Sequencing Technologies. *Nat Rev Genet* 2016, *17*, 333–351, doi:10.1038/nrg.2016.49.
9. Kaiser, W.; Rant, U. Conformations of End-Tethered DNA Molecules on Gold Surfaces: Influences of Applied Electric Potential, Electrolyte Screening, and Temperature. *J. Am. Chem. Soc.* 2010, *132*, 7935–7945, doi:10.1021/ja908727d.
10. Tsoi, P.Y.; Yang, J.; Sun, Y.; Sui, S.; Yang, M. Surface Plasmon Resonance Study of DNA Polymerases Binding to Template/Primer DNA Duplexes Immobilized on Supported Lipid Monolayers. *Langmuir* 2000, *16*, 6590–6596, doi:10.1021/la9912951.
11. Tsoi, P.Y.; Yang, M. Surface Plasmon Resonance Study of the Molecular Recognition between Polymerase and DNA Containing Various Mismatches and Conformational Changes of DNA–Protein Complexes. *Biosensors and Bioelectronics* 2004, *19*, 1209–1218, doi:10.1016/j.bios.2003.11.004.
12. Xu, L.; Vaidyanathan, V.G.; Cho, B.P. Real-Time Surface Plasmon Resonance Study of Biomolecular Interactions between Polymerase and Bulky Mutagenic DNA Lesions. *Chem Res Toxicol* 2014, *27*, 1796–1807, doi:10.1021/tx500252z.
13. Zhang, H.; Tang, Y.; Lee, S.-J.; Wei, Z.; Cao, J.; Richardson, C.C. Binding Affinities among DNA Helicase-Primase, DNA Polymerase, and Replication Intermediates in the Replisome of Bacteriophage T7. *Journal of Biological Chemistry* 2016, *291*, 1472–1480, doi:10.1074/jbc.M115.698233.
14. Walsh, M.T.; Roller, E.E.; Ko, K.-S.; Huang, X. Measurement of DNA Polymerase Incorporation Kinetics of Dye-Labeled Nucleotides Using Total Internal Reflection Fluorescence Microscopy. *Biochemistry* 2015, *54*, 4019–4021, doi:10.1021/acs.biochem.5b00269.
15. Bickley, J.; Short, J.K.; McDowell, D.G.; Parkes, H.C. Polymerase Chain Reaction (PCR) Detection of Listeria Monocytogenes in Diluted Milk and Reversal of PCR Inhibition Caused by Calcium Ions. *Lett Appl Microbiol* 1996, *22*, 153–158, doi:10.1111/j.1472-765x.1996.tb01131.x.

16. Kuffel, A.; Gray, A.; Daeid, N.N. Impact of Metal Ions on PCR Inhibition and RT-PCR Efficiency. *Int J Legal Med* 2021, *135*, 63–72, doi:10.1007/s00414-020-02363-4.
17. Opel, K.L.; Chung, D.; McCord, B.R. A Study of PCR Inhibition Mechanisms Using Real Time PCR. *Journal of Forensic Sciences* 2010, *55*, 25–33, doi:10.1111/j.1556-4029.2009.01245.x.
18. Combs, L.G.; Warren, J.E.; Huynh, V.; Castaneda, J.; Golden, T.D.; Roby, R.K. The Effects of Metal Ion PCR Inhibitors on Results Obtained with the Quantifiler ® Human DNA Quantification Kit. *Forensic Science International: Genetics* 2015, *19*, 180–189, doi:10.1016/j.fsigen.2015.06.013.
19. Stengel, G.; Knoll, W. Surface Plasmon Field-Enhanced Fluorescence Spectroscopy Studies of Primer Extension Reactions. *Nucleic Acids Res* 2005, *33*, e69, doi:10.1093/nar/gni067.
20. Buckle, M.; Williams, R.M.; Negroni, M.; Buc, H. Real Time Measurements of Elongation by a Reverse Transcriptase Using Surface Plasmon Resonance. *Proc Natl Acad Sci U S A* 1996, *93*, 889–894.
21. Greive, S.J.; Weitzel, S.E.; Goodarzi, J.P.; Main, L.J.; Pasman, Z.; von Hippel, P.H. Monitoring RNA Transcription in Real Time by Using Surface Plasmon Resonance. *Proc. Natl. Acad. Sci. U.S.A.* 2008, *105*, 3315–3320, doi:10.1073/pnas.0712074105.
22. Vijayan, K.; Diego, S.; Abashin, M.; Diego, S.; Zhang, Y.; Diego, S.; Kahatt, E.; Diego, S.; Wilson, K.; Diego, S.; et al. (54) SEQUENCING DEVICE.
23. Joyce, C.M. Techniques Used to Study the DNA Polymerase Reaction Pathway. *Biochim Biophys Acta* 2010, *1804*, 1032–1040, doi:10.1016/j.bbapap.2009.07.021.
24. Krieg, A.; Laib, S.; Ruckstuhl, T.; Seeger, S. Real-Time Detection of Nucleotide Incorporation During Complementary DNA Strand Synthesis. *ChemBioChem* 2003, *4*, 589–592, doi:10.1002/cbic.200200549.
25. Sandin, P.; Stengel, G.; Ljungdahl, T.; Börjesson, K.; Macao, B.; Wilhelmsson, L.M. Highly Efficient Incorporation of the Fluorescent Nucleotide Analogs TC and TCO by Klenow Fragment. *Nucleic Acids Research* 2009, *37*, 3924, doi:10.1093/nar/gkp266.

PART III.

CONCLUSIONS AND FUTURE DIRECTIONS

Chapter 5

Concluding remarks

5.1 Conclusions

Molecules are the fundamental building blocks of every aspect in living cells and organisms, and life would not exist without molecules interacting with each other. For this reason, the objective of this PhD project was mainly focused on characterizing several types of interactions between different classes of molecules, from small molecules and aptamers, to proteins and big enzymes. The aim is to provide detailed insights on how different molecular mechanisms work, advancing the knowledge on the biophysical aspects of molecular interactions and promoting the drug discovery field. Three case studies on different types of molecules have been chosen and herein presented, fully characterized with the switchSENSE® technology, which, thanks to the DNA-based biochip combined with fluorescence detection and a microfluidic system, allows the in-depth characterization of molecular interactions on a surface.

In the first case study (chapter 2), the switchSENSE® DNA-based chip was converted into an aptasensor for binding to specific molecular targets. Aptamers are short synthetic DNA or RNA strands that recognize and bind a specific target molecule, and they are gaining increasing interest for therapeutic and diagnostic purposes. The thrombin-binding DNA aptamer (TBA) was chosen as a proof-of principle study and thoroughly characterized. In this project, TBA folding and unfolding induced by ion kinetics were studied, showing that different types of ions can induce different aptamer folding orientations. The dependency on the salt species of the thrombin affinity for its aptamer was investigated, demonstrating that buffers containing KCl represent the best environment to promote TBA-thrombin binding. In addition, the described approach can be easily adapted to various DNA/RNA aptamers, finding different applications in the biomedical field.

In the second case study (chapter 3), the supramolecular DNA Y-structure was introduced as a novel tool to study protein-protein interactions. With its dual-colored arms, the Y-structure is an unique approach for characterizing the formation of ternary complexes induced by PROteolysis TArgeting Chimeras (PROTACs), small molecules designed to induce the targeted protein degradation via the ubiquitin-proteasome system. Therefore, PROTACs represent a new strategy in the drug discovery process, that allows to understand the biological function of target proteins, and that helps the development of new therapies in cancer research. In this project, two model systems based on different E3 ligases (VHL and CRBN) were studied, and a set of different PROTAC molecules were analyzed to determine the kinetic rates of ternary and binary complexes formation with the bromodomain (Brd) proteins. Noteworthy, it is the first time that the real-time kinetics of the formation of the ternary complex involving CRBN as ligase were resolved on a surface-based platform.

In the third case study (chapter 4), a versatile method to measure the binding kinetics and activity rates of DNA-modifying enzymes (*i.e.* polymerases, transcriptases, helicases, etc.) was described. These enzymes play fundamental roles inside the nucleus of cells, taking part in genome replication and transcription, and the understanding of their mechanism is essential in the biomedical field. DNA polymerases find also broad applications in the biotechnological field for their application in PCR and in sequencing techniques. In this chapter, the Taq DNA Polymerase performing DNA elongation using another DNA strand as template was used as a model system, and the same strategy was successfully adopted also for reverse transcriptases using RNA strands as template, and also for helicases performing DNA unwinding using ATP as substrate. In addition, the same workflow explained herein, can be used for activity inhibition assays and for high throughput screening of enzymes inhibitors.

In conclusion, during my PhD project I was able to deeply study and characterize the kinetic behavior of different and diverse biological interactions, using the switchSENSE® technology. I was able to study in a straightforward manner DNA aptamers kinetics and DNA polymerases activity, and to establish a new tool for studying protein-protein interactions. By using the dual-color fluorescence detection for FRET analysis and the novel supramolecular DNA Y-structure, I was able to study and fully characterize in an innovative way ternary complexes formation induced by PROTACs.

Appendix

A1. proFIRE®: pure protein-DNA conjugates

A2. Binding Kinetic Theory

A3. Kinetic Fit Operations

A1. proFIRE®: pure protein-DNA conjugates

Protein-DNA conjugates are not only essential components of switchSENSE® workflows, but they are also widely used in biomedical research (DNA repair, DNA modifying enzymes, etc.), and in the DNA nanotechnology field [1]. For example, oligonucleotide-conjugated antibodies are commonly used in therapeutic cell targeting and protein diagnostics [2], and the generation of defined protein-oligonucleotide conjugates as covalent DNA-protein crosslinks (DPCs) is crucial for the understanding of fundamental processes of genome instability [3]. However, conventional purification methods usually require *ad hoc* optimization for each sample to be purified, and generally yield heterogenous mixtures of conjugates. A valuable solution of this major challenge is the proFIRE®, a chromatography system specifically designed for purification of protein-DNA conjugates (Figure A1) [1–3].

Figure A1. *proFIRE® instrument. It is a system based on ion-exchange chromatography, that can be controlled via a tablet-based software. This system has been implemented for purifying DNA-protein conjugates, separating them from the free DNA and unreacted proteins from the coupling process. Source: Dynamic Biosensors.*

A1.1 proFIRE® system

The proFIRE® system performs the purification of DNA-protein conjugates. The proFIRE® is composed of different parts (figure A2):

i. The instrument is equipped with a tablet-based software, that is used for controlling the instrument and for the analysis of the conjugation results. The software allows automatic recognition and quantitation of the conjugates products;
ii. The portable buffer deck can accommodate the two phosphate buffers (named buffer A and B) needed for the purification process;
iii. The ASM (Active Solvent Modulation) module contains: 1) the UV detector, to measure absorbance at 260 nm for detection of DNA in the conjugate sample, 2) the port valves for the injection and for the fractionation, 3) the ion-exchange chromatographic column that allows to separate the DNA-protein conjugates from the free protein and the free DNA based on their charge;
iv. The pump module contains the pump head and the valves needed to distribute the buffers across the system, as well as the compartment for the fraction collection.

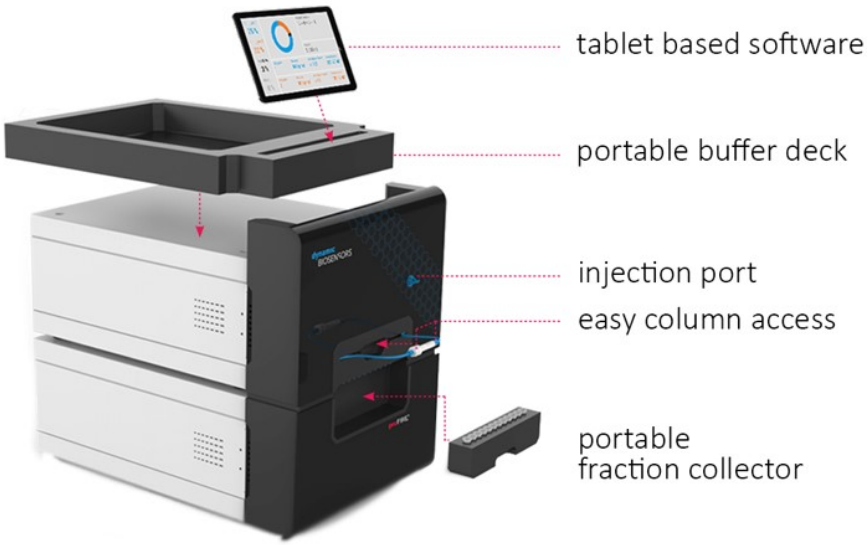

Figure A2. *proFIRE® system components, from top to bottom: tablet equipped with the proFIRE® software, buffer deck, ASM module, pump module. The software installed in the tablet allows to control the device and analyze the purification results. The portable buffer deck can accommodate the buffer bottles. The ASM module includes the chromatographic column and the injection port. The pump module at the bottom includes the portable fraction collector. Source: Dynamic Biosensors.*

The proFIRE® automatically recognizes, purifies and quantitates DNA-protein conjugates from unreacted species independent on DNA length and protein molecular weight. The sample to be purified is injected in the sample loop with the syringe, and then it passes through the ion-exchange chromatographic column, separating the sample mixture based on the charge. The proFIRE® system pumps two different buffers, Buffer A (50 mM Na_2HPO_4/NaH_2PO_4 pH 7.2, 150 mM NaCl) and Buffer B (50 mM Na_2HPO_4/NaH_2PO_4 pH 7.2, 1 M NaCl) at 1 mL/min, creating a buffer gradient that allows the separation of the DNA-protein conjugate from the free DNA and free protein (Figure A3).

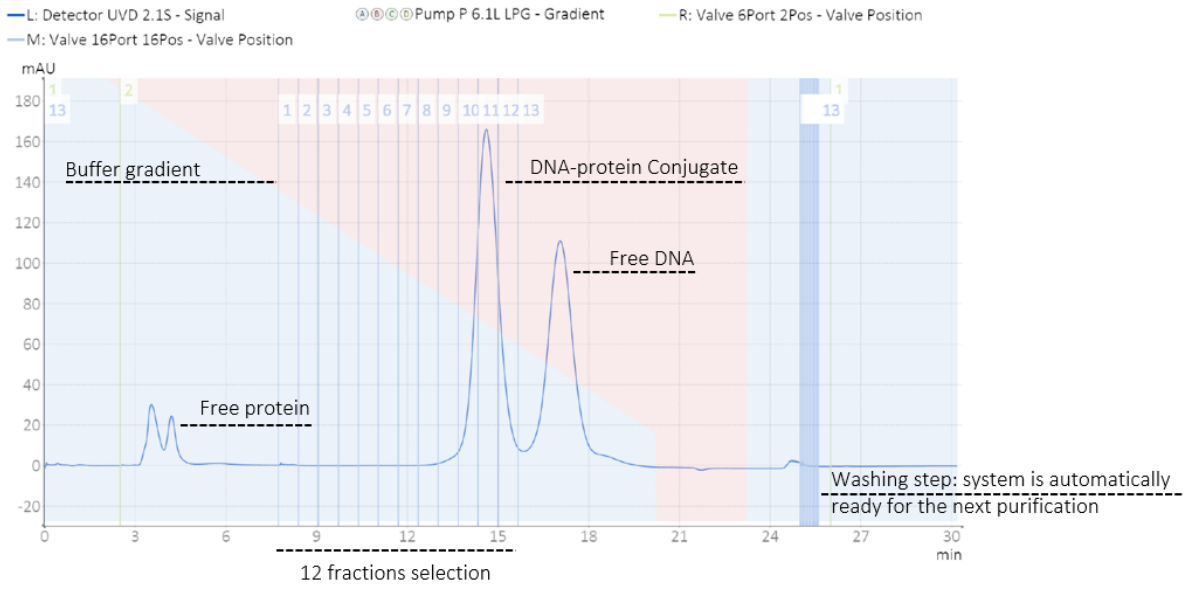

Figure A3. *Example of a raw proFIRE® chromatogram. The two different color-coded areas show the buffer gradient created by the Buffer A (light blue area) and Buffer B (light pink area). It is possible to observe several peaks: the first peak is the one of free protein, the second peak is the one of the DNA-protein conjugate, and the third peak is the one of free DNA. There are 12 fractions where the DNA-protein conjugate can be collected (in this example, in fractions 10, 11 and 12). At the end of the run, a washing step prepares the proFIRE® system for the next purification.*

Molecules with a molecular weight around or lower than 5 kDa require special care during the purification process: small molecules and some peptides may not be properly purified using the standard chromatographic column provided by Dynamic Biosensors. Finally, the proFIRE® software algorithm automatically detects, separate and quantify the conjugate peaks from the free DNA (and unreacted protein), as shown in figure A4.

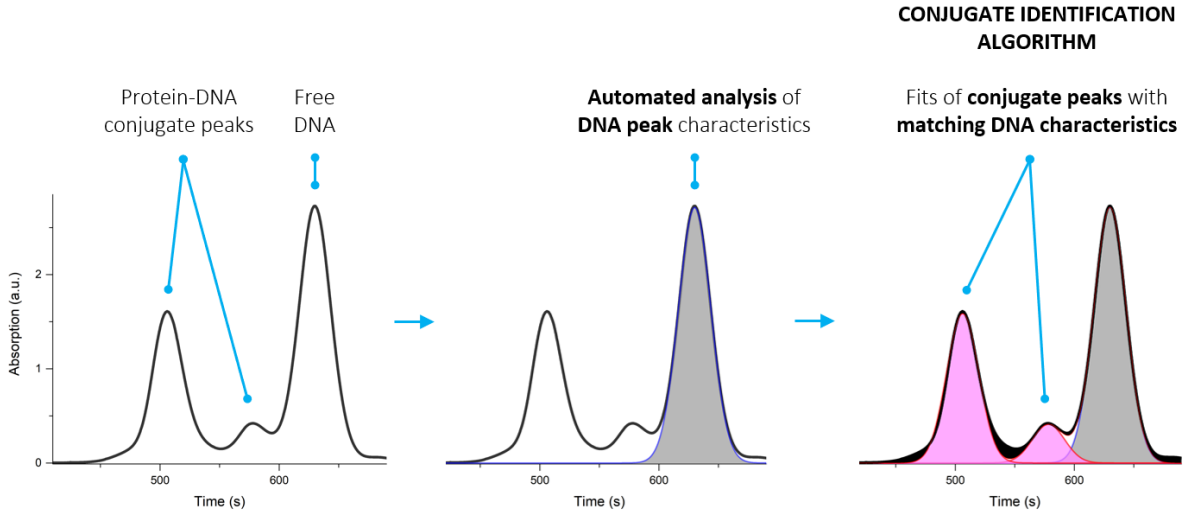

Figure A4. *proFIRE® software smart algorithm automatically detects the peaks and distinguishes the conjugate peak from the free protein and free DNA peaks. Source: Dynamic Biosensors.*

proFIRE® instrument specifications are summarized in the table below:

DNA length	10 – 150 nt
Protein molecular weight	5 – 500 kDa
Injection volume	50 – 1000 µL
Number of fractions	12
Fraction volume	200 – 800 µL
Temperature range	10 – 30°C

A1.2 Conjugation methods

The first step to obtain pure protein-DNA conjugates is to choose the preferred coupling strategy. Dynamic Biosensors provides different coupling kits for covalent coupling of proteins to DNA oligos by employing different coupling strategies:

i. Amine coupling: it allows for coupling of biomolecules with primary amines (e.g. NH_2-terminus, lysines) to the DNA strand (NHS chemistry) [2,3];
ii. Thiol coupling: it allows for coupling of biomolecules with free thiols (e.g. cysteines) to the DNA strand (Maleimide chemistry);
iii. His-mediated amine coupling: it allows for oriented coupling of His-tagged biomolecules with primary amines (e.g. NH_2-terminus, lysines) in the proximity of the His-tag to the DNA strand (NHS chemistry) [4].

The amine coupling is the conjugation method used to couple proteins to DNA oligos in all the cases described in Part II of this PhD thesis. To conjugate proteins to DNA oligonucleotides, a water-soluble crosslinker was used: S-SMCC (sulfosuccinimidyl-4-(N-maleimidomethyl) cyclohexane-1-carboxylate (Figure A5). S-SMCC is a heterobifunctional amine-to-sulfhydryl crosslinker, which contains two reactive groups at opposite ends: N-hydroxysuccinimide (NHS) ester and maleimide. The NHS ester end of the reagent can react with primary amine groups on proteins to form stable amide bonds. The maleimide end of S-SMCC is specific for coupling to sulfhydryls when the reaction pH is in the range of 6.5 to 7.5 [5].

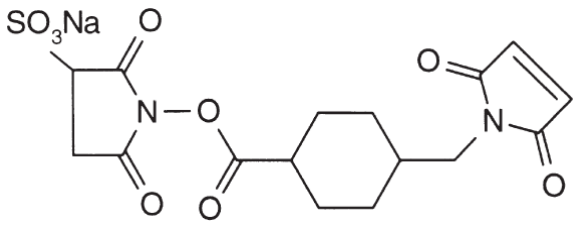

Figure A5. *Structure of S-SMCC (sulfosuccinimidyl-4-(N-maleidomethyl) cyclohexane-1-carboxylate), the heterobifunctional crosslinker used to covalently conjugate DNA oligonucleotides to proteins. Adapted from [5].*

The DNA oligonucleotides that are used for the amine coupling of proteins are modified with a thiol group by the manufacturer (Ella Biotech, Germany), reacting therefore with the maleimide group of S-SMCC. Once the DNA oligo gets *activated* with the crosslinker, it is incubated with the protein of interest, that will be coupled via its primary amines to the NHS group of S-SMCC. In fact, the protein primary amine group reacts as nucleophile and attacks the carbonylic group of the NHS ester. A reaction intermediate is formed, that, with an electron rearrangement, leads to the formation of an amide bond and to the release of the NHS as leaving group. A schematic representation of the NHS chemistry used to conjugate proteins is depicted below in Figure A6.

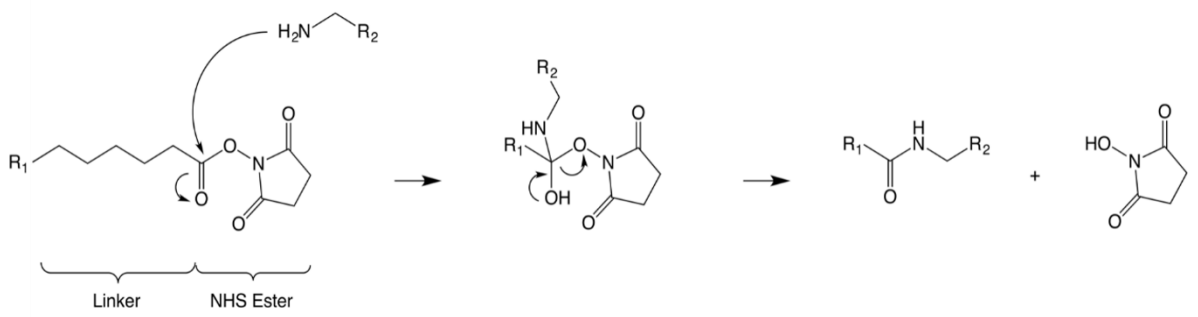

Figure A6. *Reaction mechanism of NHS chemistry used to covalently link proteins via their reactive amine groups (R_2-NH2) with subsequent amide bond formation. This strategy is adopted to covalently link proteins to DNA oligonucleotides. Adapted from [6].*

A1.3. Conjugation and purification protocol

In part II of this thesis, for all the case studies which required protein immobilization on the biochip surface, a standard amine coupling kit (HK-NHS-1) has been used for conjugating proteins to a 48mer DNA strand and obtaining protein-DNA conjugates, and the purification of the DNA-protein conjugates has been performed with the proFIRE® system. The amine coupling kit allows for coupling of biomolecules with primary amines to the DNA (ligand strand) in a single reaction tube. Primary amines exist at the N-terminus of each polypeptide chain and in the side-chain of lysine amino acid residues, thus the accessibility of these groups will affect the conjugation reaction. It is also important to avoid using any buffers containing primary amines (i.e. Tris, Glycine) that can compete with the protein conjugation process, and thiol-based reducing agents (Dithiothreitol, 2-mercaptoethanol, etc.), that can impair the coupling reaction. The conjugation-purification protocol is described in detail below and summarized in figure A7. The protocol is divided in four main steps:

1. The first step consists in the modification of the DNA strand, or ligand strand, with a crosslinker;
2. In the second step, the protein, or ligand, is incubated with the activated DNA;
3. The third step is the purification of the DNA-protein conjugate via the proFIRE®;

4. The fourth step consists in the concentration of the DNA-protein conjugate and buffer exchange for optimal storage conditions.

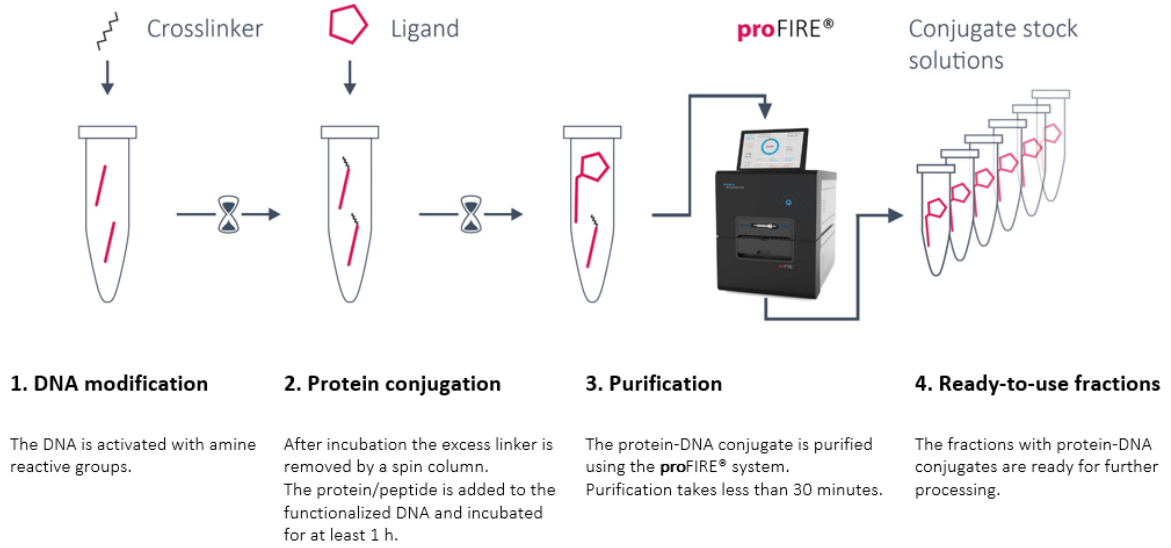

Figure A7. *Conjugation-purification workflow. The first step involves the activation of the ligand strand with a crosslinker. After that, the excess crosslinker is removed through a spin column, and the ligand is added in the solution with the activated ligand strand. The hands-on time for the conjugation is circa 30 min. After a proper incubation time, the ligand-DNA conjugate is then purified with the proFIRE® system. The purification yields fractions solutions ready to be stored or further processed. Source: Dynamic Biosensors.*

Step I: DNA modification

In the first step, a 48mer DNA strand, also called Ligand strand, is incubated with the crosslinker, yielding an intermediate activated product that will react with the reactive amine groups of the protein in the second step.

1. Dissolve Ligand strand NHS in 40 µL Buffer A (50 mM Na_2HPO_4/NaH_2PO_4 pH 7.2, 150 mM NaCl, Dynamic Biosensors) prior to use, vortex until all solids are completely dissolved and briefly spin down.
2. Dissolve the crosslinker (Dynamic Biosensors) by adding 100 µL ddH_2O, vortex until all solids are completely dissolved and briefly spin down.
3. Add 10 µL of the freshly prepared linker solution to one Ligand strand aliquot. Discard the remaining linker solution from step 2.
4. Vortex the reactants for 10 sec, spin down and incubate for 20 minutes at room temperature. In this step it is important to not exceed incubation time or the reaction yield will decrease.
5. In the meantime, equilibrate two purification spin columns for coupling reaction:
    a. Remove the column's bottom seal and loosen cap (do not remove cap).
    b. Place the column in a 2.0 mL reaction tube.
    c. Centrifuge at 1,500 × g for 1 minute to remove the storage solution.

d. Add 400 µL of Buffer C (50 mM Na_2HPO_4/NaH_2PO_4 pH 8.0, 150 mM NaCl, Dynamic Biosensors) to the column's resin bed. Centrifuge at 1,500 × g for 1 minute to remove buffer.
e. Repeat step d and discard the resulting buffer from the reaction tube. The purification spin column should now be in a dry state.

6. Sample loading:
   a. Place the columns from step 5 in new 1.5 mL reaction tubes.
   b. Remove the cap of spin column number 1 and apply the sample from step 4 to the top of the resin bed.
   c. Centrifuge at 1,500 x g for 2 min to collect the sample (flow-through). Discard the Purification spin column after use.
   d. Remove the cap of spin column number 2 and apply the sample from step c to the resin bed.
   e. Centrifuge at 1,500 x g for 2 min to collect the sample (flow-through). Discard the Purification spin column after use.

Step II: Protein conjugation

In the second step, the protein ligand is added to the activated DNA sample, in order to achieve the conjugation through the protein amine groups.

7. Add approx. 100 µg (up to a maximum of 200 µg) of the protein (concentration approximately 0.5 – 50 mg/mL) to the sample from step 6.
8. Mix the reaction by pipetting up and down (it is important to not vortex) and let it react at room temperature for at least 1 hour. If necessary, the reaction can be carried out at 4°C with a longer reaction time (e.g. overnight).

Step III: Purification

In the third step, the DNA-protein conjugate sample is purified via the proFIRE® in order to separate the conjugate from the free DNA and the unreacted protein.

9. Perform a purification using the appropriate proFIRE® workflow. The sample volume must be 160 µL: if the volume is less than 160 µL, make up the missing volume with Buffer C; if the volume exceeds 160 µL, please perform additional 160 µL runs until all of the sample is consumed.
10. Use the Data Viewer software of the proFIRE® to identify which fractions contains pure conjugate. Examples of chromatograms are shown in figure A8-10 here below.
11. Remove the recommended fractions from the fraction collection.

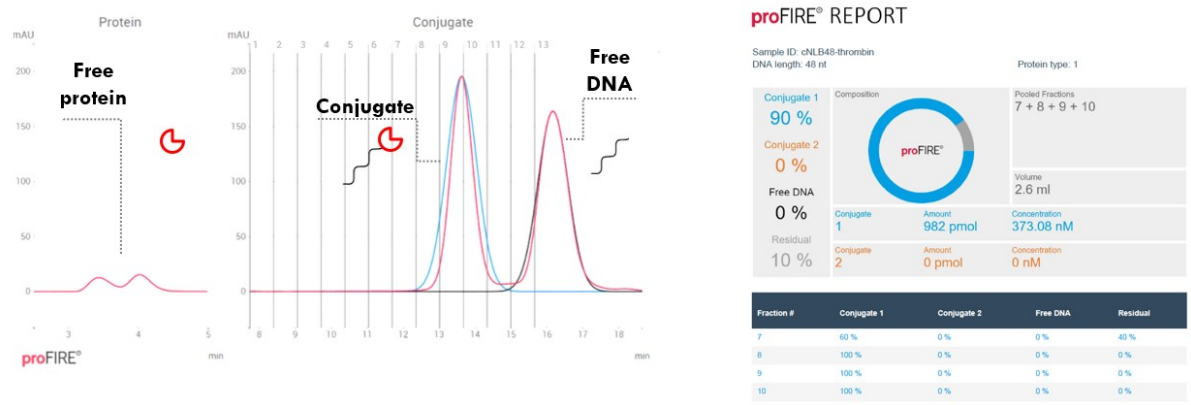

Figure A8. *Example of proFIRE® chromatogram and resulting report of a DNA-protein conjugate of a medium-sized protein (thrombin, 37 kDa). In the chromatogram, multiple peaks can be observed: the first peak belongs to the unreacted free protein, the second peak is the protein-DNA conjugate, the third peak is the free DNA peak that did not react with the protein. The purification is performed via ion exchange in a buffer gradient that allows to separate the conjugate from the free DNA. Buffers used: Buffer A and Buffer B. Column: DBS-Chromatographic column. Flow: 1 mL/min. Used program: DNA length 48, Type 1. The proFIRE® software provides a report with indications regarding the amount and concentration of conjugate in each selected fraction.*

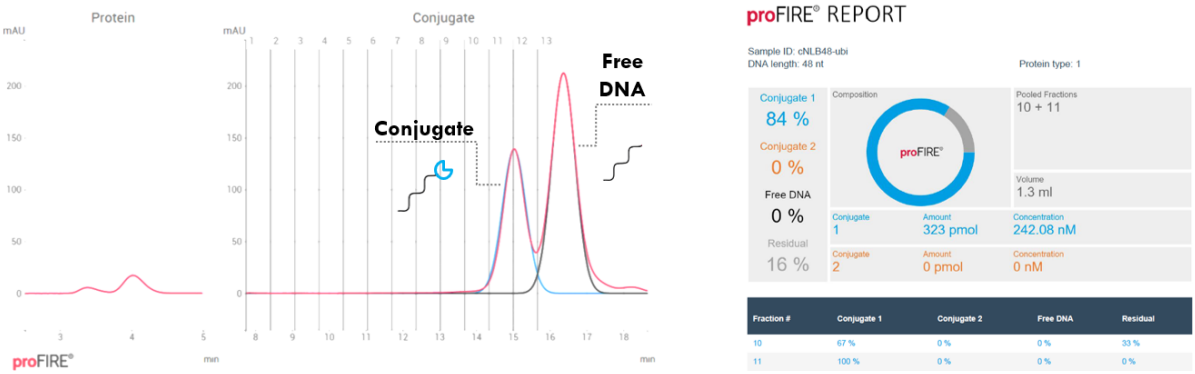

Figure A9*. Example of proFIRE® chromatogram and resulting report of a DNA-protein conjugate of a small-sized protein (ubiquitin, 8 kDa). Buffers used: Buffer A and Buffer B. Column: DBS-Chromatographic column. Flow: 1 mL/min. Used program: DNA length 48, Type 1. The proFIRE® software provides a report with indications regarding the amount and concentration of conjugate in each selected fraction.*

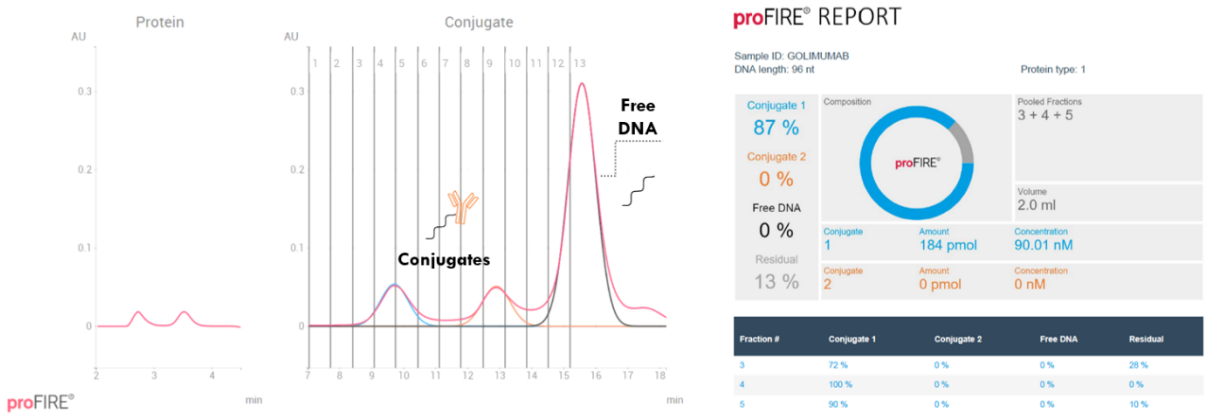

Figure A10. *Example of proFIRE® chromatogram and resulting report of a DNA-protein conjugate of an antibody (Golimumab, 150 kDa). Buffers used: Buffer A and Buffer B. Column: DBS-Chromatographic column. Flow: 1 mL/min. Used program: DNA length 96, Type 1. The proFIRE® software provides a report with indications regarding the amount and concentration of conjugate in each selected fraction.*

Step IV: Ready-to-use fractions

Since the last buffer used during the purification step is high in salt concentration, for optimal storage, the buffer exchange to low salt content is an important step to preserve the DNA-protein conjugate.

12.

a. Add 500 µL of the first proFIRE ® fraction containing the Ligand strand conjugate to the centrifugal filter unit. Centrifuge at 13,000 x g (up to 14,000 x g) for 10 minutes and discard flow-through.
b. Add the remaining fractions to the same filter unit and repeat the centrifugation step in order to collect all samples in one tube.
c. Add 350 µL of desired storage buffer (e.g. PE40, HE40, TE40, which are respectively phosphate-, hepes- and tris-based buffers containing 40 mM of NaCl) and centrifuge at 13,000 x g for 10 minutes. Discard the flow-through again.
d. Add 350 µL of desired storage buffer and centrifuge at 13,000 x g for 15 minutes. Discard the flow-through again.
e. To recover the Ligand strand conjugate, place the centrifugal filter unit upside down in a new centrifugal collection tube. Spin for 2 minutes at 1,000 x g to transfer the sample to the tube. Check Ligand strand conjugate concentration after buffer exchange by using absorbance at 260 nm and the following equation (Lambert-Beer equation):

$$\mathbf{C = A/(\varepsilon \times d)}$$

C = concentration ligand strand conjugate
A = absorbance at 260 nm
ε = extinction coefficient Ligand strand = 490,000 L mol^{-1} cm^{-1}
d = optical path length (usually 1 cm)

13. Adjust the concentration to 200 nM – 1 µM in the desired storage buffer (including up to 10 % glycerol if needed).
14. Store between 8°C and -86°C as desired.

A2. Binding kinetics theory

A2.1 Studying molecular interactions

Molecules and proteins exert their actions by interacting with their specific molecular targets. When two interacting species, such as a ligand molecule (L) and a target analyte molecule (T), are in the same environment, they can bind forming a reversible complex at equilibrium. The mechanism of interaction is composed by 2-steps process: 1) association phase, when the complex is formed, and 2) a dissociation phase, when they dissociate into free species (Figure A11). These two phases are described by association and dissociation rates, indicated with k_{ON} and k_{OFF}, respectively. Thus, studying binding reaction kinetics means describing the rates at which an interaction between two molecules occurs [7,8], allowing to infer the strength of the interaction and the stability of the complex formed between the two molecules.

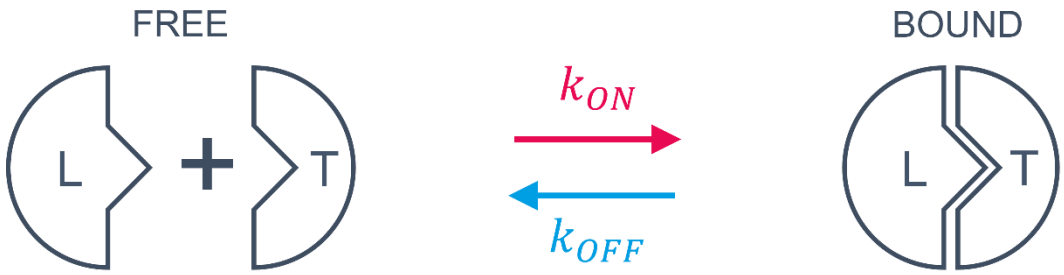

***Figure A11**. Whenever two interacting molecular partners, e.g. a ligand L and a target analyte T, are free to move and interact, they can bind and form a molecular complex. Generally the complex formation is a reversible process, thus we can see an association phase and a dissociation phase. The association into a complex and the dissociation into free molecules is described by binding rates, the association rate (k_{ON}) and the dissociation rate (k_{OFF}).*

There are two possible ways to study the interactions label-free: in solution (e.g. ITC), or on a surface in a flow channel (e.g. SPR and switchSENSE®). These two ways to study interactions differ in the information content they provide:

- in solution-based methods, the main advantage of studying interacting molecules is their availability to freely interact in a native-like environment. However, the main disadvantage is that once molecules are added in the solution environment, they cannot be removed, which means that only the affinity or dissociation constant *(K_D)* can be calculated from the reaction at the equilibrium via titration of the two species. In addition, normally large volumes and wide range of concentrations need to be used for accurate affinity calculation, which are not always available for biological systems;
- in surface-based methods (e.g. in a flow channel), the main advantage is that the interacting molecules can be removed after being added in the reaction environment, through the flow, providing full kinetic information of the binding reaction. Therefore,

association rate *(k_{ON}),* dissociation rate *(k_{OFF}),* and the affinity *(K_D)* can be calculated from real-time measurements. Here, the main disadvantage is the requirement of having one of the two interacting molecule immobilized on the surface, in order to follow the dynamism of the interaction.

Since all the kinetics measurements presented in chapters 2, 3 and 4 have been measured by using the switchSENSE® technology, the description of the binding kinetic theory in the next paragraph is focused only on interactions studied with surface-based methods.

A2.2 Binding at equilibrium

In surface-based methods, the ligand molecule is immobilized on the surface, and the target analyte molecule is carried on the surface with a flow. The association with the ligand starts when the target analyte is injected on the biosensor surface. Then, the dissociation is achieved through a buffer injection, that allows to separate the target analyte from the ligand. Thus, their interaction can be formulated as:

$$L + T \underset{k_{OFF}}{\overset{k_{ON}}{\rightleftharpoons}} LT \qquad \text{(I)}$$

where LT is the resulting ligand-analyte complex. The association and dissociation of the two molecular species are described by the association rate k_{ON} (M^{-1} s^{-1}) and by the dissociation rate k_{OFF}.(s^{-1}). At equilibrium, the rate of complex formation equals the rate of complex dissociation into the singular molecular species, and can be expressed as:

$$k_{ON}\,[L][T] \rightleftharpoons k_{OFF}\,[LT] \qquad \text{(II)}$$

where the square brackets indicate the concentration of each molecular species at equilibrium. The dissociation constant K_D (M) is defined by:

$$K_D = \frac{k_{OFF}}{k_{ON}} = \frac{[L][T]}{[LT]} = \frac{1}{K_A} \qquad \text{(III)}$$

where K_A (M^{-1}) is the association constant. Based on this equation, that is known as *law of mass action* in solution [9], an interaction with a fast association rate and a slow dissociation rate, has a high association constant and a low dissociation constant, and consequently a high

binding affinity. It is often preferred to consider the K_D rather than the K_A, because it has a unit of a concentration (M) and can be more easily correlated to the reactant concentrations.

The theory behind binding kinetics at equilibrium describes interactions between molecules in solution. Therefore, assumptions must be made for surface-based technologies, that require the ligand to be immobilized on the surface, while the target analyte is free in solution. When proper theoretical and experimental considerations are applied, surface-based technologies are tools that provide reliable data that match with the ones obtained with solution-based technologies [10]. A practical consequence for surface-based technologies like switchSENSE® is the constant number of ligand molecules (n_{L0}) immobilized on the biosensor surface:

$$n_{L0} = n_L + n_{LT} = constant \quad \text{(IV)}$$

where n_L is the number of free binding sites of the ligand, and n_{LT} is the number of ligand binding sites occupied by the target analyte. This equation introduces another important term in surface biosensor analysis, the *fraction bound* (f), that correlates with the output signal, and is determined by the number of ligand binding sites occupied with the target analyte over the total number of ligand binding sites:

$$f = \frac{n_{LT}}{n_{L0}} \quad \text{(V)}$$

The fraction bound is 0% when no analyte is injected through the surface, and it is 100% when the ligand binding sites are fully occupied by analyte molecules. As a consequence, the law of mass action can be rearranged for surface-based biosensors into:

$$f_{eq}[T] = \frac{[T]}{[T]+K_D} \quad \text{(VI)}$$

that correlates with the Langmuir isotherm for gas molecules adsorbed to a surface, and it implies that the fraction of analyte bound at the equilibrium is only dependent on the analyte concentration and on the dissociation constant [11]. If the target analyte concentration is equal to the dissociation constant, the fraction bound is 50% and half of the total number of ligand binding sites are occupied.

Characterizing a binding reaction kinetics means not only to understand how strong is the interaction, but also to study how the ligand and the analyte interact during a specific period of time (t). During the association phase of the target analyte at a given concentration, the fraction bound can be described as:

$$f(t,[T]) = f_{eq}\,[T] \cdot \left[1 - exp\{-k_{ON}^{obs} \cdot t\}\right] \quad \text{(VII)}$$

where k_{ON}^{obs} is the observable association rate and it is inversely correlated with the time constant τ:

$$k_{ON}^{obs} = [T] \cdot k_{ON} + k_{OFF} \quad \text{(VIII)}$$

$$k_{ON}^{obs} = \frac{1}{\tau_{ON}^{obs}} \quad \text{(IX)}$$

In order to observe the dissociation of the target analyte from the ligand, pure buffer solution, not containing the analyte $([T] = 0)$, is injected through the surface. The fraction bound therefore is measured as:

$$f(t) = a \cdot exp\{-k_{OFF} \cdot t\} \quad \text{(X)}$$

where a is the amplitude and corresponds to the fraction bound just before the dissociation phase (Figure A12).

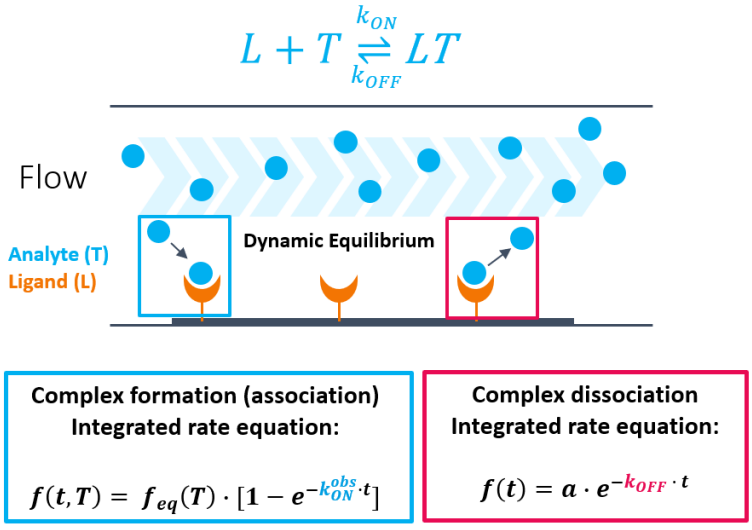

Figure A12. *The fraction bound (f) correlates with the number of ligand binding sites occupied with the target analyte over the total number of ligand binding sites. The target analyte associates and dissociates from the ligand*

in a dynamic equilibrium, and the fraction of analyte bound at the equilibrium is only dependent on the analyte concentration and on the dissociation constant.

Hence, the dissociation of the target analyte is dependent only on the dissociation rate constant and the time constant:

$$k_{OFF} = \frac{1}{\tau_{OFF}} \quad \text{(XI)}$$

The observable dissociation time constant τ_{OFF} is therefore not dependent on the analyte concentration. Moreover, the dissociation phase is always represented by the same dissociation rate k_{OFF}, regardless of the duration of the association phase and therefore of the surface saturation state (Figure A13).

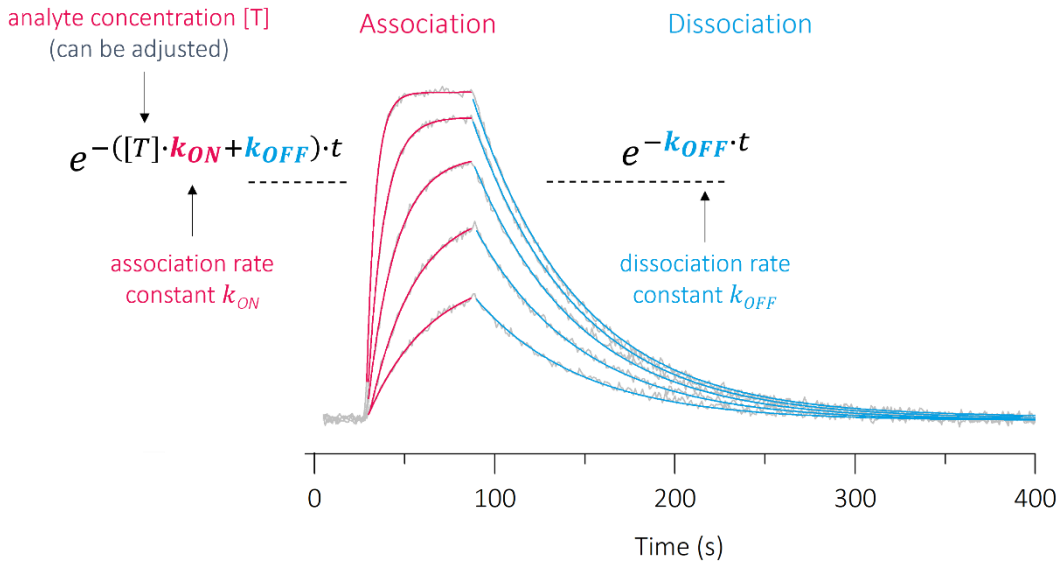

Figure A13. *Example of a sensorgram of an interaction studied on switchSENSE® biosensor surface. In this example, a DNA-DNA interaction was studied by immobilizing a DNA ligand of 9bp and injecting a DNA analyte of 7bp at increasing concentrations (from 30nM to 500nM). The association rate and dissociation rate are studied with single-exponential functions as described above.*

The binding model explained above describes the simplest cases, where one type of target analyte interacts with one type of surface-bound ligand (1:1 interaction or *binary* interaction). However, in nature exist more complex cases with multivalent interactions, e.g. bivalent antibody binding to two target antigens at the same time. For instance, molecules that are able to interact with two different binding partners, are referred to as *bispecific* molecules (*ternary* interaction), which are often described by mono or biphasic associations and biphasic dissociations. Nevertheless, even more complex situations can occur, and it is important to

select the fit model based on a scientific hypothesis, and test this hypothesis against the experimental data.

In a classic bispecific case, equation (X) can be expanded to take into account more than one dissociation:

$$f(t) = a_1 \cdot exp\{-k_{OFF,1} \cdot t\} + a_2 \cdot exp\{-k_{OFF,2} \cdot t\} + \ldots \quad \text{(XII)}$$

The amplitudes describing these kind of interactions ($a_1, a_2, \ldots$) reflect the contributions of each dissociating species to the full dissociation curve, e.g. biexponential binding curves are the sum of two monoexponential curves with distinct amplitudes (Figure A14).

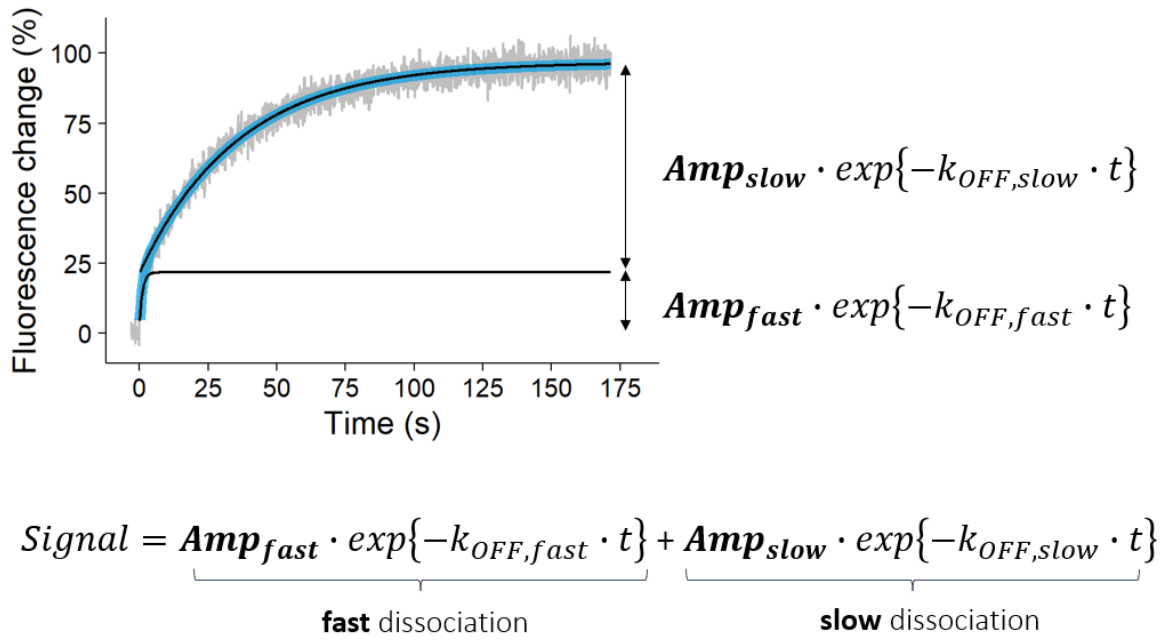

Figure A14. *Kinetics of bispecific analytes described by biphasic dissociations are characterized by a fast-dissociating and a slow-dissociating populations of the bispecific analyte. This biphasic dissociation is described by two distinct amplitudes, reflecting the contribution of each dissociating species. Adapted from [12].*

The interaction of bispecific analytes with their ligands is described by two distinct binary interactions (Figure A15). The coexistence of two interactions can result in an increased apparent affinity, usually called *avidity*, and increased target residence time [13]. This is due to the fact that when a bivalent molecule forms the first binary interaction, this could engage and trigger the formation of the second binary interaction with the second target, which is in close

proximity of the biosensor surface (Figure A15), leading to a ternary complex. Therefore, it is extremely important to discriminate between the single affinity of each binary interaction from the avidity resulting from the ternary complex interaction, and in addition to distinguish the avidity from the classic rebinding artefacts.

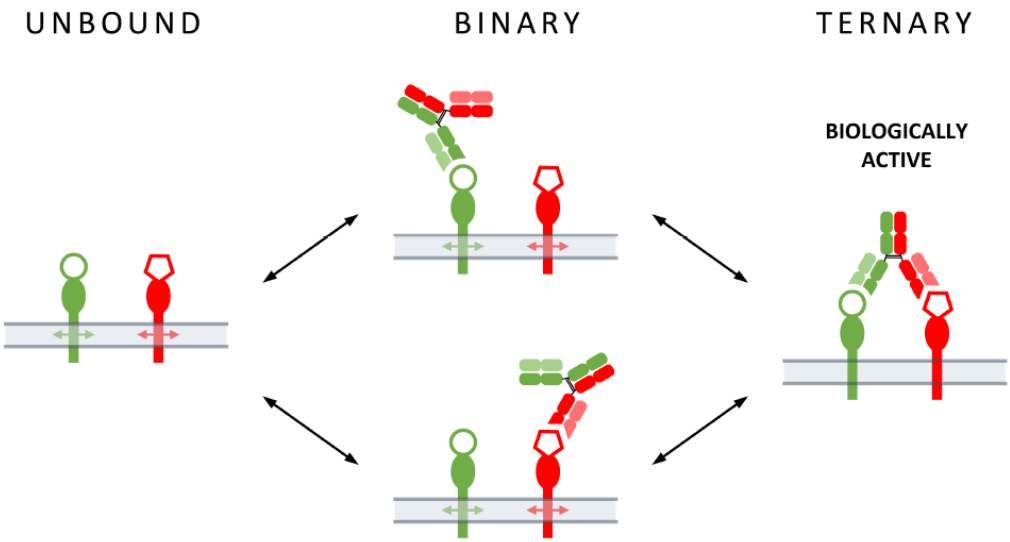

Figure A15. *Bispecific analytes can interact with two different ligands at the same time. Their interaction is therefore described by two distinct binary interactions with both ligands, giving rise to a ternary interaction. Adapted from [12].*

Another crucial parameter to consider in studying kinetics with surface-based technologies is the effect of the mass transport limitation (MTL) [14], that can lead to a difference in the concentration of the analyte in the flow and close to the surface (Figure A16). The more ligand binding sites are present on the surface, the more effective the analyte mass transport needs to be in order to replace the analyte drawn to the surface. Analyte molecules can diffuse only when they are not bound; therefore, their effective diffusion on the surface is slower than the diffusion in the solution flow. This results into analyte concentration gradients, that can affect the resulting binding kinetics: the association rate constant k_{ON} is slower than the true k_{ON}, and the dissociation rate constant k_{OFF} is slower than the true k_{OFF}. The MTL effect is easy to be visually recognised, since the binding curves (both in association and dissociation) are better described by a simple linear fit, rather than a first order exponential fit. Working at low ligand densities highly prevents this rebinding artefacts due to overcrowding surface [15], circumventing the MTL effect. In addition, working with high flow rates helps on making more effective the transport and removal of the analyte on the surface, preventing MTL effect.

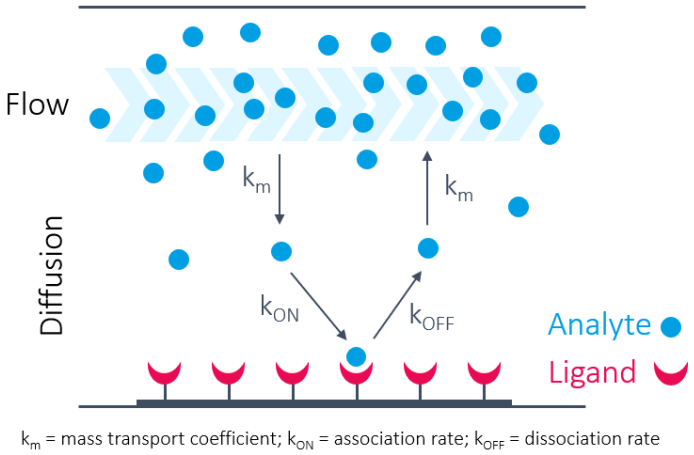

Figure A16. *Measurements artefacts can include mass transport limitations given by a different analyte diffusion on the surface compared to the flow, and by rebinding effects of the analyte when the ligand density is too high.*

Based on these considerations, it is clear how important is to properly study the full real-time kinetics with the relative association and dissociation rates *(k_{ON}* and *k_{OFF}*), and not only the affinity at the equilibrium (K_D), since molecular complexes that are characterized by a similar binding strength might have completely different kinetics and rates of formation and disruption.

In conclusion, when studying the binding kinetics of molecular interactions with surface-based methods, it always important to work in the proper range of analyte concentrations and pay attention to artifacts that can occur when the experimental conditions are not chosen properly, such as high ligand density or slow flow rate, which can heavily impact the estimated association and dissociation rates, and as consequence the binding affinity.

All the kinetics measurements studied and presented in the previous chapters have been analyzed with switchANALYSIS software (Dynamic Biosensors GmbH) or heliOS software (Dynamic Biosensors GmbH), that provide different data analysis options and kinetics fit operations (described in appendix A3).

A2.3 Enzyme kinetics on a biosensor surface

Another complex case existing in nature regards the reactions catalyzed by enzymes. Enzymes have the peculiarity to be able to convert substrate molecules into different product molecules without being affected by the reaction itself, *i.e.* they are not consumed during the reaction process. Enzymatic reactions do not follow the law of mass action [8,16], since the reaction rate does not increase linearly with the substrate concentration, but it reaches a maximal velocity at high substrate concentrations.

The first model developed to describe reversible enzymatic reactions was proposed by Michaelis and Menten (1913), where the enzyme (E) first forms a complex (ES) with the substrate (S), that can then form the product (P) releasing the enzyme:

$$E + S \underset{k_{OFF}}{\overset{k_{ON}}{\rightleftharpoons}} ES \xrightarrow{k_{cat}} E + P \quad \text{(XIII)}$$

where the rate of ES formation is described by an association rate k_{ON} that can reversibly dissociate with a dissociation rate k_{OFF}, and the rate of product formation (or *catalytic rate*) is described by k_{cat}.

In this first model, it was assumed that the substrate reaches an instantaneous equilibrium with the complex (*equilibrium approximation*):

$$k_{ON}[S][E] = k_{OFF}[ES] \quad \text{(XIV)}$$

And since $E + ES = E_0$, it is possible to formulate:

$$[ES] = \frac{[E_0][S]}{K_S + [S]} \quad \text{(XV)}$$

Where K_S is k_{OFF}/k_{ON}. Therefore, the velocity (V) of the reaction, or the rate of product formation, is obtained by:

$$V = \frac{d[P]}{dt} = k_{cat}[S] = \frac{k_{OFF}[E_0][S]}{K_S + [S]} = \frac{V_{max}[S]}{K_S + [S]} \quad \text{(XVI)}$$

And $V_{max} = k_2[E_0]$ is the maximum reaction velocity, reached when all the enzyme is in complex with the substrate (that is, at saturating concentration of substrate). At $[S] = K_S$, the reaction rate is at half of the maximum.

In 1925 Briggs and Haldane proposed a different way to analyze the enzymatic reactions, taking into consideration a *quasi-steady-state approximation*. In this model, the rates of formation and dissociation of the ES complex were essentially equal at all times. Therefore, $d[ES]/dt$ should be approximately zero. Through some rearrangements of equation (XVI), they introduced the *Michaelis-Menten law*:

$$V = \frac{d[P]}{dt} = -\frac{d[S]}{dt} = \frac{k_{cat}[E_0][S]}{[S] + K_M} = \frac{V_{max}[S]}{[S] + K_M} \quad \text{(XVII)}$$

where the constant $K_M = \frac{k_{OFF} + k_{cat}}{k_{ON}}$.

As with the law of mass action, the *Michaelis–Menten law* (XVII) is not universally applicable but is a useful approximation.

Being switchSENSE® a DNA-based surface technology, it is an ideal system to study enzymatic reactions [17], since DNA ligands are embedded in the biochip surface (Chapter 1, section 1.4.2). The presence of a fluorescent dye at the distal end of the DNA nanolevers provides information on the distance of the dye from the gold surface, thus acting as a *molecular ruler*, since the proximity to the surface provokes quenching of its fluorescence [18]. Therefore, by measuring the emitted fluorescence intensity, it is possible to analyze in real-time the DNA elongation activity of DNA polymerases upon deoxynucleoside triphosphates (dNTPs) substrate injection (Figure A17). Upon the addition of dNTPs substrate to the polymerase-DNA complex, the recorded fluorescence intensity increases significantly. This is thanks to the elongation of the primer DNA by using the ligand strand as a template. The polymerase converts the upper part of the DNA from a flexible single-stranded DNA to a more rigid double-stranded DNA, thereby effectively moving away the dye from the fluorescence-quenching surface.

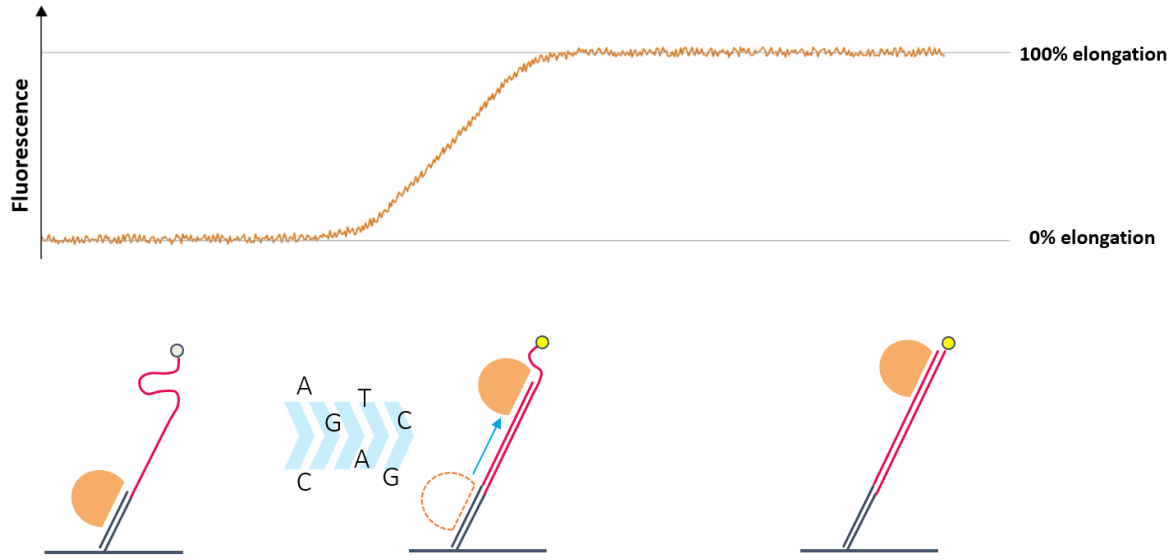

***Figure A17**. The DNA elongation activity of DNA polymerases can be studied with the molecular ruler strategy. The presence of the fluorescent dye on the top of the ligand strand allows to infer its distance from the surface, therefore correlating the increase in fluorescence with the DNA elongation. The ligand on the biochip surface can be used as a template for the elongation of the primer DNA by the DNA polymerase upon the injection of dNTPs.*

In chapter 4, the DNA elongation activity of the Taq Polymerase (Pol) upon dNTPs injection is experimentally described and correlated to the increase in fluorescence change. The kinetic parameters to characterize the enzymatic reaction are extracted and elaborated by using a

Michaelis-Menten model for nucleotide incorporation by a DNA Polymerase described by Walsh and coauthors [19].

Here below, the theory behind the kinetic calculations will be briefly explained. To describe a polymerase reaction, equation (XIII) can be formulated as:

$$Pol \cdot DNA_n + dNTP \rightleftharpoons Pol \cdot DNA_n \cdot dNTP \rightarrow Pol + DNA_{n+1} + PPi \quad \text{(XVIII)}$$

where $Pol \cdot DNA_n$ is the Polymerase-DNA primer/template complex, $Pol \cdot DNA_n \cdot dNTP$ is the complex formed by Polymerase, DNA and dNTP substrate, and $Pol + DNA_{n+1}$ is the one-base extension product. As in equation (XIII), the complex formation is reversible and described by association rate k_{ON} and dissociation rate k_{OFF}, and the rate of product formation is described by k_{cat}. Association and dissociation of nucleotides are faster than the chemical reaction step [20], with a dissociation constant (K_D) equal to $[Pol \cdot DNA_n][dNTP]/[Pol \cdot DNA_n \cdot dNTP]$. The rate of product formation is then given by:

$$\frac{d[Pol+DNA_{n+1}]}{dt} = \left(\frac{k_{cat}}{K_D}\right)[Pol \cdot DNA_n][dNTP] \quad \text{(XIX)}$$

Since the total enzyme is conserved, it can be formulated:

$$[Pol \cdot DNA]_{total} = [Pol \cdot DNA_n] + [Pol \cdot DNA_n \cdot dNTP] + [Pol + DNA_{n+1}] \quad \text{(XX)}$$

Using equation (XX) and assuming large excess of dNTP used, the equation (XIX) can be solved to obtain the concentration of extension product as a function of time:

$$[Pol + DNA_{n+1}] = [Pol \cdot DNA]_{total}\{1 - e^{-\left[\frac{k_{cat}[dNTP]}{K_D+[dNTP]}\right]t}\} \quad \text{(XXI)}$$

$[Pol + DNA_{n+1}]$ is linearly proportional to the fluorescence change increase (Figure A18). The values are plotted as a function of time and fitted to equation (XXI) using a nonlinear least-squares regression method to extract the observed reaction rate constant (k_{obs}):

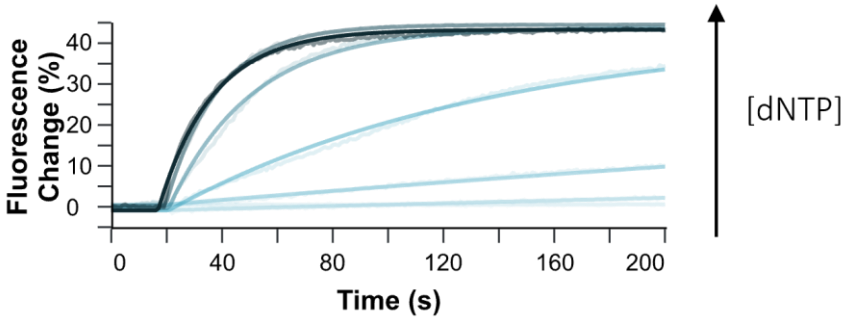

Figure A18. *DNA elongation activity of a Polymerase described by fluorescence change increase as a function of time upon increasing concentrations of dNTP. Each curve is analyzed to obtain the observed reaction rate constant* k_{obs}.

In equation (XXI), the observed reaction rate constant is given by:

$$k_{obs} = k_{cat}[dNTP]/(K_D + [dNTP]) \quad \text{(XXII)}$$

By plotting the k_{obs} values as a function of nucleotide concentration and analyzing the curves using equation (XXII), the dNTPs substrate dissociation or affinity constant (K_D) and enzyme turnover number (k_{cat}) are determined (Figure A19). Given that $K_M = (k_{OFF} + k_{cat})/k_{ON}$, it is possible to consider K_D= K_M if rapid equilibrium of nucleotide association and dissociation is assumed (k_{OFF} >> k_{cat}) [19].

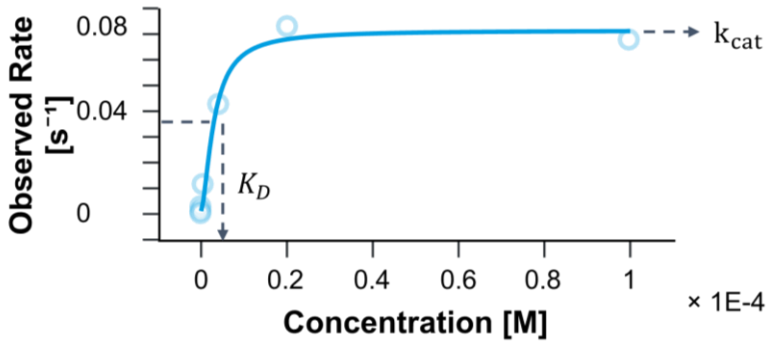

Figure A19*. The DNA elongation activity of the polymerase is characterized in terms of catalytic rate (*k_{cat}*) and substrate affinity (*K_D*), values that are extrapolated by plotting the observed rate as a function of nucleotide concentration.*

The study of enzyme kinetics, such as polymerases, are defined by complex mechanisms of binding and activity; however, switchSENSE® technology, with its DNA-based biochip, allows the study in real-time of these dynamic and complex mechanisms. Indeed, the most important parameters that describe the enzyme kinetics, such as k_{ON}, k_{OFF}, k_{cat}, K_D and K_M, can be resolved and analyzed with common and well-known kinetics equations. Nevertheless, some important

assumptions must be taken in consideration for the interpretation of the experimental results, as visually summarised in Figure A20, and listed below:

- the total enzyme concentration bound to the DNA is constant, and that the enzyme associates and dissociates to the DNA ligand in a rapid equilibrium;
- the substrate concentration injected over the surface is constant;
- the catalytic reaction of product formation is irreversible;
- the effects of allostericity and cooperativity of eventual multi-domains of an enzyme complex are neglected.

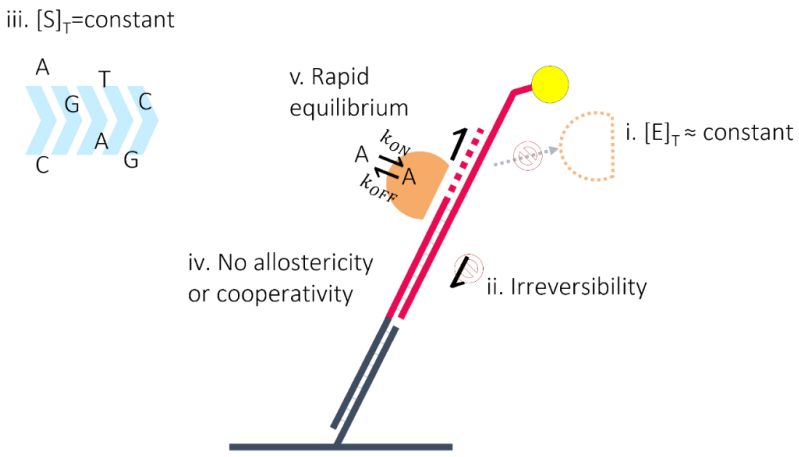

Figure A20. Surface-based technologies necessitate measurements conditions that in turn require assumptions and approximations for the interpretation of the results. In the case of enzyme kinetic measurements, those fundamental assumptions are: i) the concentration of the enzyme must be constant, as well as iii) the flux substrate concentration, ii) the reaction must be irreversible and directional, iv) no allostericity or cooperativity effect are considered and v) a rapid equilibrium between association and dissociation of the dNTPs is considered.

A3. Kinetic Fit Operations

The heliOS software (Dynamic Biosensors) offers a range of binding kinetics fit models for one-to-one and biphasic interactions [21]. The fit models are listed below sorted by increasing complexity (number of free fit parameters). It is usually better to preselect the fit model based on a scientific hypothesis, and then test this hypothesis against the data. In case of multiple possible fit models, the choice is based on the goodness of fit measures (Chi-squared and information criteria).

A3.1 One-to-one kinetics

A3.1.1 Continuous amplitude

The Continuous Amplitude binding model is the standard model that describes binary interactions (1:1 interactions). The Continuous Amplitude describes kinetics that have the same signal amplitudes in the association phase and in the dissociation phase. This model forces the fit to return to baseline.

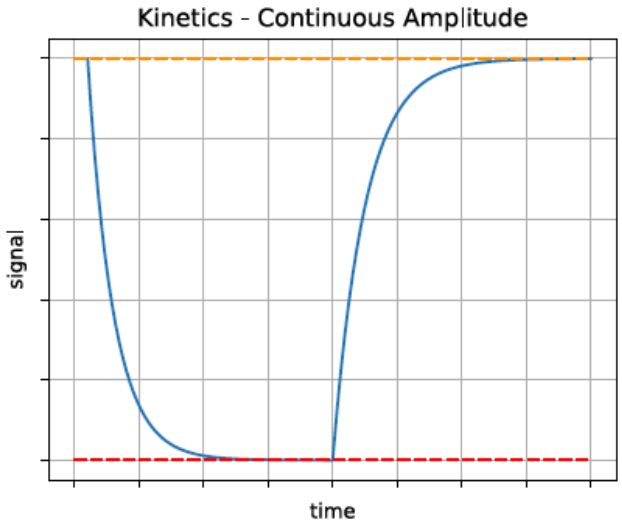

Figure A21. 1:1 interaction fit model: Continuous Amplitude. Adapted from [21].

A3.1.2 Free amplitudes

The Free Amplitudes is the binding model that describes 1:1 interactions that have different amplitudes in the association phase and in the dissociation phase. The Free Amplitudes

describes kinetics of analytes that do not dissociate completely during the measurement time. This model allows for a remaining offset from baseline to infinite (at $t \rightarrow \infty$).

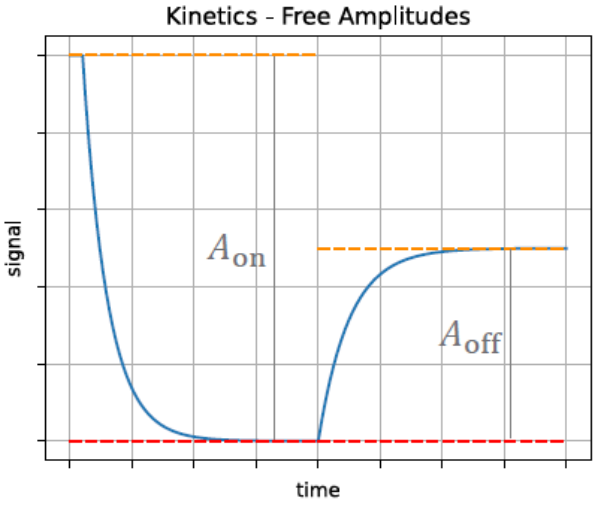

Figure A22. 1:1 interaction model: Free amplitudes. Adapted from [21].

A3.1.3 Time constants

The Time constants is the binding model that describes 1:1 interactions where association and dissociation rates are uncoupled and expressed in terms of time constant. This model allows for a remaining offset from baseline to infinite (at $t \rightarrow \infty$).

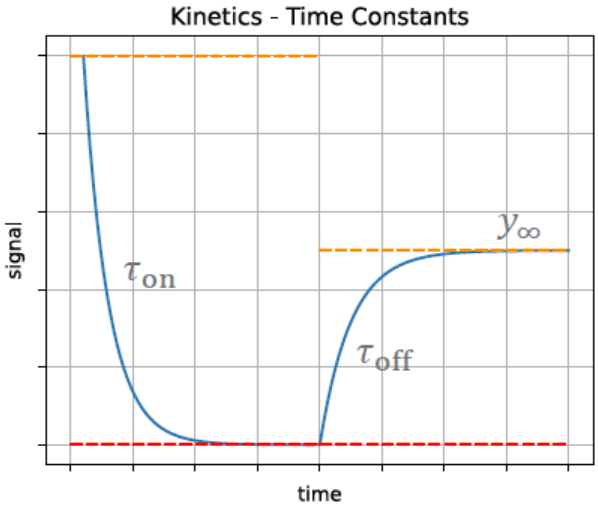

Figure A23. 1:1 interaction model: Time constants. Adapted from [21].

A3.1.4 Discontinuous

The Discontinuous model is the binding model that describes 1:1 interactions and it allows for a jump at the association-dissociation transition. This model allows for a remaining offset from baseline to infinite (at $t \rightarrow \infty$).

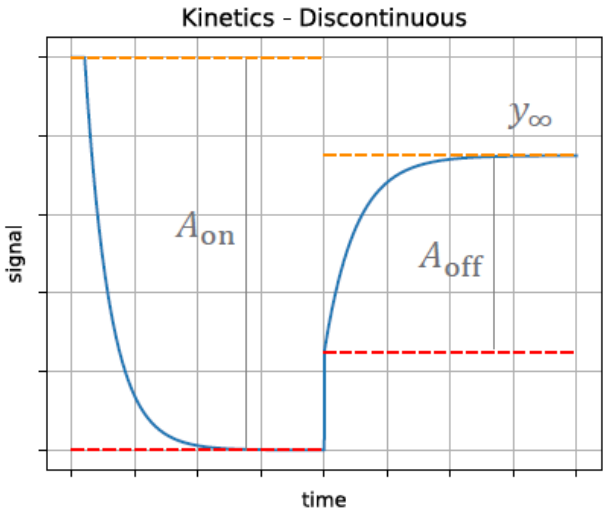

Figure A24. 1:1 interaction model: Discontinuous. Adapted from [21].

A3.2 Monophasic association – biphasic dissociation kinetics

A3.2.1 Continuous amplitude

The Continuous Amplitude model describes kinetics that have the same signal amplitudes in the association phase and in the dissociation phase. The Monophasic association and biphasic dissociation - Continuous Amplitude binding model is the model that describes interactions of analyte binding in a monophasic way during association, but dissociating in a biphasic manner. This model forces the fit to return to baseline.

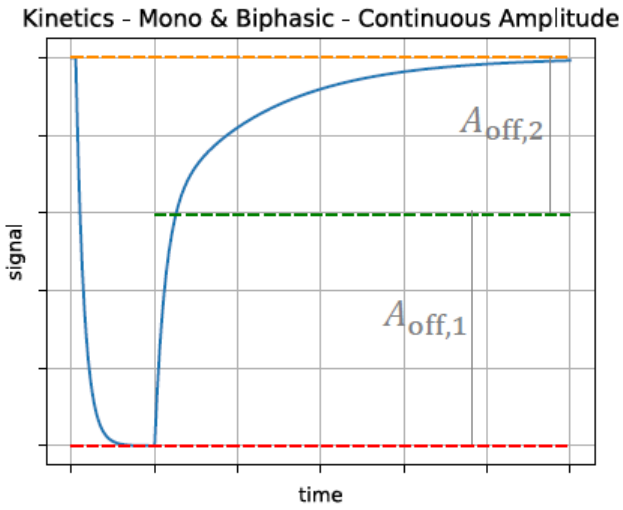

Figure A25. *Monophasic association and biphasic dissociation model: Continuous Amplitude. Adapted from [21].*

A3.2.2 Free amplitudes

The Free Amplitudes is the binding model that describes interactions that have different amplitudes in the association phase and in the dissociation phase. The Free Amplitudes describes kinetics of analytes that do not dissociate completely during the measurement time. This model allows for a remaining offset from baseline to infinite (at $t \rightarrow \infty$).

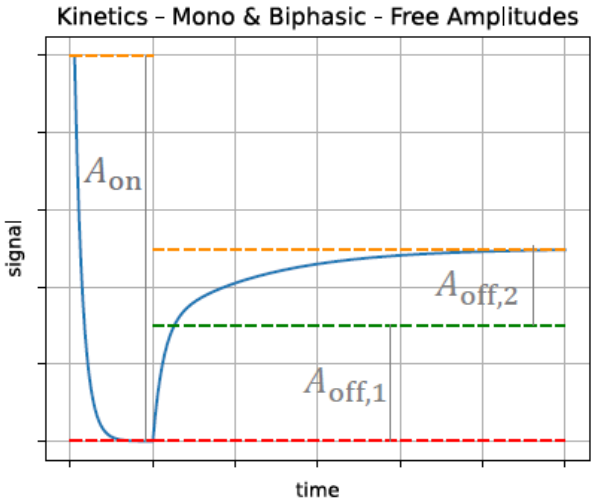

Figure A26. *Monophasic association and biphasic dissociation model: Free amplitudes. Adapted from [21].*

A3.3 Biphasic kinetics

A3.3.1 Continuous amplitude

The Biphasic model - Continuous Amplitude is the model that describes interactions of analyte binding in biphasic way during both in association and dissociation phases. The Continuous Amplitude biphasic model describes kinetics where dissociation amplitudes are equal to the respective association amplitudes at the association-dissociation transition. In the example below, the association signal saturates, and so the dissociation amplitudes are equal to the respective overall association amplitudes (for $t \rightarrow \infty$). This model forces the fit to return to baseline.

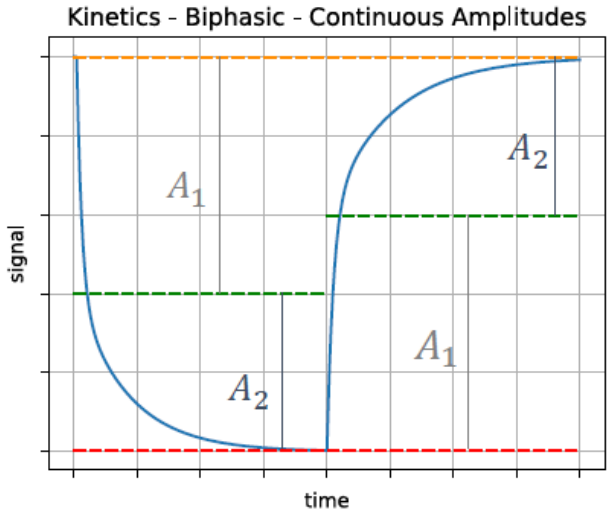

Figure A27. Biphasic kinetics model: Continuous amplitude. Adapted from [21].

A3.3.2 Continuous total amplitudes

The Biphasic model - Continuous total amplitude is the model that describes interactions where the total dissociation amplitude is equal to the sum of the association amplitudes at the association-dissociation transition. The Continuous Amplitude biphasic model describes kinetics where the relative dissociation amplitudes are independent from relative association amplitudes. This model forces the fit to return to baseline.

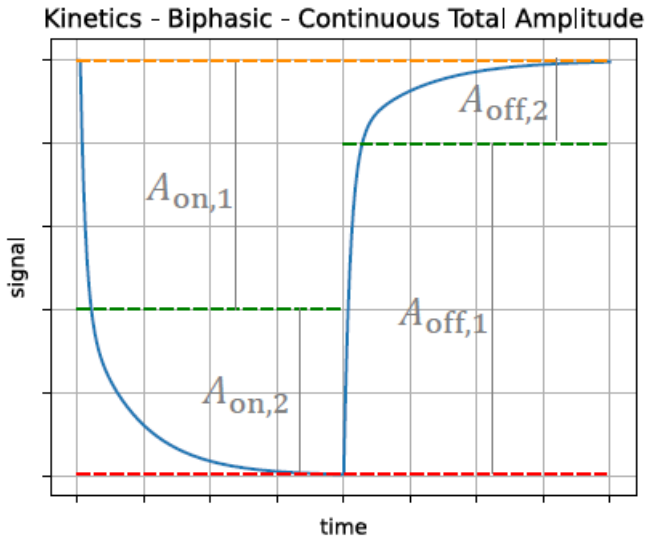

Figure A28. Biphasic kinetics model: Continuous total amplitude. Adapted from [21].

A3.3.3 Free amplitudes

The Free Amplitudes is the binding model that describes interactions that have dissociation amplitudes independent from the association amplitudes. The Free Amplitudes describes kinetics of analytes that do not dissociate completely during the measurement time. This model allows for a remaining offset from baseline to infinite (at $t \rightarrow \infty$).

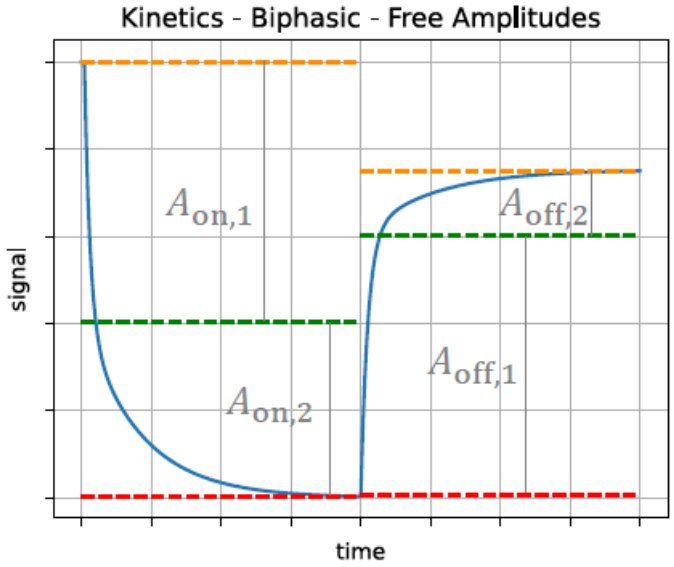

Figure A29. Biphasic kinetics model: Free amplitudes. Adapted from [21].

References

1. Wang, Y.; Baars, I.; Fördös, F.; Högberg, B. Clustering of Death Receptor for Apoptosis Using Nanoscale Patterns of Peptides. *ACS Nano* 2021, *15*, 9614–9626, doi:10.1021/acsnano.0c10104.
2. Wiener, J.; Kokotek, D.; Rosowski, S.; Lickert, H.; Meier, M. Preparation of Single- and Double-Oligonucleotide Antibody Conjugates and Their Application for Protein Analytics. *Scientific Reports* 2020, *10*, 1457, doi:10.1038/s41598-020-58238-6.
3. Reinking, H.K.; Stingele, J. Protein-Oligonucleotide Conjugates as Model Substrates for DNA-Protein Crosslink Repair Proteases. *STAR Protoc* 2021, *2*, 100591, doi:10.1016/j.xpro.2021.100591.
4. Rosen, C.B.; Kodal, A.L.B.; Nielsen, J.S.; Schaffert, D.H.; Scavenius, C.; Okholm, A.H.; Voigt, N.V.; Enghild, J.J.; Kjems, J.; Tørring, T.; et al. Template-Directed Covalent Conjugation of DNA to Native Antibodies, Transferrin and Other Metal-Binding Proteins. *Nat Chem* 2014, *6*, 804–809, doi:10.1038/nchem.2003.
5. Hermanson, G.T. Heterobifunctional Crosslinkers. In *Bioconjugate Techniques*; Elsevier, 2013; pp. 299–339 ISBN 978-0-12-382239-0.
6. Glen Reports | Glen Research Available online: https://www.glenresearch.com/reports/gr32-26.
7. Goodrich, J.A.; Kugel, J.F. *Binding and Kinetics for Molecular Biologists*; Cold Spring Harbor Laboratory Press, 2007; ISBN 978-0-87969-736-5.
8. Keener, J.; Sneyd, J. Biochemical Reactions. In *Mathematical Physiology: I: Cellular Physiology*; Keener, J., Sneyd, J., Eds.; Springer New York: New York, NY, 2009; pp. 1–47 ISBN 978-0-387-75847-3.
9. Atkins, P.W.; De Paula, J. *Physical Chemistry: Thermodynamics, Structure, and Change*; Tenth edition.; W.H. Freeman: New York, 2014; ISBN 978-1-4292-9019-7.
10. Day, Y.S.N.; Baird, C.L.; Rich, R.L.; Myszka, D.G. Direct Comparison of Binding Equilibrium, Thermodynamic, and Rate Constants Determined by Surface- and Solution-Based Biophysical Methods. *Protein Science* 2002, *11*, 1017–1025, doi:https://doi.org/10.1110/ps.4330102.
11. Dynamic Biosensors GmbH TechNote - Binding Theory Equations for Affinity and Kinetics Analysis 2016.
12. Mak, S.; Marszal, A.; Matscheko, N.; Rant, U. Kinetic Analysis of Ternary and Binary Binding Modes of the Bispecific Antibody Emicizumab. *mAbs* 2023, *15*, 2149053, doi:10.1080/19420862.2022.2149053.
13. Kaufman, E.N.; Jain, R.K. Effect of Bivalent Interaction upon Apparent Antibody Affinity: Experimental Confirmation of Theory Using Fluorescence Photobleaching and Implications for Antibody Binding Assays.
14. Schuck, P.; Zhao, H. The Role of Mass Transport Limitation and Surface Heterogeneity in the Biophysical Characterization of Macromolecular Binding Processes by SPR Biosensing. In *Surface Plasmon Resonance*; Mol, N.J., Fischer, M.J.E., Eds.; Methods in Molecular Biology; Humana Press: Totowa, NJ, 2010; Vol. 627, pp. 15–54 ISBN 978-1-60761-669-6.
15. Stengel, G.; Knoll, W. Surface Plasmon Field-Enhanced Fluorescence Spectroscopy Studies of Primer Extension Reactions. *Nucleic Acids Res* 2005, *33*, e69, doi:10.1093/nar/gni067.
16. Bisswanger, H. *Enzyme Kinetics - Principles and Methods*; Wiley VCH, 2017;
17. Langer, A.; Schräml, M.; Strasser, R.; Daub, H.; Myers, T.; Heindl, D.; Rant, U. Polymerase/DNA Interactions and Enzymatic Activity: Multi-Parameter Analysis with Electro-Switchable Biosurfaces. *Scientific Reports* 2015, *5*, 12066, doi:10.1038/srep12066.
18. Kaiser, W.; Rant, U. Conformations of End-Tethered DNA Molecules on Gold Surfaces: Influences of Applied Electric Potential, Electrolyte Screening, and Temperature. *J. Am. Chem. Soc.* 2010, *132*, 7935–7945, doi:10.1021/ja908727d.

19. Walsh, M.T.; Roller, E.E.; Ko, K.-S.; Huang, X. Measurement of DNA Polymerase Incorporation Kinetics of Dye-Labeled Nucleotides Using Total Internal Reflection Fluorescence Microscopy. *Biochemistry* 2015, *54*, 4019–4021, doi:10.1021/acs.biochem.5b00269.
20. Johnson, K.A. The Kinetic and Chemical Mechanism of High-Fidelity DNA Polymerases. *Biochim Biophys Acta* 2010, *1804*, 1041–1048, doi:10.1016/j.bbapap.2010.01.006.
21. Dynamic Biosensors GmbH HeliX Quick Start Guide_v6.1 2022.